Isotopic Heterogeneity in Calcium-Aluminum-Rich Meteoritic Inclusions

Thesis by

Cheryl A. Brigham

In Partial Fulfillment of the Requirements
for the Degree of
Doctor of Philosophy

California Institute of Technology
Pasadena, California

1990

(Submitted January 12, 1990)

This Work is Dedicated to D. and L.

ACKNOWLEDGEMENTS

I first want to thank my advisor, Professor G.J. Wasserburg for his support and advice, and for providing excellent laboratory facilities. I especially want to thank Drs. Ian Hutcheon and Dimitri Papanastassiou for sharing their time, knowledge, and insight, in measures far and above the call of duty. Ian and Dimitri patiently taught me the intricacies of operating complex instruments, writing papers, thinking through scientific problems, and they helped guide me through many obstacles.

I also want to acknowledge the faculty who provided me with advice and useful discussions. Donald Burnett first got me interested in studying meteorites. Sam Epstein advised me on science, careers and life. George Rossman provided terrestrial samples for standards. John Armstrong helped with chemical analyses by EDS. Herbert Palme of the Max Planck Institute in Mainz kindly provided neutron activation analyses of several samples. I thank Peter Goldreich for his friendly advice.

I owe more appreciation than I can ever put into words to some very special friends who have provided moral support and encouragement, who have listened to me, and who have earned my deepest trust. First and foremost, I owe my deepest thanks to David Brin for his companionship, his endless patience, and his constant support. I thank David Paige for his advice and help, and for giving me a computer which forced me to sit down and write my thesis. Thanks to Dave Crisp for being a confidant, and seeing me through a difficult time. Thanks to Alain

Prinzhofer, a special friend who provided me with encouragement, interesting diversions, and French chocolate. I thank Rob Ripperdan for listening to me, and being a very understanding friend. I also thank Pat McGulpin who has been a long time friend, and who provided interesting conversations through many extended lunches.

I would like to thank Chris Price for typing manuscripts and tables, often under rushed conditions. I acknowledge Lindsey Hedges for her meticulous preparation of samples, and for producing slides for conferences. Last but not least, I thank the taxpayers of the United States of America, who paid for this research.

Cheryl A. Brigham

ABSTRACT

Calcium-Aluminum-rich inclusions (CAI), found in meteorites, are among the oldest known solids identified in the solar system. Analyses of CAI have provided constraints on physical and chemical conditions that existed just prior to, and during planetary formation. A few rare inclusions, called FUN (for Fractionation and Unknown Nuclear effects), exhibit large isotopic anomalies and have provided insight into nucleosynthetic and nebular processes.

In this thesis, data obtained on the petrography, chemistry and isotopic compositions of CAI, identified in the carbonaceous chondrite Allende, are used as tracers to address several specific questions: 1) What are the relationships between fine and coarse-grained CAI? 2) What are the differences, in composition and origin, between FUN inclusions and isotopically normal CAI? 3) What was the role of volatility-controlled processes, such as distillation and condensation, in the evolution of CAI? 4) What was the role of chemical alteration and isotopic reequilibration in the evolution of CAI?

Isotopic data were obtained by thermal ionization and ion microprobe mass spectrometry for individual grains within both fine and coarse-grained CAI, and correlated with petrographic and chemical observations. Evidence is presented for the enrichment of fine-grained inclusions in the lighter isotopes of Mg, in contrast to coarse-grained CAI, which are enriched in the heavier isotopes. Isotopic heterogeneity was observed within both fine and coarse-grained inclusions.

Heterogeneity is discussed in the context of primary and secondary phases, mineral alteration processes, and isotopic reequilibration.

A new class of coarse-grained inclusion, characterized by a distinct purple color and high spinel contents (≥50%), were identified and found to exhibit a high frequency (20%) of FUN isotopic anomalies. Four new FUN inclusions were identified and studied in detail. The correlated isotopic fractionation for Mg, Si, and Cr in these inclusions, suggests the importance of volatility-controlled formation processes. A model is presented for the evolution of FUN inclusions, involving distillation of ordinary chondritic material, with a mass loss of around 70%, followed by exchange with isotopically normal reservoirs. The high spinel contents and large isotopic fractionation of these inclusions, may indicate that they formed at higher temperatures than isotopically normal CAI.

TABLE OF CONTENTS

TABLE OF FIGURES

TABLE OF TABLES

Figure 1.1a. Fine-grained inclusion AlC1-E from Allende (4 x 14 mm), consisting Fe-rich spinel, fassaite and anorthite, with a white mantle of anorthite and diopside.

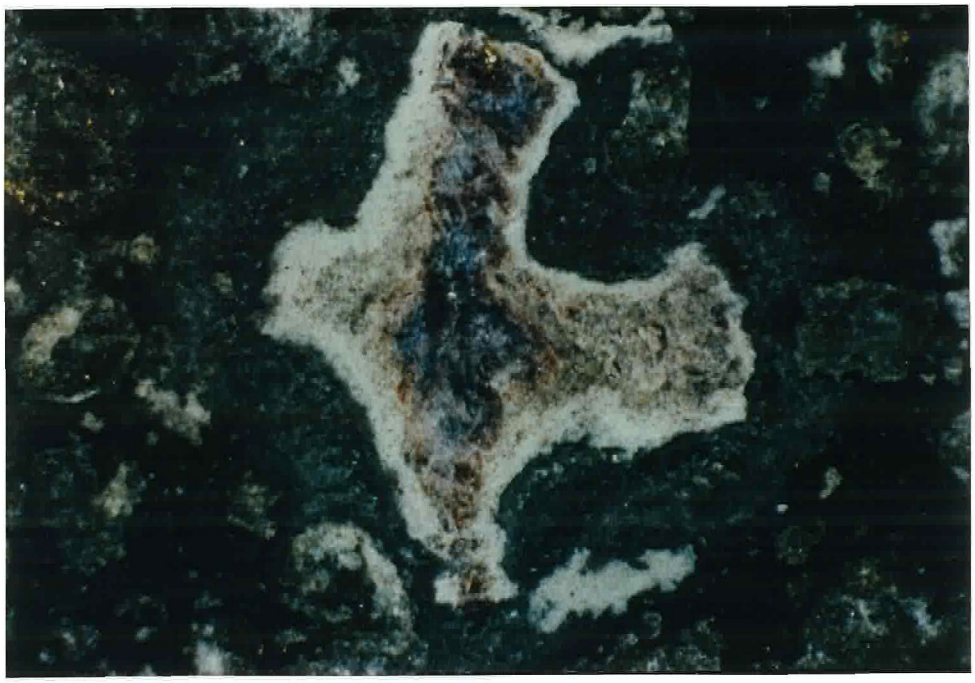

Figure 1.1b. Coarse-grained inclusion in Allende, with a diameter of 5 mm. HB1 is a purple, spinel-rich inclusion, with major phases spinel and melilite.

CHAPTER ONE

INTRODUCTION

Meteorites have proven important because they retain a record of early solar system formation events, all traces of which have been destroyed in larger planetary bodies by processes such as melting, chemical differentiation, and outgassing. Experimental studies of meteorites provide insight into physical and chemical conditions in the presolar nebula, as well as later events, including the formation of proto-planetary bodies, fragmentation, brecciation, collisional shock, and chemical alteration.

Meteorites exhibit isotopic compositions for many elements which are distinct from those in terrestrial materials. Isotopic variations in meteorites can be used as tracers to investigate solar system formation processes. For example, the solar nebula was previously believed to have been isotopically homogeneous; however, discoveries of unusual isotopic compositions in meteorites indicate incomplete mixing of distinct components in the solar nebula. Isotopes are used to investigate the degree of heterogeneity in the presolar nebula, the possible mixing of isotopically distinct reservoirs, timescales for the formation of solid bodies, and the physical processes such as condensation and evaporation which acted on the evolving proto-solar system.

A remarkable increase in knowledge about the early solar nebula occurred after the identification in chondritic meteorites of refractory inclusions, which appear to be primitive materials formed early in the history of the solar system (review by Grossman, 1980). This thesis presents new chemical, isotopic and petrographic data for refractory meteoritic inclusions. The data are used to develop constraints on processes involved in the formation of these inclusions, and to draw new insights into physical and chemical conditions that must have existed in the presolar nebula.

1.1. BACKGROUND

Carbonaceous meteorites consist predominantly of fine-grained silicate matrix, surrounding olivine-pyroxene chondrules and fragments. Refractory mineral assemblages termed Calcium-Aluminum-rich Inclusions (CAI), were first identified in the Allende meteorite, a carbonaceous chondrite of Type C3V, which struck Mexico in 1969 (Clarke et al., 1970; Marvin et al., 1970).

Ca-Al-rich inclusions are millimeter to centimeter-sized, white or pink objects (Figure 1.1), which consist predominantly of refractory minerals such as melilite, Ti-pyroxene, anorthite, spinel, and perovskite (Grossman, 1975, 1980). Measured chemical compositions and mineralogy are similar to those calculated from thermodynamic models, for the condensation of phases from a cooling gas of solar composition (Lord, 1965; Grossman, 1972), prompting suggestions that CAI may represent early condensates from the solar nebula (Larimer and Anders, 1970; Boynton, 1975). Subsequent petrographic and isotopic observations indicated that

the inclusions are indeed primitive, but are not simply direct nebular condensates; rather they appear to have undergone multiple-stage processing including melting, distillation and chemical alteration (cf. Clayton et al., 1977; Meeker et al., 1983).

Isotopic data reveal that Ca-Al-rich inclusions are among the oldest known solids identified in the solar system. CAI yield the most primitive $^{87}Sr/^{86}Sr$ isotopic ratios ever measured (Gray et al., 1973), and $^{207}Pb/^{206}Pb$ model ages as old as 4.565 billion years (Chen and Tilton, 1976; Tatsumoto et al., 1976; Manhes et al., 1987).

Early formation of these inclusions in the solar nebula is further supported by measurements in many CAI of excesses in Magnesium-26, attributed to in situ decay of the short-lived isotope ^{26}Al (Lee et al., 1976, 1977; Wasserburg and Papanastassiou, 1982). This observation requires that refractory inclusions formed within a few million years after a late-stage episode of nucleosynthesis contributed material to the proto-solar cloud. Evidence for early formation is preserved in CAI despite indications of later chemical alteration.

The primitive character of Ca-Al-rich inclusions is further substantiated by observations of large isotopic anomalies for oxygen (Clayton et al., 1973), as well as for heavier elements such as Ca, Ti and Cr (reviews by Lee, 1979; Wasserburg et al., 1980). These anomalies for heavy elements indicate that the inclusions retain evidence of several distinct nucleosynthetic components, which were homogenized in later-forming solar system materials. The nucleosynthetic origin of isotopic anomalies has been investigated by comparing observed patterns, with those predicted from theoretical astrophysical models (Niederer et al., 1980; Birck and Allegre 1984; Papanastassiou, 1986).

There are two distinct classes of Ca-Al-rich inclusions: coarse-grained and fine-grained. These classes are distinguished by grain size, petrographic textures, and mineralogy (Clarke et al., 1970; Grossman 1975). Most petrographic and isotopic studies have concentrated on coarse-grained inclusions. A petrographic classification of coarse-grained CAI is presented by Grossman (1975). Coarse-grained inclusions consist predominantly of refractory mineral phases (of grain size 100 μm to 1 mm), such as melilite, fassaite, anorthite, perovskite and spinel (review by Grossman, 1980). Inclusions also contain numerous opaque assemblages of metal alloys, sulfides, oxides and phosphates, which are enriched in refractory siderophile elements (El Goresy et al., 1978). Textures of many inclusions indicate that they have undergone melting (Blander and Fuchs, 1975; Stolper, 1982), and varying degrees of nebular alteration or planetary metamorphism (Clayton et al., 1977; Meeker et al., 1983). In addition, inclusions are often surrounded by a sequence of thin rims containing lower-temperature phases similar to those observed in fine-grained inclusions: Fe-bearing spinel, perovskite, feldspathoid and hedenbergite (Wark and Lovering, 1977; MacPherson et al., 1981).

Fine-grained inclusions are also abundant in the Allende meteorite (≈9 volume percent estimated by Clarke et al., 1970), but have not been as well-studied due to technical difficulties in analyzing grains of sizes 0.5 to 100 μm. Fine-grained inclusions are loosely-packed collections of refractory phases (spinel, fassaite, anorthite and hibonite), coupled with lower-temperature Fe- and Na-rich phases such as hedenbergite, hercynite, nepheline and sodalite. The presence of these Fe and

Na-rich phases suggests evolution of fine-grained inclusions to lower temperatures than coarse-grained inclusions. In spite of this evidence for chemical alteration, many fine-grained inclusions retain large isotopic fractionation effects.

Fine-grained inclusions differ from coarse-grained inclusions in their enrichment of volatile elements, in their depletion of refractory and volatile siderophile elements (Grossman and Ganapathy, 1976), and in exhibiting fractionated rare earth element patterns (Mason and Martin, 1977). The mechanisms of formation, and the relationships between coarse-grained and fine-grained inclusions, have not been well-understood. One aim of this thesis is to relate and compare the processes likely to have influenced the formation of fine and coarse-grained inclusions.

A few rare coarse-grained Ca-Al-rich inclusions, called FUN (for Fractionation and Unknown Nuclear effects) have provided insight into a broad range of nucleosynthetic and nebular processes. FUN inclusions were first identified by their large isotopic fractionation for magnesium and oxygen, and by apparent deficits in ^{26}Mg (Clayton and Mayeda, 1977; Wasserburg et al., 1977).

The large mass-dependent fractionation observed for O and Mg in FUN inclusions, as well as for Si, Ca and Cr, have provided insight into early nebular processes involving condensation, evaporation, and the mixing and preservation of isotopically-distinct reservoirs (Clayton et al., 1975; Niederer and Papanastassiou, 1984).

FUN inclusions exhibit isotopic anomalies for all elements measured: O, Mg, Si, Ca, Ti, Cr, Sr, Ba, Sm (cf., review by Lee, 1979; Wasserburg et al., 1980; Niederer et al., 1980; Papanastassiou, 1986). The patterns for nuclear anomalies are

correlated over relatively broad regions of the chart of the nuclides, and have been attributed to the preservation of isotopic signatures of distinct nucleosynthetic components (cf. reviews by Wasserburg et al., 1980; Begemann, 1980). Nuclear anomalies provide information on the degree of primordial heterogeneity in the early solar nebula, and constraints on stellar models of nucleosynthesis. Part of this thesis involves a search for, and characterization of, a new class of FUN inclusion.

1.2. THESIS APPROACH

This thesis attempts to use isotopes as tracers to address several problems: 1) the relationship between fine-grained and coarse-grained Ca-Al-rich inclusions; 2) the formation of FUN inclusions and their relationship to isotopically normal inclusions; 3) the role of volatility-controlled processes, such as distillation and condensation, in the evolution of CAI; 4) the degree of mixing of isotopically-distinct reservoirs in the presolar nebula; and 5) the role of isotopic reequilibration and low-temperature chemical alteration in the evolution of CAI.

In the course of this work, I have identified a new class of coarse-grained inclusions, which exhibit an unusually high abundance of FUN isotopic anomalies (≈ 20% of inclusions analyzed), compared to fewer than 6% of typical coarse-grained inclusions. These inclusions are identified by macroscopic characteristics, including a distinct purple color and high spinel contents (Figure 1.1b). A study was undertaken of the new FUN inclusions to characterize their petrography and isotopic composition; and to understand their relationship to isotopically normal CAI.

The thesis presents experimental data obtained on the petrography, chemistry and isotopic composition of both coarse and fine-grained Ca-Al-rich inclusions, and attempts to interpret these data in the context of models for the formation and alteration of the inclusions. The experiments involved measuring in situ isotopic compositions for individual phases in inclusions, and correlating these data with chemical and petrographic observations. Isotopic fractionation measurements were obtained for several elements (Mg, Si, Cr, Fe), and a search for correlated fractionation effects was undertaken, in order to determine the importance of volatility-controlled processes. The degree of variation of isotopic fractionation from mineral to mineral within an inclusion is used to constrain the degree of isotopic re-equilibration and the extent of secondary alteration reactions. Isotopic and petrographic data are also used to distinguish primary and secondary phases.

Experimental studies of both fine and coarse-grained CAI entailed an initial isotopic survey of a large number of inclusions. Mg isotopic compositions were determined by thermal ionization mass spectrometry, to identify inclusions with large isotopic effects. Special techniques were required for handling fine-grained materials, and extremely small sample sizes.

Petrographic observations were obtained by optical microscopy and by scanning electron microscopy. Chemical abundances were measured by energy dispersive x-ray analysis, and by instrumental neutron activation analysis.

The ion microprobe was used for a more detailed study of the isotopic compositions of individual phases in inclusions, which exhibited large isotopic effects. The aim of the ion probe studies was to: 1) determine variations in

fractionation from mineral to mineral within an inclusion; 2) correlate isotopic measurements with petrography or mineral chemistry; 3) measure fractionation in secondary phases and regions of alteration; 4) search for correlated fractionation for several elements; and 5) determine the presence of excess ^{26}Mg.

1.3. THESIS SCOPE

This thesis consists of two distinct parts. The first part describes the petrography and isotopic composition of a group of spinel-rich, coarse-grained inclusions, which exhibit an unusually high abundance of FUN isotopic anomalies. The second part deals with the petrography, chemistry and magnesium isotopic characteristics of fine-grained inclusions. A summary of the contents of each thesis chapter follows.

The physical principles of isotope systematics are presented in Chapter 2. The first part of the chapter deals with mass-dependent fractionation; including physical processes that fractionate isotopes, such as distillation and condensation. Fractionation is considered in terms of equilibrium and kinetic processes. A detailed presentation is given for the Rayleigh model, which allows calculation of isotopic profiles resulting from fractional distillation and condensation. Complications to this model, including the mixing of reservoirs and evolution by multistage processes, are discussed. Isotopic fractionation laws are also reviewed.

The second part of Chapter 2 reviews the use of short-lived radionuclides (such as ^{244}Pu, ^{129}I and ^{26}Al) to constrain the time interval between addition of

nucleosynthetic material to the solar nebula and formation of CAI. Isotopic systematics for radiogenic nuclides, and the means for determining in situ radiogenic effects are also presented.

Chapter 3 presents the analytical techniques used in this work, including criteria for the selection and sampling of inclusions for study, and techniques for preparing samples for petrographic and isotopic analysis. Thermal ionization and ion microprobe instrumentation are presented in detail. The chapter also discusses how standards are used to determine instrumental fractionation, in order to estimate isotopic precision and reproducibility, and to determine the magnitude of isotopic effects intrinsic to the samples.

Chapter 4 presents petrographic, chemical and isotopic data for Purple, Spinel-rich coarse-grained Inclusions (PSI), which exhibit a high frequency of FUN isotopic anomalies. Four new FUN inclusions were identified and studied in detail. Ion probe measurements of Mg, Si, and Cr isotopes are reported for individual phases. Correlated isotopic fractionation for the elements suggests the importance of volatility-controlled processes. Extreme isotopic heterogeneity is observed within the inclusions. A model is presented for the evolution of FUN inclusions by distillation of ordinary chondritic material, followed by reaction with isotopically normal material to produce isotopically heterogeneous compositions.

Isotopic and petrographic data are presented in Chapter 5 for opaque assemblages within the coarse-grained inclusions. The first in situ measurements of Mg, Cr and Fe isotopic compositions of opaque assemblages in FUN inclusions are reported. The data are used to constrain processes involved in the evolution of

opaque assemblages, such as element transport and secondary alteration reactions.

Chapter 6 describes petrographic, chemical and Mg isotopic data obtained for fine-grained Ca-Al-rich inclusions. Evidence is presented for enrichment of the fine-grained inclusions in the lighter isotopes of Mg, in contrast to coarse-grained inclusions which are enriched in the heavier isotopes. Substantial isotopic heterogeneity for Mg was observed within individual inclusions. These data are used to distinguish primary and secondary phases, and to constrain mineral alteration processes and isotopic reequilibration. A multistage model for the evolution of fine-grained inclusions is presented.

In conclusion, the experimental data presented in this thesis indicate distinct isotopic compositions for the coarse and fine-grained CAI. The FUN inclusions examined in this study exhibit large isotopic fractionation for Mg, Si, Cr and Fe, as well as substantial nuclear effects for Ca, Ti and Cr. The large fractionation effects and the refractory chemical compositions of the FUN inclusions may result from distillation of chondritic material. The fine-grained CAI can be understood as recondensates. Detailed formation models are presented in this thesis. Isotopic heterogeneity in both fine and coarse-grained inclusions indicates varying degrees of equilibration with normal material.

CHAPTER TWO

ISOTOPE SYSTEMATICS

2.1. INTRODUCTION

Isotopic variations in Ca-Al-rich inclusions can be categorized as: 1) fractionation effects; 2) radiogenic anomalies due to the decay of unstable nuclei; and 3) nuclear anomalies involving excesses or deficits in individual isotopes. The emphasis of this work has concerned mass-dependent isotopic fractionation. This chapter reviews the physical principles and models dealing with isotopic fractionation.

Isotopic fractionation occurs when an element is partitioned among various reservoirs by chemical exchange reactions, or by physical processes such as distillation, condensation or diffusion. Fractionation will be considered in terms of equilibrium and kinetic processes. All isotopic fractionation effects discussed in this chapter are observed to be mass-dependent; although non-mass-dependent fractionation has been reported for chemical reactions involving oxygen.

A Rayleigh model, which describes isotopic fractionation resulting from fractional distillation or condensation, is detailed, and used to model the physical processes involved in the formation and evolution of CAI. The Rayleigh model can provide an estimate of the degree of evaporation required to produce the magnitudes of

isotopic fractionation observed for CAI.

Finally, the isotope systematics of radioactive decay are reviewed, with an emphasis on short-lived nuclides, which were present in the early solar system, but are now extinct. Radiogenic anomalies due to the decay of the short-lived nuclide ^{26}Al are discussed.

2.2. DEFINITIONS

The fractionation factor α_{AB} is defined as the quotient resulting from dividing the ratio of the number of isotopes i, j in phase A ($R^{ij}_A = N^j_A / N^i_A$), by the ratio of the number of isotopes i, j in phase B ($R^{ij}_B = N^j_B / N^i_B$):

$$\alpha_{AB} = R^{ij}_A / R^{ij}_B = (N^j_A / N^i_A) / (N^j_B / N^i_B).$$

Isotopic compositions are reported relative to the isotopic ratio of a standard, in delta notation (in permil or parts per thousand):

$$\delta^{ij}_A = \{(R^{ij}_A / R^{ij}_{st}) - 1\} \times 10^3,$$

where R^{ij}_{st} is the isotopic ratio of a standard. For small fractionation, δ-values and the factor α_{AB} are approximately related by:

$$\delta^{ij}_A - \delta^{ij}_B = \Delta^{ij}_{AB} \cong 10^3 \ln\alpha_{AB}.$$

For this work, measured or unnormalized isotopic ratios, are reported as Δ-values expressing the deviation (in permil) of the measured isotopic ratio for the sample (R^{ij}_m), relative to the normal value (R^{ij}_t), determined by measurements of standards:

$$\Delta^{ij} = \{(R^{ij}_m / R^{ij}_t) - 1\} \times 10^3 \quad \text{(in permil)}.$$

Isotopic fractionation is reported as deviations of the measured isotopic ratios per mass unit: $F^{ij} = \Delta^{ij} / (m_j - m_i)$ (in permil per amu),

where m_j, m_i are the masses of isotopes i and j.

Nuclear anomalies, which are also called nonlinear effects, are defined as excesses or deficits in individual nuclides, which are superimposed upon the general mass-dependent fractionation trend. In this work, δ-values will be used only to report nonlinear effects, after mass-dependent fractionation effects have been removed:

$$\delta^{jk}_c = \{(R^{jk}_c / R^{jk}_{st}) - 1\} \times 10^3 \quad \text{(in permil)}.$$

where R^{jk}_c is the isotopic ratio after correction for mass fractionation, using the fractionation laws discussed in Section 2.3.6.

In order to resolve nuclear anomalies, the element must have at least three isotopes; however, the assignment may not be unique for small effects if there are only three isotopes. Figure 2.1 illustrates isotopic fractionation for Mg, which has three isotopes of masses 24, 25 and 26. Positive fractionation is defined as an enrichment in the heavier isotopes (Figure 2.1b); negative fractionation as an enrichment in the lighter isotopes (Figure 2.1c). Figure 2.1d illustrates excesses in ^{26}Mg superimposed upon the isotopic fractionation trend, as determined by the ^{25}Mg/^{24}Mg ratio. For example, the decay of radiogenic ^{26}Al may result in excesses in ^{26}Mg. If the mass-dependent fractionation trend had instead been determined from the ^{26}Mg/^{24}Mg ratio (Figure 2.1e); then the nonlinear effect would appear as a deficit in ^{25}Mg, of a magnitude half that observed for the excess in ^{26}Mg in Figure 2.1d:

$$\delta^{26}\text{Mg} = \delta^{24}\text{Mg} = -2\delta^{25}\text{Mg}.$$

Figure 2.1. Schematic diagrams illustrating isotopic fractionation and nonlinear isotopic anomalies for Mg. Mg has three isotopes of masses 24, 25, 26, with approximate abundances of 79%, 10% and 11%, respectively. Figure 2.1a arbitrarily assigns equal abundances to the three isotopes of Mg, and for illustration purposes this will be considered the normal distribution. Figure 2.1b portrays positive fractionation, with an enrichment in the heavier isotopes; while Figure 2.1c shows negative fractionation, with an enrichment in the lighter isotopes. Figure 2.1d illustrates a nonlinear anomaly consisting of an excess in ^{26}Mg superimposed upon the positive fractionation trend, assuming that fractionation is determined by the ratio of masses 25 and 24. In Figure 2.1e, fractionation is instead determined from the $^{26}Mg/^{24}Mg$ ratio, and the nonlinear anomaly appears as a deficit in 25, but with a magnitude half that of the ^{26}Mg excess in Figure 2.1d. The assignment is not unique for small effects, if there are only three isotopes.

Mg ISOTOPE FRACTIONATION AND NONLINEAR EFFECTS

a) NORMAL

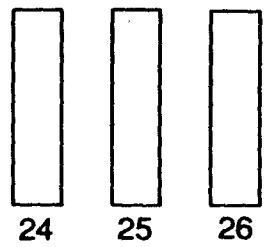

b) POSITIVE FRACTIONATION

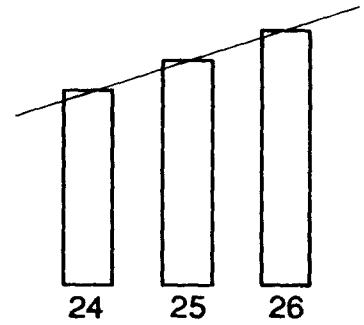

c) NEGATIVE FRACTIONATION

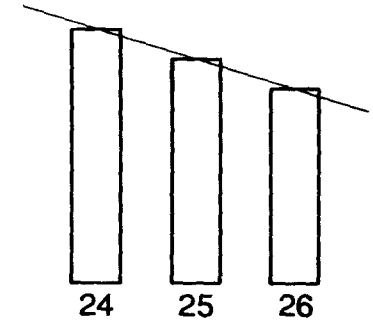

d) POSITIVE FRACTIONATION
EXCESS 26

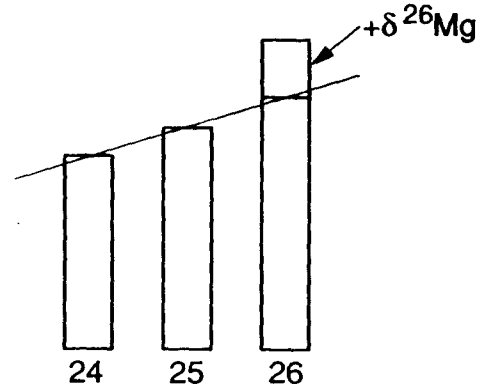

e) POSITIVE FRACTIONATION
DEFICIT 25

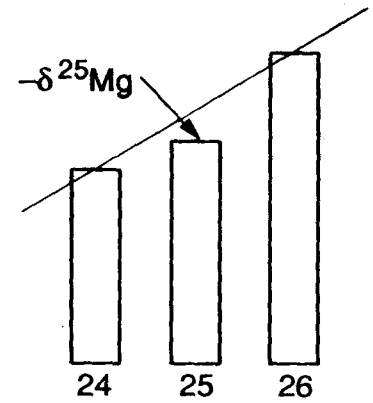

2.3. ISOTOPIC FRACTIONATION

2.3.1. PHYSICAL AND CHEMICAL PROCESSES

Isotopic fractionation occurs when an element is partitioned among various reservoirs, usually by a mass-dependent process, resulting in reservoirs which contain different proportions of the isotopes of that element. The characteristic signature of mass-dependent isotopic fractionation is a smooth dependence of isotopic effects on the mass difference of the isotopes, such that the magnitude of fractionation between species of masses M and M+2 is approximately twice as large as the fractionation between masses M and M+1. Large deviations of individual isotopes from this generally linear trend cannot be caused by small degrees of mass fractionation, and are attributed instead to nuclear anomalies (Figure 2.1).

Chemical and physical processes which produce isotopic fractionation include:

1) Isotopic exchange reactions, in which the isotopes of an element are redistributed between different chemical substances;

2) Kinetic or unidirectional reactions, which depend upon differences in the reaction rates of molecules containing different isotopes; and

3) Physical processes, including condensation, evaporation, melting, crystallization and diffusion.

Mass-dependent isotope fractionation occurs because the physical and chemical properties of molecules are dependent upon the masses of their constituent atoms.

This mass-dependence is attributed to quantum-mechanical effects, involving differences in vibrational energy, as discussed below. Quantum mechanical calculations attribute different zero-point energies to molecules which are chemically identical, but contain atoms of different isotopic weights. (Zero-point energy denotes the energy of a molecule above the minimum of the potential energy curve at an absolute temperature of zero.) Molecules containing heavier isotopes have lower zero-point energies; therefore, more energy is required to dissociate these heavier molecules, and they react less readily than species containing lighter isotopes.

Non-mass-dependent isotope fractionation effects, such as those chemically produced during the synthesis of ozone by electrical discharge (Thiemens and Heidenreich, 1983), have been attributed to the effect of isotope substitution (symmetrical or nonsymmetrical) on the number of available rotational states (Robert et al., 1983).

2.3.2. EQUILIBRIUM ISOTOPIC FRACTIONATION

Isotopic fractionation occurs between phases in thermodynamic equilibrium, if the free energies of the phases depend on isotopic composition. This is due to the mass dependence of the ground-state vibrational energy of the isotopic species. In theory, isotopic fractionation factors can be calculated for equilibrium isotope exchange processes, by statistical mechanical methods, using experimentally-determined vibrational frequencies. The theory of equilibrium isotope effects has

been discussed by Urey (1947), Bigeleisen and Mayer (1947) and Oppenheim and Friedman (1961).

Consider the isotope exchange reaction between molecules A and B containing isotopes i and j: $A^i + B^j = A^j + B^i$. The isotopic fractionation factor α_{AB} between the two molecules A and B is defined as the quotient of two isotopic ratios: $\alpha_{AB} = R^{ij}_A / R^{ij}_B$, where R^{ij}_A ($= N^j_A / N^i_A$) and R^{ij}_B ($= N^j_B / N^i_B$) are the ratios of the two isotopes i and j, in species A and B.

The isotopic fractionation factor is related to the equilibrium constant by $\alpha_{AB} = K^{1/n}_{AB}$, where n represents the number of atoms exchanged. For the exchange of only one atom, $\alpha_{AB} = K_{AB}$.

Using statistical mechanics, the equilibrium constant K_{AB} for this exchange reaction, can be expressed as the ratio of the partition functions Q_A and Q_B for the two isotopic species of compounds A and B: $K_{AB} = (Q_A^j/Q_A^i) / (Q_B^j/Q_B^i)$.
The partition function Q is defined as the summation over all the allowed energy levels of the species: $Q = \sum_i\{g_i\exp(-E_i/kT)\}$, where g_i is the statistical weight of E_i, and T is the absolute temperature.

The important point is that only the vibrational energy levels exhibit a mass dependence. The ground-state vibrational energy $E_v = (1/2)h\nu$ is a function of the vibrational frequency ν, which is proportional to the mass as $m^{-1/2}$. Vibrational frequencies are determined experimentally from spectroscopic data. In this manner, the isotopic fractionation factor α_{AB} can be calculated from experimental vibrational frequencies. However, vibrational frequency data for isotopic substitution are not known for most molecular species. Calculations are complicated by lattice effects

which need to be considered for partitioning between solid phases. In addition, the fractionation factor is a function of temperature, such that isotopic fractionation decreases at higher temperatures: $\ln\alpha_{AB} \propto 1/T^2$, where T is the absolute temperature.

Experimental calculations for hydrogen (Bigeleisen and Mayer, 1947; Oppenheim and Friedman, 1961) yield fractionation values in close agreement with experimental observations. Theoretical calculations of equilibrium constants for sulfur isotopic exchange reactions, between sulfur dioxide and hydrogen sulfide, were found to agree with experimental results within ≈1‰ for the temperature range studied (Thode et al., 1970).

Clayton et al. (1978) have estimated the isotopic fractionation of Si for the equilibrium isotopic exchange reaction, between solid forsterite and gaseous silicon monoxide (SiO) and gaseous silicon sulfide (SiS). Vibrational frequency data for isotopic substitution of the gaseous species SiO and SiS were used to calculate partition functions for these species. Neglecting lattice effects for the solid, the gas-solid isotopic fractionation of Si at a temperature of 1400°K was calculated to be ≈2‰ amu^{-1}. Clayton et al. estimated that the magnitude of this Si fractionation increases with decreasing temperature at the rate of 0.3‰ per 100 degrees. Si fractionation by equilibrium exchange processes at higher temperatures would be negligible.

Interpreting isotopic effects as equilibrium effects has the advantage that the results are independent of the reaction pathways or processes undertaken to reach equilibrium. However, it appears that equilibrium effects are small at the high temperature ranges under consideration.

2.3.3. KINETIC ISOTOPIC FRACTIONATION

As indicated above, isotopic fractionation due to equilibrium processes is negligible at high temperatures. A better description of fractionation occurring at high temperatures is provided by kinetic processes, as in solid-vapor transitions, such as condensation and evaporation. Kinetic effects result from physical processes or chemical reactions in which the rate depends upon the atomic mass of the species. It is necessary to understand the reaction mechanisms involved.

The focus of this discussion is on kinetic isotope effects due to mass-dependent differences in the velocities of the isotopes. Assuming that equipartition of energy holds in a reservoir at a given temperature, molecules containing isotopes of different masses will exhibit the same average kinetic energy. Lighter molecules in the reservoir will thus have a higher velocity, which is equivalent to a greater flux per number density for removal of the lighter isotopes from the reservoir. Therefore, kinetic effects result in the preferential vaporization or condensation of the lighter isotopes from a reservoir.

There are two relevant fractionation factors which need to be distinguished: 1) the fractionation factor of the process (α), which describes the relative difference in fractionation between two phases, as a result of removing an infinitesimal amount of material; and 2) the final fractionation factor (F) of the resulting bulk materials, relative to isotopically normal material. Consider a distillation process: the

fractionation factor of the process is assumed to be constant throughout distillation, while the bulk fractionation values change as distillation proceeds.

The following discussion concerns the fractionation factor of the process. The relevant quantities necessary to describe isotopic effects are the magnitude and sign of the fractionation factor. By convention, a positive fractionation factor favors the heavier isotopes, while a negative fractionation factor reflects enrichment of the lighter isotopes. These two cases are illustrated schematically in Figure 2.1. According to the kinetic model above, a negative fractionation factor would characterize the vapor resulting from distillation of a solid where equipartition of energy holds, since the lighter isotopes are preferentially volatilized.

Estimation of the magnitude of kinetic effects may be seen for the case that the process behaves like effusion from a Knudsen cell. Isotopic fractionation is assumed to follow a mass-dependence of $(m_i/m_j)^{-1/2}$, where m_i and m_j are the masses of the relevant isotopic species. Experimental verification for the inverse square-root mass-dependence has been demonstrated by observations of the effusion of gases and by evaporation of alkalis (Eberhardt et al., 1964).

The magnitude of kinetic effects depends upon the atomic or molecular species in the gas phase. Assuming an inverse square root mass-dependence, kinetic fractionation factors can be calculated as: $\alpha = [1 - (m_i / m_j)^{-1/2}] \times 10^3$, where m_i and m_j are the isotopic masses. Calculated magnitudes for kinetic fractionation factors are given in Table 2.1, assuming the species listed are the most abundant gas phase species.

Table 2.1. Kinetic Fractionation Factors

Mg	20.6‰ amu^{-1}
SiO	11.3‰ amu^{-1}
SiO_2	9.0‰ amu^{-1}
Ca	12.2‰ amu^{-1}
Cr	9.6‰ amu^{-1}
Fe	9.0‰ amu^{-1}

To illustrate the application of the fractionation factors, consider condensation of Mg from an isotopically normal gas phase, following a kinetic model. Using the fractionation factors given above, the earliest condensates will be enriched in the lighter isotopes of Mg by -20.6‰ amu^{-1} relative to the starting composition. The fractionation factor of the process, which describes the difference in fractionation between condensates and the reservoir, remains constant; therefore the isotopic composition of later condensates will not be so light, because the reservoir will become progressively heavier as lighter isotopes are lost.

The fractionation factor provides the maximum limit for the final isotopic fractionation (F) of the bulk condensates. More extreme values could only be produced by the operation of multiple processes. However, the vapor reservoir can exhibit final fractionation values of any magnitude in the direction opposite to that of the fractionation factor. In this case, the reservoir would exhibit increasingly positive fractionation as condensation progressed. This will be explained in more detail in Section 2.3.4b.

2.3.4. RAYLEIGH PROCESSES

Evaporation and condensation processes have been modelled by a Rayleigh calculation, which describes isotopic fractionation resulting from fractional distillation and condensation. For a single process (i.e. distillation only), a Rayleigh calculation provides an estimate of the isotopic composition as a function of the extent of the process. The Rayleigh model assumes that material is instantaneously and continuously removed from a reservoir, without further isotopic exchange with the reservoir.

Assume a reservoir containing N^i and N^j numbers of atoms of isotopic species i and j. An infinitesimal number of atoms n^i and n^j are removed by distillation. The amount of material removed is related to the number of atoms remaining in the reservoir by a factor K: $n^j / n^i = (-dN^j) / (-dN^i) = K\ N^j / N^i$.

A general form of the Rayleigh equation (Rayleigh, 1896, 1902) for distillation from a reservoir may be presented in differential form as:

$$dN^j / dN^i = (1 + \alpha)\ N^j / N^i.$$

A logarithmic form of this equation is written: $d\ln N^j = (1 + \alpha)\ d\ln N^i$, which after integration yields: $N^j / N^j_o = (N^i / N^i_o)^{1+\alpha}$, where N^i_o, N^j_o are the initial numbers of atoms of species i and j in the reservoir. Then we define $f = N^i / N^i_o$ as the fraction of material of a given species remaining in the reservoir. The integrated form of the Rayleigh equation above can now be rewritten:

$$N^j/N^j_o = (N^i / N^i_o)^{1+\alpha} = f^{(1+\alpha)}.$$

The fractionation factor is defined by the quotient resulting from dividing the ratio of the number of atoms of i and j at a given time ($R^{ij} = N^j / N^i$), by the initial ratio ($R^{ij}_o = N^j_o / N^i_o$):

$$R^{ij} / R^{ij}_o = (N^j / N^i) / (N^j_o / N^i_o) = (N^j / N^j_o) \times (N^i_o / N^i).$$

Using substitutions from above, this equation can be rewritten as:

$$R^{ij} / R^{ij}_o = (1/f) \times f^{1+\alpha} = f^{\alpha} \text{ , or finally: } \quad R^{ij} / R^{ij}_o = f^{\alpha}.$$

a. Distillation

The Rayleigh model can be illustrated by application to a distillation process. Using the kinetic model previously discussed, distillation of a reservoir containing isotopically normal material will produce a residue enriched in the heavy isotopes. The Rayleigh model provides an estimate of the magnitude of the fractionation of the residue, as a function of the amount of a particular element remaining in the residue.

The relevant Rayleigh equation for the residue (r) of a specific isotope system (Mg) may be written:

$$(^{25}Mg/^{24}Mg)_r = (^{25}Mg/^{24}Mg)_{ro} \, f^{1-\sqrt{(25/24)}}, \text{ or}$$

$$R_r = R_{ro} \, f^{1-\sqrt{(25/24)}},$$

where R_r and R_{ro} are respectively, the instantaneous and initial isotopic compositions of the residue.

The results of this Rayleigh calculation for the distillation of atomic Mg are shown in Figure 2.2. Vaporization of 80% of the Mg in the reservoir will result in

a fractionated residue, enriched in the heavier isotopes by +34‰ amu^{-1}, while vaporization of 95% results in a residue fractionated by +65‰ amu^{-1}.

Now the isotopic composition of the vapor will be considered. The isotopic composition of the infinitesimal vapor removed (R_v) is given by:

$$R_v / R_{vo} = (1/\sqrt{(25/24)})\ f^{1-\sqrt{(25/24)}}.$$

The vapor resulting from distillation is enriched in the lighter isotopes. The first vapor removed exhibits Mg fractionation of -20.6‰ amu^{-1}.

As the reservoir becomes heavier (depleted in the light isotopes), the instantaneous vapor also becomes progressively heavier, and exhibits an apparently normal isotopic composition after loss of 63% of the Mg in the reservoir. After this point, the instantaneous vapor removed exhibits positive fractionation.

However, note from Figure 2.2 that the final fractionation value of the integrated or total vapor, resulting from the accumulation of vapor from the onset of distillation, exhibits Mg fractionation which is always negative, until reaching the starting normal composition after distillation of 100% of the reservoir.

The Rayleigh equation for the bulk isotopic composition of the accumulated vapor $R_{v,av}$ can be given as:

$$R_{v,av} / R_{ro} = \{1 - f^{1/\sqrt{(25/24)}}\} / (1 - f).$$

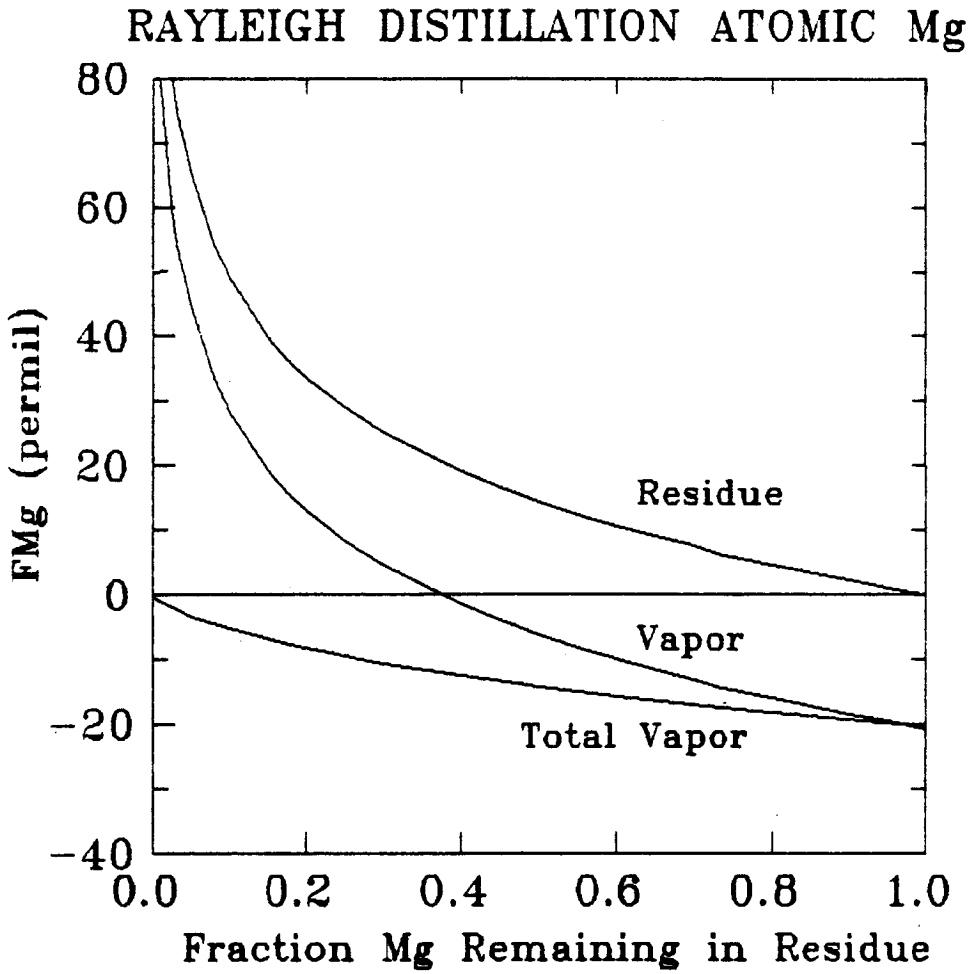

Figure 2.2. Rayleigh calculation for the distillation of atomic Mg showing the resulting F_{Mg} for the vapor and evaporative residue, as a function of the fraction of ^{24}Mg remaining in the residue. The isotopic composition of the residue is given by: $(^{25}Mg/^{24}Mg)_r = (^{25}Mg/^{24}Mg)_o \, f^{1-\sqrt{25/24}}$. The composition of the accumulated vapor is also shown. The fractionation factor of the process was assumed to be constant, with a magnitude of -20.6‰ amu^{-1}.

b. Condensation

The application of the Rayleigh model to condensation is complicated because the instantaneous removal of condensates postulated by the Rayleigh model is not consistent with the need to grow or accumulate a reservoir of the condensed material. Two cases will be considered for condensation. Figure 2.3 shows Rayleigh curves for Mg isotopic fractionation of both the condensates and residual vapor for condensation with a) a positive, and b) a negative fractionation factor. The kinetic model discussed above is consistent with a negative fractionation factor for condensation. In these calculations, the magnitude of the fractionation factor of the process (20.6‰ amu^{-1}) is assumed to be constant throughout condensation. The relevant Rayleigh equations for condensation are given in the figure caption.

Assuming a negative fractionation factor, the first condensates from an isotopically normal vapor are enriched in the lighter isotopes of Mg, by -20.6‰ amu^{-1}. With increased condensation, the vapor reservoir will become increasingly heavy, exhibiting positive isotopic fractionation for Mg. After condensation of 63% of the Mg, the reservoir will be fractionated by +20.6‰, while the material condensing at the time will appear isotopically normal.

With further condensation, both the condensates and vapor will exhibit increasingly positive fractionation. Therefore, the most extreme negative value observed for condensates in a single-stage process is -20.6‰ amu^{-1}, while positive values of any magnitude can be produced.

For the case of a positive fractionation factor, the values of fractionation are reversed, with the earliest condensates exhibiting +20.6‰ amu^{-1}.

Figure 2.3. Rayleigh calculation for the condensation of atomic Mg from an isotopically normal gas reservoir. The resulting isotope fractionation, F_{Mg}, is shown for the condensates and for the residual vapor, as a function of the fraction of Mg condensed. Two cases are illustrated: the fractionation factor of the process was assumed to be positive with a magnitude +20.6‰ amu^{-1} in Figure 2.3a, and negative (-20.6‰ amu^{-1}) in Figure 2.3b.

The Rayleigh equation for the instantaneous vapor is given by:

$$(^{25}Mg/^{24}Mg)_v = (^{25}Mg/^{24}Mg)_{v,o}\ f^{1 - \sqrt{25/24}}.$$

The equation for the accumulated condensates is given by:

$$(^{25}Mg/^{24}Mg)_{c,ave} = (^{25}Mg/^{24}Mg)_{v,o}\ \{1 - f^{\sqrt{25/24}}\} / (1 - f),$$

where $(^{25}Mg/^{24}Mg)_{v,o}$ is the initial composition of the vapor.

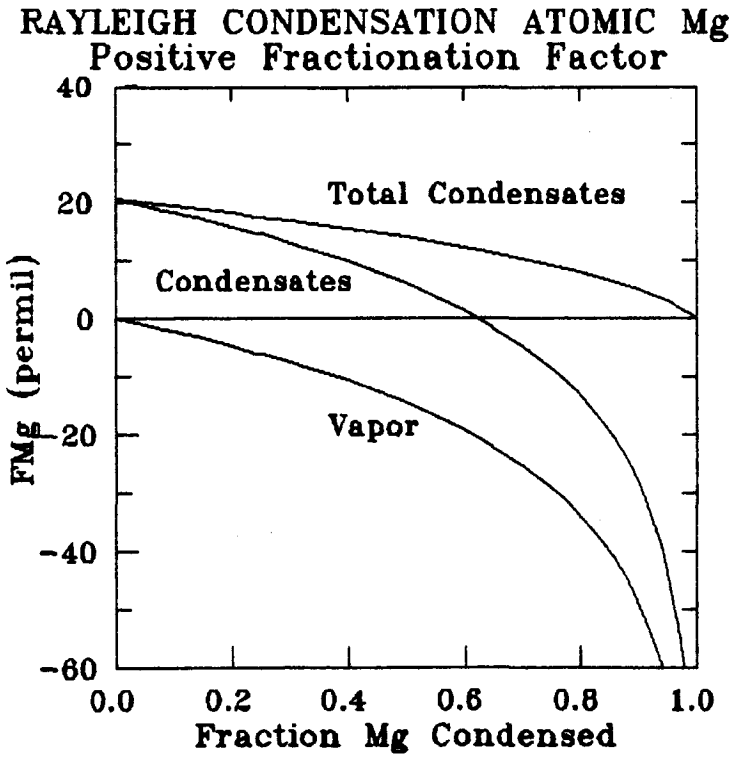
RAYLEIGH CONDENSATION ATOMIC Mg
Positive Fractionation Factor
40
20
0
-20
-40
-60
FMg (permil)
Total Condensates
Condensates
Vapor
0.0
0.2
0.4
0.6
0.8
1.0
Fraction Mg Condensed

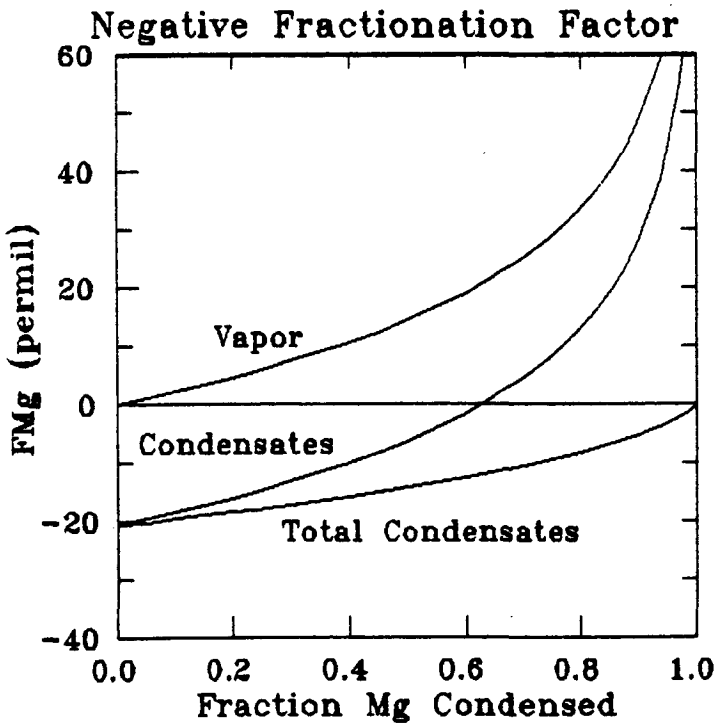
Negative Fractionation Factor
60
40
20
0
-20
-40
FMg (permil)
Vapor
Condensates
Total Condensates
0.0
0.2
0.4
0.6
0.8
1.0
Fraction Mg Condensed

c. Correlated Effects

A Rayleigh model assumes continuous, unidirectional condensation (or evaporation), which would be expected to produce correlated isotopic fractionation effects for elements of similar volatility. A correlation between isotopic fractionation for Mg and Si, which exhibit similar volatility, has been reported for FUN inclusions by Clayton et al. (1985).

Figure 2.4 illustrates an example of a correlation diagram which will be used in this work. The isotopic fractionation values for two elements are normalized by the inverse square root of the isotopic masses, using the most abundant vapor phase species. Isotopic fractionation values are calculated for a distillation residue, assuming Rayleigh fractionation of Mg and Si, with the gas phase species atomic Mg and molecular SiO. This calculation assumes the same volatility for these two species, such that the fraction of the species remaining in the reservoir is the same. The resulting fractionation values, normalized by the inverse square root of the masses, approximately define a line of slope unity. More precisely, the data yield a curve which is a function of the fraction (f) of Mg and Si remaining in the residue. Defining $\alpha_{Si} = {}^{29}Si/{}^{28}Si$ and $\alpha_{Mg} = {}^{25}Mg/{}^{24}Mg$, the slope can be given as :

$$\text{slope} = \frac{f^{1-\sqrt{\alpha Si}} - 1}{f^{1-\sqrt{\alpha Mg}} - 1} \frac{\ln \alpha_{Mg}^{1/2}}{\ln \alpha_{Si}^{1/2}}$$

A Rayleigh calculation up to a Mg fractionation value of ≈50‰ amu^{-1} yields a best fit line of slope 0.99, while F_{Mg} values up to 400‰ yield a line of slope 0.93 (Figure 2.4).

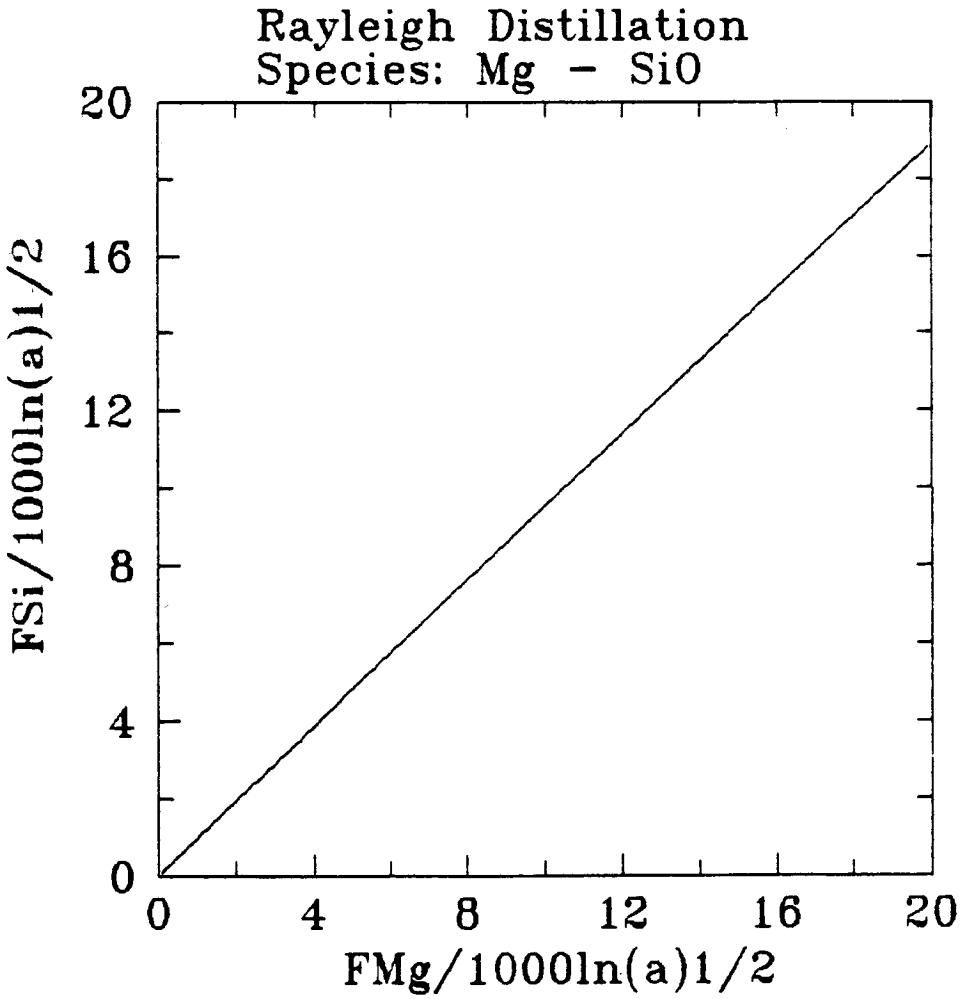

Figure 2.4. Correlation diagram of Mg and Si isotopic fractionation. Fractionation values are calculated for a distillation residue, assuming evaporation of Mg and SiO by a Rayleigh process. The species are assumed to have the same volatility, such that the fraction of the species remaining in the residue is the same. Fractionation values are normalized by the inverse square root of the masses. The equation for the slope, given in the text, is close to unity. The range of fractionation shown extends to F_{Mg} equal to 400‰ amu^{-1}.

2.3.5. NONIDEAL RAYLEIGH PROCESSES

a. Multistage Evolution

A distinction should be made between a multistage process and multiple processes. The Rayleigh model is applicable to the unidirectional evolution of a reservoir by a single process (i.e., distillation only), in contrast to the operation of multiple processes (i.e., condensation followed by evaporation and recondensation). However, the Rayleigh model describes a multistage process, where instantaneous condensates are successively removed from the reservoir.

Observations of a linear correlation for elements of similar volatility in CAI, for example, Mg and Si (Clayton et al., 1985), are consistent with unidirectional evolution of CAI by distillation following a Rayleigh model.

However, the validity of a simple unidirectional evolution for CAI has been challenged by data obtained for elements with differing volatilities. Niederer and Papanastassiou (1984) have reported on the lack of correlation of isotopic fractionation in refractory inclusions, for elements (Ca and Mg) of differing volatilities. Ca is significantly more refractory than Mg; however, the fractionation factors for Mg and Ca should exhibit the same sign for the same process.

For instance, consider condensation of Mg and Ca, assuming a negative fractionation factor. The earliest condensates will be enriched in the lighter isotopes, exhibiting negative fractionation for Mg and Ca (F_{Ca} and F_{Mg}). Due to the more refractory nature of Ca, later condensates may exhibit positive F_{Ca} and negative

F_{Mg}, finally followed by condensates with positive F_{Ca} and F_{Mg}. (See Niederer and Papanastassiou (1984) for a detailed presentation.) A consistent model of condensation cannot produce all combinations of fractionation for Mg and Ca. For example, condensation (with a negative fractionation factor) cannot produce inclusions with negative F_{Ca} and positive F_{Mg}. Niederer and Papanastassiou present data for CAI with all combinations of Mg and Ca, including cases of light Ca and heavy Mg. This is inconsistent with processing of CAI by unidirectional, single-stage processes. The presence of heavy Mg suggests that these inclusions are evaporative residues, which have lost light isotopes by volatilization. However, the presence of light Ca was attributed to an earlier condensation event, where light isotopes are preferentially condensed. Therefore, CAI appear to require processing by multiple processes, involving condensation, evaporation and recondensation.

b. Nonlinear Effects Resulting from Fractionation

The possibility exists, due to the nonlinearity of isotopic fractionation, that mixtures of components with extreme fractionation resulting from Rayleigh processes may produce what appear to be nonlinear anomalies. Mass fractionation is linear for small mass differences, but more accurately described by a power law (Section 2.3.6). Figure 2.5 illustrates a schematic three isotope diagram for an element with isotopes 1, 2 and 3. The isotope ratio N^2/N^1 is plotted against the ratio N^3/N^1. A mixture of isotopically normal material (B) with highly fractionated material (A), will result in isotopic compositions (M), which lie along a mixing line AB off the fractionation curve, producing what appear to be nonlinear effects.

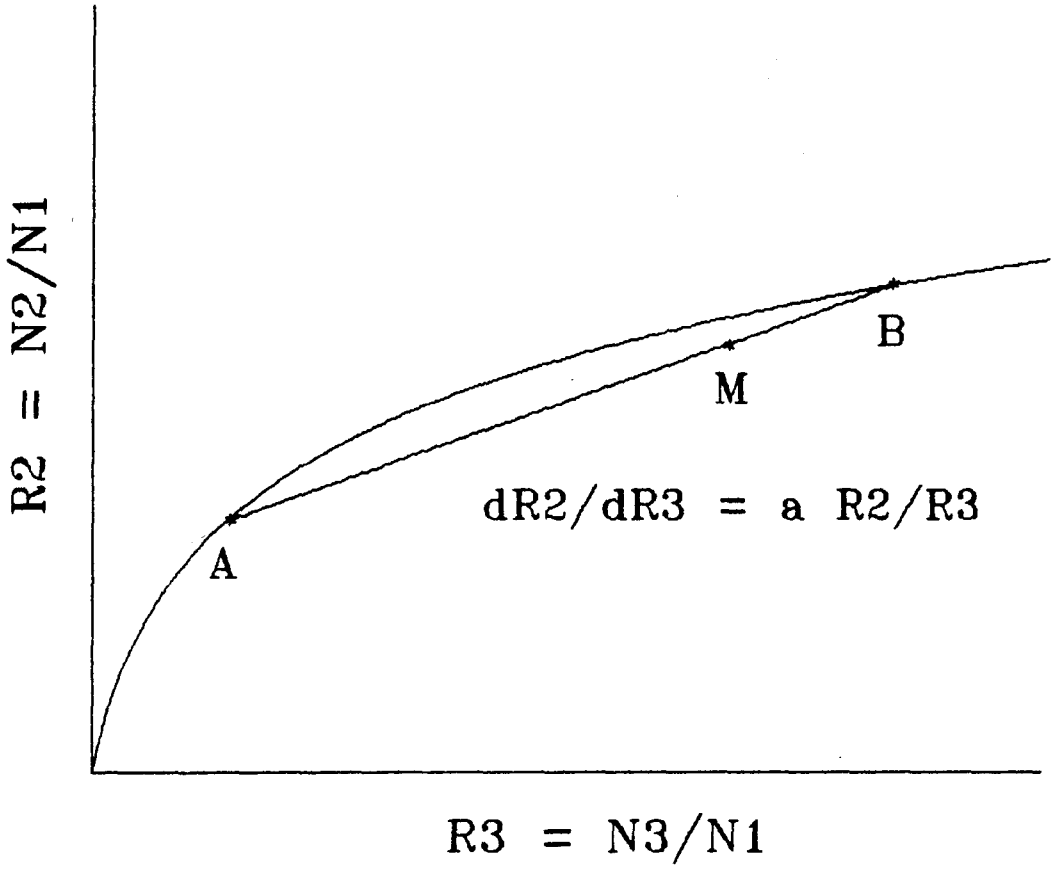

Figure 2.5. Three isotope diagram showing the abundance number ratios N^3/N^1 plotted against N^2/N^1 for a three isotope system. Due to the nonlinearity of isotopic fractionation, the ratios plot along a curve. The fractionation is given by the tangent to the curve, yielding a line of slope approximately 1/2. The diagram illustrates how the mixing of material with extreme fractionation (A) with normal material (B), can produce intermediate compositions (M), which lie off the mass fractionation curve, and can appear to be nonlinear or nuclear effects.

Experimental work has been undertaken to determine if nonlinear effects are produced during the extreme mass fractionation resulting from distillation. Esat et al. (1986) performed distillation experiments on terrestrial minerals, and observed both isotopic fractionation and nonlinear effects. The nonlinear effects consisted of a depletion of ^{26}Mg for the residues, and enrichment of ^{26}Mg in the condensates, regardless of the fractionation correction procedure used. They found a general, but not precise correlation between F_{Mg} and $\delta^{26}Mg$ of the resulting residues. However, evaporation experiments of Si distillation using a solar furnace by Molini-Velsko et al. (1987) produced fractionation effects, but no nonlinear anomalies.

Papanastassiou and Wasserburg (1987) performed calculations of the Rayleigh process for the distillation of Mg, and showed that distillation residues may exhibit small deficits in ^{26}Mg, while the integrated condensates may exhibit small excesses in ^{26}Mg ($\leq$0.8‰), after correction for fractionation by a power law. Mixtures of distillation residues with a normal reservoir exhibit only small excesses in ^{26}Mg. Papanastassiou and Wasserburg concluded that the data of Esat et al. must be attributed to a more complex process than Rayleigh distillation, and that large excesses in ^{26}Mg observed for many CAI, cannot be considered artifacts and must be attributed to ^{26}Al decay (Section 2.4).

2.3.6. ISOTOPIC FRACTIONATION LAWS

For small fractionation effects, a linear law adequately describes observations:

$R^{ij}_m = R^{ij}_t (1 + \alpha m_{ij})$, where R^{ij}_m and R^{ij}_t are the measured and true isotopic ratios respectively, and α is the mass fractionation factor (R^{ij}_m / R^{ij}_t). However, this linearity of mass fractionation is only approximate. The mathematical description of isotopic fractionation laws has been discussed by Russell et al. (1978). Precise isotopic measurements have shown that fractionation is better fit by a power law: $R^{ij}_m = R^{ij}_t (1 + \alpha)^{mij}$, where m_{ij} is the mass difference between the isotopes i and j.

For fractionation over large mass ranges, the fractionation factor may not be constant over the entire mass range. An exponential law of the form: $R^{ij}_m = R^{ij}_t (m_i / m_j)^{\alpha}$, which produces decreasing mass fractionation for increased isotopic mass, was found to provide a good fit for Ca isotopic fractionation by thermal ionization (Russell et al., 1978). However, isotopic fractionation in nature may be described by a different law than that observed for thermal ionization.

Isotopic data are corrected for mass-dependent fractionation, using a pair of reference isotopes, in order to resolve nonlinear effects. This correction removes both instrumental and natural fractionation. There are two uncertainties in this correction procedure: 1) the choice of reference isotopes; and 2) the fractionation law used. Reference isotopes for normalization are chosen somewhat arbitrarily, with consideration given to the isotopes which are not radiogenic, or are not likely to show nuclear effects, based upon nucleosynthetic scenarios.

Measured isotopic ratios include both instrumental fractionation and natural fractionation intrinsic to the sample. Instrumental fractionation may be caused by mass discrimination during chemical separation procedures; during thermal ionization or detection in the mass spectrometer; or during sputtering, ionization and detection

in the ion probe. Fractionation intrinsic to samples cannot be resolved unless that intrinsic magnitude is greater than the range of instrumental fractionation. Instrumental effects are calibrated by measuring standards, as discussed in Chapter 3. For elements of four or more isotopes by thermal ionization analysis, laboratory and instrumental fractionation can be uniquely corrected by the use of a double spike technique, which involves the addition of an internal isotopic standard to the sample before laboratory processing (Eugster et al., 1969).

Isotopic data for elements with three isotopes are presented on a three isotope correlation diagram of measured Δ-values, where Δ^{ij} is plotted against Δ^{ik}, for example Δ^{25}Mg vs. Δ^{26}Mg and Δ^{29}Si vs. Δ^{30}Si. To a first order, isotopic measurements related by mass fractionation define a line of slope 1/2, which passes through the normal composition. As discussed previously, mass fractionation is not precisely linear, and the data actually fall along a curve (Figure 2.5). A maximum slope tangent to the curve can be calculated by assuming a $m^{-1/2}$ dependence: slope = $(\alpha_{25}^{1/2} - 1) / (\alpha_{26}^{1/2} - 1)$, where $\alpha_{25} = {}^{25}Mg/{}^{24}Mg$, yielding 0.515 for Mg. However, for small fractionation, the linear approximation is sufficient. Samples exhibiting positive fractionation plot at higher Δ-values along the line, while samples with negative fractionation plot at lower values along the line. Nonlinear anomalies are observed as deviations from the mass fractionation line. A three isotope diagram can be used to identify endmembers for mixing of isotopic reservoirs. On this diagram, mixtures of two components with different isotopic compositions plot along a line between the two endmembers.

2.4. RADIOGENIC ANOMALIES: SHORT-LIVED NUCLIDES

2.4.1. SYSTEMATICS OF RADIOGENIC EFFECTS

Short-lived nuclides are those which were present in the early solar system, but have now completely decayed due to their short half-lives. The basic issues involved in establishing the in situ decay in meteoritic materials, of a radiogenic nuclide which is now extinct include: 1) the identification of primitive objects from the early solar system, which have not been extensively altered; 2) the identification of an excess of the daughter nuclide, which is resolved from the normal isotopic composition, and from isotopic fractionation effects; and 3) establishing that this excess of the daughter nuclide is correlated with the imputed abundance of the parent nuclide, demonstrating that the daughter nuclide follows the same chemical behavior of the parent.

^{26}Al will be used as an example to demonstrate the isotope systematics of short-lived nuclides (Lee et al., 1977; Wasserburg, 1985). The present Mg isotopic composition $(^{26}Mg/^{24}Mg)_m$ is the sum of the initial isotopic ratio $(^{26}Mg/^{24}Mg)_o$ at the time of formation, and excess $^{26}Mg^*$ produced by the decay of ^{26}Al:

$$(^{26}Mg/^{24}Mg)_m = (^{26}Mg/^{24}Mg)_o + (^{26}Mg^*/^{24}Mg)_m$$

$$= (^{26}Mg/^{24}Mg)_o + (^{26}Al/^{27}Al)_o\ (^{27}Al/^{24}Mg)_m,$$

where $(^{26}Al/^{27}Al)_o$ is the initial ratio at the time of formation. The present Mg isotopic composition $(^{26}Mg/^{24}Mg)_m$ is thus a linear function of the chemical composition $(^{27}Al/^{24}Mg)_m$, with a slope given by $(^{26}Al/^{27}Al)_o$ and intercept given by

$(^{26}Mg/^{24}Mg)_o$.

An Al evolution diagram is presented in Figure 2.6. Consider a sample (A) formed at time τ_1. The sample A is originally isotopically homogeneous, and contains coexisting phases 1, 2, 3 with different chemical compositions $^{27}Al/^{24}Mg$. After decay of ^{26}Al, the phases will lie along a line passing through A, with a slope $(^{26}Al/^{27}Al)_o$. If this system remains undisturbed, the phases 1, 2, 3 will retain a linear correlation between $(^{26}Mg/^{24}Mg)_m$ and chemical composition $(^{27}Al/^{24}Mg)_m$. An object formed at a later time τ_2 from the same initial composition A, would exhibit a line of lower slope $(^{26}Al/^{27}Al)_o exp(-\lambda\tau_2)$.

The linear correlation can be obliterated by later disturbances involving isotopic re-equilibration. In addition, a linear correlation will not be observed if the system was originally isotopically heterogeneous. To illustrate later isotopic disturbance, consider the sample formed at time τ_1. If the sample is remelted and isotopically homogenized at time τ_3, then the newly formed phases would lie along a horizontal line on the evolution diagram, with a higher initial $(^{26}Mg/^{24}Mg)$ at point B. If the remelting occurs before the complete decay of ^{26}Al, then these newly formed phases would subsequently define a line of lower slope $(^{26}Al/^{27}Al)_o exp(-\lambda\tau_3)$ and higher initial $(^{26}Mg/^{24}Mg)$ at point B.

It is important to distinguish a linear correlation due to in situ decay, from linear mixing relationships. Consider the case of fossil nuclides. D. D. Clayton (1982) proposed that interstellar dust grains may contain excess $^{26}Mg^*$ due to the decay of ^{26}Al, which is extinct in the grains. Mixtures of these dust grains with isotopically

Figure 2.6. Al evolution diagram, illustrating isotope systematics for the in situ decay of ^{26}Al. If ^{26}Al decays in a isotopically homogeneous reservoir (A), coexisting phases 1, 2, 3 with different chemical compositions formed at τ_1, will lie along a line passing through A with a slope $(^{26}Al/^{27}Al)_o$. An object formed at a later time $\tau 2$ from the same initial reservoir (A), would exhibit phases lying upon a line of lower slope $(^{26}Al/^{27}Al)_o exp(-\lambda\tau)$. If the sample formed at time τ_1 is remelted and isotopically homogenized at a later time τ_3, then the newly formed phases would lie along a horizontal line with a higher intercept $(^{26}Mg/^{24}Mg)_o$ at point B. If this rehomogenization occurred before the complete decay of ^{26}Al, the newly formed phases would subsequently define a line of lower slope $(^{26}Al/^{27}Al)_o exp(-\lambda\tau)$, and higher initial $(^{26}Mg/^{24}Mg)_o$ at point B.

^{26}Al *IN SITU* DECAY

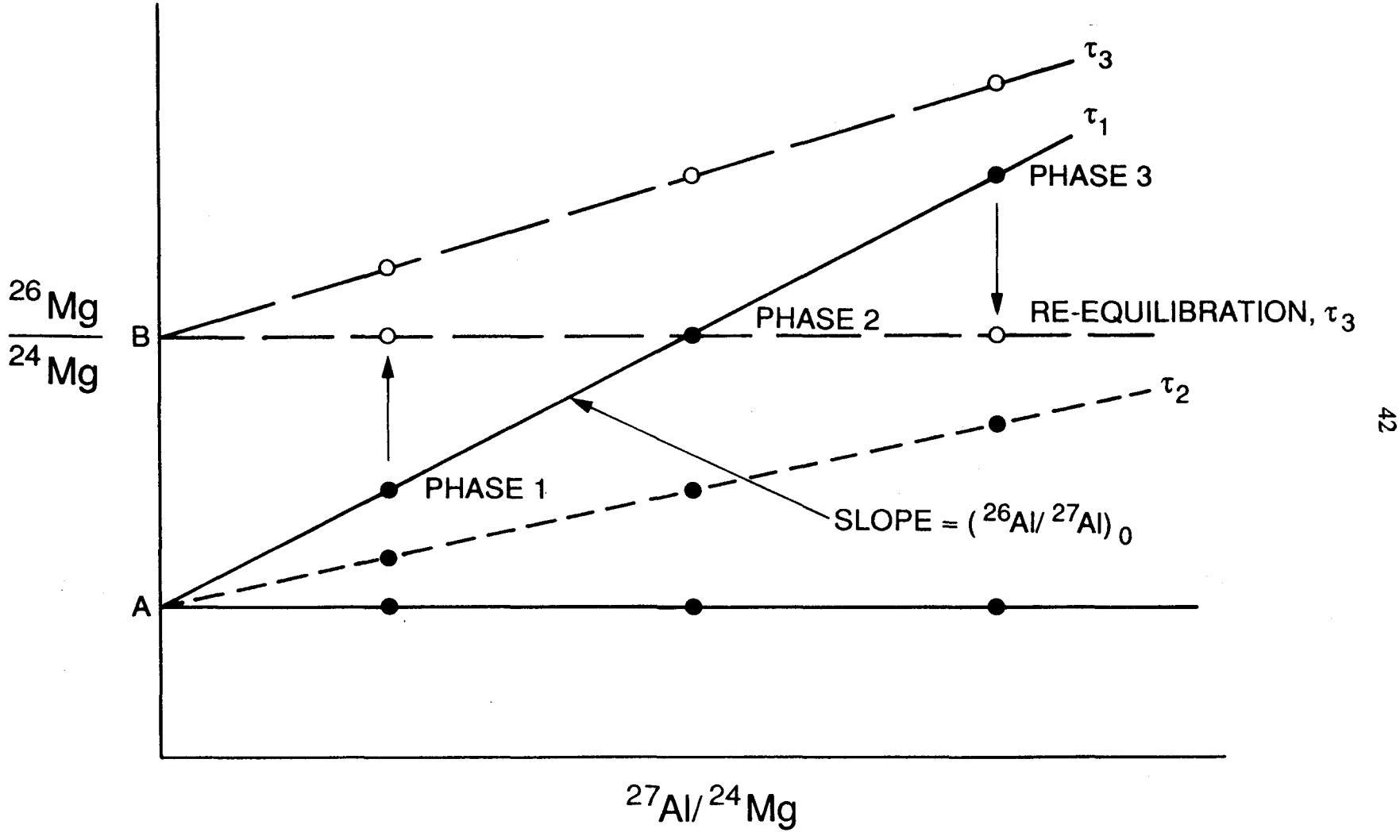

normal solar system material (low in Al), will define a straight line passing through the normal Mg isotopic composition, but the slope will bear no relation to the original ^{26}Al content. In order to demonstrate that a linear correlation is due to in situ decay and not mixing, it is necessary to demonstrate that isotopic analyses are for pure phases and not for mixtures.

2.4.2. IDENTIFICATION OF SHORT-LIVED NUCLIDES

Many meteorites have been shown to exhibit excesses in specific isotopes, due to the decay of short-lived nuclides (^{26}Al, ^{107}Pd, ^{129}I, ^{244}Pu, ^{146}Sm) which were present in the early solar system. These short-lived nuclides have been used to constrain timescales for formation of the early solar system, in particular the time interval (T) between the last nucleosynthetic event that injected material into the solar nebula and the formation of small planetary bodies (Wasserburg, 1986). Consider an element with a radioactive nuclide (N_τ) with a half-life τ, and a stable nuclide N_s, formed during nucleosynthesis, with a production ratio $(N_\tau / N_s)_p$. At the time of formation of solid objects in the solar nebula, following a time interval T after the completion of nucleosynthesis, the ratio of the radioactive nuclide abundance to that of the stable nuclide is given by:

$$(N_\tau/N_s)_o = (N_\tau/N_s)_p \exp(-T/\tau).$$

The original impetus for investigations into the presence of short-lived nuclides came from the work of H. Suess, H. Brown and H. Urey. Urey (1955) proposed that short-lived nuclides could provide a possible mechanism for the heating and

melting of small planetary bodies. ^{26}Al had recently been discovered in the laboratory (Simanton et al., 1954), and was proposed as one possible candidate. Early searches for another short-lived nuclide, ^{129}I, were undertaken by Wasserburg and Hayden (1955).

The first positive identification of a short-lived nuclide was of ^{129}Xe enrichments, which were correlated with ^{129}I (Reynolds, 1960; Jeffrey and Reynolds, 1961). This nuclide was used to constrain the timescale for the last major contribution of r-process nuclides, to be on the order of 10^8 years prior to solar system formation. However, the subsequent identification of anomalies due to nuclides with shorter half-lives, required a later addition of $\approx 10^{-4}$ solar masses of freshly synthesized material, at a time interval of less than 3×10^6 years before formation of solid objects in the solar system. The strongest evidence for this late-stage introduction comes from ^{26}Al ($\tau_{1/2} = 0.72 \times 10^6$ y), as discussed below.

2.4.3. EVIDENCE FOR ^{26}Al

In order to identify ^{26}Al effects, extensive efforts were undertaken to identify and separate crystals of high-Al, low-Mg phases in refractory inclusions, where the effects would be most pronounced. The first identification of small excesses in ^{26}Mg was made by Gray and Compston (1974) and Lee and Papanastassiou (1974). Lee and Papanastassiou also reported small deficits in ^{26}Mg. Large excesses in ^{26}Mg (up to 100‰ amu^{-1}) were observed in high-purity mineral phases in CAI, and demonstrated to be correlated with ^{27}Al/^{24}Mg ratios (Lee et al., 1976, 1977),

providing evidence for the in situ decay of ^{26}Al. The samples exhibited $^{25}Mg/^{24}Mg$ that is consistent with the terrestrial value within a few permil, demonstrating that $^{26}Mg^{*}$ has been added to normal solar system material.

The strongest evidence for the in situ decay of ^{26}Al was provided by the excellent correlation observed for the Allende inclusion WA, which exhibited a slope $(^{26}Al/^{27}Al)_o = (5.1 \pm 0.6) \times 10^{-5}$ (Lee et al, 1977). The texture of WA indicates a molten origin.

An isochron has been established for different regions of an individual anorthite crystal, with different $^{27}Al/^{24}Mg$ ratios (Hutcheon et al., 1978).

Subsequently, excesses in ^{26}Mg correlated with $^{27}Al/^{24}Mg$ have been observed in a wide variety of CAI (cf. review by Wasserburg and Papanastassiou, 1982). Extremely large excesses of ^{26}Mg up to 800‰ have been identified in individual crystals by ion probe measurements (Bradley et al., 1978; Hutcheon et al., 1978; Ireland et al., 1989). Excess ^{26}Mg has also been observed in Leoville refractory inclusions (Lorin et al., 1978).

Many Type B CAI exhibit a correlation line of slope $(^{26}Al/^{27}Al)_o = 5 \times 10^{-5}$. However substantially lower and higher values have been reported for CAI:
$5 \times 10^{-8} \leq (^{26}Al/^{27}Al)_o \leq 7 \times 10^{-5}$. Many Al-rich, Mg-poor phases in CAI exhibit no excesses in ^{26}Mg (Lee et al., 1979). Consistently lower initial values for $(^{26}Al/^{27}Al)_o$ have been reported for the FUN inclusions; HAl exhibits $(^{26}Al/^{27}Al)_o = 5 \times 10^{-8}$ (Fahey et al., 1987). A range in the initial value $(^{26}Al/^{27}Al)_o$ may be due to formation at different times, or due to initial heterogeneity in Al isotopic composition. Heterogeneity in $^{26}Al/^{27}Al$ or in Mg isotopic compositions may be the

source of deficits in ^{26}Mg in FUN inclusions.

The use of ^{26}Al as a chronometer is limited by uncertainty concerning the original heterogeneity of $(^{26}Al/^{27}Al)_o$ and Mg isotopic compositions. Further complications arise from evidence of a nonlinear relation between excess ^{26}Mg and $^{27}Al/^{24}Mg$ in several inclusions (Esat et al., 1978; Esat et al., 1979; Armstrong et al., 1984; Hutcheon, 1982), indicating that the systems have been disturbed with partial isotopic rehomogenization (Lee et al., 1977).

The isotopic abundance of ^{26}Al observed in CAI requires the addition of $\approx 10^{-4}$ solar masses of freshly synthesized material from a supernova or nova source, which may have either initiated collapse of the solar nebula, or merely been nearly coincident with this collapse (Truran and Cameron, 1978). For the observed initial ratio in CAI of $(^{26}Al/^{27}Al)_o = 5 \times 10^{-5}$, a predicted supernova production ratio $(^{26}Al/^{27}Al)_p = 10^{-3}$ (Woosley and Weaver, 1982) would require that 5% of all ^{27}Al in the solar system came from a late stage nucleosynthetic event. This high percentage seems improbable, for the addition of a major element to the solar nebula. Alternatively, a production ratio in red giants of $(^{26}Al/^{27}Al)_p \approx 1$, requires the addition of less freshly synthesized material (Arnould et al., 1980; Champagne et al., 1983).

The presence of ^{26}Al in the interstellar medium was positively identified by HEAO-3 detection of gamma ray emission (Mahoney et al., 1984). The high abundance of ^{26}Al observed served to eliminate supernova sources, due to the rarity of supernova events. Observations of ^{26}Al in the interstellar medium also eliminate local production by solar irradiation, a theory which had been excluded on a

theoretical basis by Lee (1978).

There is no clear evidence that ^{26}Al was the source of heating for planetary objects. Basaltic achondrites, which have undergone melting and planetary differentiation, do not show evidence of ^{26}Al. However, ordinary chondrites have been shown to exhibit excesses in ^{26}Mg (Hutcheon et al., 1988, 1989).

The preceding discussion of isotopic fractionation and radiogenic decay will be used as a context for the interpretation of measurements of ^{26}Al and isotopic fractionation in CAI, presented in the following chapters.

CHAPTER THREE

ANALYTICAL TECHNIQUES

3.1. INTRODUCTION

This chapter describes the analytical techniques used to investigate the petrography, chemistry and isotopic composition of refractory inclusions in the Allende meteorite. The emphasis of this work has involved isotopic measurements by thermal ionization and ion microprobe mass spectrometry.

Thermal ionization measurements were obtained for individual grains from inclusions, as well as for larger samples after dissolution and chemical separation. The ion microprobe was used to obtain in situ isotopic measurements of minerals in polished sections. Although isotopic data obtained with the ion microprobe typically exhibit lower precision than obtained by thermal ionization, the former allows for spatial resolution on the scale of a few microns. Individual phases can be analyzed in situ, to determine isotopic variations within inclusions. In addition, isotopic compositions of several elements can be measured on a single phase, to search for correlated effects.

Experimental studies of both fine-grained and coarse-grained CAI involved a preliminary petrographic and isotopic survey of many inclusions, followed by detailed studies of selected cases. Mg isotopic compositions of individual grains

were determined by thermal ionization using the direct loading technique (DLT, Lee et al., 1977), in order to identify inclusions with large isotopic effects and to determine the frequency of such effects. To characterize their mineralogy and chemistry, grains were examined by scanning electron microscopy (SEM) and by energy dispersive x-ray analysis. These techniques required only small samples (≥ 20 μm crystals), so that the remainder of the inclusion was left intact in the meteorite surface for further work.

Inclusions exhibiting large isotopic fractionation were subjected to detailed petrographic, chemical and isotopic analyses. The ion microprobe was used to determine variations of Mg, Si, Cr and Fe isotopes from mineral to mineral. Larger samples from several inclusions were dissolved and chemically separated for more precise isotopic analysis by thermal ionization.

Due to the small size of the inclusions analyzed (largest dimension = 1 to 16 mm), particular care was given to the conservative use of samples, so that comprehensive chemical, petrographic and isotopic data could be obtained for a single inclusion. In addition, special techniques were required for handling and analyzing grains in fine-grained inclusions (with grains 0.5 to 100 μm in size).

3.2. SELECTION OF INCLUSIONS AND SAMPLE PREPARATION

3.2.1. FINE-GRAINED INCLUSIONS

a. Selection of Inclusions

Whole Allende fragments covered with fusion crust were cut into 1 cm thick slabs using a diamond-embedded steel blade (0.4 cm thickness), using distilled water as coolant. Many of the slabs examined in this study were cut from Allende fragments labeled BG82 (obtained from A.L. Burlingame). Slabs sliced from one fragment are labeled consecutively, e.g., BG82DA to BG82DJ; inclusions identified on a slab are further numbered consecutively, e.g., BG82DA-1. In the following discussions the prefix BG82 is deleted from the inclusion name. Allende slabs ($\approx$20x15x1 cm^3) were examined under a binocular microscope in order to identify fine-grained pink or white inclusions with a linear dimension $\geq$5 mm. Preference was given to larger inclusions ($\geq$10 mm) in order to have sufficient material for comprehensive petrographic, chemical and isotopic analyses. Inclusions were photodocumented on the slab surfaces. Table 3.1 presents a brief description of the seventeen fine-grained CAI analyzed and a summary of the analytical techniques used for each inclusion.

b. Sample Preparation

A flowchart outlining the processing of samples from seventeen fine-grained inclusions for petrographic, chemical and isotopic analysis is shown in Figure 3.1. For five inclusions which were visible on two opposing slabs, a thin section was prepared from one slab, while the opposing half was sampled for isotopic work. For two inclusions (B14-B and EA-1), a thin section was prepared from a chip excavated from the inclusions. Thin sections were used for SEM and ion probe analyses.

TABLE 3.1. FINE-GRAINED INCLUSIONS ANALYZED

Inclusion	Description	Size (mm)	Thin Section	INAA	Isotopic Data DLT	Chem.	Ion Probe
BG82D-I	pink; white rim; islands	16 x 6	Y	Y	Y	Y	Y
B14-B	pink; white rim	12 x 3	Y	Y	Y	Y	Y
A47-2	pink; white rim	11 x 5	Y	-	Y	Y	-
BG82C-M	pink; white rim	15 x 7	Y	Y	Y	Y	-
BG82EA-1	pink; no rim; gray patches	10 x 5	Y	-	Y	Y	Y
B9Z-1	pink; white rim	10 x 3	-	-	Y	Y	-
B14	pink; white rim	10 x 10	-	-	Y	Y	-
A1C1-E	pink; white mantle	14 x 4	Y	-	Y	Y	-
BG82EA-2	pink; white rim	4 x 3	-	-	Y	Y	-
B9Z-2	pink; no rim	9 x 4	-	-	Y	Y	-
BG82I-F	pink; no rim	8 x 3	Y	-	Y	Y	-
A47-1	pink; white rim	8 x 3	-	-	Y	-	-
BG82I-C	pink; white rim	6 x 3	-	-	Y	-	-
BG82I-I	pink; no rim	9 x 2	-	-	Y	-	-
BG82JB-1	pink; no rim	9 x 5	-	-	Y	-	-
BG82DI-14	pink; white rim	5 x 4	-	-	Y	-	-
BG82CJ-3	pink; white rim	4 x 4	-	-	Y	-	-

a. Instrumental netron activation analysis by Palme (1987).
b. Mg isotopic analysis by the direct loading technique (Lee et al., 1977). Samples analyzed denoted by Y.
c. Chemical dissolution of samples, followed by Mg isotopic analysis for soluble fraction and residue.
d. Mg isotopic analysis by ion microprobe analysis.

Figure 3.1. Flowchart outlining the experimental procedures used for the sampling and analysis of fine-grained Ca-Al-rich inclusions by SEM, ion microprobe and thermal ionization mass spectrometry. Inclusions are identified in slabs of Allende. Microsamples are excavated: the mineralogy of the grains is examined by SEM and EDS; while Mg isotopic compositions are determined by the direct loading technique (DLT). Larger samples are dissolved in order to separate soluble silicates from insoluble phases. Minerals in the residues were examined by SEM; Mg isotopic compositions were determined by DLT. The solutions were either analyzed by DLT, or after chemical separation by ion exchange. Thin sections were prepared of inclusions in order to characterize their petrography. The ion microprobe was used for a detailed in situ study of Mg isotopic variations in the inclusions.

EXPERIMENTAL PROCEDURES:
FINE-GRAINED Ca-Al-RICH INCLUSIONS

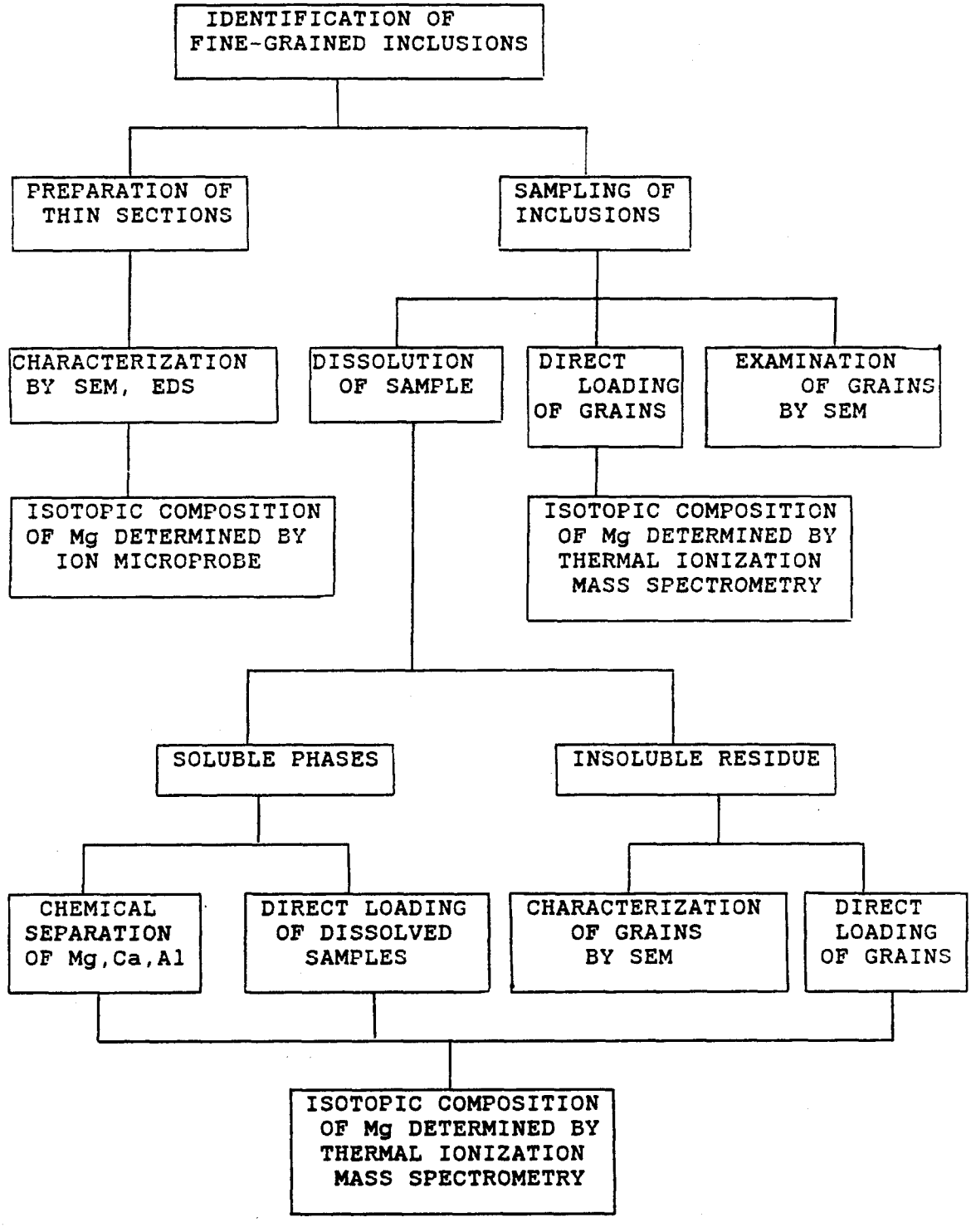

A fraction of the material obtained by sampling each inclusion was stirred into a suspension in a solution of methyl alcohol, and distributed on pyrolytic graphite discs, using a syringe and polyethylene tubing. The graphite discs were carbon-coated and examined on the SEM in order to identify mineral phases.

Seventeen fine-grained CAI were sampled using tungsten and tungsten carbide micro-chisels and needles to obtain 0.5 to 10 mg of powdery material from the center of the inclusions. The samples were inspected under a binocular microscope to ensure that there was no matrix contamination. Microsamples from eight CAI were analyzed for Mg isotopic composition by the direct loading technique (DLT). Since the fine-grained nature of these inclusions (0.5 to 100 μm grains) precluded the handling of individual grains, the use of DLT for the analysis of both bulk inclusions and acid residues entailed the dispersion of grains into a suspension in water. A fraction of this suspension was removed with polyethylene tubing and a syringe, mixed with silica gel and loaded on a filament. The loading technique for DLT will be discussed Section 3.4.4.

Due to the difficulty of obtaining high-purity mineral separates of fine-grained CAI, larger samples (1 to 3 mg) of eleven inclusions were dissolved in order to separate soluble silicates from insoluble phases. Samples were dissolved in small amounts of high-purity HF and HNO_3; the resulting solutions were centrifuged to obtain soluble fractions and insoluble residues. This permitted a comparison of the isotopic composition of the soluble and insoluble fractions of the same sample. Parts of the residues were distributed on pyrolytic graphite discs and studied on the

SEM, prior to isotopic analysis by DLT. The residue of inclusion DI consisted predominantly of hibonite. For all other inclusions, the residues consisted of Fe-rich spinel, with occasional traces of hibonite. For four of the dissolved samples, Mg was chemically separated by ion exchange from an aliquot of the soluble fraction, before isotopic analysis. The soluble fractions of most inclusions were analyzed without chemical separation of Mg. For inclusion DI, two microsamples were initially analyzed by DLT; subsequently two larger samples were excavated and analyzed for Mg isotopic compositions after dissolution and chemical separation.

3.2.2. COARSE-GRAINED INCLUSIONS

a. Selection of Inclusions

Coarse-grained inclusions (1 to 11 mm) were identified on Allende slabs on the basis of a distinct purple color. Ethyl alcohol was used to coat the Allende slabs during examination and photographing to enhance the color contrast. A summary of the characteristics of the twenty-seven coarse-grained CAI analyzed is given in Table 3.2. Also listed are the analytical techniques used for each inclusion. Some of the smaller inclusions listed near the end of the table were identified and examined in thin section only.

b. Sample Preparation

A flowchart illustrating the processing of samples from coarse-grained inclusions for petrographic, chemical and isotopic analyses is shown in Figure 3.2. Inclusions

TABLE 3.2. PURPLE COARSE-GRAINED INCLUSIONS ANALYZED

Inclusion	Description	Size (mm)	Grain Mount	Polished Section	INAA	Isotopic Data DLT	Isotopic Data Ion Probe
BG82DH8	purple-white	4 x 3	Y	Y	Y	Y	Y
B7H10	purple-gray	3 x 2	Y	Y	-	Y	Y
BG82HB1	purple; white mantle	4 x 4	Y	Y	Y	Y	Y
B7F6	purple-pink	5 x 2	Y	Y	Y	Y	Y
BG82CH3	purple-white	3 x 2	-	Y	-	Y	Y
C1B10	white-red	11 x 5	Y	-	-	Y	-
BG82HB5	purple-white	3 x 1	Y	-	Y	Y	-
A11-16	purple-white	x	Y	-	-	Y	-
B7L3	purple-white sulfide rim	5 x 2	Y	Y		Y	Y
B7F7	purple-white sulfide rim	4 x 2	Y	Y	-	Y	-
BG82DI6	purple-pink	4 x 2	Y	-	Y	Y	-
A1-2-3	purple-gray-white	2 x 1	Y	Y	-	Y	-
BG82GB1	purple-white	5 x 2	Y	Y	-	Y	-
BG82HB10	purple-white	5 x 3	Y	Y	-	Y	-
B7M11	gray-pink	3 x 3	Y	-	-	Y	-
B7C3	pink-gray-white	10 x 3	Y	-	-	Y	-
BG82GH2	purple-white	4 x 4	Y	-	-	Y	-
BG82CJ7	purple-pink	2 x 1	Y	-	-	Y	-
BG82II3	pink-white	5 x 4	Y	-	Y	Y	-
BG82GH10	purple-white	4 x 2	Y	-	-	Y	-
A1-2-6	purple-white sulfide rim	2 x 2	-	Y	-	-	-
BG82DF3	pink-gray-white	6 x 3	Y	-	-	-	-
BG82CH4	red-white sulfide rim	3 x 1	-	Y	-	-	-
P20	purple-white	2 x 2	-	Y	-	-	-
P21	purple-white	1 x 1	-	Y	-	-	-
BG82GA1	pink-purple sulfide rim	4 x 4	-	Y	-	-	-
A1-2-2	purple-gray sulfide rim	3 x 2	-	Y	-	-	-

a. Instrumental neutron activation analysis by Palme (1987).
b. Mg isotopic analysis by the direct loading technique (Lee et al., 1977).
c. Mg, Si and Cr isotopic analysis by ion microprobe analysis.

Figure 3.2. Flowchart outlining the experimental procedures used for the sampling and analysis of coarse-grained Ca-Al-rich inclusions by SEM, ion microprobe and thermal ionization mass spectrometry. Inclusions were identified on slab surfaces of Allende, and microsamples were excavated. Grains were characterized by SEM; Mg isotopic compositions were determined by DLT. Polished sections were prepared in order to obtain petrographic observations by SEM, and measurements of Mg, Si, Cr and Fe isotopes by ion microprobe analysis. More extensive sampling was undertaken of several inclusions. Chemical compositions were determined by INAA, and Mg, Ca, Ti, Cr and Nd isotopes by thermal ionization.

EXPERIMENTAL PROCEDURES:
PURPLE SPINEL-RICH INCLUSIONS

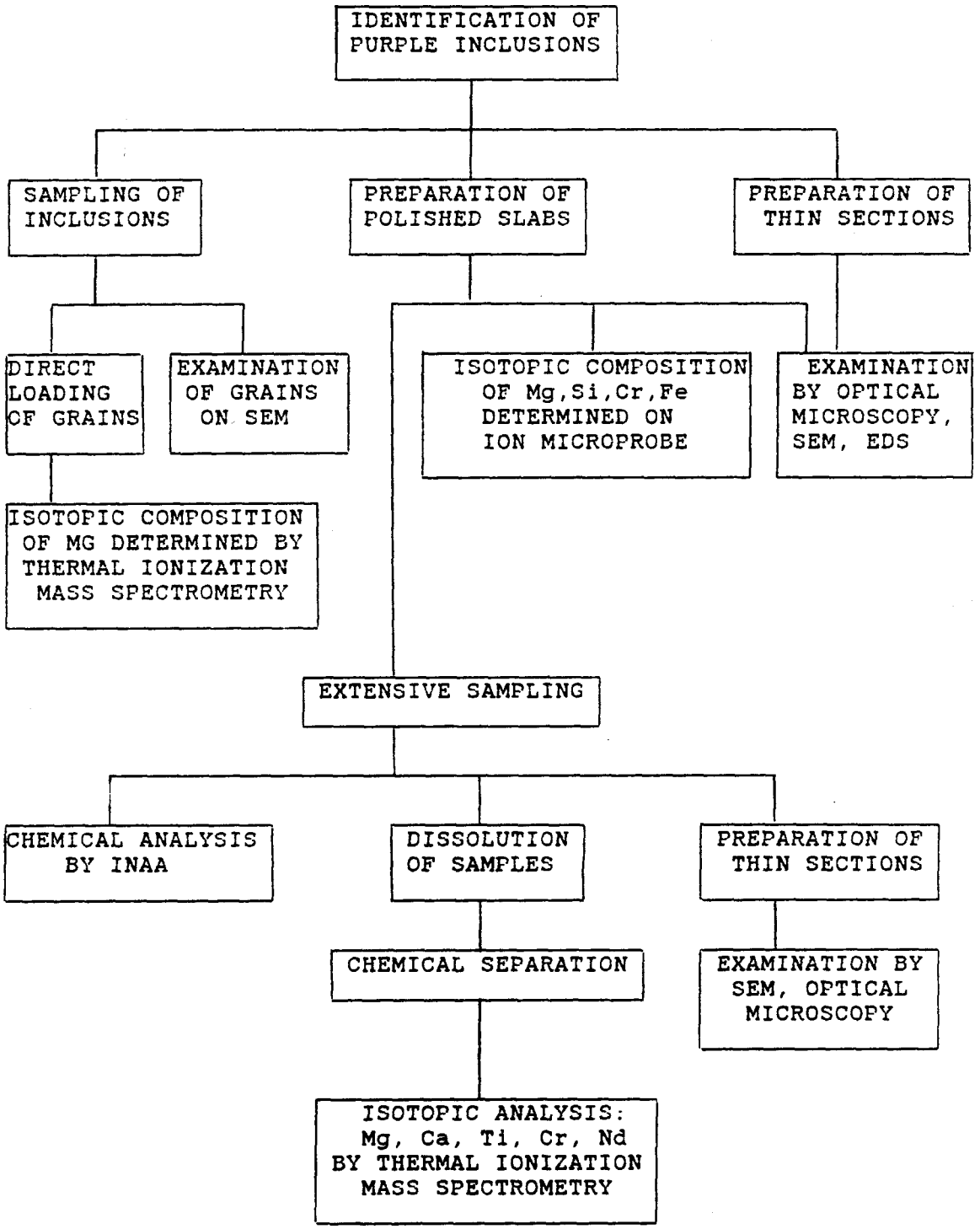

were sampled with tungsten carbide micro-chisels to obtain microsamples (0.1 to 0.5 mg) free of matrix contamination for isotopic and petrographic analyses. Grain mounts were prepared for each inclusion sampled by mounting one or two grains (100 to 200 μm) in Araldite epoxy in small depressions of varying depths in stainless steel cylinders (0.64 cm diameter). These grain mounts were ground on SiC paper and polished with diamond paste before carbon-coating and examination on the SEM. Thin sections were prepared of several inclusions for petrographic and ion probe analysis.

Grains obtained by sampling were analyzed for Mg isotopic composition by DLT to identify inclusions with extreme Mg isotopic fractionation ($\geq$10‰ amu^{-1}) for further study. Four inclusions were identified as exhibiting FUN isotopic characteristics on the basis of the Mg isotopic composition. Thin sections were not prepared of entire FUN inclusions due to the small size of the inclusions ($\leq$ 5 mm) and the desire to conserve material. Cubes ($\approx$1 cm^3) of the meteorite encompassing the FUN inclusions were sawed from the Allende slabs. Polished thick sections were prepared by covering the inclusion surface with Araldite epoxy, grinding with diamond discs and alcohol, and polishing with diamond paste. The cubes for two inclusions (DH8 and HB1) were sliced by sawing parallel to the inclusion surface to produce a thin wafer ($\approx$0.3 mm) for petrographic and ion microprobe analysis. The remainder of the inclusions were excavated for more extensive thermal ionization measurements of Mg, Ca, Ti, Cr and Nd (Papanastassiou and Brigham, 1987, 1988, 1989). Polished thick sections containing the other two inclusions (B7F6 and B7H10) were first analyzed on the SEM and ion probe, then sliced by sawing

perpendicular to the inclusion surface. One inclusion half was saved for further petrographic or ion probe analysis, while epoxy was removed from the other half by ashing in O_2 gas in a plasma asher prior to excavation of the inclusions.

Excavation of the four inclusions entailed the use of tungsten carbide micro-chisels to separate the inclusions from the surrounding Allende matrix. This procedure was undertaken on a clean bench in a laminar-flow clean room to minimize contamination and sample loss. The grains were examined under a binocular microscope and any remaining matrix was removed using the micro-chisel and tungsten tweezers. Samples were dissolved in HF and HNO_3, and chemically separated by ion exchange for the analysis of Mg, Ca, Ti, Cr and Nd isotopes (Papanastassiou and Brigham, 1987, 1988, 1989). During excavation of inclusion HB1, several green aggregates (opaque assemblages) were separated from the inclusion for isotopic and chemical analysis. Thin sections of the inclusions were prepared from remnants of inclusions left after excavation.

3.3. PETROGRAPHIC AND CHEMICAL ANALYSIS

3.3.1. PETROGRAPHIC ANALYSIS

Petrographic analyses entailed the use of four types of samples: 1) standard thin sections (30 μm-thick), as well as ultrathin (10 μm-thick) sections for fine-grained inclusions; 2) polished thick sections of Allende inclusions (Section 3.2.2); 3) grain mounts of individual grains from coarse-grained inclusions (Section 3.2.2); and

4) grain dispersions of fine-grained inclusions on pyrolytic graphite discs. The polished thick or thin sections were carbon-coated and examined by backscattered electron imaging with a JEOL JSM-35CF scanning electron microscope (SEM). Grain dispersions of fine-grained inclusions were examined for mineral phase identification. Petrographic and textural observations were obtained for inclusions examined in thin sections and polished sections. Backscattered electron maps were prepared of the entire inclusions; backscattered electron images (BEI) are shown for several CAI. Modal abundances of minerals were obtained by point-counting on the SEM.

Quantitative chemical analyses were obtained for minerals in the polished thick or thin sections and grain mounts by energy dispersive x-ray analysis (EDS) with a Tracor-Northern TN-5500 system. Analyses were performed at 15 KV and 0.075 nA. EDS spectra were integrated over 100 seconds. Data for oxide and silicate phases were compared against pure oxide and silicate standards, and corrected using the procedures of Bence and Albee (1968) and Packwood and Brown (1981), as modified by Armstrong (1984). Analyses of metal and sulfide phases were corrected using the ZAF correction procedures of Love and Scott (1978), as modified by Armstrong (1982, 1984). The reproducibility of the chemical analyses is estimated to be $\leq$5%, based upon replicate analyses of secondary standards. Secondary standards included Burma Spinel, Miakajima Plagioclase and synthetic Ti-pyroxene glass. Replicate analyses of standards are given in Appendix 1.

Estimates of the bulk chemical compositions of the inclusions were obtained by averaging several EDS analyses obtained by rastering the beam over a large region

($\approx$250 μm^2) of the inclusion.

Polished thick and thin sections were examined on the SEM to select grains $\geq$ 10 μm for ion microprobe analysis. The sections were also examined on the SEM after ion probe analyses to confirm the identification of the phases analyzed and to obtain measurements of chemical compositions.

3.3.2. BULK CHEMICAL ANALYSIS

Bulk chemical compositions of several coarse-grained and fine-grained inclusions were generously provided by Dr. H. Palme (Max Planck Institute, Mainz) for selected major and minor elements and rare earth elements by instrumental neutron activation analysis (INAA). Small samples (0.02 to 0.4 mg) of several inclusions, as well as a fraction of the opaque assemblage excavated from HB1 were analyzed after irradiation with thermal neutrons.

3.4. THERMAL IONIZATION ISOTOPIC ANALYSIS

3.4.1. INSTRUMENTATION

Samples were measured on the Lunatic I mass spectrometer (Wasserburg et al., 1969). This instrument is a single-focusing mass spectrometer, with a 30.48 cm radius, 60° sector magnet. A programmable, computer-controlled magnetic field scans the center of each mass peak and backgrounds on either side of the peaks.

Isotope ratios are determined by time interpolation of measured intensities. The instrument provides high ion transmission (≈100%) and data are collected under conditions of low mass resolution (≈600). The thermal ionization source is regulated by a programmable filament power supply. A Vacsorb pump is used for rough pumping of the source after venting for sample loading. Two Vacion pumps are used for the source and analyzer.

This is a single collector instrument. Ion currents are detected with an offset Faraday cup or electron multiplier, measured with a vibrating-reed Cary electrometer, and the signal is integrated using a digital voltmeter. An HP9845 computer monitors beam intensity and beam growth during data collection.

3.4.2. CHEMICAL SEPARATION PROCEDURES

Chemical procedures for the separation and analysis of Mg have been developed by Schramm, Tera and Wasserburg (1970). Samples (1 to 3 mg) from eleven fine-grained inclusions were dissolved in small amounts (≈150 μL) of high-purity HF and HNO_3. The acids were added one at a time and the sample was dried to a small drop before subsequent additions of acid. The material was then taken up in 1.5N HNO3 and centrifuged to obtain soluble fractions and insoluble residues. The Mg content of several of the solutions was determined by isotope dilution, using a ^{25}Mg spike. For most samples, aliquots of both the soluble and insoluble fractions were analyzed by DLT. For four fine-grained inclusions, Mg was chemically separated using an ion exchange column (Dowex AG50x8 resin, in a 0.1N HNO3

medium) from an aliquot of the soluble fraction. Two column passes were required for most samples due to the high Al/Mg. Column yields were determined by isotope dilution to be ≈95%. Typical Mg blanks, determined by isotope dilution using a ^{25}Mg spike for the entire chemical and loading procedure, were 25 to 30 ng, due primarily to contributions from the ion exchange column.

Four of the coarse-grained FUN inclusions (DH8, HB1, B7F6 and CH4) were dissolved and chemically separated by ion exchange for the mass spectral analysis of Mg, Ca, Ti, Cr and Nd isotopes (Papanastassiou and Brigham, 1987, 1988, 1989). The spinel-rich residues were also dissolved and chemically separated for Mg and Cr isotopic analysis.

A normal solution, consisting of spectrographically pure MgO dissolved in dilute HCl, was analyzed periodically during the course of the mass spectrometer analyses.

3.4.3. FILAMENT LOADING PROCEDURES

The filament loading procedure was critical to obtaining stable Mg analyses on the mass spectrometer. Zone-refined Re "short-V" filaments (ReSV), obtained by folding the mid-portion of Re ribbons (0.76 mm wide, 0.030 mm thick, 25.4 mm long) lengthwise into V-shaped boats, were outgassed for two hours at 2100°C under vacuum. Solution aliquots consisting of 100 to 150 ng Mg were mixed with small amounts of silica gel and 0.5N H_3PO_4 in a teflon beaker. Polyethylene tubing on a syringe was used to load the resulting slurry along the filament. Loading was performed on an X-Y stage under a binocular microscope. The silica gel-phosphoric

acid (SiO_2-H_3PO_4) mixture is gradually heated to remove water; more H_3PO_4 is added and the heating repeated so that the silica gel adheres to the filament and the current is $\leq$ 2.0 A. To fuse the SiO_2-H_3PO_4 mixture to the filament, the current is briefly increased for 2 sec. and the filament glows a dull red color. The final appearance is of a mass of glazed silica.

3.4.4. DIRECT LOADING TECHNIQUE

The direct loading technique, developed by Lee, Papanastassiou and Wasserburg (1977), enables the Mg isotopic composition of samples to be determined without chemical separation. This technique allows for the analysis of small samples (Esat et al., 1979), including individual crystals ($\geq$20 μm if 10%MgO). For analysis of chemically unseparated solutions by DLT, the blank is substantially reduced by not using the isotope exchange column. DLT was used in this work for four types of samples: 1) grains of fine-grained inclusions; 2) insoluble residues from the dissolution of fine-grained inclusions; 3) aliquots of dissolved sample solutions which have not been chemically separated; and 4) crystals obtained by sampling coarse-grained inclusions.

Direct loading of coarse-grained crystals involved picking up the selected grain (typically 50 to 100 μm) from a glass slide, using a fine-tipped tungsten needle mounted in a micromanipulator assembly. A drop of a sticky sucrose-citric acid mixture was used to ensure that the grain would adhere to the needle. The needle is used to deposit the grain on a filament filled with silica gel and H_3PO_4. The

silica gel was dried and fused as described previously. For the fine-grained samples and residues, the grains were first dispersed in water. An aliquot of this suspension was removed with polyethylene tubing and a syringe, mixed with silica gel and H_3PO_4 in a teflon beaker, and loaded onto a filament, similar to the procedure described for solutions. No special procedures were required for loading chemically unseparated solutions.

Standards for the direct loading technique included terrestrial spinel for the determination of normal Mg isotopic composition in an Al-rich sample, and terrestrial olivine for normal composition in an Al-poor sample. Crystals from ^{25}Mg-spiked glasses of known composition determined by gravimetry (Armstrong et al., 1982), were analyzed by DLT to check my ability to precisely measure the magnitude of large isotopic fractionation.

Lee et al. (1977) have shown by replicate analyses of terrestrial and meteoritic minerals, that DLT can be used to determine the isotopic composition of chemically unseparated Mg with a sensitivity and precision comparable to those of the conventional technique of analyzing Mg from chemically separated samples. However, there is an unexplained, but well-behaved offset in ^{26}Mg observed for Al-rich samples, discussed in Section 3.4.6.

3.4.5. MASS SPECTROMETER ANALYTICAL CONDITIONS

The filament is heated in the mass spectrometer to a temperature of 1400°C, then baked at 1400°C for one hour. The current is then gradually increased over

two to three hours until a stable, growing ^{24}Mg ion signal larger than 10^{-11} A is obtained. Data are collected at temperatures of 1470 to 1510°C; samples loaded by DLT occasionally run at higher temperatures (≤1540°C). A typical analysis consists of three hundred cyclical measurements of ^{24}Mg-^{25}Mg-^{26}Mg-^{24}Mg. The intensity of ^{27}Al was monitored periodically throughout the analysis. For chemically separated Mg, the intensity ratio $I(^{27}Al^+)/I(^{24}Mg^+)$ was typically 0.2 to 0.5. For directly loaded samples, initial $I(^{27}Al^+)/I(^{24}Mg^+)$ ratios as high as 11 would decrease to ≈2 during the course of the analysis.

The peak shapes were monitored periodically; data were not collected unless the peak top was flat for ≥ 1.2 gauss, for the slit widths used (0.008" for the source, 0.025" for the collector, yielding a mass resolving power of 600). A peak shape for mass 24 taken under these instrumental conditions is illustrated in Figure 3.3.

For Mg analyses, the mass range from 23.3 to 27.6 was also scanned to ensure that there were no interferences. Lee and Papanastassiou (1974) and Lee et al. (1977) have discussed the presence of a broad peak due to ^{27}Al ions scattered from the spectrometer tube for Al-rich samples which were not chemically unseparated. Figure 3.4 illustrates the nature of this background for an Al-rich sample analyzed by DLT. This ^{27}Al scattered beam starts from mass 24.6, peaks at mass 24.2 with a flat background under mass 24, and gradually decreases toward lower masses. The scattered beam intensity at mass 24 is typically $\approx 10^{-3}$ the intensity of the primary ^{27}Al beam. This effect was observed for all samples which were not chemically separated.

The ionization and transmission efficiency of Mg (defined as the number of singly-ionized Mg at the collector divided by the total Mg on the filament) has been

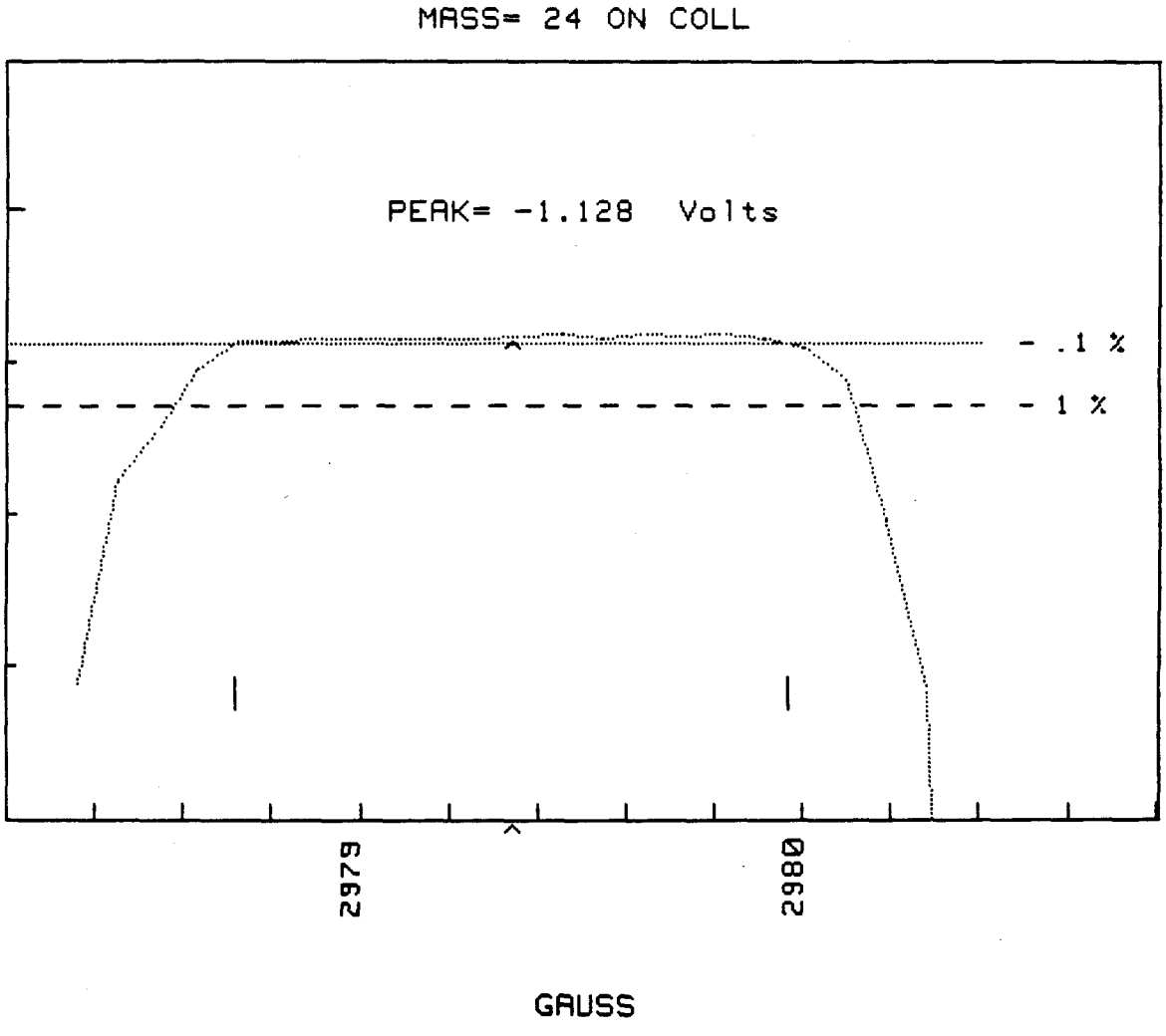

Figure 3.3. A scan of the peakshape for mass 24 on the Lunatic mass spectrometer. The beam intensity is measured with a Cary electrometer as the magnetic field is changed in small steps. Isotopic data were not collected unless the peak top was flat for ≥ 1.2 gauss for the slit widths used (0.008" for the source, 0.025" for the collector). The mass resolution is approximately 600.

Figure 3.4. Mg mass spectra obtained by monitoring the beam intensity over the mass range 23.3 to 27.6. A broad background due to a $^{27}Al^{+}$ scattered beam is observed for Al-rich samples which were not chemically separated. The background starts at mass 24.6, peaks at mass 24.2 with a flat background under mass 24, and gradually decreases toward lower masses.

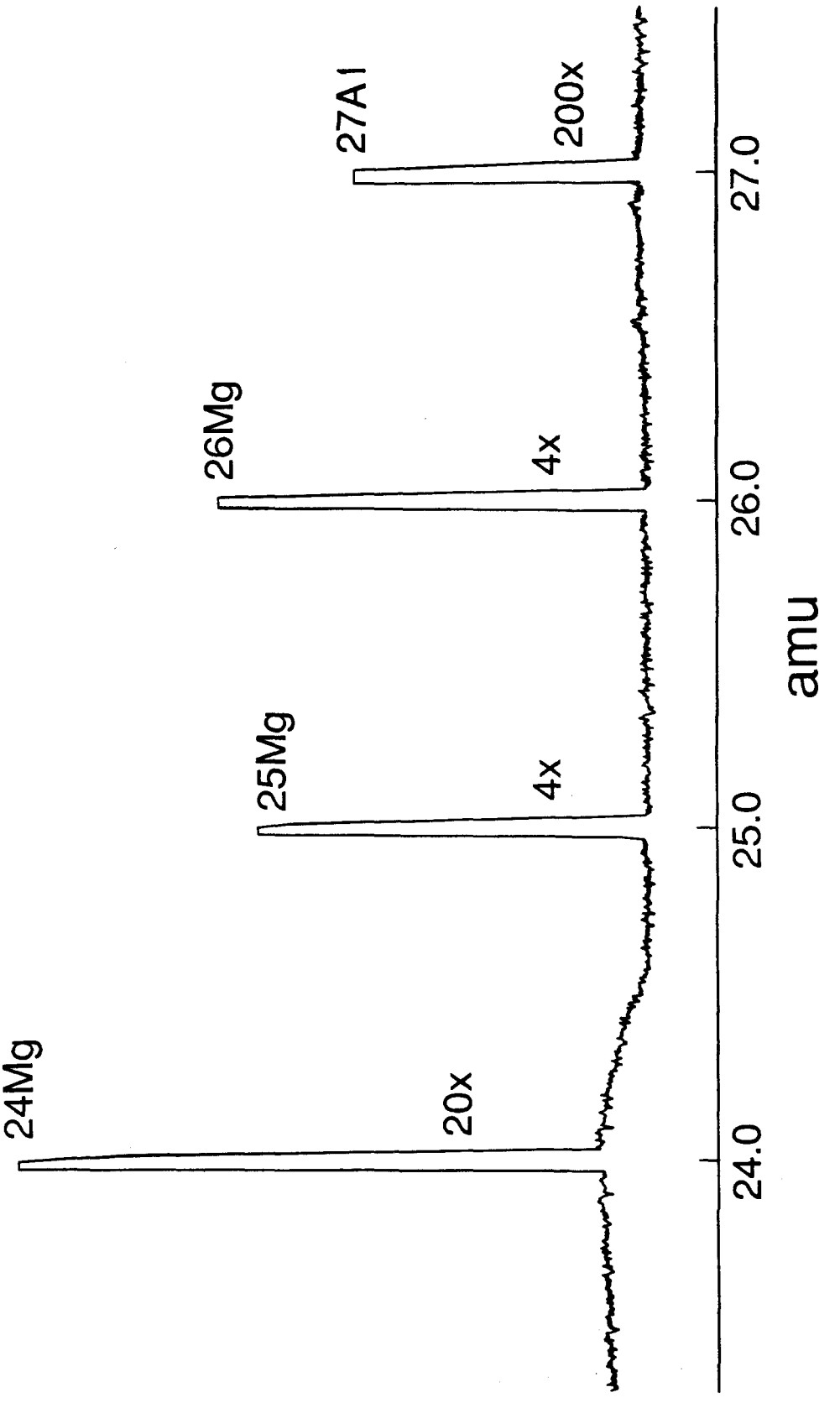
24Mg
20x
25Mg
4x
26Mg
4x
27Al
200x
24.0
25.0
26.0
27.0
amu

determined to be $\geq 4 \times 10^{-4}$ using the silica gel loading technique (Schramm et al., 1970). Special procedures developed in this laboratory for the analysis of extremely low quantities of Mg in interplanetary dust particles achieved an efficiency as high as 10^{-2} (Esat et al., 1979).

3.4.6. ISOTOPIC RATIOS

Ten sequential cycles of Mg isotopic intensity measurements are grouped in one set for data analysis. A fractionation factor $\Delta^{25}Mg$ (in permil) is calculated from the measured $^{25}Mg/^{24}Mg$ ratios for each set, relative to the assumed normal value 0.12663 (Catanzaro et al., 1966):

$$\Delta^{25}Mg = \{[(^{25}Mg/^{24}Mg)_{meas}/0.12663] - 1 \} \times 1000.$$

The mean $^{25}Mg/^{24}Mg$ of all normal analyses in this laboratory has been determined to be 0.12475 (Lee et al., 1976). The present work is in agreement with this value (Table 3.3). The Mg fractionation (F_{Mg}) is calculated as:

$$F_{Mg} = \Delta^{25}Mg - \Delta^{25}Mg_{normal}.$$

The measured $^{26}Mg/^{24}Mg$ ratios were corrected for mass fractionation effects using a power law (Russell et al., 1978):

$$(^{26}Mg/^{24}Mg)_{corr} = (^{26}Mg/^{24}Mg)_{meas}/[(\Delta^{25}Mg/1000) + 1]^2.$$

The corrected values reflect nonlinear effects that are expressed as the fractional deviation in permil of $(^{26}Mg/^{24}Mg)_{corr}$ relative to the normal value 0.139805 (Schramm et al., 1970; Lee and Papanastassiou, 1974):

$$\delta^{26}Mg = \{[(^{26}Mg/^{24}Mg)_{corr}/0.139805] - 1\} \times 1000.$$

Standards of normal Mg isotopic composition were analyzed regularly during

these experiments. Table 3.3 and Figure 3.5 present data in chronological order for measurements of F_{Mg} and $\delta^{26}Mg$ for a standard solution of pure Mg salt analyzed by the conventional loading technique (CC). The last four measurements represent DLT analyses for terrestrial spinel and olivine crystals. Replicate analyses of standard solutions analyzed by the conventional loading technique exhibited a range in the measured F_{Mg} from 0 ± 0.6 to -1.6 ± 0.7‰ amu^{-1}, with a mean FMg equal to -0.8‰.

Table 3.3. Thermal Ionization Standards

Sample	F_{Mg} (‰ amu^{-1})	$\delta^{26}Mg$ (‰)	Tech
nMg-1	-1.3±0.7	-0.9±0.5	CC
	-1.0±1.0	0.0±0.8	CC
	-0.5±0.3	-0.5±0.1	CC
	-0.3±0.3	-0.8±0.3	CC
	-0.8±0.4	-0.9±0.3	CC
	-0.4±0.8	-1.1±0.4	CC
	-1.2±0.5	0.0±0.3	CC
	-0.1±0.6	0.7±0.2	CC
	-0.6±0.4	-0.1±0.2	CC
	-1.6±0.7	0.2±0.2	CC
	-0.4±0.3	-0.6±0.1	CC
	-0.7±0.3	0.2±0.2	CC
	0.0±0.6	-0.9±0.2	CC
	-1.1±0.4	-0.2±0.3	CC
	-1.4±0.4	0.2±0.2	CC
	-1.2±0.5	-0.2±0.2	CC
	-0.7±0.6	0.2±0.4	CC
	-1.0±0.6	0.0±0.2	CC
	-0.7±0.9	0.3±0.3	CC
	-0.2±1.8	0.0±0.2	CC
Spinel	-1.0±1.0	-0.1±0.3	DLT
Olivine	1.7±0.6	0.1±0.2	DLT
Spinel	-2.4±0.4	-0.2±0.1	DLT
Spinel	-1.8±1.5	0.2±0.1	DLT

Figure 3.5. Thermal ionization measurements of F_{Mg} (in permil per amu) and $\delta^{26}Mg$ (in permil) for Mg standards. Analyses are plotted vertically in chronological order, corresponding to the values listed in Table 3.3. Most measurements are for standard solutions of pure Mg salt, analyzed by the conventional loading technique. The last four measurements are for terrestrial samples of olivine and Mg-spinel analyzed by DLT.

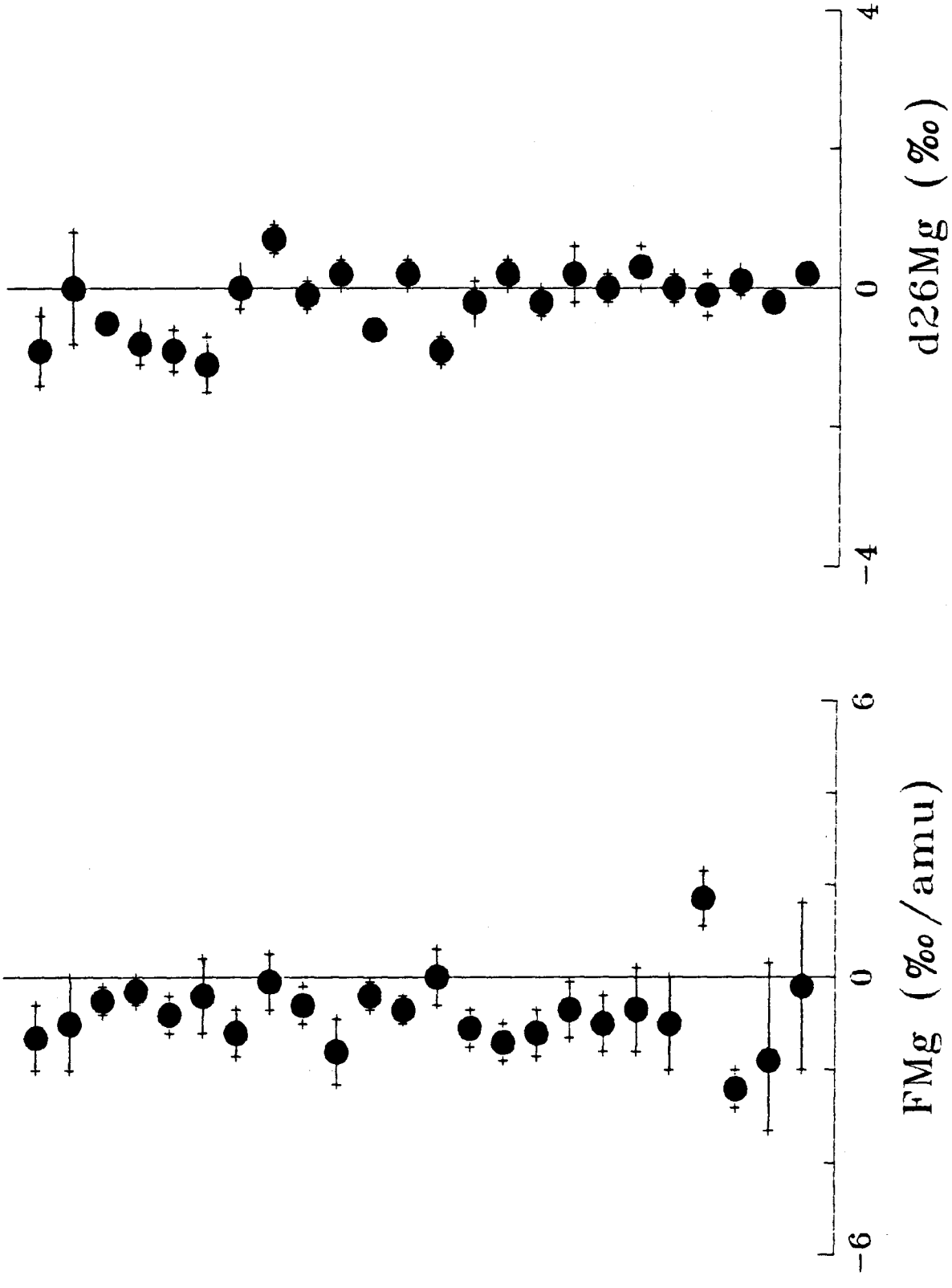
4
0
−4
d26Mg (‰)
6
0
−6
FMg (‰/amu)

This measured range in instrumental fractionation is comparable to the range of ±1.5‰ in $^{25}Mg/^{24}Mg$ reported by Wasserburg et al. (1977). Isotopic fractionation outside this range can be attributed to intrinsic fractionation of the inclusions. Reported uncertainties in F_{Mg} are calculated as $2\sigma_{mean}$ of the distribution of F_{Mg} of all the sets of 10 ratios. For an individual mass spectrometer run with stable Mg intensities, an uncertainty less than 1.5‰ is often observed; however, we believe that the ±1.5‰ reproducibility observed for replicate analyses provides the true measure of uncertainty in F_{Mg}. The dominant contribution to the uncertainty is provided by the beam stability obtained with the silica gel technique.

Repeat analyses of terrestrial spinel standards by DLT exhibited F_{Mg} ranging from -1.0 to -2.4‰ amu^{-1}. The F_{Mg} value for olivine appears to be anomalously high. The range of instrumental fractionation appears to be comparable for DLT and the conventional loading technique.

After correction for mass-dependent fractionation, the $^{26}Mg/^{24}Mg$ ratios for standard Mg solutions (free of Al) are in agreement with the normal value 0.139805 (Schramm et al., 1970). Lee et al. (1977) have shown by replicate analyses of terrestrial and meteoritic minerals, that the presence in our mass spectrometer of a high ^{27}Al beam for chemically unseparated samples analyzed by DLT leads to an offset in $\delta^{26}Mg$ of -1.5‰. This effect is unexplained but appears to be well-behaved for Al-rich samples. The offset appears to be constant in spite of varying $I(^{27}Al^+)/I(^{24}Mg^+)$ intensity ratios. To correct for this effect, 1.5‰ was added to the observed data from samples which exhibited a measured intensity ratio $I(^{27}Al^+/I(^{24}Mg^+)$ larger than 0.5. Terrestrial spinel standards analyzed by DLT

confirm the reported shift of -1.5‰ in $\delta^{26}Mg$, and yield $\delta^{26}Mg = 0$ when adjusted by the addition of the 1.5‰ correction (Table 3.3, Figure 3.5). The quoted uncertainty for $^{26}Mg/^{24}Mg$ is $2\sigma_{mean}$ and is typically ±0.2‰ for analyses by both the conventional loading technique and DLT. The reproducibility of normals and of repeat analyses of samples is consistent with this uncertainty estimate.

2.4.7. REPRODUCIBILITY AND PRECISION

Replicate analyses obtained for aliquots of solutions of dissolved CAI samples are presented in Table 3.4. Values for $\delta^{26}Mg$ are consistent within ±0.3‰, while values for F_{Mg} agree within ±1.2‰ amu^{-1}. For the samples of HB1 listed in the Table, one aliquot was analyzed by DLT without chemical separation, while the other aliquot was analyzed by the conventional loading technique after chemical separation of Mg. ($\delta^{26}Mg$ values for DLT samples in Table 3.4 were corrected for the -1.5‰ offset). The results obtained for F_{Mg} and $\delta^{26}Mg$ by the two techniques, DLT and the conventional loading technique (CC), are identical within errors.

Table 3.4. Replicate Analyses for Thermal Ionization

Sample	F_{Mg} (‰ amu^{-1})	^{26}Mg (‰)	Tech.
B14-B Soln.	-12.2±1.2	3.0±0.2	DLT
"	-12.0±2.0	3.1±0.6	DLT
B7F6 Soln.	11.4±1.4	-1.0±0.4	DLT
"	11.2±1.2	-1.6±0.4	DLT
HB1 Soln.	13.5±1.6	-1.3±0.2	DLT
"	14.6±1.4	-1.5±0.5	CC
DH8 Soln.	25.6±1.0	-0.7±0.2	CC
"	27.9±1.8	-0.6±0.2	CC

3.4.8. COMPARISON OF TECHNIQUES: THERMAL IONIZATION AND ION MICROPROBE

In order to establish the precision of Mg isotopic data obtained by thermal ionization and ion microprobe analysis, samples which had previously been analyzed in this laboratory were analyzed so that my data could be compared with published data. Mg fractionation of ^{25}Mg-spiked anorthite glasses (AnMg) have been reported for ion probe measurements and for gravimetric determinations (Armstrong et al., 1982). I analyzed AnMg grains by DLT. FUN inclusion C-1 has been analyzed extensively by ion microprobe (Huneke et al., 1983) and by thermal ionization (Esat et al., 1978). I obtained a spinel residue of C-1 by acid dissolution; spinel grains (≥75 μm) were polished in individual grain mounts and analyzed by ion probe. Table 3.5 presents Mg isotopic data and published data, which agree within a couple of permil.

Several CAI were analyzed for Mg isotopic composition by both ion microprobe and thermal ionization. However, a comparison of isotopic data is complicated because the inclusions are isotopically heterogeneous, with different minerals exhibiting different fractionation. Individual minerals are analyzed by the ion probe, whereas thermal ionization measurements yield bulk averages for a dissolved sample. Mineral separates were not obtained for thermal ionization analyses: the acid residues consist predominantly of spinel with minor hibonite, while the soluble fractions include fassaite, melilite, and feldspathoid. Even a 100 μm grain analyzed by DLT consists of multiple phases (spinel + fassaite). However, there appears to be no serious disagreement between thermal ionization and ion probe measurements.

Table 3.5. Mg Isotopic Compositions from Ion Probe and Thermal Ionization

Δ25Mg (permil per amu)

	Published Data			This Work	
Sample	Grav.	Ion Probe	Therm. Ionzn	DLT	Ion Probe
AnMg6	9.4	9.1 2.3	_____	8.0 0.8	_____
AnMg7	28.9	29.6 4.8	_____	26.6 1.0	_____
				25.9 1.2	
C-1 spinel	____	31.3 1.5	30.9 1.0	_____	31.5 1.0
					31.3 1.4
					31.9 1.2

a. Armstrong et al. (1982)
b. AnMg values: Armstrong et al. (1982)
   C-1 values: Huneke et al. (1983)
c. Esat et al. (1978)

3.5. ION MICROPROBE ISOTOPIC ANALYSES

3.5.1. INTRODUCTION

Chemical and isotopic information on the composition of sample surfaces can be obtained by secondary ion microprobe analysis. Recent reviews of ion microprobe applications to geochemistry have been given by Shimizu and Hart (1982) and Williams (1985). In this work, isotopic compositions were measured using PANURGE, a modified CAMECA IMS-3F ion microprobe (Huneke et al., 1983). Samples are bombarded with primary ions of keV-energy in order to sputter and ionize material from the surface. Secondary ions are accelerated and focused by electrostatic lenses, then analyzed by a double-focusing mass spectrometer.

The following sections will briefly review the instrumentation, sputtering processes and analytical conditions specific to ion microprobe isotopic analyses presented in this work.

3.5.2. ION MICROPROBE INSTRUMENTATION

General reviews of ion probe instrumentation have been given by Liebl (1975a,b) and Slodzian (1980). Figure 3.6 shows a schematic drawing of the components of the CAMECA IMS-3F ion probe. The following discussion refers to components labeled in this figure.

a. Primary Beam Source and Optics

The primary ion source consists of a hollow cathode duoplasmatron (DP in Figure 3.6). A low-pressure oxygen gas is ionized by an arc maintained between the Ni cathode and anode. The resulting plasma is confined mechanically and magnetically between the cathode and anode. The polarity of the anode can be selected to produce positive or negative primary ions. An intermediate electrode can be offset to select negative ions, which are concentrated toward the outer edges of the plasma. Negative oxygen ions are used in this work because oxygen enhances the positive secondary ion yield (Section 3.5.3); in addition, negative ions tend to reduce sample charging.

The primary O^- beam is accelerated to 10 KV, extracted from the -10 KV potential on the anode by a grounded lens. The oxygen ions are not mass separated. The primary beam column consists of two electrostatic lenses, a condenser and objective lens; deflectors and limiting apertures. The voltage on the condenser lens (L1) adjusts the primary current density passing through a limiting aperture which eliminates scattered ions. The objective lens (L3) focuses the beam on the sample. Three X-Y beam deflectors and a stigmator are used for beam alignment and for rastering the beam. Primary beam currents were typically 0.1 to 2 nA, with a beam spot on the sample of 3 to 10 microns. The primary beam intensity is typically stable to 0.1% over 30 minutes. The primary beam is inclined 30° to the normal to the sample.

Figure 3.6. Schematic diagram of the components of the CAMECA IMS-3F ion probe. In the primary column, DP indicates the duoplasmatron source, L1 the condenser lens and L3 the objective lens. The primary column is oriented 60° to the sample. In the ion extraction system, IL denotes the immersion lens, TL the transfer lenses, CA the contrast aperture, Slit1 the spectrometer entrance slit and FA denotes the field aperture. ESA indicates the electrostatic analyzer, E the energy slit, M the magnet, d1-4 indicate deflectors, Stig denotes the stigmator and PL the projection lenses.

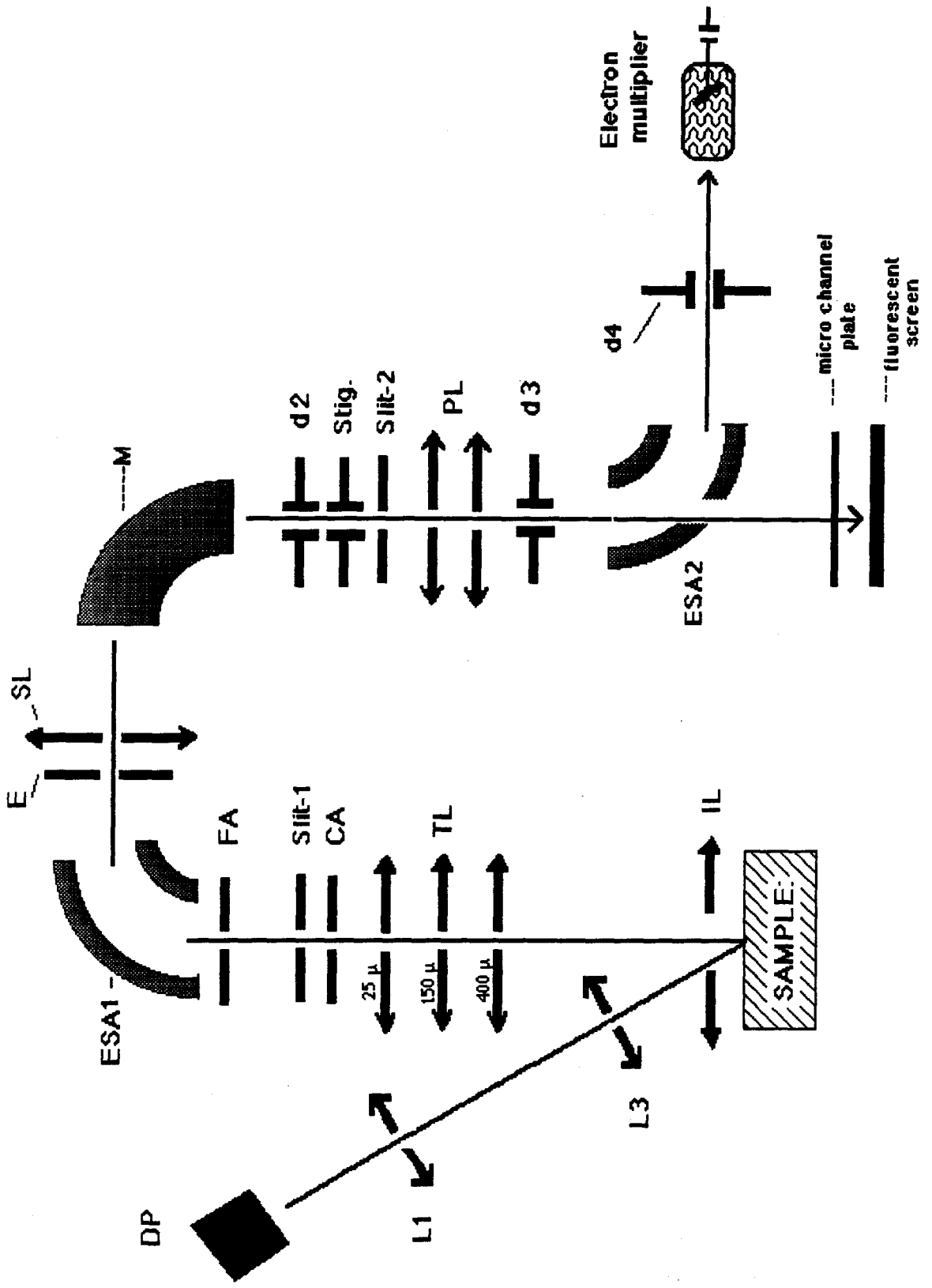
DP
L1
L3
SAMPLE
ESA1
ESA2
E
SL
M
FA
Slit-1
CA
25 μ
150 μ
400 μ
TL
IL
d2
Stig.
Slit-2
PL
d3
d4
Electron multiplier
micro channel plate
fluorescent screen

The polished sample surface is viewed through an 80x optical microscope. The specimen chamber pressure is typically $\approx 10^{-8}$ torr. A liquid nitrogen-cooled cold plate is used to condense water vapor and hydrocarbons in the vicinity of the sample.

b. Secondary Ion Extraction System

The secondary ion extraction system serves to accelerate and focus the sputtered ions. Secondary ions from the sample, which is maintained at a potential of +4.5 KV, are accelerated and focused by an immersion lens (IL). Small offsets (5 to 15 V) are applied to the accelerating potential to compensate for sample charging. Three transfer lenses (TL) serve to limit the collection angle in order to optimize secondary ion transmission from a 25, 150, or 400 μm diameter area; only the 150 μm lens was used. The TL acts to form a virtual image of the sample at the entrance to the ESA.

The secondary ion beam passes through a contrast aperture (CA) which serves to limit the solid angle and energy of the secondary ion beam. The CA and an adjustable spectrometer entrance slit (Slit1) lie in the image plane of the crossover. Interchangeable field apertures (FA) located in the image plane of the virtual image of the sample, allow ions sputtered only from the central 8, 60 or 150 μm diameter region to enter the mass spectrometer. The smallest aperture was used for the analysis of fine-grained phases, but this aperture also sharply restricts the beam intensity. For the larger field apertures, the dimension of the area on the sample analyzed is a function of the primary beam current and focusing; for the smallest field aperture, the resolution is limited to 8μm.

Tuning of the instrument, which is critical to optimizing the secondary ion intensity, involves adjusting the lens voltages in the secondary ion extraction system in an iterative manner. Tuning specifically involves adjustment of the transfer lens, spectrometer lens, contrast apertures, immersion lens and projector lenses. Typical operating parameters for the ion probe are shown in Table 3.6.

Table 3.6. Ion Probe Operating Parameters

O arc current	50 mA
Primary accelerating voltage	-10 kV
Secondary accelerating voltage	+4500 V
Immersion lens voltage	+4717 V
Transfer lens voltage	+6391 V
Spectrometer lens voltage	+4411 V
Projector lens voltage	+6929 V
Electron multiplier voltage	-3000 V
Imaged field	150 um
Contrast aperture	60 um
Focused beam diameter	10 um
Energy bandpass	60 V
Sample chamber pressure	$2x10^{-8}$ torr
Primary column pressure	$2x10^{-6}$ torr

c. Energy and Mass Analysis

Due to the wide energy spread of the sputtered ions, averaging a few ev, a double-focusing system (in energy and momentum) is necessary. Ions are distinguished by mass using a magnetic sector (M), and by energy using a spherical electrostatic analyzer (ESA1). Energy filtering serves to improve mass resolution and reduce aberrations. An energy slit (E) located at the crossover plane after the electrostatic analyzer, serves to limit the bandpass in energies. A wide energy

window was used to minimize changes in instrumental fractionation due to sample charging. A spectrometer lens (SL) refocuses the ions on the exit slit of the magnet. The SL creates a virtual image of the sample or slit inside the magnetic analyzer (M).

The magnet (12.7 cm) separates ions according to the mass to charge ratios. The mass resolving power (defined as $M/\Delta M$, where ΔM is the peak width at 10% of the peak height) is determined by the widths of the mass spectrometer entrance (Slit1) and exit slits (Slit2). The resolving power can be adjusted between 600 and 10000, however a resolving power between 3000 and 5000 was typically used in this work. The magnet is operated in an automated peak-jumping mode, by cycling through a preselected series of magnetic field settings in order of increasing mass. The magnet stability is ≤ 5 ppm over short timescales. The program monitors drift in the magnetic field.

A stigmator is located between the magnet and the spectrometer exit slit (Slit2). The exit slit is located at the crossover plane of the mass spectrometer. The projector lenses (PL) focus the ions onto a microchannel analyzer plate (MCA) used to produce an image which is viewed on a television screen. Ion images can be used to determine chemical distributions in a sample.

d. Ion Detection System

Ions exiting the mass spectrometer can be deflected by an electrostatic analyzer (ESA2) to an electron multiplier. The electron multiplier (Balzers SEV217) is operated in a pulse counting mode at a gain of $\approx 10^7$ electrons/ion and a voltage of

-3000 volts.

Secondary ion intensities were measured by pulse counting; background intensities between peaks were always less than 0.1 counts/sec. A block diagram of the components in the ion counting system is illustrated in Figure 3.7. Signals from the electron multiplier were amplified by a factor of ten by a preamplifier, and pulses exceeding a discriminator threshold of 50 mv were registered by a Philips PM6654 programmable high-resolution counter. Data are acquired under the control of, and analyzed by a Hewlett-Packard 9845B computer.

Counting rates are corrected for deadtime losses in the detection system by the following equation:

$$N = N' / (1 - N'\tau),$$

where N is the true count rate, N' is the measured count rate and τ is the instrumental deadtime. Ti isotopic ratios were determined on a Ti metal standard and fitted to normal ratios using a power law. The deadtime is determined by the deviation of the most abundant isotope ^{48}Ti from this best fit line. The deadtime appears to be independent of the Ti count rate. The dead time varied over a time interval of several months from 12 to 19 ns, due to aging of the electron multiplier.

Reported isotope ratios have been corrected for deadtime counting losses, using the appropriate deadtime determined at the beginning of each data collection period. Standards and unknowns were measured at the same count rates to minimize uncertainties in the deadtime.

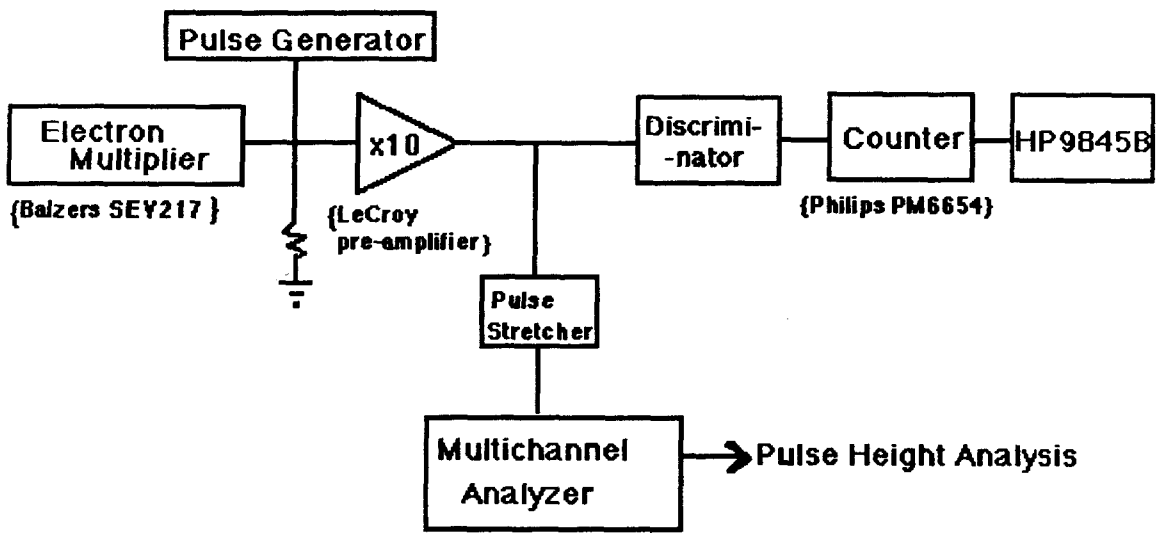

Figure 3.7. Block diagram of the ion counting system in the CAMECA IMS-3F ion probe. The 17-stage Balzers electron multiplier is operated in a pulse counting mode at a gain of 10^7 electrons/ion and a voltage of 3000 volts. Signals are amplified by ten by a preamplifier; pulses exceeding a discriminator threshold of 50 mv are registered by a Philips high-resolution counter. Data are analyzed by a Hewlett-Packard 9845B computer.

Deadtime corrections typically resulted in a correction of ≤2‰ in the isotope ratios for the counting rates used. An uncertainty of 2 ns in the deadtime results in an uncertainty of ≈0.5‰ in the isotopic ratio. The deadtime uncertainty has less effect on the isotopic ratios at lower count rates.

3.5.3. SPUTTERING AND SECONDARY ION FORMATION

a. Sputtering and Ion Production

Sputtering in the ion microprobe involves the bombardment of a solid surface with high-energy (keV) ions, leading to the ejection of neutral and ionic species. This process has been described as a collision cascade, where the primary ion transfers its energy through a series of elastic and inelastic collisions with the crystal lattice. Atoms from the outer few atomic layers of the surface may be ejected if they acquire kinetic energy greater than the binding energy of the solid, and momentum directed back toward the surface. The observation that secondary ion energy distributions peak at low energies (5 to 10 ev), in spite of bombardment by high-energy ions, demonstrates that high-energy recoils are not the dominant mechanism for sputtering. Sputtering occurs on a timescale of $\approx 10^{-13}$ sec. (Williams, 1979).

Secondary particles consist mostly of excited neutral atoms, accompanied by positive and negative ions, as well as molecular species. The secondary ion current measured is a function of several variables (Werner, 1974):

1) the primary ion current,

2) the sputtering yield = the number of atoms sputtered per primary ion,

3) the degree of ionization = the number of secondary ions per secondary neutral particle,

4) the concentration of the element in the substrate, and

5) the transmission of the mass spectrometer.

A comprehensive theory for the physics of secondary ion emission is not available. Reviews have been provided by Werner (1974), Schroeer (1975), Slodzian (1980) and Williams (1979, 1983, 1985) and Sigmund (1981). There are several experimental observations which need to be explained by any model for secondary ion emission. First, secondary ion yields vary by many orders of magnitude for different elements and appear to be a function of the electronic and chemical properties of the solid surface. Second, positive secondary ion yields approximately exhibit an inverse dependence on the ionization potential of the sputtered species. In addition, positive secondary ion yields are enhanced by the presence of electronegative species such as oxygen at the sample surface. This effect is observed for oxygen present in the sample surface (as an oxide), in the bombarding primary ion species, or in the residual vacuum of the instrument.

Most models for secondary ion emission assume that secondary ions are generated within the target as part of the atomic collision process. The most widely-held model for ionic materials is the bond-breaking model of Slodzian (1975), which postulates that ion emission occurs through the dissociation of pre-existing ion pairs near the surface. For oxide materials with only partial ionic

character, collisions cause the breaking of chemical bonds, leading to the excitation and loss of electrons to the surrounding matrix. The presence of electronegative elements, such as oxygen, increases the positive secondary ion yield by decreasing the availability of electrons for the neutralization of sputtered ions. This model is qualitative rather than quantitative.

b. Isotopic Fractionation during Sputtering

It is important to note that sputtering processes have been shown to exhibit a mass dependence which leads to differential sputtering for isotopes (Russell et al., 1980; Gnaser and Hutcheon, 1987). This isotopic fractionation appears to be a function of the kinetic energy of the secondary ions. Lighter isotopes are preferentially sputtered since they acquire higher velocities. Gnaser and Hutcheon (1987) have shown that fractionation in sputtering exhibits a linear dependence on the inverse velocity of the secondary ions ejected.

Ion probe experiments by Gnaser and Hutcheon (1988) have shown that the sputtered ions are initially enriched in the lighter isotopes (up to 54‰ for Li); however, this light isotope enrichment decreases monotonically with increased sputtering and erosion until reaching the steady state value for the sample. These experimental results have been explained, by comparison with computer simulations, by a model involving momentum asymmetry: a greater fraction of light atoms preferentially escape because more light atoms are scattered by large angles during collision cascades and carry net momentum back toward the sample surface.

c. Matrix Effects: Chemistry

The ionization efficiency and isotope composition of secondary ions of a particular element depend upon matrix effects, including sample chemical composition and variations in bond strength of the element with other matrix elements. The measured isotopic fractionation of an element has been shown to be dependent upon substrate mineralogy and chemical composition (Hutcheon, 1982; Huneke et al., 1983; Slodzian, 1980). For example, ion probe instrumental fractionation for Mg (Δ^{25}Mg) typically ranges from -2‰ to -12‰ amu^{-1} for silicate and oxide phases. Hutcheon et al. (1987) found that Δ^{25}Mg values for spinel, fassaite and iron metal fall within this range, while magnetite exhibited more extreme Δ^{25}Mg values ranging from -15 to -22‰ amu^{-1}.

I have attempted to clarify the extent of matrix effects on isotope fractionation of Mg for varying chemical compositions of minerals of interest to isotopic measurements on CAI phases. This has involved measurements of Mg isotope fractionation (Δ^{25}Mg) on a series of spinel and olivine standards with a range in chemical compositions. Table 3.7 lists the instrumental fractionation (Δ^{25}Mg) for individual analyses of standards of varying chemical compositions. The iron content is indicated by the hercynite content (Hc) for spinel, by the forsterite (Fo) content for olivine. Instrumental fractionation of Mg appeared to be constant as a function of Fe content for the spinel and olivine standards measured. However, the measured Al^+ intensity was much higher for Fe-rich spinel than for Mg-spinel.

Table 3.7. Fractionation as a Function of Chemical Composition

Sample	Chemistry	$\Delta^{25}Mg$ ($^{o}/_{oo}$ amu^{-1})
Burma Spinel	Hc1	-12.1±1.2
Herc. Spinel	Hc32	-14.0±1.5
Herc. Spinel	Hc56	-14.2±1.4
Marj. Olivine	Fo90	- 9.3±0.9
Spring.Olivine	Fo82	- 8.1±1.2
Horton.Olivine	Fo53	- 9.0±1.4

d. Relevance to Ion Probe Measurements

The observation that electronegative elements such as oxygen enhance the emission of positive secondary ions has led to the common use of oxygen as a bombarding species in the analysis of geological samples, where positive secondary ions are typically measured. A negative oxygen primary beam is used because this decreases sample charging and increases the secondary ion beam stability.

The fact that sputtering causes erosion of the sample surface and generation of secondary ions from successive depths in the sample means that repeated measurements are not simply replicate analyses of the same material, but analyses of material from increasing depth in the sample.

The observation that secondary ion yields may vary by several orders of magnitude for different elements as a function of the ionization potential of the sputtered species, complicates chemical analysis and phase identification by ion probe analysis. This requires the use of standards for each element analyzed.

Finally, the presence of matrix effects which influence the ionization efficiencies and instrumental fractionation requires the use of standards of chemistry and mineralogy similar to the phases under analysis. Extensive efforts were undertaken to obtain terrestrial standards with chemical compositions similar to each CAI phase analyzed.

3.5.4. ANALYTICAL CONDITIONS

The ion microprobe was used to measure isotopic compositions of Mg, Si, Cr and Fe in Allende inclusions. Procedures relevant to ion microprobe analyses have been discussed by Huneke et al. (1983) and Hutcheon et al. (1987). Instrumental conditions were adjusted for each set of analyses to obtain the required mass resolving power and spatial resolution, and will be discussed below.

Carbon or gold-coated polished sections were sputtered with a 14.5 kV O^- primary beam using a 0.1 to 2 nA current focused to a 3 to 10 micron spot. Figure 3.8 shows a secondary electron image of two holes produced by ion probe analysis. At the beam currents used, the depth of sputtering is typically a few microns per hour.

Grains preselected on the SEM were located in the ion probe with the use of the optical microscope and reflected light maps of the inclusions. Prior to data collection, the ion intensities of relevant elements (Na, Mg, Al, Si, Ca, Ti and Fe) were measured to ensure that the beam is located on the desired phase, and to ensure that there is no beam overlap onto adjacent phases. Single-mineral phases were particularly difficult to locate for fine-grained inclusions, which consist of

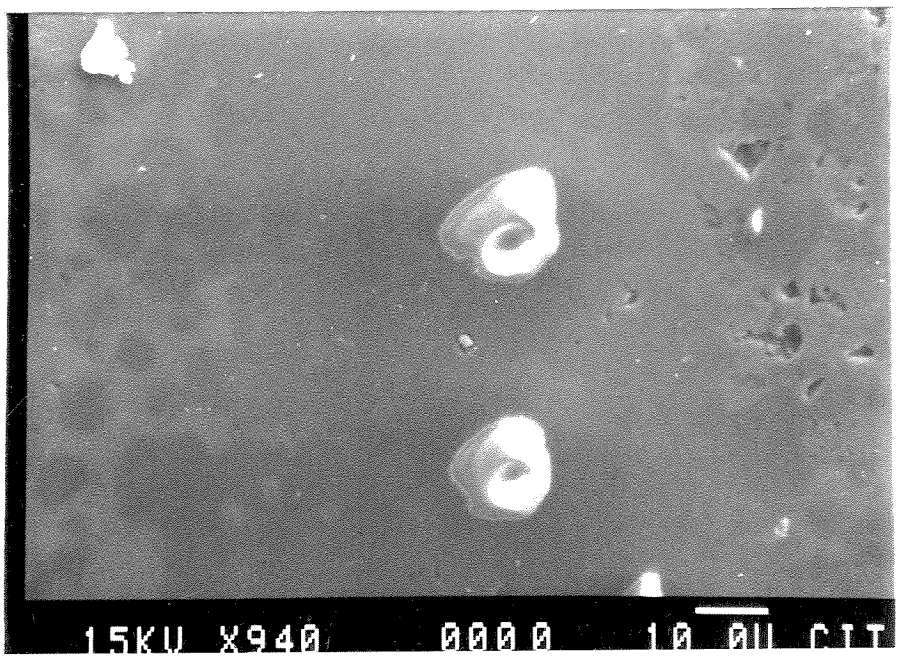

Figure 3.8. Secondary electron photograph showing two holes excavated by ion probe analysis during approximately one hour of sputtering.

minerals frequently intergrown on a micron scale.

Prior to analysis, a high-resolution scan (measuring ion intensity as a function of the magnetic field) is obtained for each mass peak to check the instrumental tuning, and to check that the mass resolution is sufficient to exclude interferences. Figure 3.9 shows a high-resolution scan for mass 25 which is resolved from the smaller hydride ($^{24}MgH^+$) peak at a mass resolving power of 3170. Peaks are typically flat for 3 to 10 milli atomic mass units.

A typical analysis consists of 50 to 200 cycles of measurements of a mass sequence in order of increasing mass. The magnetic field steps successively to each mass peak, measuring the ion current at the peak center and at the half-intensity positions on the low and high mass sides of each peak, to determine if the magnetic field value has shifted from the previous cycle. The magnet control program will compensate for any drift in the magnetic field during analysis. For analysis of extremely low-intensity peaks, e.g., for measurements of Mg in anorthite, the mass dispersion of the lower abundance isotopes (masses 25 and 26) can be fixed with respect to a higher intensity peak (mass 24). In this case, only the peak centroids are measured for masses 25 and 26.

One ion species in the mass sequence is used as a reference isotope to ratio all other ion currents, to compensate for any drift in the primary beam and sputtered ion yield.

Gradual removal of the conductive coating during sputtering typically caused the sample to charge by a few volts. Charging causes shifts in the energy distribution of the emitted ions, possibly affecting the measured isotopic composition. Our

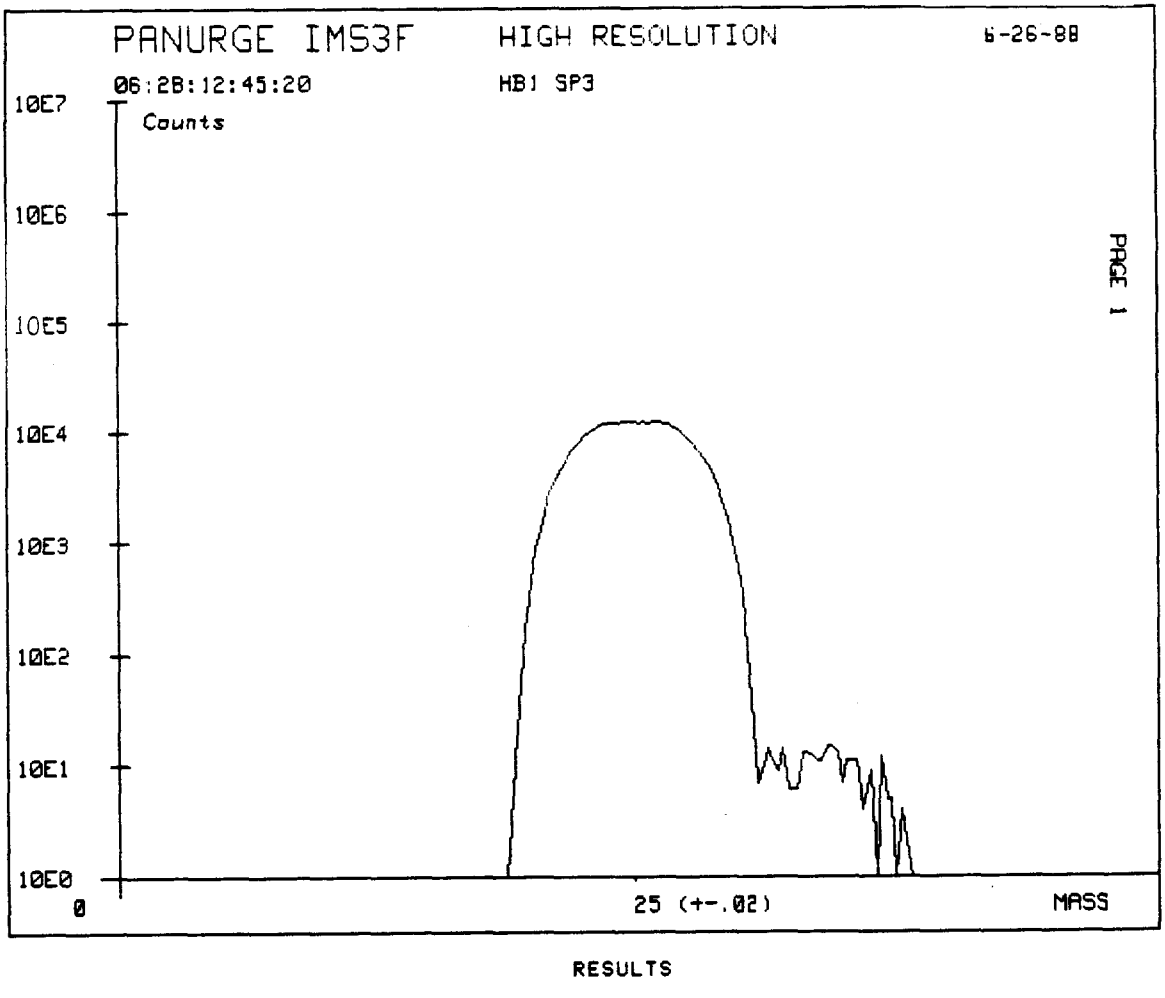

Figure 3.9. Peakshape obtained mass 25 on the CAMECA IMS-3F ion probe, using a mass resolution of 3171. The peak intensity is monitored as the magnetic field is changed in small steps. The $^{25}Mg^{+}$ peak is adequately resolved from the smaller $^{24}MgH^{+}$ hydride peak at this resolving power.

experiments show that charging causes the measured instrumental fractionation to become increasingly positive by a few permil during the time of acquisition of ≈100 cycles. These charging effects were limited by recoating samples, and by limiting the number of successive data sets collected on small grains. Fractionation was determined from the first 50 to 100 cycles to minimize shifts due to charging.

Standards similar to phases analyzed in the CAI were analyzed daily. It was important that instrumental tuning conditions be the same for standards and samples. For analysis of thin sections, the instrument tuning is checked by focusing on the ion image of fine-grained matrix minerals. Isotopic data were periodically collected on olivine chondrules in the matrix near the refractory inclusions to check for differences in instrumental fractionation between standards in grain mounts and inclusions in thin sections. No differences were observed.

A grain mount of FUN inclusion C-1 was analyzed periodically for Mg and Si isotopic compositions during the course of ion probe analyses as a check on the magnitude of the measured isotopic fractionation. This inclusion has been analyzed extensively by thermal ionization (Esat et al., 1978) and ion microprobe analysis (Huneke et al., 1983) and has been shown to be isotopically homogeneous. Mg fractionation was measured for spinel and fassaite, while Si fractionation was determined for fassaite.

a. Isotope Ratios; Standards

For determination of isotopic ratios, the ion intensities are corrected for deadtime counting losses, using the deadtime determined at the beginning of each set of data

collection. Two types of isotopic fractionation data are presented in this work: 1) measured or unnormalized data (Δ^{ij}) for standards, representing instrumental fractionation; and 2) fractionation measurements (F) for samples, corrected for instrumental fractionation. For measurements of isotope fractionation, the unnormalized data (Δ^{ij}) are calculated as deviations (in permil per mass unit) of the measured isotope ratios for the sample (R^{ij}), relative to the normal values (R^{ij}_o) reported for terrestrial isotopic abundances:

$$\Delta^{ij} = \{(R^{ij} / R^{ij}_o) -1 \} \times 10^3 / (m_i - m_j) \quad \text{(units: ‰ amu}^{-1}\text{)}.$$

Isotope ratios determined on the ion probe may deviate from the composition in the sample due to two mass-dependent effects: 1) instrumental fractionation accompanying sputtering and detection; and 2) fractionation intrinsic to the inclusion. Isotope fractionation intrinsic to the CAI phases is determined from the difference in the measured isotope ratios for the samples relative to the isotope ratios of terrestrial standards (std) of similar mineralogy and chemistry:

$$F^{ij} = \Delta^{ij} - \Delta^{ij}_{std.}$$

Uncertainties reported in F^{ij} include both the uncertainty in an individual isotope ratio measurement (due primarily to counting statistics) and the uncertainties in instrumental fractionation for each standard.

b. Ion Probe Analysis

For fine-grained inclusions, only Mg isotopes were measured. Phases analyzed by ion probe analysis in fine-grained inclusions include: spinel, hedenbergite, feldspathoid, olivine and fassaite. For coarse-grained inclusions, the phases analyzed

for Mg, Si, Cr and Fe isotopes are listed in Table 3.8.

Table 3.8. Phases Analyzed in Coarse-Grained Inclusions.

Sample	Isotopes Analyzed in Each Phase			
	Mg	Si	Cr	Fe
DH8	Spinel		Spinel	Spinel
	Fassaite	Fassaite		
	Anorthite	Anorthite		
B7F6	Spinel			
	Fassaite	Fassaite		
	Anorthite			
	Olivine			
		Hedenberg		
B7H10	Spinel			
	Fassaite	Fassaite		
	Olivine	Olivine		
HB1	Spinel	Spinel	Spinel	Metal
		Melilite		Pentlandite
	Grossular	Grossular		
	Andradite			
	Fassaite			
	Hibonite			

Mg isotopes

Data were collected using a mass resolution of 3000, which is sufficient to resolve all molecular interferences in the regions of interest, such as Mg hydrides (Hutcheon, 1982). A typical analysis consisted of 50 to 200 cycles of the sequence $^{24}Mg^{+}$-$^{25}Mg^{+}$-$^{26}Mg^{+}$. $^{27}Al^{+}$ was also measured for Mg-rich phases, while $^{40}Ca^{++}$ and $^{44}Ca^{+}$ were measured for Mg-poor anorthite in order to determine Al/Mg ratios. Count rates for $^{24}Mg^{+}$ ranged from $5x10^{5}$ counts/sec for Mg-rich phases such as spinel and pyroxene, to $5x10^{3}$ counts/sec for anorthite.

Δ^{25}Mg values express the deviation (in permil) of the measured $^{25}Mg/^{24}Mg$ relative to 0.12663 (Catanzaro et al., 1966). Nonlinear isotope effects (δ^{26}Mg) are expressed as the fractional deviation (in permil) of $^{26}Mg/^{24}Mg$, relative to 0.13955, after correction for mass fractionation using a power law (Russell et al., 1978). This normal value differs from the value 0.139805 obtained for standards by thermal ionization, but is closer to the value 0.13932 reported by Catanzaro et al. (1966). This discrepancy between values used for normalization for the two techniques is not well understood.

Terrestrial standards include Mg-spinel, hercynitic spinel (Hc56), Ti-pyroxene glass, anorthite, hibonite, diopside, grossular, nepheline, forsteritic olivine (Fo90) and fayalitic olivine (Fo70, Fo53), where Fo denotes the forsterite content and Hc the hercynite content. Table 3.9 lists average values of Δ^{25}Mg and δ^{26}Mg for these mineral standards. Errors are $2\sigma_{mean}$. Instrumental fractionation (Δ^{25}Mg) ranges from -8.1‰ for olivine to -14.5‰ amu^{-1} for grossular. Replicate analyses of Δ^{25}Mg for individual Mg-rich standards yield a reproducibility of ±1.4‰ amu^{-1}. Δ^{25}Mg for spinel appeared to be independent of Fe content, as indicated by overlapping ranges of Δ^{25}Mg for Mg-spinel and hercynitic spinel. A three isotope diagram of the unnormalized Mg ratios for individual analyses of Mg-spinel and hercynitic spinel is shown in Figure 3.10. The data lie along a line of slope 1/2. Similarly, forsteritic olivine and the more fayalitic olivine standards yielded overlapping Δ^{25}Mg.

In addition to Mg isotopic ratios, the $^{27}Al^{+}/^{24}Mg^{+}$ secondary ion ratio was monitored to check that the beam had not penetrated into a new phase, and to determine the atomic Al/Mg ratio: Al/Mg = (sensitivity factor) x $^{27}Al^{+}/^{24}Mg^{+}$.

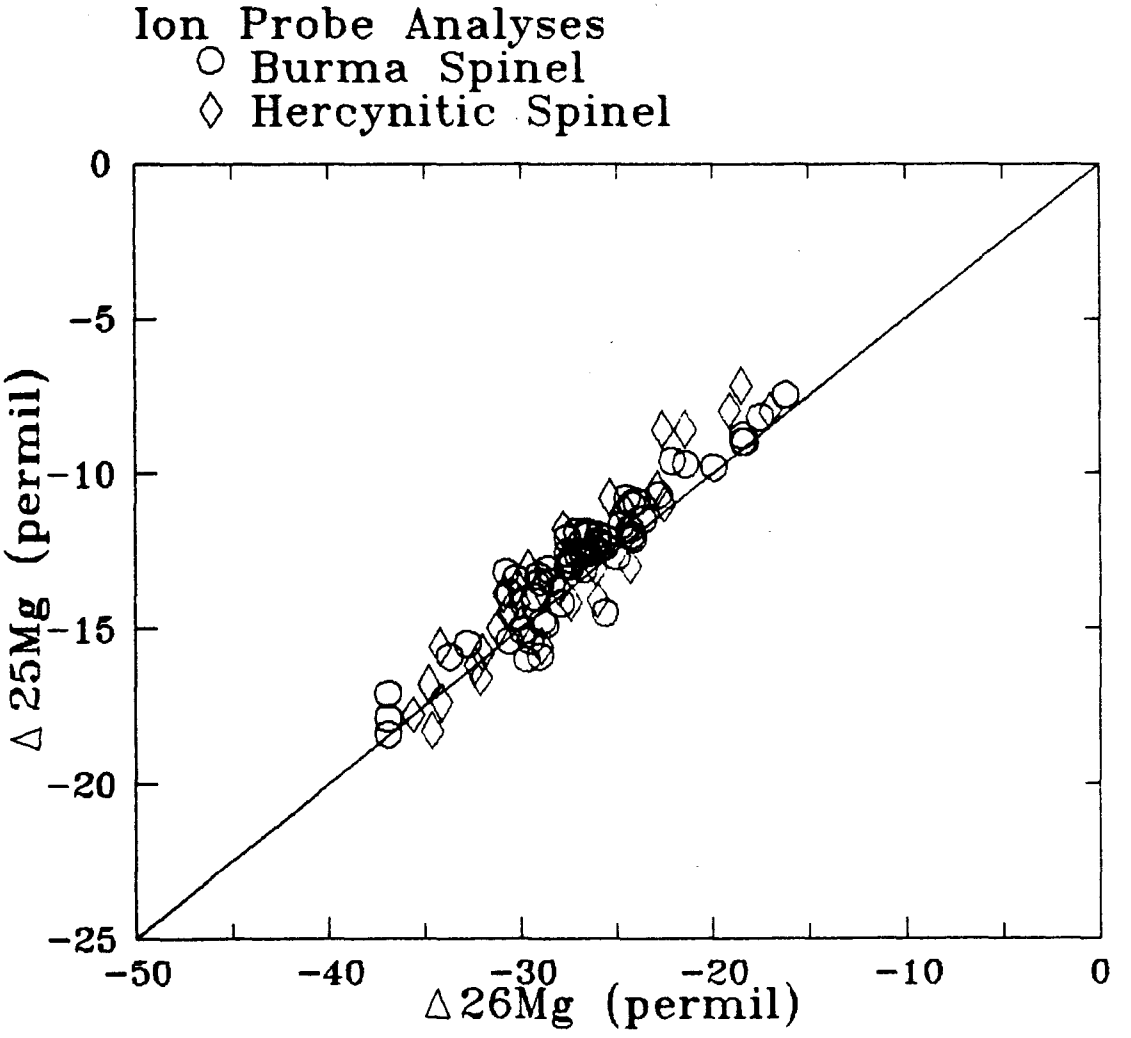

Figure 3.10. Three isotope correlation plot for Mg, showing measured ratios for the terrestrial standards Burma spinel (Mg-rich) and hercynitic (Fe-rich) spinel. The data plot along a mass fractionation line of slope 1/2, with a total range in instrumental fractionation of ≈ 10‰ amu^{-1}.

A composition-dependent sensitivity factor was determined for each mineral by measuring the secondary ion ratio $^{27}Al^+/^{24}Mg^+$ on the ion probe, and the Al/Mg atom ratio by EDS or electron probe analysis (Hutcheon, 1982; Huneke et al., 1983). Sensitivity factors were 1.25 ± 0.06 for spinel and pyroxene. For anorthite, the $^{27}Al^+$ signal was too intense to measure at the high primary beam currents used to obtain sufficient $^{24}Mg^+$ signal. $^{27}Al/^{24}Mg$ ratios for anorthite were determined by comparing $^{40}Ca^{++}/^{24}Mg^+$ and $^{44}Ca^+/^{24}Mg^+$ measured in anorthite with respective ratios measured in terrestrial plagioclase (≈An95) with a well-determined Mg content and major element composition.

Si isotopes

Isotopic data were obtained for the mass sequence $^{28}Si^+$-$^{29}Si^+$-$^{30}Si^+$ and collected at a mass resolution of 3000, sufficient to resolve hydride interferences and $^{14}N^{16}O^+$. Counting times of ten seconds were used for masses 29 and 30. Typical count rates for $^{28}Si^+$ using a 1 nA primary beam current were $2x10^5$ counts/sec. $\Delta^{29}Si$ values reflect the deviation of the measured $^{29}Si/^{28}Si$ ratio relative to 0.05063 while nonlinear effects ($\delta^{30}Si$) reflect the deviations in 30Si/28Si relative to 0.03362 (Barnes et al., 1975) after correction for fractionation using a power law.

Values of $\delta^{30}Si$ for terrestrial standards (Table 3.9) exhibit a consistently negative offset of a few permil with respect to the quoted normal value. Data for inclusions are reported relative to the average value of the standard analyses.

Standards included synthetic Ti-rich pyroxene and melilite glasses, terrestrial hedenbergite, anorthite, melilite, hercynitic spinel, olivine and nepheline. Figure

3.11 shows unnormalized $\Delta^{29}Si$ and $\Delta^{30}Si$ data for individual analyses of standards, which plot along a line of slope 1/2. The precision of Si isotopic measurements is typically ±1.8‰ amu^{-1} for $\Delta^{29}Si$ analyses.

Table 3.9. Mg and Si Isotopes in Ion Probe Standards

Sample	$\Delta^{25}Mg$ ‰ amu^{-1}	$\delta^{26}Mg$ ‰	$\Delta^{29}Si$ ‰ amu^{-1}	$\delta^{30}Si$ ‰
Burm Sp	-14.9±1.2	0.2±0.6	--	--
Herc Sp	-14.2±1.4	0.1±1.0	-43.7±7.0	4.7±1.3
Marj Ol	- 9.3±0.9	0.2±0.9	--	--
Spr Ol	- 8.1±0.9	0.6±1.6	-39.0±2.0	-6.2±3.6
Chond	-10.0±0.9	1.6±2.3	--	--
Ti-pyx	- 9.2±1.2	0.3±1.3	-37.2±0.7	-3.9±1.1
Plag	- 8.5±3.5	2.6±2.3	-32.2±0.8	-2.2±1.7
Hib	- 8.4±1.2	0.5±2.1	--	--
Diop	- 8.8±1.1	-0.6±1.8	--	--
Mel	--	--	-39.0±1.2	-5.9±2.0
Gross	-14.5±1.7	0.8±0.7	-40.2±0.9	-5.2±1.6
Hedenb	- 9.5±1.6	-0.8±2.3	-37.5±1.0	-3.9±1.8
Neph	--	--	-30.0±0.9	-4.2±2.1

Cr isotopes

Isotopic data were collected at a mass resolution of 4600, with measurements obtained for the mass sequence $^{50}Cr^{+}$-$^{52}Cr^{+}$-$^{53}Cr^{+}$. ^{54}Cr was not measured due to interferences from ^{54}Fe. Counting times of ten seconds were used for masses 50 and 53. A beam current of 1 nA was typically used, with count rates of $3x10^5$ counts/sec for ^{52}Cr. Data are corrected for isotope fractionation by normalizing to $^{50}Cr/^{52}Cr = 0.051859$. The principal interference is due to ^{50}Ti. Standards include Cr-metal and Cr-rich spinel. Precision of Cr isotopic measurements is typically ±2‰ amu^{-1} for spinel analyses.

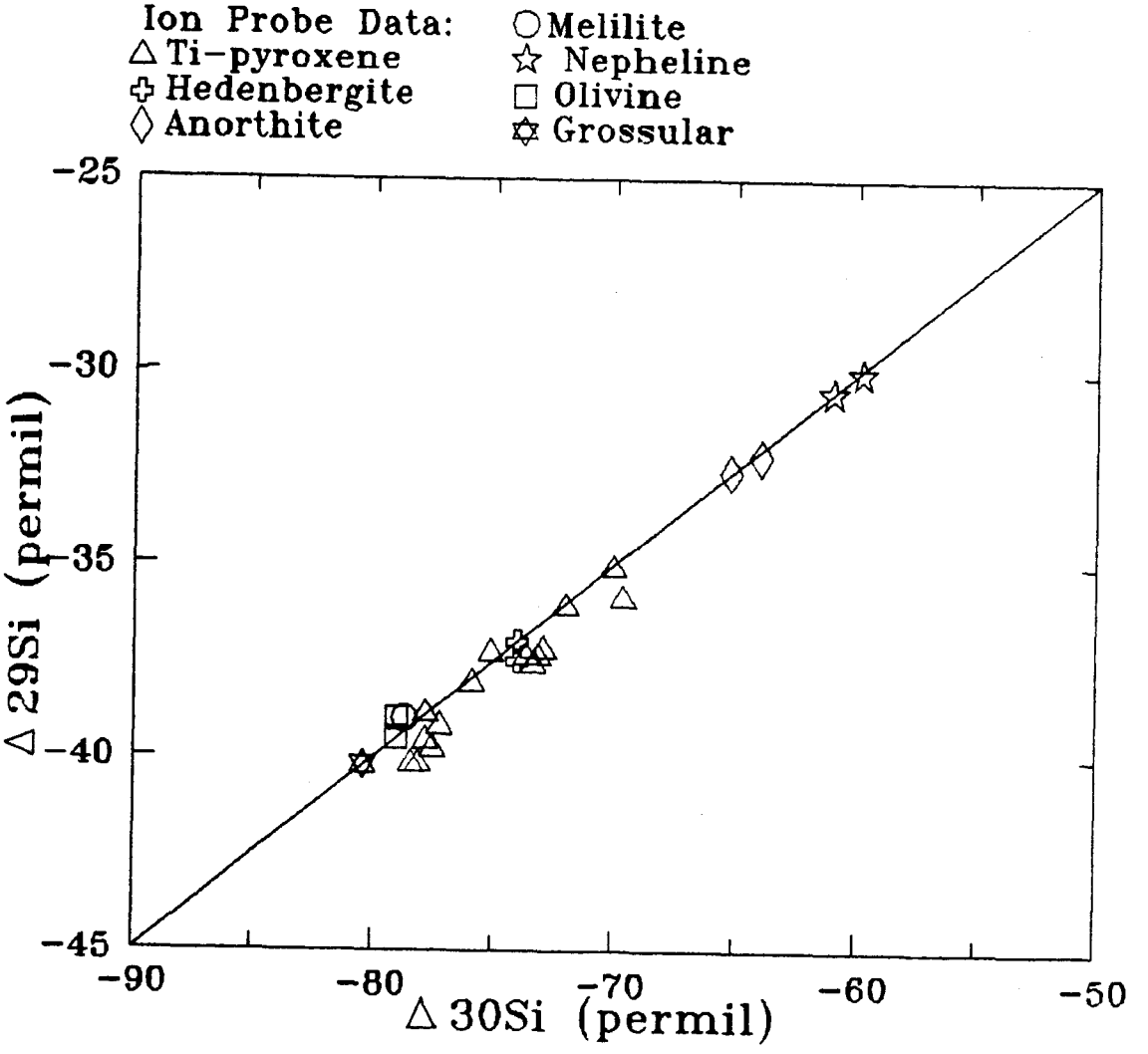

Figure 3.11. Three isotope correlation plot for Si, showing unnormalized data from several terrestrial standards. The data plot along a mass fractionation line of slope 1/2, with a total range in instrumental fractionation of ≈ 10‰ amu^{-1}.

Fe isotopes

Measurements were obtained for spinel and phases in opaque assemblages, for the mass sequence $^{54}Fe^{+}$-$^{56}Fe^{+}$-$^{57}Fe^{+}$ with counting times of ten seconds for masses 54 and 57. Typical count rates for ^{56}Fe were $5x10^{4}$ counts/sec for a 1 nA primary beam current.

Data were collected using a mass resolution of 5500, which is sufficient to resolve $^{56}FeH^{+}$ and $^{57}Fe^{+}$. Molecular interferences such as Si_2^{+}, MgO_2^{+} and CaO^{+}, are well-separated from the Fe peaks at this resolving power. Interferences by $^{54}Cr^{+}$ and $^{58}Ni^{+}$ remain unresolved from ^{54}Fe and ^{58}Fe respectively; peak stripping procedures are required to separate these interferences. Cr interferences can be corrected by measuring the $^{52}Cr^{+}/^{56}Fe^{+}$ ratio and assuming $^{54}Cr/^{52}Cr = 0.027535$. Analyses were obtained only for Fe-rich spinels with low Cr contents, so that corrections from Cr interferences were no more than a couple of permil. Due to the high abundance of Ni in the metal phases in the opaque assemblages, the $^{58}Fe/^{56}Fe$ ratio was not measured.

Terrestrial standards included: Fe and FeNi metals, pentlandite, magnetite, ilmenite, hercynitic spinel, hedenbergite and Fe-rich olivine. The instrumental fractionation for Fe isotopes in standards is illustrated in Figure 3.12. Fractionation is determined from the $^{54}Fe/^{56}Fe$ ratio. Two distinct ranges of fractionation were observed. Metals, oxides and sulfides exhibit fractionation $\approx$31‰ amu^{-1}, while spinel and silicate standards exhibit fractionation $\approx$17‰ amu^{-1}.

This strong dependence of instrumental fractionation on phase composition necessitated careful location of the primary ion beam when analyzing phases in CAI

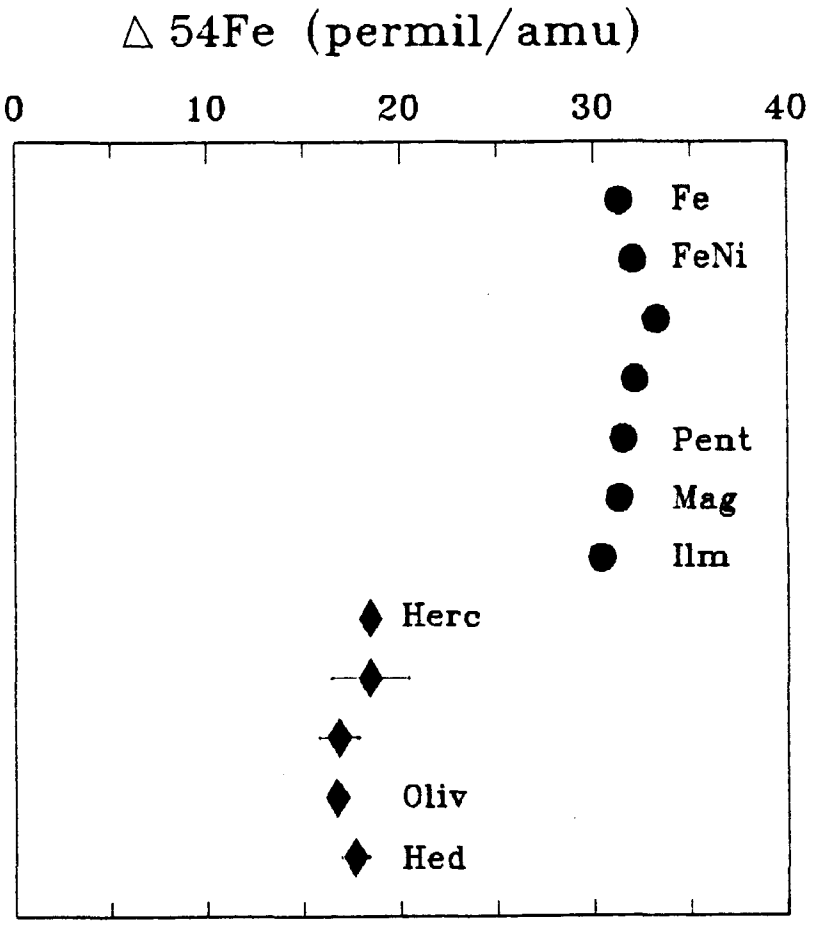

Figure 3.12. Instrumental fractionation (in permil/amu) for iron isotopes, determined from the $^{54}Fe/^{56}Fe$ ratio. Two distinct ranges were observed. Metals, oxides and sulfides exhibit fractionation of 31‰ amu^{-1}, while spinel and silicates exhibit fractionation of ≈17‰ amu^{-1}. Errors are smaller than the size of the symbols, except where indicated.

and a definitive identification of the phase analyzed, so that the relevant standard could be used for correction of the data. In the majority of cases, analyses were obtained for single phases, as determined by measuring ion intensities of relevant elements on the ion probe, and by studying the regions on the SEM after ion probe analysis. In selected cases, analyses appeared to be for mixtures of phases. In these cases, it was important to carefully estimate the percentages of each phase present, by examination of the analyzed region using the SEM. Then the instrumental fractionation for the mixture of phases was estimated, using the percentages of each phase present, and the measured fractionation of each phase.

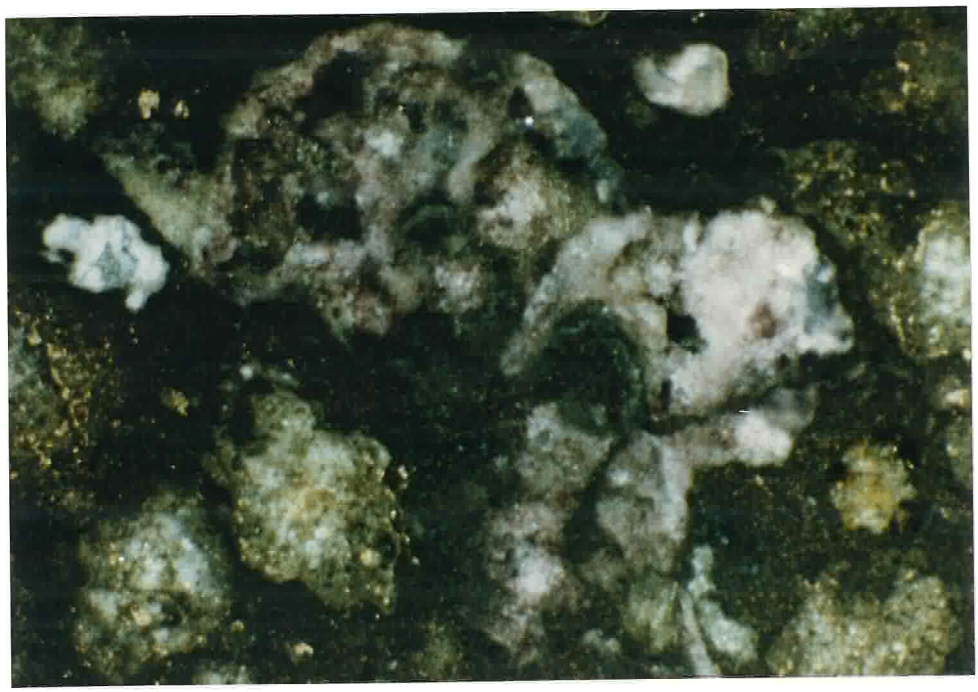

Figure 4.1. Purple Spinel-rich Inclusion B7F6 (5x2 mm). B7F6 is a FUN inclusion, consisting predominantly of spinel, fassaite and feldspathoid. Note the abundant void space and the irregular shape of the inclusion.

CHAPTER FOUR

FUN ISOTOPIC ANOMALIES AND ISOTOPIC HETEROGENEITY IN PURPLE SPINEL-RICH INCLUSIONS

4.1. INTRODUCTION

A few rare Ca-Al-rich inclusions in carbonaceous chondrites have retained evidence of primordial heterogeneity in the presolar nebula. The inclusions exhibit large, correlated isotopic anomalies for many elements, and have provided insight into a broad range of nucleosynthetic and nebular processes.

The inclusions have been named FUN inclusions for isotopic Fractionation and Unknown Nuclear effects (Clayton and Mayeda, 1977; Wasserburg et al., 1977). These refractory inclusions show characteristic isotopic effects consisting of large mass-dependent fractionation for O, Mg and Si, coupled with nuclear anomalies for all elements measured (O, Mg, Si, Ca, Ti, Cr, Sr, Ba, Sm).

The large isotope fractionation effects in FUN inclusions have provided constraints on early nebular processes such as condensation, evaporation, and the mixing and preservation of reservoirs (Niederer and Papanastassiou, 1984; Clayton et al., 1985). The unique patterns measured for isotopic anomalies are correlated over

relatively broad regions of the chart of nuclides. Comparisons of observed isotopic patterns with predictions from theoretical astrophysical models, have provided insight into possible sources of nucleosynthetic material injected into the solar nebula (cf. reviews by Wasserburg et al., 1980; Begemann, 1980).

An understanding of the origin of FUN anomalies has been hindered by: a) the rarity of inclusions exhibiting FUN anomalies; b) the lack of petrographic or chemical characteristics which distinguish FUN inclusions from isotopically normal CAI; and c) observations that some inclusions exhibit large isotopic fractionation effects ($\geq$10‰ amu^{-1}), which are not accompanied by nuclear anomalies. These issues will be addressed in this chapter.

I have identified a new class of coarse-grained inclusion in Allende, which are important because they exhibit an unusually high frequency of FUN isotopic anomalies. Approximately 20% of these inclusions exhibit FUN anomalies, in contrast to $\leq$6% of typical coarse-grained inclusions. The inclusions in this class are distinguished by macroscopic characteristics, including high spinel contents and a distinct purple color (Figures 1.1b, 4.1), hence the name: Purple, Spinel-rich Inclusions (PSI; Brigham et al., 1987). Four new FUN inclusions have been identified among twenty CAI analyzed. These FUN inclusions exhibit large fractionation favoring the heavier isotopes for Mg (ranging from 12 to 39‰ amu^{-1}) and Si (up to 17‰ amu^{-1}), as well as small deficits in ^{26}Mg and ^{30}Si (Brigham et al., 1987, 1988). Large nonlinear effects in Ca, Ti and Cr have been measured

(Papanastassiou and Brigham, 1989), confirming the identification of the inclusions as FUN.

This chapter presents a) thermal ionization measurements of Mg isotopic compositions of twenty PSI, including four new FUN inclusions identified by this survey; b) detailed petrographic and isotopic data for three fassaite and spinel-rich inclusions (B7F6, B7H10, DH8) and one melilite and spinel-rich inclusion (HB1), all of which exhibit FUN isotopic anomalies; and c) ion microprobe measurements of Mg, and Si isotopic compositions in these FUN inclusions.

Specific problems investigated include the following: 1) the degree of isotopic reequilibration was determined by measuring variations in isotopic fractionation for coexisting mineral phases within individual inclusions; 2) the importance of volatility-controlled processes in the evolution of CAI was studied, by searching for correlated fractionation for Mg, Si and Cr; 3) the degree of mineral alteration and chemical migration was determined by analyzing fractionation in secondary phases; and 4) timescales for formation were constrained by determination of the presence of the short-lived isotope ^{26}Al.

4.2. FUN INCLUSIONS: PREVIOUS WORK

FUN isotopic anomalies were first identified in two Type B coarse-grained Allende inclusions (C-1 and EK-1-4-1), which exhibited large fractionation, and small nonlinear effects for O and Mg (Wasserburg et al., 1977; Clayton and Mayeda, 1977). The observed nonlinear effects consisted of small apparent deficits

in ^{26}Mg and excesses in ^{16}O. Oxygen isotopic compositions of FUN inclusions plot off the mixing line of slope unity observed for Allende CAI, and can be explained as resulting from fractionation of an ^{16}O-enriched reservoir, followed by exchange with isotopically normal material. Large Mg fractionation effects were observed: +30‰ for C-1 and +20‰ amu^{-1} for EK-1-4-1. Nonlinear effects for ^{26}Mg, -1.7‰ for C-1 and -3.7‰ for EK-1-4-1, are not correlated with the magnitude of Mg fractionation. Similar effects are reported for silicon, consisting of large isotopic fractionation and small deficits in ^{30}Si (Clayton et al., 1978). Petrographically, these two coarse-grained FUN inclusions consist predominantly of fassaite, melilite, and spinel, with minor anorthite. The inclusions do not appear petrographically distinct from typical Type B CAI; however, EK1-4-1 has not been studied in detail.

Subsequently, isotopic anomalies were identified in these two inclusions for all other elements measured: Si, Ca, Ti, Cr, Sr, Ba and Sm, plus Nd anomalies for EK-1-4-1 only (cf. review by Lee, 1979; Wasserburg et al., 1980; Niederer et al., 1980; Papanastassiou, 1986). The isotope patterns for nonlinear effects in C-1 and EK-1-4-1 are distinct, and not complementary for any of the elements. In other words, one can not obtain the normal solar system composition, by a mixture of the two exotic components represented by the two inclusions. This can be illustrated using data for Ti isotopes (Niederer et al., 1980). Both inclusions C-1 and EK-1-4-1 show small excesses in ^{47}Ti (after normalization to ^{48}Ti); however, C-1 also exhibits deficits in ^{49}Ti and ^{50}Ti, while EK-1-4-1 exhibits excesses in these isotopes. Ti isotopic anomalies for the two inclusions, coupled with observations of endemic excesses in ^{50}Ti in most CAI, require the addition of at least three isotopically

distinct nucleosynthetic components to the solar nebula (Niederer and Papanastassiou, 1981). One further important observation is of a general correlation in FUN inclusions, between effects for the most neutron-rich isotopes of three elements, ^{50}Ti, ^{48}Ca and ^{54}Cr, suggesting contributions from a neutron-rich equilibrium nucleosynthetic process (Niederer et al., 1985).

The observations for O and Mg isotopes for inclusions C-1 and EK-1-4-1 suggested that large fractionation effects are associated with, and may be indicative of more general isotopic anomalies for other elements. Two forsterite-bearing, Type B inclusions were subsequently identified (CG-14 and EK-25-S2-TE), which exhibit strongly fractionated O, Mg and Si (Clayton et al., 1984). Mg fractionation was determined to be 18 and 14‰ amu^{-1}, respectively, for the two inclusions. However, no nuclear (UN) anomalies were observed for heavy elements (Papanastassiou and Wasserburg, 1983; Shimamura et al., 1983); therefore, the inclusions can not be considered FUN. These data indicate that the presence of large fractionation effects may not be sufficient for the identification of UN anomalies. It is important to note that UN effects for Mg, consisting of deficits in ^{26}Mg, may not be indicative, because these deficits may be obscured by radiogenic decay of ^{26}Al to its daughter ^{26}Mg.

A hibonite-rich inclusion HAL was identified, which exhibits O, Ca and Ti isotopic anomalies (Lee et al., 1979), and appears to be a FUN inclusion. Furthermore, extremely large isotopic anomalies have been measured, using the ion microprobe, in some hibonite grains isolated from CM chondrites (Fahey et al., 1985; Hinton et al., 1987; Zinner et al., 1986). The hibonite grains exhibit deficits

and excesses in both ^{50}Ti (-50 to +104‰) and ^{48}Ca (-46 to +54‰). The magnitude of these anomalies is larger than those observed in FUN inclusions; however the presence of these effects in hibonite grains is not well understood.

4.3. PETROGRAPHIC DESCRIPTIONS

4.3.1. CLASSIFICATION OF PSI INCLUSIONS

Purple, spinel-rich inclusions vary widely in petrography. Approximately half of the PSI consist predominantly of fassaite and spinel, and appear petrographically related to Type B CAI (Grossman, 1975), but differ in their high spinel content (≈ 50%), low modal abundances of melilite and anorthite, and high abundances of Na- and Fe-rich phases. These will be called Type B PSI inclusions, where the classification is determined by their major mineralogy (spinel plus fassaite).

About 25% of the PSI consist predominantly of melilite and spinel, and are petrographically similar to Type A CAI. The remaining PSI are rich in spinel and anorthite, with minor olivine, and resemble Type C CAI (Wark, 1987).

Table 4.1 lists the inclusions studied, and the major minerals observed in each inclusion in order of decreasing abundance. Modal mineral abundances are listed for several of the inclusions. Detailed petrographic and chemical descriptions are given below for the FUN inclusions, and an isotopically normal PSI. Three of the FUN inclusions (DH8, B7F6 and B7H10), resemble Type B inclusions; the fourth (HB1) appears similar to a compact Type A inclusion.

Table 4.1. Purple, spinel-rich CAI: Mg isotopic results and petrography

Sample[a]		F_{Mg}[b] °/oo/amu	$\delta^{26}Mg$[c] °/oo	Tech.	Mineralogy[d]	Petrographic Type[e]
			"F-UN"			
BH82DH8		31.1±1.0	-1.6±0.2	DLT	Sp50,Fs36,Me6,Fp4,An3,Ol	B
BG82DH8	sol1	31.2±2.0	-0.8±0.3	CC		
	sol2	25.6±1.0	-0.7±0.2	CC		
	"	27.9±1.8	-0.6±0.2	CC		
B7H10		30.6±1.3	-2.2±0.2	DLT	Sp44,Fs49,Fp5,Hd,Ol	B
BG82HB1		15.4±0.5	-1.5±0.2	DLT	Sp,Me,Hb,Gr,Fd,Ol	A_c
BH82HB1	res	14.7±1.0	-1.5±0.2	DLT		
	sol	13.5±1.6	-1.3±0.3	DLT		
	sol	14.6±1.4	-1.5±0.5	CC		
B7F6		12.1±0.8	-0.8±0.1	DLT	Sp60,Fp10,Fs25,An4,Me2,Ol	B
B7F6	sol1	13.8±1.2	-0.4±0.2	DLT		
	sol2	11.4±1.4	-1.0±0.4	DLT		
	"	11.2±1.2	-1.6±0.4	DLT		
			"F-"			
BG82CH3		13.5±0.7	0.6±0.3	DLT	Sp,Me,An,Fp,Pv	A_f
C1B10		7.2±0.3	0.5±0.1	DLT	Sp,Fs,Pv	A
BG82HB5		6.7±0.8	0.6±0.2	DLT	Sp,Fs,Hd,Fp	B
"		5.7±0.9	0.7±0.2	DLT	"	
A11-16		5.6±1.3	3.9±0.3	DLT	Me,Sp	A_c
B7L3		-6.2±0.7	1.2±0.2	DLT	An,Sp,Ol,Fs,Hb	C
			"NON-FUN"			
B7F7		-1.5±0.5	0.6±0.1	DLT	An,Sp,Ol	C
BG82DI6		-0.4±0.5	0.7±0.1	DLT	Me,Sp,Fs,An,Pv	A
A1-2-3		-0.6±4	0.5±0.9	DLT	Sp,Fs,Hd,Fp,Ol,Pv,Il	
BG82GB1		-0.3±0.6	0.5±0.2	DLT	Fs,Sp,Fp	
BG82HB10		-0.5±0.9	0.2±0.2	DLT	Sp,Ol,An,Fp	C
B7M11		2.3±1.0	0.7±0.2	DLT	Fs,Sp,Fp	B
B7C3		1.2±2.0	1.0±0.4	DLT	Fs,Sp,Hd	B
BG82GH2		-0.8±0.9	1.1±0.2	DLT	An,Sp,Fs	C
BG82CJ7		1.5±1.3	0.4±0.3	DLT	Fs,Sp,Fp	B
BG82II3		0.0±2.0	1.7±0.5	DLT	Fs,Fp,Sp,An	
BG82GH10		-0.8±0.6	0.8±0.2	DLT		A_f

[a] Grains analyzed by DLT. Several samples were also dissolved to obtain residues (res) and solutions (sol), analyzed after chemical separation (cc).

[b] Mass-dependent isotope fractionation factor from $^{25}Mg/^{24}Mg$, relative to normal Mg (errors are 2σ).

[c] Deviations in $^{26}Mg/^{24}Mg$ ratio from normal after correction for mass fractionation. Errors are $2\sigma_{mean}$.

[d] Modal abundances estimated from SEM images. Minerals are listed for each ψ in order of abundance. Sp = spinel; Fs = fassaite; Me = melilite; An = anorthite; Hb = hibonite; Ol = olivine; Fp = feldspathoid; Pv = perovskite; Hd = hedenbergite; Gr = grossular; Il = ilmenite.

[e] Petrographic types: A_c = compact Type A; A_f = fluffy Type A.

4.3.2. INDIVIDUAL INCLUSIONS

B7H10 (3x2.0 mm) exhibits an angular shape (Figure 4.2), and consists mostly of fassaite (49%), spinel (44%) and feldspathoid (5%). No melilite or anorthite were observed; fayalitic olivine and hedenbergite were minor constituents. In the main body of the inclusion, fassaite encloses euhedral, poikilitic 10 to 25 μm Fe-poor spinel (0.2 to 0.8% FeO). Fassaite is surrounded by bands (Figure 4.3a) containing Fe-rich spinel (7 to 10% FeO), feldspathoid, and Fe-rich olivine (Fo71 indicates forsterite content). In these bands, the Fe-rich spinel grains are embedded in intergrowths of fayalitic olivine and sodalite (Figures 4.3a, b). Regions of olivine-sodalite intergrowths exhibit a sharp, linear boundary with adjacent fassaite (Figure 4.3a). Fe-rich spinels are confined to these olivine-feldspathoid regions, such that Fe-rich and Fe-poor spinels are juxtaposed across the fassaite and olivine-sodalite boundary.

The phases (Fe-rich spinel, fayalitic olivine and nepheline) also occur in an adjacent region of the inclusion in a different textural relationship: individual Fe-rich spinels are mantled by fayalitic olivine, and surrounded by euhedral fayalitic olivine and nepheline.

Spinel near the edge of the inclusion is typically more Fe-rich (10 to 18% FeO) than spinel in the interior. B7H10 contains numerous cracks filled with hedenbergite. The inclusion exhibits a sharp boundary with the Allende matrix; no Wark-Lovering rim sequence is present.

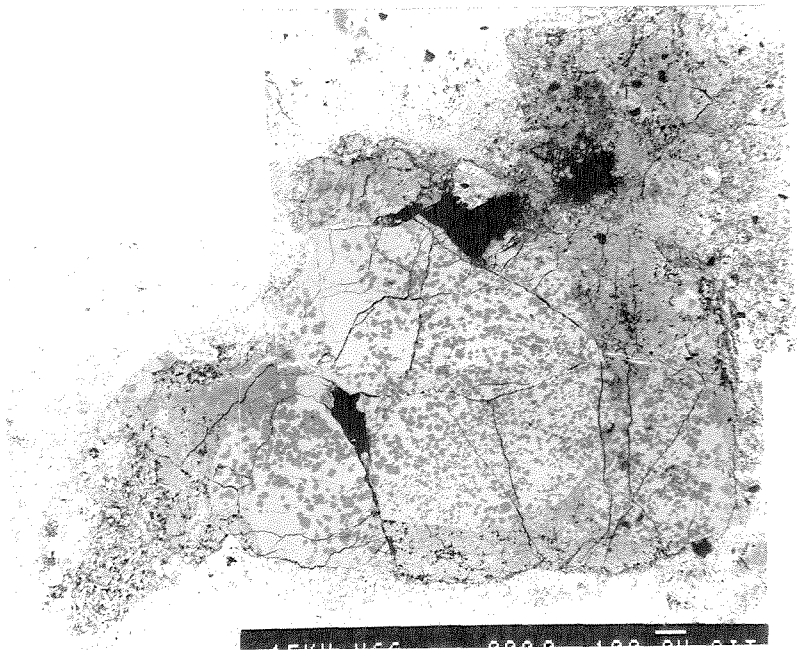

Figure 4.2. Low magnification backscattered electron photomicrograph (BEI) of B7H10 (3x2.0 mm), showing the angular outline, with no Wark-Lovering rim. The interior of the inclusion consists of low-Fe spinel poikilitically enclosed in fassaite. Bands consisting of clusters of Fe-rich spinel grains embedded in sodalite and olivine are concentrated toward the outer edges of the inclusion. Note abundant void space.

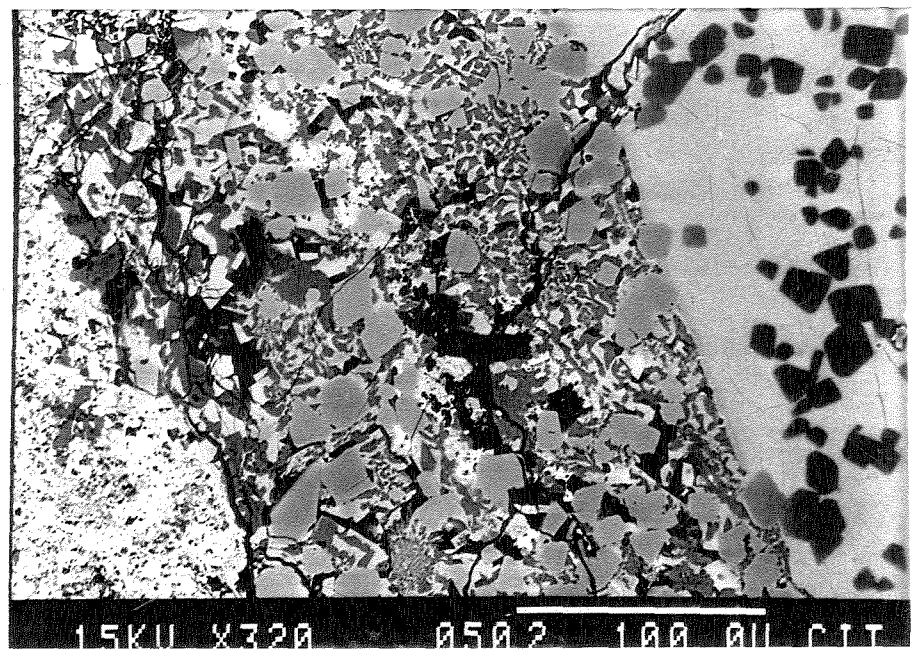

Figure 4.3a. Backscattered electron image (BEI) of B7H10, showing clusters of Fe-rich spinel grains, surrounded by intergrowths of sodalite and olivine. Note the sharp boundaries with fassaite to the right, and Allende matrix to the left.

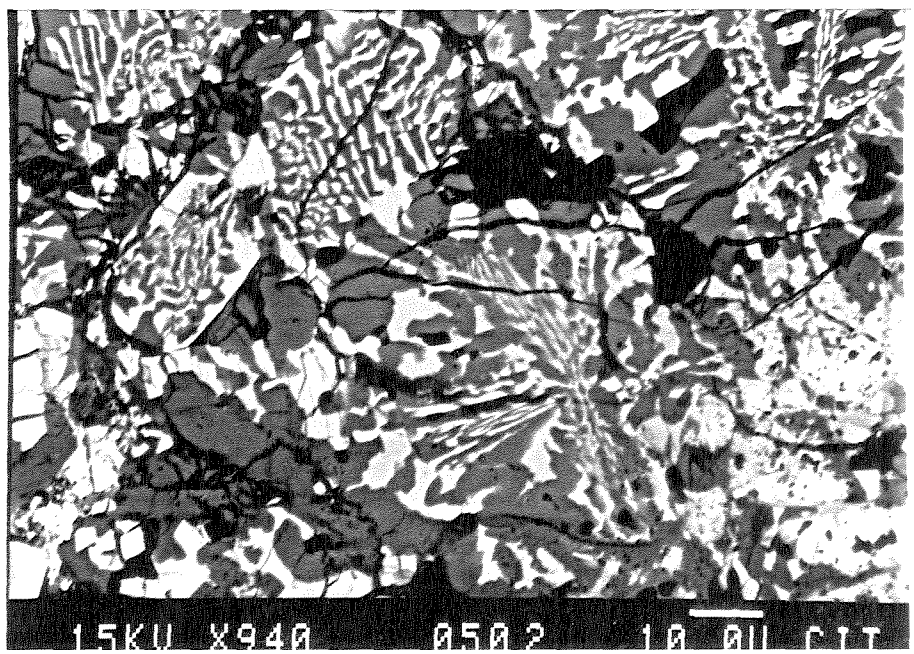

Figure 4.3b. BEI of B7H10 showing an enlargement of the intergrowths of sodalite (dark) and Fe-rich olivine, as illustrated in Figure 4.2a.

DH8 consists of several elongated lobes ranging in size from 300 μm to 4 mm. Spinel (50%) and fassaite (36%) are the dominant phases, with lesser amounts of anorthite (6%), melilite (3%) and feldspathoid (4%). Minor amounts of grossular, hedenbergite and fayalitic olivine (≈Fo70) are present. Similar to B7H10, the dominant texture is poikilitic spinel in fassaite, but, in contrast to B7H10, the poikilitic spinel is Fe-rich (1% to 7% FeO). Melilite and anorthite exhibit sharp boundaries with fassaite and enclose Fe-rich spinel (1 to 7% FeO). The melilite chemistry is ≈Ak38, where Ak indicates the akermanite or Mg content. The most Fe-rich spinel (8% to 11% FeO) occurs in clusters (Figure 4.4a,b) of 10 to 30 μm subhedral grains, surrounded by intergrowths of fayalitic olivine and sodalite. These clusters are concentrated toward the outer margin of DH8.

An unusual feature is the high ZnO content of spinel in DH8, which ranges from ≤0.2 up to 0.9% ZnO, and is highest in the more Fe-rich spinel grains. No systematic correlation of FeO and ZnO was observed. Micron-sized refractory metal nuggets (Os-Ru) are found in or near spinel grains.

One lobe of DH8 contains a distinctive hibonite-rich, fine-grained region containing Fe-rich spinel (10 to 20% FeO), fayalitic olivine (≈ Fo70), hedenbergite, grossular and Ti-rich fassaite (≤16% TiO_2). This region bears a strong textural relationship to fine-grained CAI. Indentations in the outer margin of DH8 are filled with accretionary rim material (similar to that described by MacPherson et al., 1985), with the dominant minerals being hedenbergite, wollastonite, olivine and nepheline. Clusters of forsteritic olivine (Fo94) with fayalitic rims (Fo60) occur outside the inclusion.

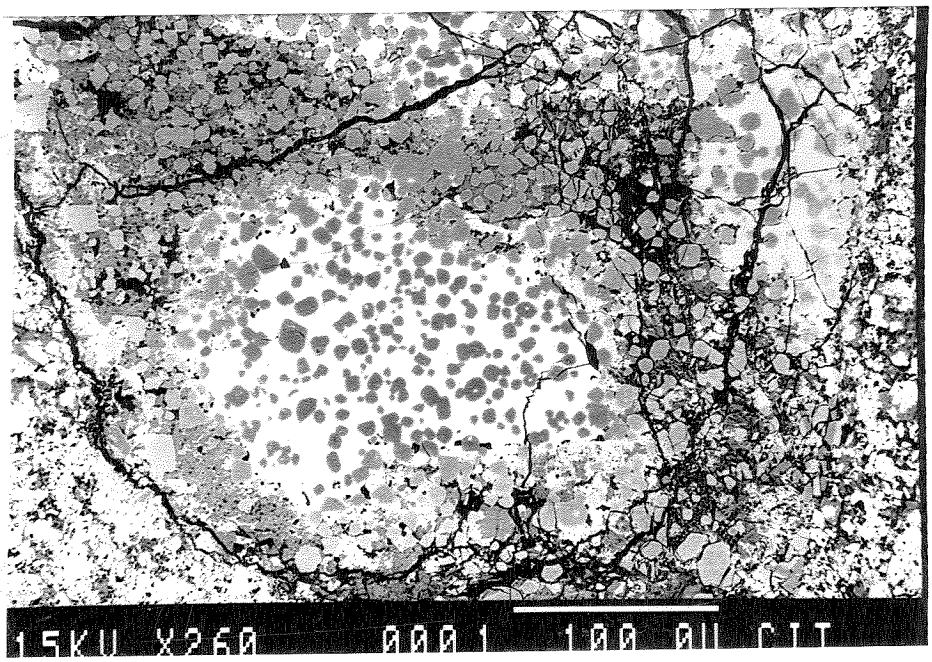

Figure 4.4a. Low magnification BEI of DH8. Clusters of Fe-rich spinel grains cut across fassaite and melilite, which contain poikilitic low-Fe spinel grains.

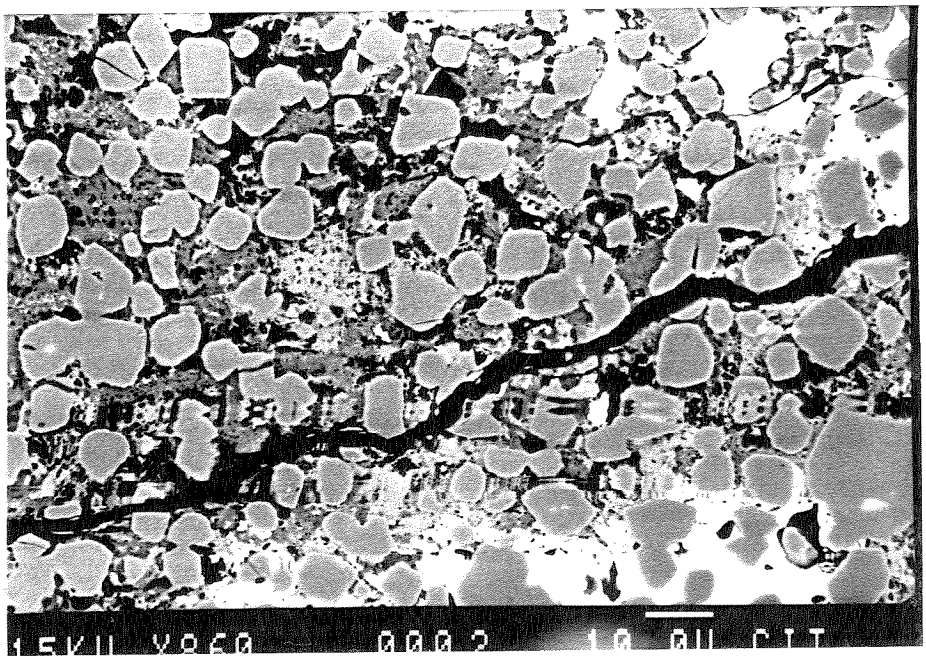

Figure 4.4b. BEI of DH8 showing enlargement of clusters of Fe-rich spinel grains, surrounded by Fe-rich olivine and sodalite intergrowths.

B7F6 (5x2 mm) is a dumbbell-shaped inclusion (see colored illustration in Figure 4.1) with abundant void space (≈20%). The major constituents are spinel (60%), fassaite (25%) and feldspathoid (10%). Small amounts of melilite (≈Ak42), anorthite, hedenbergite, and fayalitic olivine (Fo72 to 78) occur within the inclusion.

Fassaite encloses euhedral, poikilitic grains (≈10 μm) of low-Fe spinel (≈2% FeO). B7F6 differs from the other inclusions in having a large abundance of small spinels, such that there are no spinel-free regions of fassaite larger than approximately 60 μm. Bands of Fe-rich spinel (5 to 18% FeO) embedded in intergrowths of sodalite and olivine are concentrated toward the edges of B7F6, but also cut across the inclusion. Spinel contains up to 0.7% ZnO, with higher Zn contents in the more Fe-rich spinels. Rare, micron-sized refractory metal nuggets are observed in or near spinel grains.

Voids are rimmed by hedenbergite, and occasionally contain olivine laths (≈Fo74) and nepheline protruding into the void (Figure 4.5a). Adjacent to one large void is a 200 μm diameter region of fine-grained hedenbergite, olivine, nepheline and sodalite.

No Wark-Lovering rim was observed; however, the most Fe-rich spinel (11 to 20% FeO) occurs near the edge of the inclusion. Similar to DH8, clumps of forsteritic olivine with fayalitic rims, are quite abundant outside the inclusion (Figure 4.4b).

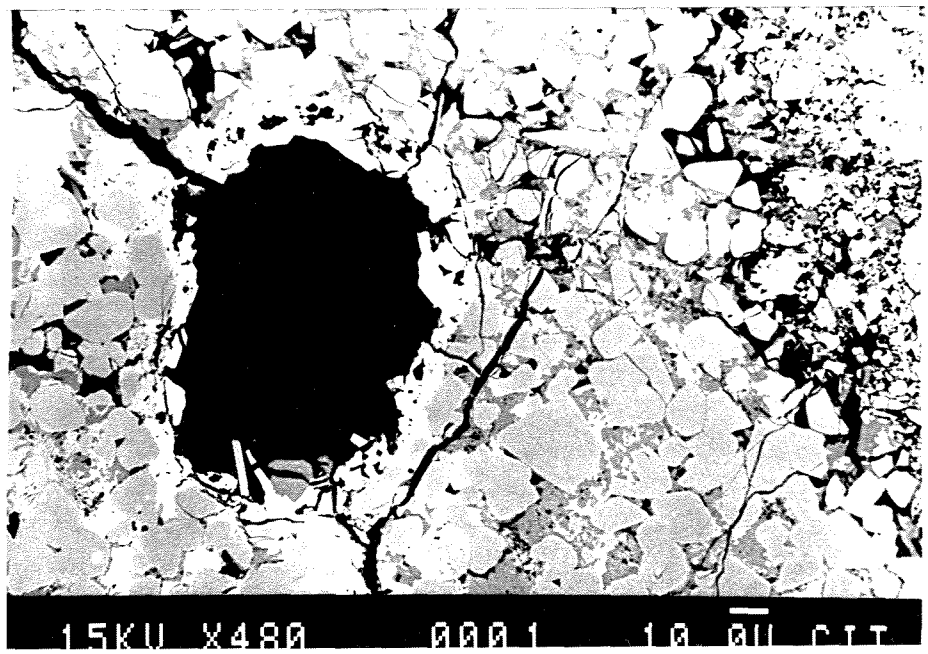

Figure 4.5a. BEI of B7F6 showing void rimmed by hedenbergite, with protruding nepheline and olivine grains. Fe-rich spinel grains occur near the void.

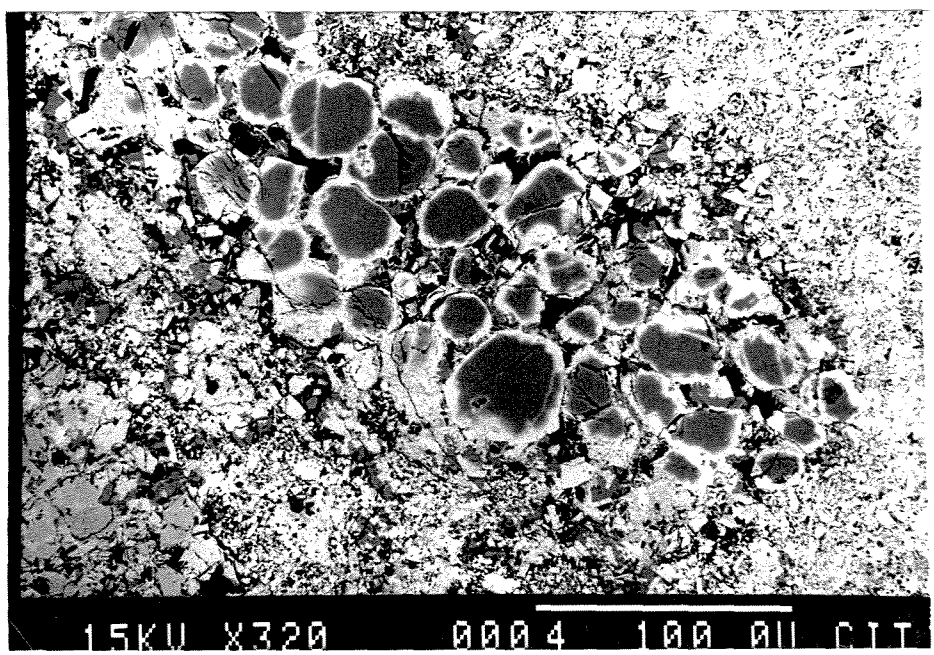

Figure 4.5b. BEI of the outer surface of B7F6, showing clusters of forsteritic olivine mantled by Fe-rich olivine. Olivine grains exhibited isotopically normal Mg.

HB1 (5x5 mm) consists of an elongated blue core (see color illustration in Figure 1.1b). The core is surrounded by a thick red mantle (200 to 450 μm) and a white rim (≈100 μm). HB1 differs mineralogically from the three other inclusions, consisting predominantly of spinel, melilite and hibonite. The core of HB1 is remarkably rich in spinel (≈70%), arranged in radiating bands of spinel clusters, alternating with gehlenitic melilite (Ak3 to 18) enclosing euhedral poikilitic spinel (Figure 4.6a).

In one-half of the inclusion, large regions (≈100 μm) of densely-packed spinel grains with interstitial melilite enclose hibonite laths (Figure 4.6b), containing 3 to 5% TiO_2 and 0.4 to 1.4% V_2O_3. Spinel in the core contains substantial FeO (2 to 5%), TiO_2 (0.5 to 1.3%) and V_2O_3 (0.5 to 0.9%). Numerous opaque assemblages (10 to 20 μm) consisting primarily of Ni_3Fe and pentlandite occur throughout the core. One large opaque assemblage (≈240 μm) consists of Ni_2Fe surrounded by pentlandite and V-rich magnetite (34 to 39% V_2O_3). Opaque assemblages in HB1 are described in detail in Chapter 5.

The spinel-melilite core is surrounded by a red mantle of loosely packed 10 to 25 μm grains of Fe-V-rich spinel (7 to 12% FeO, 1.3 to 1.6% V_2O_3), hibonite, sodalite, nepheline, grossular and olivine. One region of the mantle (1.0x0.7 mm) consists of intergrown Al-rich phases: hibonite, V-rich corundum (1.1 to 1.4% V_2O_3), V-rich hercynite (1.5 to 4.7% V_2O_3) and grossular. The mantle is surrounded by a white rim of grossular, fassaite, nepheline and sodalite. The inclusion is surrounded by a 500 μm-thick accretionary rim, consisting primarily of olivine and nepheline.

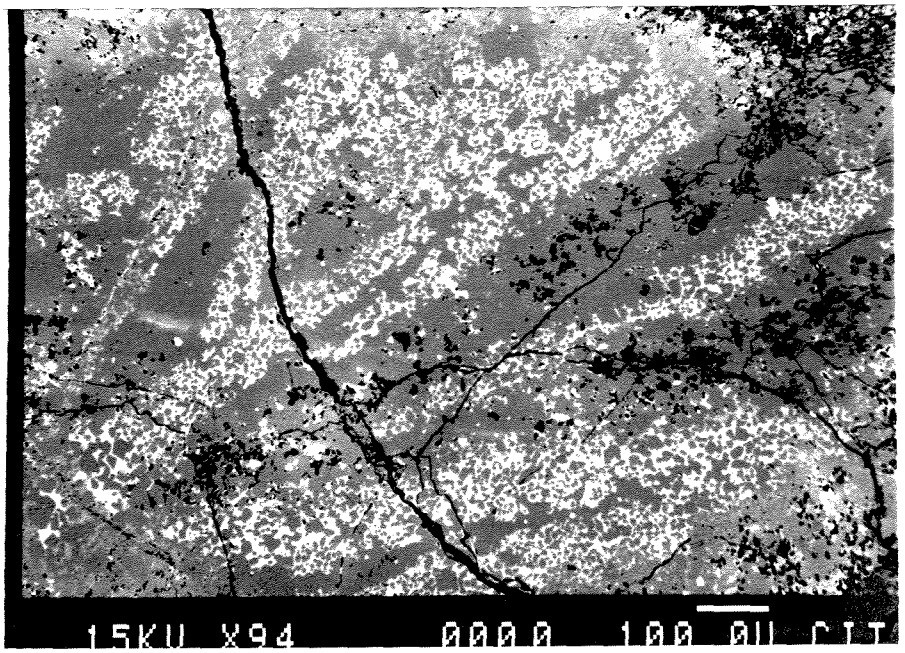

Figure 4.6a. Low magnification BEI of the core of HB1 showing radiating bands of spinel, alternating with gehlenitic melilite and poikilitic spinel. Note the abundance of opaque assemblages.

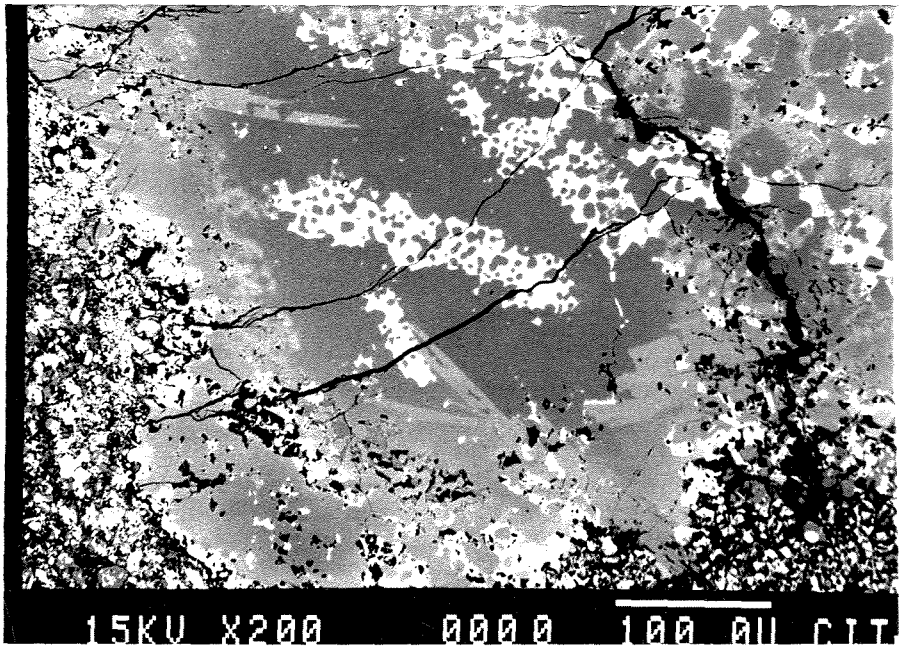

Figure 4.6b. BEI of the core and part of the mantle of HB1, showing densely-packed spinel grains (≈100 μm), enclosing hibonite laths and melilite.

B7M110 (3x3 mm) is an irregularly-shaped inclusion, with angular edges. B7M11 differs from the other Type B inclusions in being less spinel-rich, containing 64% fassaite, 30% spinel and 2% forsteritic olivine, with minor sodalite, nepheline, hedenbergite, Al-diopside, grossular and perovskite.

Spinel exhibits a large range in FeO content. Low-Fe spinels (≈0.2% FeO) occur in chains of 5 to 20 μm euhedral grains, surrounded by fassaite. These chains often enclose regions of Al-diopside and fassaite. None of the other PSI described above exhibit such low Fe contents in spinels; however, these are more typical of ordinary Type B CAI. Opaque assemblages of Ni_2Fe and pentlandite are present.

More Fe-rich spinel (7 to 12% FeO) occur as fragmented grains embedded in intergrowths of sodalite and forsteritic olivine (≈Fo80), with rare perovskite grains. Hedenbergite often surrounds these regions.

Forsteritic olivine (Fo99) occurs as subhedral 10 to 20 μm grains surrounded by more fayalitic mantles (Fo69), and embedded in fassaite. Olivine grains in fassaite were not observed in any of the inclusions described above.

There is no Wark-Lovering rim sequence, although extremely Fe-rich grains (≈18% FeO) occur near the edge of the inclusion.

4.3.3. SUMMARY OF PETROGRAPHIC OBSERVATIONS

The four spinel-fassaite inclusions are remarkably similar to each other in petrologic character, exhibiting angular or irregular outlines, without Wark-Lovering rims. The inclusions are particularly spinel-rich (44 to 60 vol%); although non-FUN

inclusions such as B7M11 appear to be somewhat less spinel-rich (≈30%). The PSI are considerably more spinel-rich than typical Type B CAI (15 to 25% spinel).

Chemical compositions of spinels are given in Table 4.2. All are enriched in FeO, relative to spinel in typical Type B CAI (usually ≤1% FeO). Note the correlation between Fe content of spinel, and location in the inclusion. Fe-rich spinels generally occur in clusters embedded in olivine-sodalite intergrowths, while lower Fe spinels are poikilitically enclosed in fassaite. Two of the inclusions (DH8, B7F6) contain Zn-rich spinel.

Assuming that fassaite is stoichiometric, EDS analyses of fassaite in the inclusions yield a much lower abundance of Ti^{3+} (10 to 30%) than is normally found in Type B CAI (60 to 80% ; Stolper et al., 1982). This low abundance of Ti^{3+} was also observed in fassaite from isotopically normal, Type B PSI.

The inclusions exhibit low modal abundances of melilite and anorthite, in contrast to typical Type B CAI. Na- and Fe-rich phases (feldspathoid, olivine, hedenbergite, grossular) are quite abundant. No opaque assemblages and only minor metal nuggets were observed in the FUN inclusions; the non-FUN inclusions contain more abundant opaque assemblages.

There are similarities between the Type B PSI and FUN inclusion C-1, which also exhibits two distinct spinel populations (Fe-rich and Fe-poor spinels) and contains clusters of Fe-rich spinel grains embedded in feldspathoid-olivine intergrowths (Wark, 1983). C-1 also exhibits an enrichment in Zn. Examination of the remnants of inclusion C-1 in the slab surface revealed a purple color.

Table 4.2. Chemical compositions of spinel in Type B purple inclusions (entries in weight percent).

	B7F6			DH8			B7H10			HB1		C1	
	I	SC	E	I	SC	SC	I	SC	E	I	SC	I	SC
MgO	27.2	21.5	16.6	26.3	21.5	22.4	27.7	23.3	21.4	26.2	25.4	28.3	23.8
Al_2O_3	70.1	67.8	65.5	70.1	67.5	67.5	71.0	68.3	66.7	69.7	69.1	71.8	68.8
SiO_2	-	0.3	-	0.4	0.3	0.3	0.2	0.3	0.4	0.1	0.1	0.1	0.1
TiO_2	0.2	0.2	0.4	0.7	0.4	0.2	0.3	0.4	0.5	0.9	0.8	0.4	0.4
V_2O_3	0.1	0.2	0.2	0.3	-	0.2	-	0.2	0.1	0.7	0.6	-	-
Cr_2O_3	0.4	0.2	0.3	0.4	0.5	0.3	0.1	0.2	0.2	0.1	0.0	0.3	0.4
FeO	1.6	9.4	17.1	1.3	9.5	8.3	0.6	7.3	10.3	2.3	3.9	0.1	6.1
ZnO	-	0.5	-	-	0.4	0.7	-	-	-	-	-	-	0.1

I = interior of inclusion
SC = spinel clusters
E = located near edge of inclusion
- = not detected: <0.1%.

Table 4.3. Bulk chemical compositions of purple inclusions (entries in weight percent).

	B2 (range)	B7F6	DH8	B7H10	HB1	C-1
Na_2O	0.1-0.9	2.1	1.9	1.0	0.5	1.7
MgO	10-16	20.0	15.0	15.8	18.8	13.8
Al_2O_3	25-28	44.5	38.4	33.1	55.6	29.6
SiO_2	30-35	19.3	24.2	29.2	10.4	31.0
CaO	22-28	6.6	13.4	15.6	8.7	21.0
TiO_2	1.2-1.6	1.2	2.5	3.1	0.5	1.0
V_2O_3	0.1	0.3	0.1	0.1	0.4	< 0.1
Cr_2O_3	0.02-0.07	0.2	0.2	< 0.1	0.2	0.1
FeO	0.45-1.7	4.5	3.7	1.6	4.2	2.0

Inclusion HB1, composed primarily of spinel, hibonite and melilite, is similar to a compact Type A inclusion. While differing mineralogically, HB1 does resemble the Type B PSI texturally, exhibiting bands of spinel grains cutting across the inclusion. There are no secondary phases in the core, but the mantle and rim contain abundant secondary phases (e.g., feldspathoid and grossular).

4.3.5. PRIMARY VS. SECONDARY PHASES

Several petrographic criteria were used to distinguish primary and secondary phases in the inclusions. Primary minerals are characterized by their refractory chemistry (high in Ca, Al, Ti), and occurrence as textures, such as interlocking mineral grains, suggestive of crystallization from a melt. Fassaite, melilite, and Mg-spinel have been observed to crystallize from melts of CAI composition, and are typically regarded as primary phases.

Secondary minerals formed during a later alteration event, such as reaction of the CAI with a gas. Secondary minerals are distinguished by 1) chemical compositions enriched in volatile elements such as Fe, Na, K and Cl; or 2) phases which are thermodynamically unstable at high temperatures, such as grossular (which decomposes above 860°C; or 3) occurrence in fine-grained interstitial regions, veins, cavities or rims of inclusions. Nepheline, sodalite, grossular, olivine and hedenbergite typically are identified as secondary phases.

4.4. BULK CHEMICAL COMPOSITIONS

Estimates of the bulk chemical compositions of the four PSI inclusions, obtained by rastered beam EDS analyses, are presented in Table 4.3. The composition of HB1 is for the core only. The bulk composition of FUN inclusion C-1 determined by instrumental neutron activation (INAA, Conard, 1976) is also listed. For comparison, the range of Type B2 CAI compositions (Wark, 1981) is given.

Compared to the melilite-poor Type B2 CAI, the PSI are highly enriched in Al_2O_3, and depleted in SiO_2 and CaO. This pattern reflects the high spinel contents of PSI. Al_2O_3 contents range from 33% for B7H10, to as high as 55% for HB1. The CaO content of B7F6 is only 6.6%, compared to the range of 22 to 28% observed for Type B2 inclusions. Ternary diagrams showing the bulk compositions (Figures 4.12 and 4.15) are presented in the Discussion, Section 4.6.

Inclusions DH8 and B7H10 exhibit fairly high levels of TiO_2 (up to 3.1%). All PSI are enriched in FeO (up to 4.5 weight percent). Inclusion C-1 is more similar in bulk composition to Type B2 inclusions, consistent with the more typical modal abundances of melilite (21%) and anorthite (6%) observed for C-1 (Wark, 1983).

Trace element data were obtained by instrumental neutron activation analysis (Palme, personal communication, 1987) for FUN inclusions B7F6, DH8, HB1; as well as for two isotopically normal Type B purple inclusions, II3 and HB5. Figure 4.7a shows elements plotted in order of increasing volatility. The REE pattern in DH8 is essentially flat at ≈50x chondritic, with depletions in La, Sm and Eu, consistent with the low abundance of melilite.

Figure 4.7a. Instrumental neutron activation (INAA) data for rare earth elements and other trace elements in the Type B (spinel-fassaite-rich) PSI inclusions: DH8, B7F6, II3 and HB5. DH8 and B7F6 are FUN inclusions; II3 and HB5 are isotopically normal. Elements are listed in order of increasing volatility. Errors are typically 4 to 12%. Upper limits on data are shown as arrows. The REE pattern in DH8 is essentially flat at ≈50x chondritic, with depletions in La, Sm and Eu. DH8 shows an extreme enrichment in Sc (94x chondritic (C1)). Data are scarce for B7F6 due to small sample size.

Figure 4.7b. Instrumental neutron activation data for refractory siderophile elements in the Type B PSI inclusions DH8, B7F6, II3 and HB5. The pattern for C-1 is shown for comparison. Errors are typically 4 to 12%. DH8 and B7F6 exhibit uniform enrichments in the refractory siderophile elements, by factors of 50 to 100x chondritic, except that DH8 shows a Mo deficit. II3 and HB5 exhibit enrichments about 25x chondritic, with Mo deficits. The W excess for II3 may be due to contamination by instruments used for sampling; this problem was also observed for fine-grained inclusions.

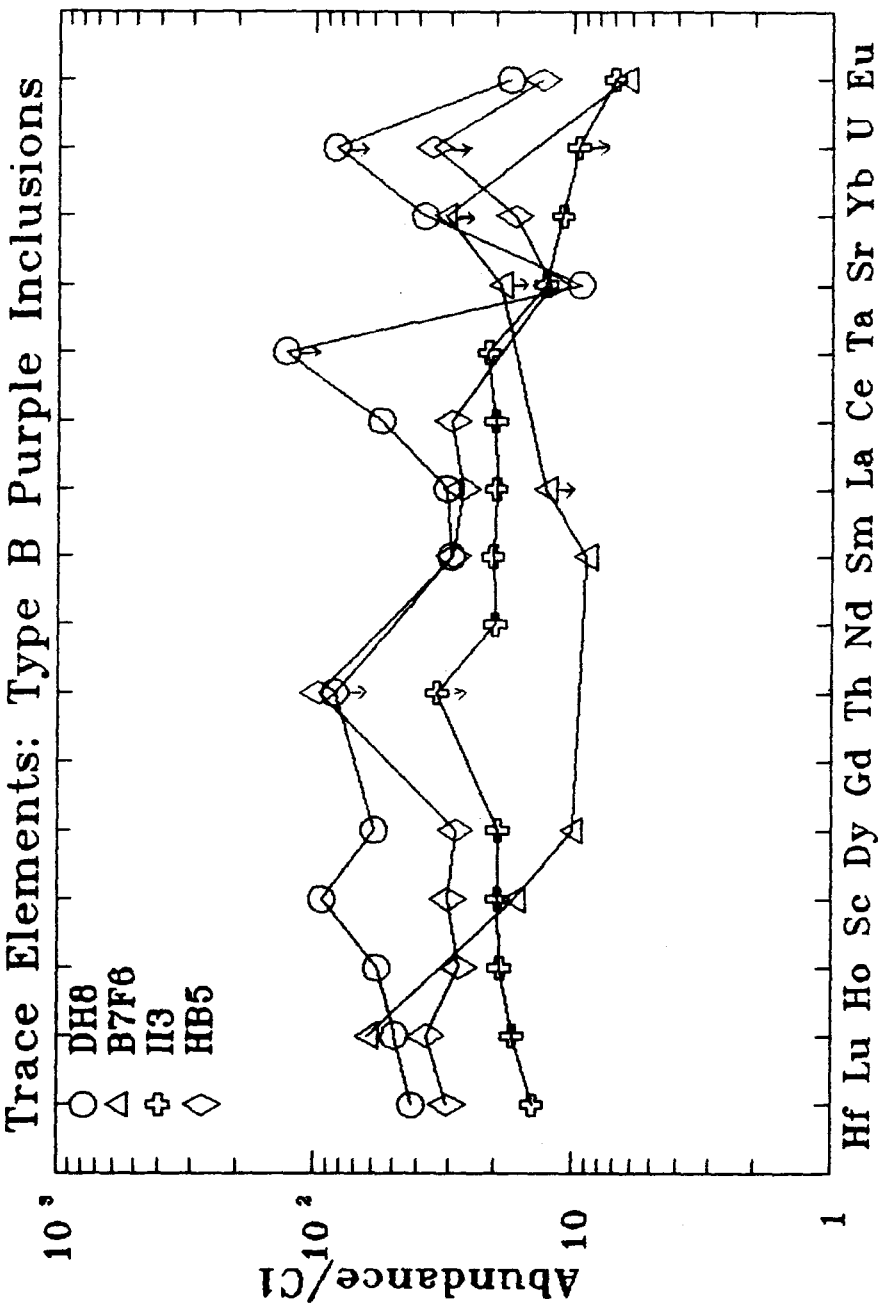
Trace Elements: Type B Purple Inclusions
DH8
B7F6
II3
HB5
Abundance/Cl
10³
10²
10
1
Hf Lu Ho Sc Dy Gd Th Nd Sm La Ce Ta Sr Yb U Eu

Figure 4.7a

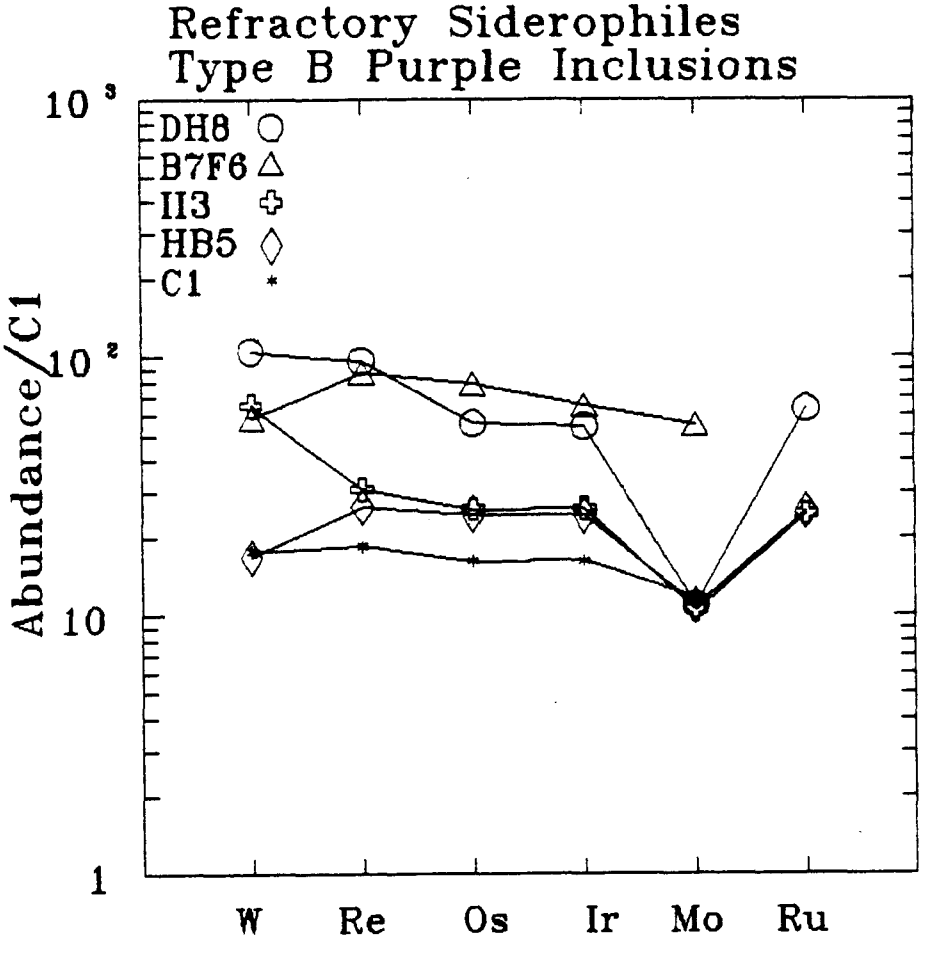
Refractory Siderophiles
Type B Purple Inclusions
Abundance/C1
10 ³
10 ²
10
1
DH8
B7F6
II3
HB5
C1
W
Re
Os
Ir
Mo
Ru

Figure 4.7b

DH8 shows an extreme enrichment in Sc (94x chondritic), compared to average Type B CAI (≈18x chondritic). There are no consistent differences in chemistry, between FUN and isotopically normal CAI.

Data for volatile elements were also obtained by INNA. DH8, B7F6 and HB1 are enriched in Zn by factors of 6, 13 and 13, respectively, over the average value for Type B CAI. Similar values are observed for the non-FUN inclusions II3 and HB5. The Zn contents approach the values for fine-grained CAI. FUN inclusion C-1 is also enriched in Zn (3 times the average for Type B CAI; Conard, 1976).

With the exception of a Mo depletion for DH8, inclusions B7F6 and DH8 exhibit uniform and substantial enrichments in refractory siderophiles of 50 to 100x chondritic, compared to an average value of 16x chondritic for Type B CAI (Figure 4.7b). However, the two inclusions do not exhibit a high abundance of opaque assemblages. Inclusions HB5 and II3 exhibited smaller enrichments in refractory siderophiles (≈25x chondritic), with Mo deficits. Insufficient data were obtained for HB1 due to small sample size.

4.5. ISOTOPIC COMPOSITIONS

Thermal ionization results for Mg isotopic compositions of twenty PSI are listed in Table 4.1 (Brigham et al., 1987). A histogram showing F_{Mg} measurements for PSI inclusions is shown in Figure 4.8, along with a representative selection of published data for coarse and fine-grained refractory inclusions.

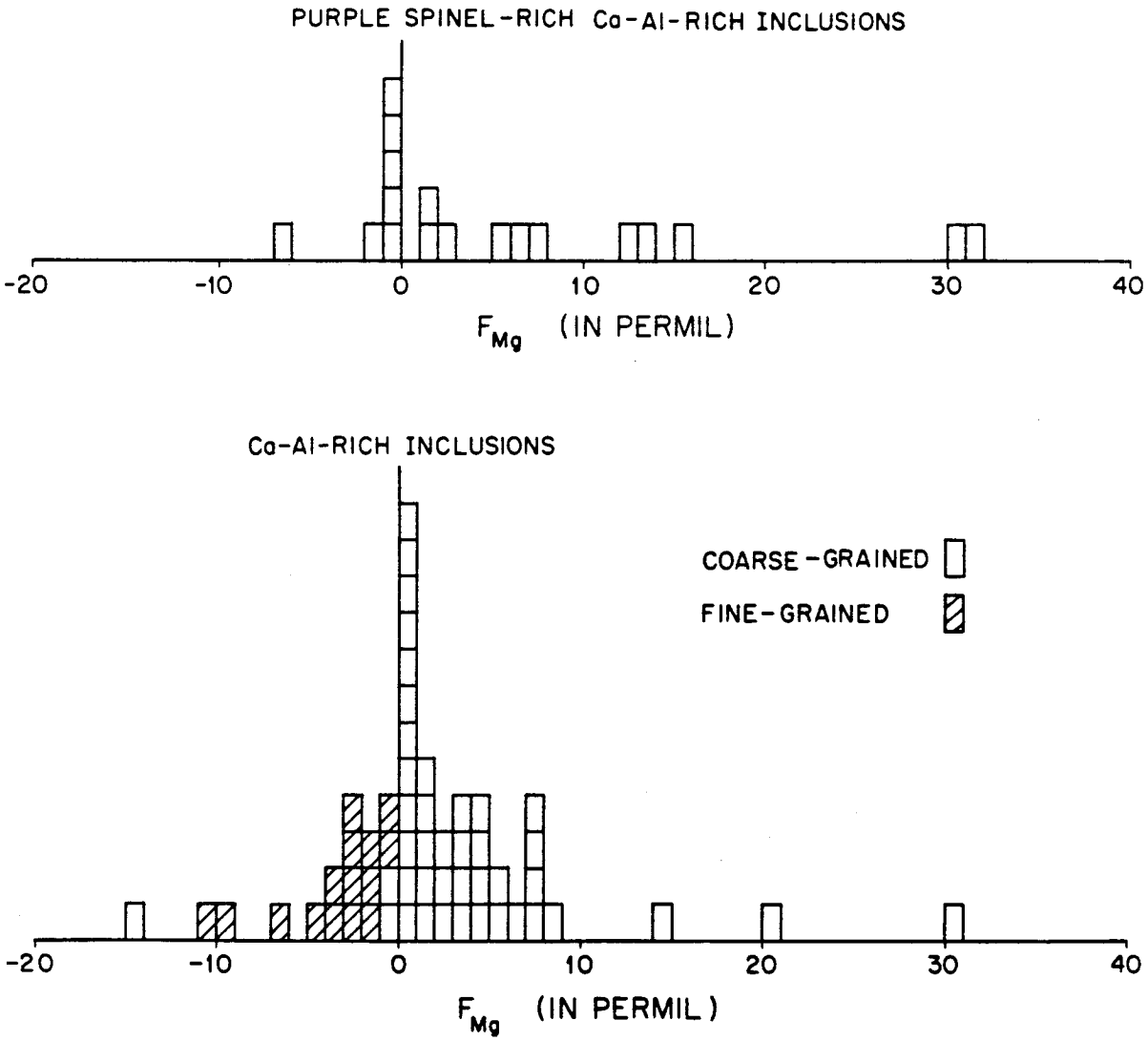

Figure 4.8. Histograms comparing thermal ionization measurements of F_{Mg} in CAI. Purple spinel-rich inclusions show a range in F_{Mg} from 0 to +30‰ amu^{-1}, with approximately 20% exhibiting FUN isotopic characteristics. The range in F_{Mg} for typical coarse- and fine-grained inclusions is shown for comparison. Fine-grained measurements shown are discussed in Chapter 6.

A significantly higher fraction, approximately 20%, of the PSI analyzed exhibit large F_{Mg} ($\geq$10‰ amu^{-1}) and negative effects in δ^{26}Mg, indicative of FUN isotopic effects, compared to $\leq$ 6% of the general population of coarse-grained inclusions.

One inclusion (CH3) exhibited large F_{Mg} = 13.5‰ amu^{-1} but δ^{26}Mg > 0 and, therefore, need not be a FUN inclusion. No nonlinear effects in other elements are observed in CH3 (Papanastassiou and Brigham, 1988).

Large correlated nonlinear anomalies in Ca, Ti and Cr (Papanastassiou and Brigham, 1988; as discussed in Section 4.6.6) were identified in three inclusions (DH8, B7F6 and HB1), selected on the basis of Mg isotopic characteristics. Thermal ionization measurements have been obtained only for Mg in B7H10, which is the fourth possible FUN inclusion; this will be verified by measuring Ca, and Ti if sufficient material is available.

Ion microprobe results for the Mg and Si isotopic compositions of individual phases in the four PSI, which exhibit FUN characteristics (B7F6, DH8, B7H10 and HB1) are presented in Tables 4.4 and 4.5. Values are given for F_{Mg}, δ^{26}Mg, F_{Si} and δ^{30}Si. Refer to Chapter 3 for a discussion of analytical conditions and the calculation of isotopic data. The locations of the analyzed grains in the inclusions are denoted in the tables. Data for analyses of FUN inclusion C-1 are also presented. Figure 4.9 presents F_{Mg} and F_{Si} measurements for individual phases analyzed in the four PSI inclusions.

Table 4.4. Ion microprobe determinations of Mg compositions isotopic in individual crystals of ψ inclusions

Sample[a]		F_{Mg}[b] ‰ amu^{-1} ($\pm 2\sigma_{mean}$)	$\delta^{26}Mg$[c] ‰ ($\pm 2\sigma_{mean}$)	$^{27}Al/^{24}Mg$[d]
B7H10				
Spin 1	I	36.2 ± 1.5	-2.1 ± 2.0	2.3
Spin 2	I	35.5 ± 1.3	-1.5 ± 2.0	2.6
Spin 3	I	36.1 ± 1.4	-1.1 ± 2.1	2.6
Spin 4	I	37.4 ± 1.4	-2.2 ± 1.9	2.7
Spin 5	I	36.1 ± 1.4	-0.2 ± 2.3	2.6
Spin 6	SC	36.6 ± 1.6	-2.6 ± 2.2	2.6
Spin 7	SC	36.7 ± 1.6	-3.1 ± 2.1	2.6
Spin 8	SC	33.7 ± 1.3	-0.1 ± 2.6	3.1
Spin 9	SC	35.9 ± 1.7	-1.7 ± 2.3	3.0
Spin 10	SC	33.5 ± 2.0	-3.7 ± 3.4	3.1
Fass 11	I	37.6 ± 1.6	-2.0 ± 2.1	2.3
Fass 12	I	38.8 ± 1.7	-1.3 ± 2.1	1.5
Fass 13	I	39.0 ± 1.6	-0.9 ± 2.3	1.6
Oliv 11	SC	13.6 ± 1.1	+0.7 ± 2.1	
Oliv 12	SC	19.4 ± 1.1	+1.0 ± 2.2	
Oliv 14	SC	12.9 ± 1.5	+2.2 ± 2.6	
Oliv 16	SC	10.7 ± 1.1	+0.8 ± 1.9	
DH8				
Spin 1	SC	38.6 ± 1.7	-2.0 ± 2.5	3.0
Spin 2	I	37.4 ± 2.1	-3.7 ± 3.1	2.7
"		36.6 ± 1.9	-5.4 ± 3.2	
Spin 3	E	32.1 ± 1.9	-1.2 ± 2.8	3.2
Spin 4	I	37.5 ± 1.8	-1.9 ± 2.6	3.6
Spin 5	SC	29.6 ± 1.8	-1.9 ± 2.7	3.3
"		30.8 ± 1.8	-2.0 ± 2.8	
Spin 6	SC	35.4 ± 1.7	-1.8 ± 2.5	3.2
"		35.0 ± 2.2	-2.5 ± 3.7	
Spin 8	I	33.5 ± 1.9	-0.6 ± 2.8	3.7
Spin 10	E	31.3 ± 2.5	-2.4 ± 4.0	2.7
Spin 11	I	34.3 ± 1.9	-1.3 ± 2.8	3.1
Spin 12	I	30.8 ± 1.8	-0.5 ± 2.7	2.5
Fass 11	I	30.0 ± 1.4	-1.9 ± 2.1	2.9
Fass 12	I	31.0 ± 1.6	-2.5 ± 2.2	2.9
Fass 13	I	30.1 ± 1.5	-0.8 ± 2.3	2.9
Anor 1	I	36 ± 13	-21 ± 22	9700
Anor 3	I	35.4 ± 6.0	-3.8 ± 6.8	310
Anor 5	I	49.5 ± 23.6	-25 ± 40	23000
B7F6				
Spin 1	SC	18.0 ± 1.8	-1.1 ± 2.6	2.8
Spin 2	SC	17.5 ± 1.6	-0.1 ± 2.2	2.8
Spin 3	I	17.7 ± 1.6	+0.2 ± 2.3	2.8
Spin 4	I	16.6 ± 1.6	+1.1 ± 2.2	2.4

Table 4.4 (continued)

Sample[a]		F_{Mg}[b] °/oo amu^{-1} ($\pm 2\sigma_{mean}$)	$\delta^{26}Mg$[c] °/oo ($\pm 2\sigma_{mean}$)	$^{27}Al/^{24}Mg$[d]
Spin 5	SC	15.0 ± 1.7		2.4
Spin 6	E	12.8 ± 2.2	+0.2 ± 3.3	3.7
Fass 1	I	15.3 ± 1.6	+1.3 ± 2.4	1.7
Fass 2	I	15.9 ± 1.8	+0.1 ± 2.6	1.5
Oliv 2	E	-0.2 ± 1.6	2.3 ± 2.7	
Oliv 3	E	12.7 ± 1.3	-3.0 ± 3.2	
Anor 1	I	21.1 ± 4.7	-5.5 ± 5.7	201
HB1				
Spin 0	I	23.0 ± 1.8	-2.6 ± 3.1	2.9
Spin 1	SC	20.0 ± 1.7	0.2 ± 2.2	2.6
Spin 2	SC	21.5 ± 1.8	1.9 ± 2.5	2.7
Spin 3	SC	17.9 ± 1.5	-0.6 ± 2.0	2.6
Spin 3		19.6 ± 1.6	-3.5 ± 2.0	
Spin 4	SC	19.4 ± 1.5	-0.1 ± 2.1	2.8
Spin 5	I	25.6 ± 1.5	-1.2 ± 2.2	2.8
Spin 6	I	22.8 ± 1.8	-2.6 ± 3.9	2.6
Spin 7	SC	19.2 ± 1.5	-1.2 ± 2.1	3.1
Spin 8	I	24.3 ± 1.6	-1.2 ± 2.0	2.7
Spin 9	I	23.8 ± 1.6	-2.8 ± 2.0	3.3
Spin 10	I	23.0 ± 1.6	2.3 ± 2.0	3.1
Spin 11	I	23.7 ± 1.6	-0.8 ± 2.2	2.7
Spin 12	I	23.8 ± 1.4	0.2 ± 2.0	2.8
Spin 13	I	23.2 ± 1.6	-0.6 ± 1.9	2.8
Spin 14	I	25.4 ± 1.7	0.2 ± 2.1	3.1
Spin 15	I	19.9 ± 1.5	0.7 ± 2.1	2.6
Hib 1	M	25.5 ± 1.8	-0.7 ± 3.2	60
"		28.3 ± 1.8	-1.6 ± 3.0	
Hib 2	M	25.3 ± 2.0	-0.1 ± 3.4	64
Gross 1	M	15.9 ± 2.1	-0.5 ± 2.9	
Gross 3	M	13.3 ± 1.9	-2.0 ± 2.4	
And 1	E	4.1 ± 1.5	-2.2 ± 2.7	
And 2	E	2.5 ± 1.6	-2.9 ± 2.8	1.7
Diop 3	E	0.1 ± 1.3	-1.3 ± 2.2	0.6
Diop 4	E	-0.5 ± 1.6	-2.0 ± 2.8	0.9
C-1				
Spin 1		30.8 ± 1.5	-3.1 ± 2.1	2.5
Spin 2		29.9 ± 1.8	-2.8 ± 2.4	
Fass 1		30.4 ± 1.5	-1.5 ± 2.3	2.3
Fass 2		31.2 ± 1.6	-1.8 ± 2.5	1.6

[a] Location of grain in inclusion: I = interior; E = edge; SC = spinel cluster; M = mantle.

Table 4.4 (continued)

[b] Mass-dependent isotope fractionation factor (in permil per atomic mass unit) determined from the raw measured $^{25}Mg/^{24}Mg$ ratios relative to the measured $^{25}Mg/^{24}Mg$ of standards of similar mineralogy analyzed during the same period of time: ($F_{Mg} = \Delta^{25}Mg - \Delta^{25}Mg_{standard}$). Uncertainties are $2\sigma_{mean}$.

[c] $\delta^{26}Mg$ is the deviation in $^{26}Mg/^{24}Mg$ from normal after correction for mass-dependent isotope fractionation using $^{25}Mg/^{24}Mg$.

[d] $^{27}Al/^{24}Mg$ is determined from measured ion ratios $^{27}Al^{+}/^{24}Mg^{+}$ corrected for different sensitivity factors for each mineral (see text). The uncertainties (not listed) are estimated at 5% based on the uncertainty in the sensitivity factor (Huneke et al., 1983). $^{27}Al/^{24}Mg$ for anorthite determined from $^{44}Ca^{++}/^{24}Mg^{+}$ (errors for anorthite: ±10%).

Table 4.5. Ion microprobe determinations of Si isotopic compositions in individual crystals of ψ inclusions

Sample[a]		F_{Si}[b] ‰ amu^{-1} ($\pm 2\sigma_{mean}$)	$\delta^{30}Si$[d] ‰ ($\pm 2\sigma_{mean}$)
B7H10			
Fass 14	I	15.9 ± 1.1	-1.6 ± 1.6
Fass 15	I	15.4 ± 1.1	-0.9 ± 1.6
Fass 16	I	17.0 ± 1.1	-2.6 ± 1.7
Fass 17	I	17.2 ± 1.5	-2.4 ± 2.3
Oliv 15	SC	-1.5 ± 2.3	+2.7 ± 4.4
Oliv 16	SC	+0.4 ± 2.2	1.1 ± 4.2
DH8			
Fass 14	I	11.4 ± 1.8	1.0 ± 3.4
Fass 15	I	12.3 ± 1.8	-0.6 ± 3.2
"		12.4 ± 2.3	0.0 ± 4.2
Fass 16	I	15.0 ± 1.3	-3.3 ± 2.4
Fass 17	I	13.4 ± 1.4	-2.8 ± 2.5
Anor 4	I	14.1 ± 1.3	2.5 ± 2.4
Anor 4'	I	15.8 ± 1.1	-0.6 ± 2.2
Anor 7	I	15.6 ± 1.2	-2.0 ± 2.5
B7F6			
Fass 3	I	14.4 ± 2.4	0.2 ± 4.4
Fass 4	I	11.1 ± 2.0	+0.5 ± 3.7
Fass 5	I	10.1 ± 2.1	-0.1 ± 3.9
Hed 1	I	0.4 ± 1.4	1.5 ± 2.6
HB1			
Spin 16	I	20 ± 16	-12 ± 25
Mel 1	I	9.1 ± 2.5	-5.7 ± 4.4
Mel 2	I	10.7 ± 2.3	-0.7 ± 4.2
Mel 3	I	8.5 ± 2.1	-2.4 ± 3.6
Gross 2	M	1.8 ± 2.1	0.7 ± 3.8
C-1			
Fass 3		15.0 ± 1.0	-1.8 ± 1.6
Fass 4		15.5 ± 2.0	-0.4 ± 3.7

a Location of grain in inclusion: I = interior; E = edge; SC = spinel cluster; M = mantle.

b Mass-dependent isotope fractionation factor (in permil per atomic mass unit) determined from the raw measured $^{29}Si/^{28}Si$ ratios relative to the measured $^{29}Si/^{28}Si$ of standards analyzed during the same period of time: $F_{Si} = \Delta^{29}Si - \Delta^{29}Si_{standard}$. Uncertainties are $2\sigma_{mean}$.

c $\delta^{30}Si$ is the deviation in $^{30}Si/^{28}Si$ from normal after correction for mass-dependent fractionation using $^{29}Si/^{28}Si$.

Figure 4.9. Mg and Si isotopic fractionation are shown for individual phases in FUN inclusions, to illustrate the degree of heterogeneity within inclusions. Fractionation is plotted on the x-axis, in permil per mass unit. Each line (vertically) represents an analysis of a new phase. If Mg and Si isotopes were measured for the same phase; then the analyses appear on the same line. Figure 4.9a illustrates isotopes for B7H10; Figure 4.9b for DH8; Figure 4.9c for B7F6; and Figure 4.9d for HB1. Symbols are as follows:

Spinel = ●

Fassaite = ▲

Olivine = ♦

Anorthite = ★

Melilite = ✸

Grossular = ■

Hibonite = ✚

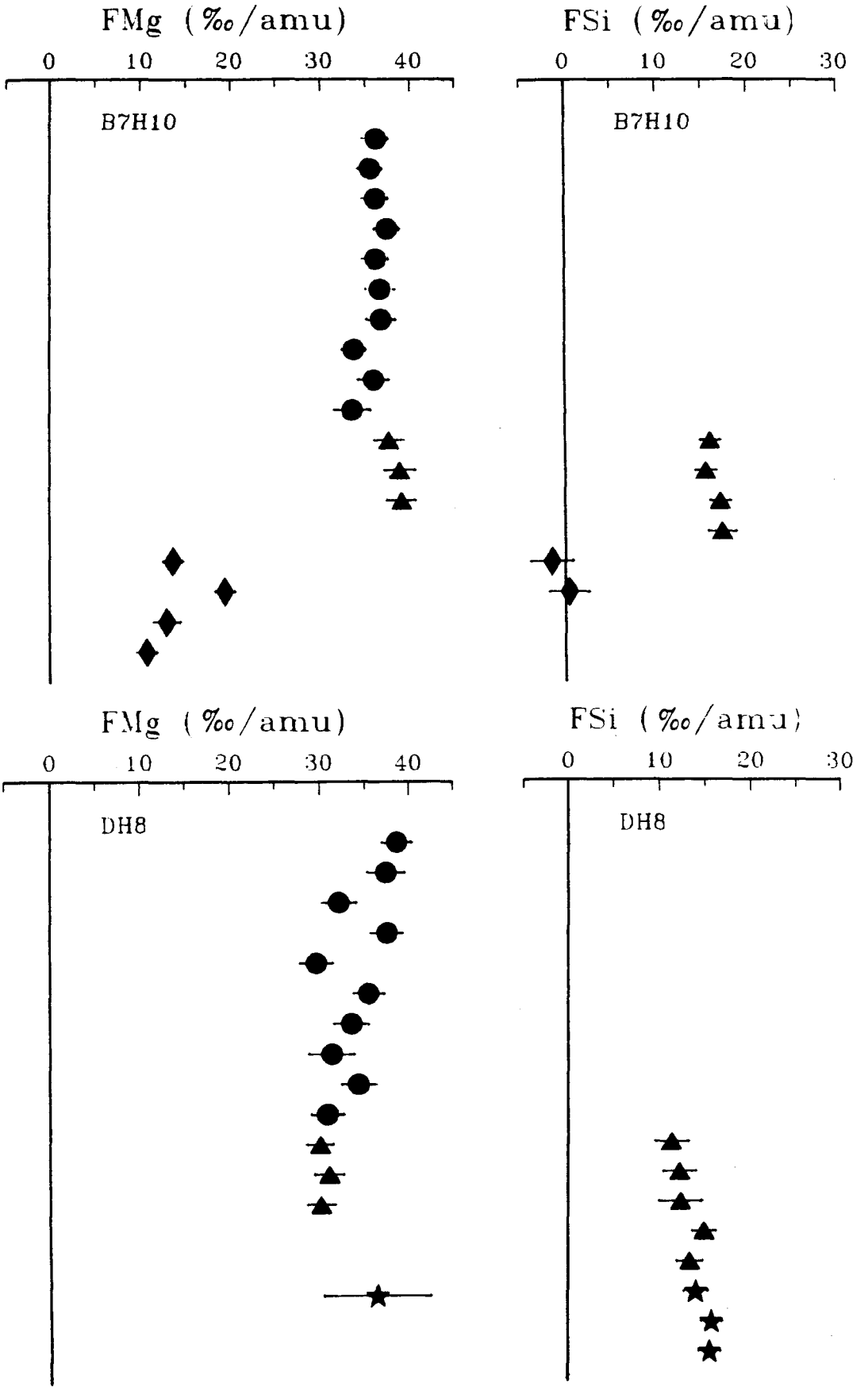
FMg (‰/amu)
0
10
20
30
40
B7H10
FSi (‰/amu)
0
10
20
30
B7H10
FMg (‰/amu)
0
10
20
30
40
DH8
FSi (‰/amu)
0
10
20
30
DH8

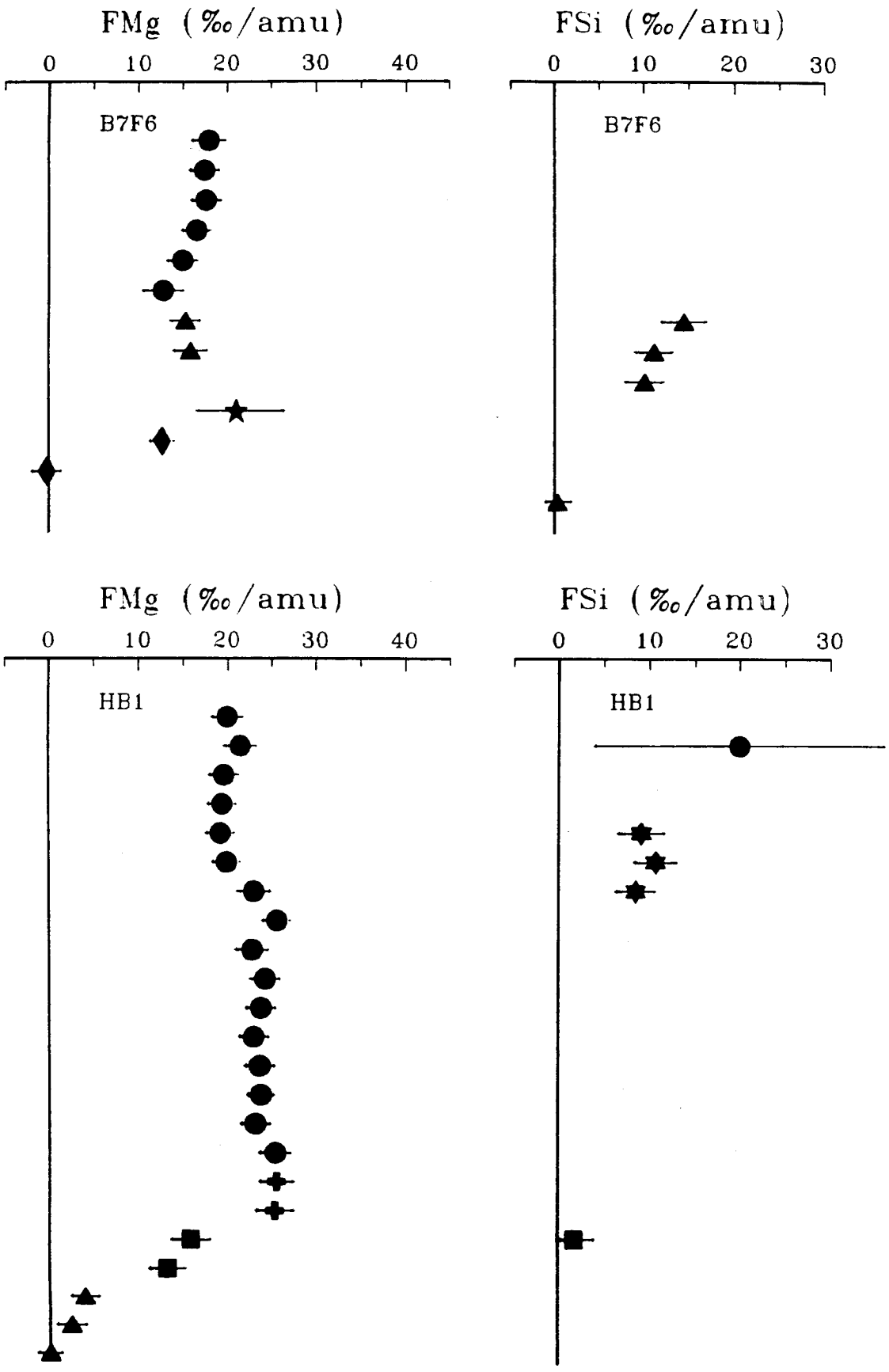
FMg (‰/amu)
0
10
20
30
40
B7F6
FSi (‰/amu)
0
10
20
30
B7F6
FMg (‰/amu)
0
10
20
30
40
HB1
FSi (‰/amu)
0
10
20
30
HB1

4.5.1. INDIVIDUAL INCLUSIONS

C-1

As a check on my ability to determine precisely F_{Mg} and F_{Si} using the ion microprobe, analyses were obtained for the FUN inclusion C-1, which has been analyzed by thermal ionization for Mg (Esat et al., 1979) and Si (Clayton et al., 1978), and by ion microprobe for Mg (Huneke et al., 1983). C-1 exhibits uniform F_{Mg} from the earlier work, and in this study. There is good agreement between published ion probe and thermal ionization data for Mg in inclusion C-1. Measurements of F_{Mg} and F_{Si} were obtained for fassaite; F_{Mg} was also measured for C-1 spinel. Ion probe data are in agreement with the published values.

B7H10

Mg and Si isotopic data were obtained for fassaite and olivine; Mg data were obtained for spinel. Most spinels exhibit uniform $F_{Mg} = 36.6 \pm 1.6‰$ amu^{-1}. No difference in F_{Mg} was observed between spinel poikilitically enclosed in fassaite, and spinel embedded in olivine and sodalite intergrowths. No correlation between F_{Mg} and FeO content was observed. Spinel with Fe contents ranging from 0.4% FeO (Sp 5) to 8.5% FeO (Sp 9), exhibited identical F_{Mg} within errors. Two spinels (Sp8, 10), which are the most Fe-rich spinels analyzed (≈10% FeO), exhibit slightly lower F_{Mg} ($F_{Mg} = 33.5 \pm 2.0‰$ amu^{-1}). These spinels are located in an olivine-nepheline-rich region near the edge of the inclusion, and are mantled by

olivine containing Mg which is significantly less fractionated (F_{Mg} = 10.7 to 19.4‰ amu^{-1}), and isotopically normal Si (F_{Si} = -1.5 ± 2.3‰ amu^{-1}). Fassaite exhibited uniform F_{Mg} = 37.6 ± 1.6‰ amu^{-1}, consistent with the value determined for spinel. Fassaite exhibited uniform F_{Si} of 16.4 ± 1.8‰ amu^{-1} and a hint of a deficit in δ^{30}Si (-2.6 ± 1.4‰).

Ion probe values for F_{Mg} in spinel and fassaite are significantly more fractionated (by 6 to 8‰ amu^{-1}), than the value obtained by thermal ionization (F_{Mg} = 30.6‰ amu^{-1}; Brigham et al., 1987). Four of the nine spinel analyses (Sp2, 4, 6, 7) exhibited values for δ^{26}Mg which suggest deficits (-1.5 ± 0.8 to -3.1 ± 2.1‰), resolved from the range of standard analyses. A sample analyzed by DLT exhibited a well-defined deficit in ^{26}Mg = -2.2 ± 0.2‰ (Table 4.1).

DH8

Mg and Si isotopic data were obtained for fassaite and anorthite; Mg data were also obtained for spinel. In contrast to B7H10, F_{Mg} in DH8 spinel is not uniform, but ranges from 29.6 to 38.6‰ amu^{-1}. F_{Mg} is not correlated with FeO contents of the spinels; spinels with very different Fe contents of 6.2% FeO (Sp2) and 14.5% FeO (Sp4) exhibit identical F_{Mg} within errors. However, the measured F_{Mg} appears correlated with the location and mineral relationships of the spinel within the inclusion. The lowest F_{Mg} value (29.6 ± 1.8‰ amu^{-1}) was obtained for spinel (Sp5) in a spinel cluster embedded in olivine and sodalite intergrowths. Spinels located near the edge of the inclusion (Sp3, 10) exhibited lower F_{Mg} (31.3‰, 32.1‰ amu^{-1}), than spinels located in the interior of the inclusion.

Fassaite in DH8 exhibited uniform F_{Mg} equal to 30.1 ± 1.5‰ amu^{-1}, consistent with the lower end of the range in F_{Mg} measured for spinel. Si isotopic fractionation in DH8 fassaite exhibits a hint of variability, with F_{Si} ranging from 11.4 ± 1.8 to 15.0 ± 1.3‰ amu^{-1}. Nonlinear effects in $\delta^{26}Mg$ and $\delta^{30}Si$ for fassaite were not clearly resolved from normal.

F_{Mg} measurements of anorthite have a lower precision due to the low Mg contents, but one analysis yielded F_{Mg} = 35.4 ± 6.0‰ amu^{-1}, consistent with spinel and fassaite analyses. Anorthite exhibited fractionated Si (F_{Si} = 14.1 ± 1.3‰ amu^{-1}), consistent with the more fractionated values in fassaite. Anorthite in DH8 exhibited variable and often exceptionally high $^{27}Al/^{24}Mg$ ratios (300 to 23,000), but no excess ^{26}Mg (-25 ± 40‰), yielding an upper limit on the initial $(^{26}Al/^{27}Al)_o \leq 1x10^{-7}$ (Figure 4.10). Thermal ionization data for DH8 using the DLT technique (Table 4.1) show a well-defined $\delta^{26}Mg$ deficit and F_{Mg} which lies on the lower end of the F_{Mg} range observed for ion microprobe measurements. Deficits in $\delta^{26}Mg$ for ion probe measurements of spinel are small, and not clearly resolved from the range for standards.

B7F6

Mg isotopic data were obtained for spinel, fassaite, olivine and anorthite; Si data were obtained for fassaite and hedenbergite. B7F6 exhibited uniform F_{Mg} = 17.5 ± 1.6‰ amu^{-1} for interior spinel. Fassaite yielded uniform F_{Mg} = 15.9 ± 1.8‰ amu^{-1}, consistent with the value obtained for spinel analyses, and variable Si fractionation with F_{Si} ranging from 10.1 to 14.4‰ amu^{-1}. A lower precision analysis of anorthite

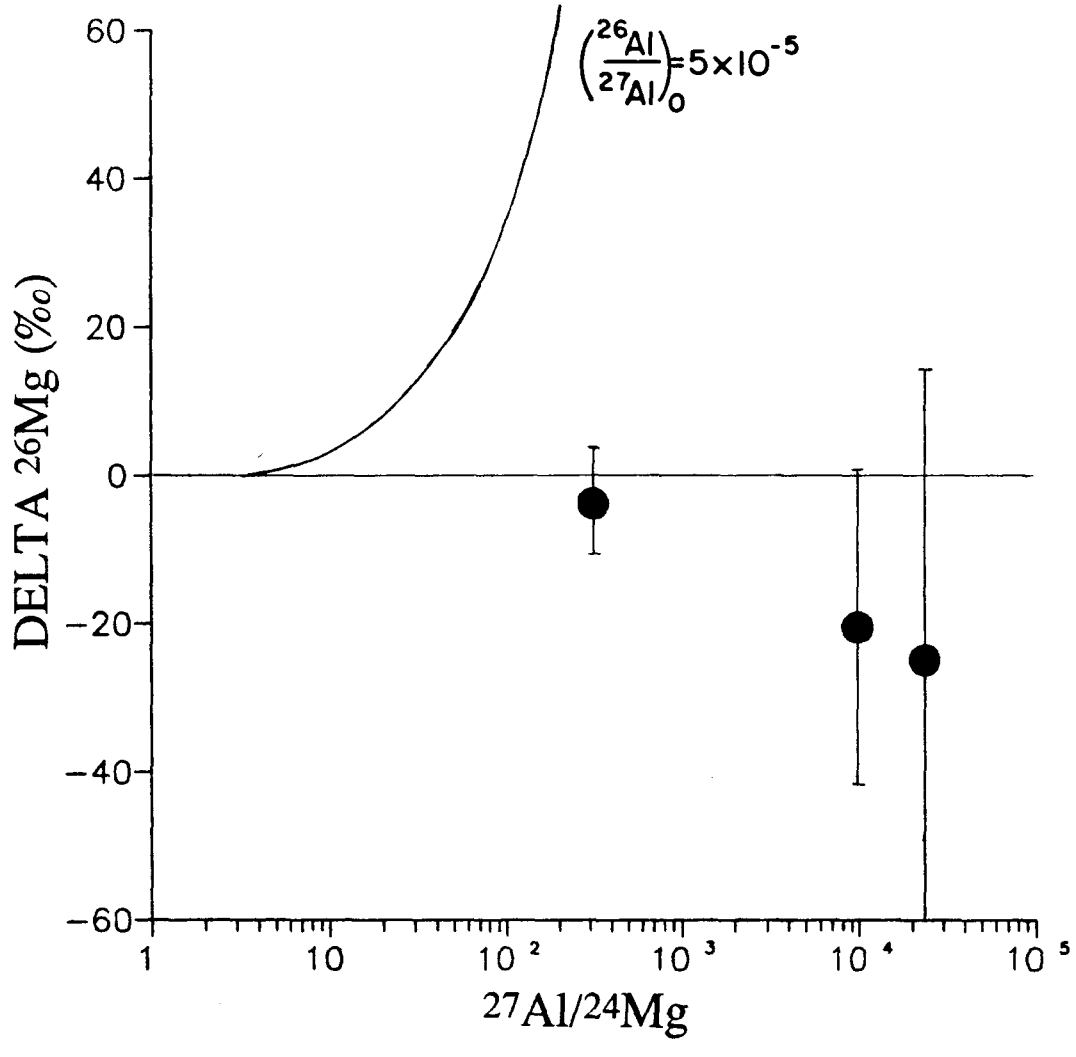

Figure 4.10. ^{26}Al-^{26}Mg evolution diagram for FUN inclusion DH8. The reference line of slope $(^{26}Al/^{27}Al)_o$ = 5 x 10^{-5}, observed for most Type B CAI, is shown for comparison. Anorthite in DH8 yielded exceptionally high ^{27}Al/^{24}Mg ratios (300 to 23000), but only small or zero excess ^{26}Mg, yielding a limit: $(^{26}Al/^{27}Al)_o \leq 1 \times 10^{-7}$.

yielded F_{Mg} = 21.1 ± 4.7‰ amu^{-1}. Anorthite with $^{27}Al/^{24}Mg$ = 300 exhibited no excess in ^{26}Mg (-5.5 ± 5.7‰), placing a limit $(^{26}Al/^{27}Al)_o \leq 5x10^{-6}$. Hedenbergite which lies along the void spaces in the inclusion (Figure 4.5a) contains isotopically normal Si (F_{Si} = 0.4 ± 1.4‰ amu^{-1}).

Spinel near the edge of the inclusion exhibited lower F_{Mg} (12.8 ± 2.2‰ amu^{-1}). An olivine grain near the edge exhibited F_{Mg} = 12.7 ± 1.3‰ amu^{-1}, identical to the value for adjacent spinels. Forsteritic olivine nodules which surround the inclusion and are mantled by more fayalitic olivine (Figure 4.5b), contain isotopically normal Mg (F_{Mg} = -0.2 ± 1.6‰ amu^{-1}).

HB1

Mg isotopic data were obtained for spinel in the core, as well as grossular and hibonite in the mantle, and andradite and diopside in the rim. Si isotopic data were obtained for melilite in the core and grossular in the mantle.

Spinel exhibited two distinct ranges of F_{Mg}, correlated with the location of the grains in the inclusion. Spinels occurring in veins or bands in the core exhibit F_{Mg} = 19.9 ± 1.5‰ amu^{-1}, while coarse spinel toward the outer edges of the core exhibit F_{Mg} = 23.8 ± 1.4‰ amu^{-1}. An isotopic profile measured across a 300 μm region of spinel near the outer edges of the core, revealed no gradient in F_{Mg}, although the FeO content of spinel changed by a factor of two.

The DLT value obtained for HB1 is substantially lower: F_{Mg} = 15.4 ± 0.5‰ amu^{-1}. Mg was not measured in melilite due to the absence of a large enough

region of melilite free of spinel. Melilite in the core contains isotopically heavy Si: F_{Si} = 10.7 ± 2.3‰ amu^{-1}.

Of the mantle phases analyzed, only hibonite contains highly fractionated Mg (F_{Mg} = 25.5 ± 1.8‰). Hibonite in the mantle with $^{27}Al/^{24}Mg$ = 64 exhibits no excess ^{26}Mg (-0.1 ± 3.4‰), placing a limit $(^{26}Al/^{24}Mg)_o \leq 7x10^{-6}$. Grossular exhibits F_{Mg} = 15.9 ± 2.1‰ amu^{-1}, substantially lower fractionation than for phases in the core. Grossular shows normal Si (F_{Si} = 1.8 ± 2.1‰ amu^{-1}). Diopside (F_{Mg} = 0.1 ± 1.3‰ amu^{-1}) and andradite (2.5 ± 1.6‰) in the rim contain isotopically normal Mg.

4.5.2. COMPARISON OF TECHNIQUES

Both thermal ionization and ion probe measurements of Mg were obtained for the four FUN inclusions. Ion probe measurements for these four exhibit F_{Mg} consistently heavier by a few permil, than values obtained by thermal ionization measurements. This discrepancy may reflect sampling scale within heterogeneous inclusions. The agreement in F_{Mg} values for standards, and for analyses of inclusion C-1 indicate no significant discrepancy (see Section 3.4.8). Deficits in $\delta^{26}Mg$ were typically not well-resolved for ion probe data, but deficits were clearly resolved by thermal ionization measurements.

4.6. DISCUSSION

4.6.1. SUMMARY OF OBSERVATIONS

Ion probe measurements of purple spinel-rich FUN inclusions provide evidence for: 1) large isotopic fractionation for Mg and Si, with the heavier isotopes preferentially enriched; 2) correlated isotopic fractionation for elements of similar volatility; 3) variations in the magnitude of isotopic fractionation among coexisting phases within a single inclusion; 4) the absence of $^{26}Mg^{*}$; and 5) the presence of FUN isotopic anomalies.

The magnitudes of isotopic fractionation observed for the purple FUN inclusions are the largest observed for any Allende CAI. The four FUN inclusions exhibit large isotopic fractionation for Mg and Si with an enrichment in the heavy isotopes. DH8 and B7H10 exhibit F_{Mg} ranging up to 39‰ amu^{-1}, and F_{Si} ranging up to 17‰ amu^{-1}. In contrast, FUN inclusion C-1 exhibited F_{Mg} = 30‰ amu^{-1} and F_{Si} = 14‰ amu^{-1}. Thermal ionization measurements of two of the FUN inclusions (HB1, DH8) revealed substantial isotopic fractionation for Cr, but no fractionation for the more refractory Ca or Ti (Papanastassiou and Brigham, 1989). A remarkably good correlation is observed between the magnitudes of isotopic fractionation for Mg, Si and Cr, when the fractionations are scaled by the inverse square root of the masses (Section 4.6.3).

Isotopic fractionation is variable between primary phases within the interior of single inclusions. DH8 exhibits constant F_{Mg} for fassaite, but a range of 9‰ amu^{-1} in F_{Mg} for spinels, similar to the range in F_{Mg} observed within fine-grained CAI (Brigham et. al., 1986). F_{Mg} is not correlated with the FeO content of the spinels. DH8 also exhibits a systematic difference in F_{Mg} between spinel and fassaite, such that F_{Mg} for fassaite lies at the lower end of the range in F_{Mg} for spinel. Secondary phases (olivine, hedenbergite, grossular) in all of the inclusions exhibit substantially lower F_{Mg} than primary phases and contain isotopically normal Si. Finally, anorthite in PSI exhibits substantial Mg and Si fractionation, and can be regarded as a primary phase, but it does not contain excess $^{26}Mg^{*}$.

4.6.2. ISOTOPIC FRACTIONATION

The magnitudes of isotopic fractionation measured (for DH8: F_{Mg} = 39‰ amu^{-1}, F_{Si} = 15‰ amu^{-1}, F_{Cr} = 18‰ amu^{-1}) are much larger than values predicted to result from gas-solid isotopic equilibrium (estimated to be a few permil for Si using vibrational frequency data, Clayton et al., 1978). The measured fractionation values are comparable to, or larger than the magnitudes expected for kinetic isotope effects associated with gas-solid exchange processes involving evaporation or condensation, which are assumed to follow a mass dependence of $m^{-1/2}$, where m is the mass of the relevant species. The kinetic fractionation factor calculated for a mass dependence of $m^{-1/2}$ is: 20.6‰ amu^{-1} for Mg; 11.3‰ amu^{-1} for SiO molecules; and 9.6‰ amu^{-1} for Cr atoms, where the vapor is enriched in the lighter isotopes.

In this discussion, isotopic variations are used as tracers of nebular and planetary processes leading to the formation of PSI. In particular, isotope fractionation is used to constrain the kinetic processes required to have produced the observed isotopically heavy Mg and Si, and to investigate the mixing of isotopically distinct components and reservoirs. Of primary importance is the possibility of using isotopic measurements to distinguish and characterize primary and secondary phases, and to constrain the reaction mechanisms and major element transport required to form secondary phases.

4.6.3. DISTILLATION

This discussion will examine models for the origin of FUN inclusions using constraints from the petrographic, chemical and isotopic data. Distillation is one process known to produce an enrichment of the heavier isotopes of moderately volatile species in the residue.

Several workers have proposed that the refractory chemical compositions of CAI could be produced by distillation of material of chondritic composition (Chou et al., 1976; Clayton, 1978; Wood, 1981). These models are supported by experimental studies by Hashimoto et al. (1979) and Hashimoto (1983), involving the distillation of Murchison (C2) matrix material, as well as of oxide mixtures of chondritic composition. The experiments resulted in evaporative residues with chemical compositions resembling those of CAI.

Distillation of a reservoir of chondritic composition will be considered, to determine if the end product resembles PSI in chemical and isotopic composition. Following the experiments of Hashimoto et al. (1979), an evaporative sequence can be constructed (Figure 4.11). Initially, volatile elements such as Na and Fe are completely lost, followed by the partial loss of moderately volatile lithophile elements (Mg, Si, Cr). The resulting residue would appear enriched in the more refractory Al and Ca, and depleted in Mg and Si. Presumably most primary Fe was lost prior to Mg and SiO loss, so that Fe presently in the inclusions represents a later addition by recondensation or by Fe-Mg exchange reactions during alteration.

Volatilization of a reservoir containing isotopically normal material will produce a residue enriched in the heavier isotopes, since kinetic effects will cause the lighter atoms, which have a greater flux per number density, to be preferentially volatilized (see Section 2.2.3). Therefore, the residue would be expected to exhibit positive isotopic fractionation, for moderately volatile elements that were not completely lost. The magnitude of fractionation should be correlated with volatility, and the extent of loss of material. A correlation between the bulk chemical and isotopic composition of the residue would be expected, since the degree of isotopic fractionation increases as the element is depleted in the residue.

This distillation process can be modeled by a Rayleigh calculation (see Section 2.3.4 for a detailed presentation), where it is assumed that the solid reservoir is at equilibrium with the instantaneous vapor, which is removed continuously without further isotopic exchange. The Rayleigh model calculates the isotopic fractionation as a function of the fraction of each element remaining in the residue. According

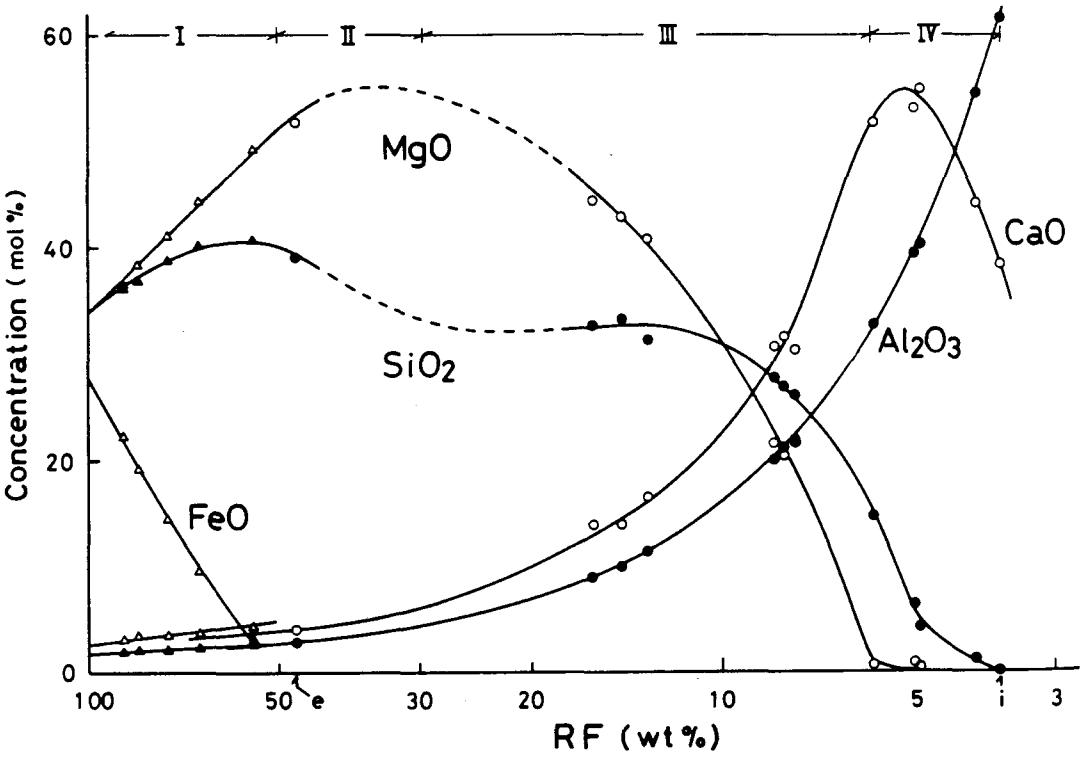

Figure 4.11. Sequential changes in chemical composition of an evaporative residue as a function of the fraction (RF) of residue remaining (from Hashimoto, 1983). Data points represent experimental data from vacuum evaporation of a multi-component melt FeO - MgO - SiO_2 - CaO - Al_2O_3.

to the Rayleigh model, the instantaneous isotopic ratio (R^{ij}) is a function of the extent of reaction, or the fraction (f) of the element remaining in the residue: $R^{ij} / R_i^{ij} = f^{(\alpha - 1)}$, where R_i^{ij} is the initial isotopic ratio, and α the mass fractionation factor (Rayleigh, 1896).

To evaluate the possibility of forming PSI by distillation, consider the simplest cases: inclusions B7F6 and B7H10 exhibit the minimum and maximum F_{Mg} (17‰ amu^{-1} and 39‰ amu^{-1}, respectively), and are isotopically homogeneous for Mg in the major phases. Assuming mass fractionation factors proportional to $m^{-1/2}$ for a volatility-controlled process (Section 2.3.3), loss of 44 and 84% of Mg, respectively (see Rayleigh curve in Figure 2.2) would be required to produce F_{Mg} as observed for B7F6 and B7H10. A similar loss of Si (as SiO) would be required to produce the observed F_{Si}. Assuming that Mg and SiO were the only major species lost during distillation, a total mass loss of 39 and 72% would be required for these two inclusions.

An original bulk composition of a precursor object can be estimated, using the calculated mass losses of Mg and SiO required by Rayleigh distillation, to produce the measured Mg and Si isotopic fractionation. For this calculation, it is assumed that the inclusions are isotopically homogeneous, and that only Mg and SiO are lost during distillation. Calculated compositions are obtained by adding back the Mg and Si oxides calculated to have been lost, and renormalizing the bulk composition.

For B7H10, this calculated precursor composition contains 27% MgO, 58% SiO_2, 9% Al_2O_3, and 4% CaO. Although relatively high in CaO and Al_2O_3, this composition is within the range of bulk compositions reported for ferromagnesian

chondrules in carbonaceous chondrites. Similar precursor compositions are obtained for DH8 and C-1. The calculated precursor for B7F6 is fairly Si-poor (37% SiO_2) and Al-rich (20% Al_2O_3), due to the relatively low F_{Mg} and F_{Si} observed for this inclusion.

A ternary diagram for SiO_2 - $CaO+Al_2O_3$ - MgO+FeO (Figure 4.12) presents ranges in composition for Ca-Al-rich inclusions and ferromagnesian chondrules within carbonaceous chondrites (McSween, 1977). Measured bulk compositions of B7F6, DH8, B7H10 and C-1 plot within the field for CAI, while the calculated precursor compositions (based upon the mass loss required to produce the isotopic fractionation observed) plot within the range of compositions observed for ferromagnesian chondrules.

Both the chemical and isotopic data for the FUN inclusions are consistent with formation of PSI by distillation of ferromagnesian chondrule-like objects. This model attempts to provide a consistent explanation for the chemical composition and extreme isotope fractionation in PSI, starting with a simple precursor and a well-understood process, e.g., distillation.

However, this model does not explain a) the absence of F_{Mg} and F_{Si} in many PSI which are chemically and petrographically similar; b) the association of UN effects with extreme fractionation; or c) the relation of PSI to normal CAI.

Most CAI do not exhibit extreme isotopic fractionation. Wood (1981) suggested that the rate of evaporation may determine whether isotopic fractionation accompanies distillation. Slow distillation may be required to produce isotopic

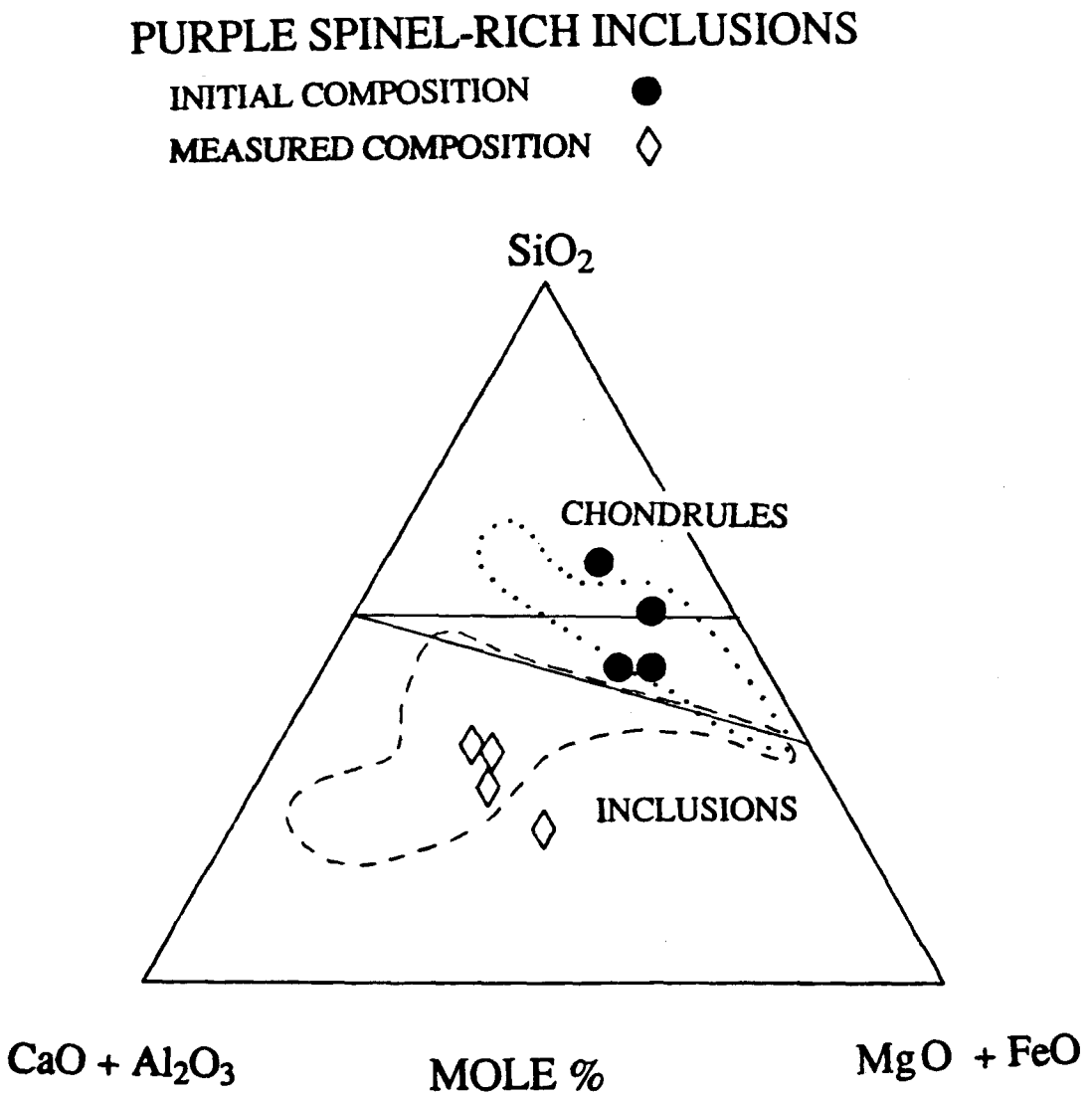

Figure 4.12. Ternary diagram SiO_2 - $CaO+Al_2O_3$ - Mgo+FeO shows ranges in chemical composition for Ca-Al-rich inclusions and ferromagnesian chondrules in carbonaceous chondrites. Measured bulk compositions for DH8, B7F6, B7H10 and C-1 plot within the field for CAI. Initial compositions were calculated assuming loss of Mg and Si by evaporation, based on a Rayleigh law. Calculated initial compositions plot within the range of compositions for ferromagnesian chondrules.

fractionation. The precursor material for the FUN PSI would still need to sample a reservoir of exotic nuclides, to explain the occurrence of UN effects.

The importance of volatility-controlled processes in the formation of FUN inclusions, is evidenced by a remarkably good correlation between the magnitudes of isotopic fractionation for Mg, Si and Cr (Figure 4.13). Measured fractionations have been scaled by the inverse square root of the masses, using Mg, Cr and SiO (see Section 2.3.4c, Figure 2.4). The major gas phase species for Si is generally assumed to be SiO (Porter et al., 1954); however, SiO_2 results in a closer fit of the data to a 1:1 line. Conditions sufficiently oxidizing to produce SiO_2 are also likely to produce MgO instead of Mg. This problem is not resolved.

The tendency for the data to lie along a 45° line emphasizes the importance of mass-dependent processes, involving kinetic effects during gas-solid exchanges such as distillation for elements of similar volatility. The importance of volatility-related processes is further evidenced by the observation that the more refractory elements, Ca and Ti, do not exhibit significant mass fractionation (Niederer et al., 1985; Papanastassiou and Brigham, 1987, 1988).

One problem with the distillation model is that there is no simple correlation between the measured bulk chemical compositions, and isotopic fractionation for these FUN inclusions. If these inclusions were simple distillation residues from a single reservoir, the inclusions with the most extreme F_{Mg} and F_{Si} values should have the lowest MgO and SiO_2 contents. This lack of correlation between isotopic fractionation and chemical abundances makes it unlikely that these inclusions are distillation residues from a single reservoir; therefore, a unique precursor object

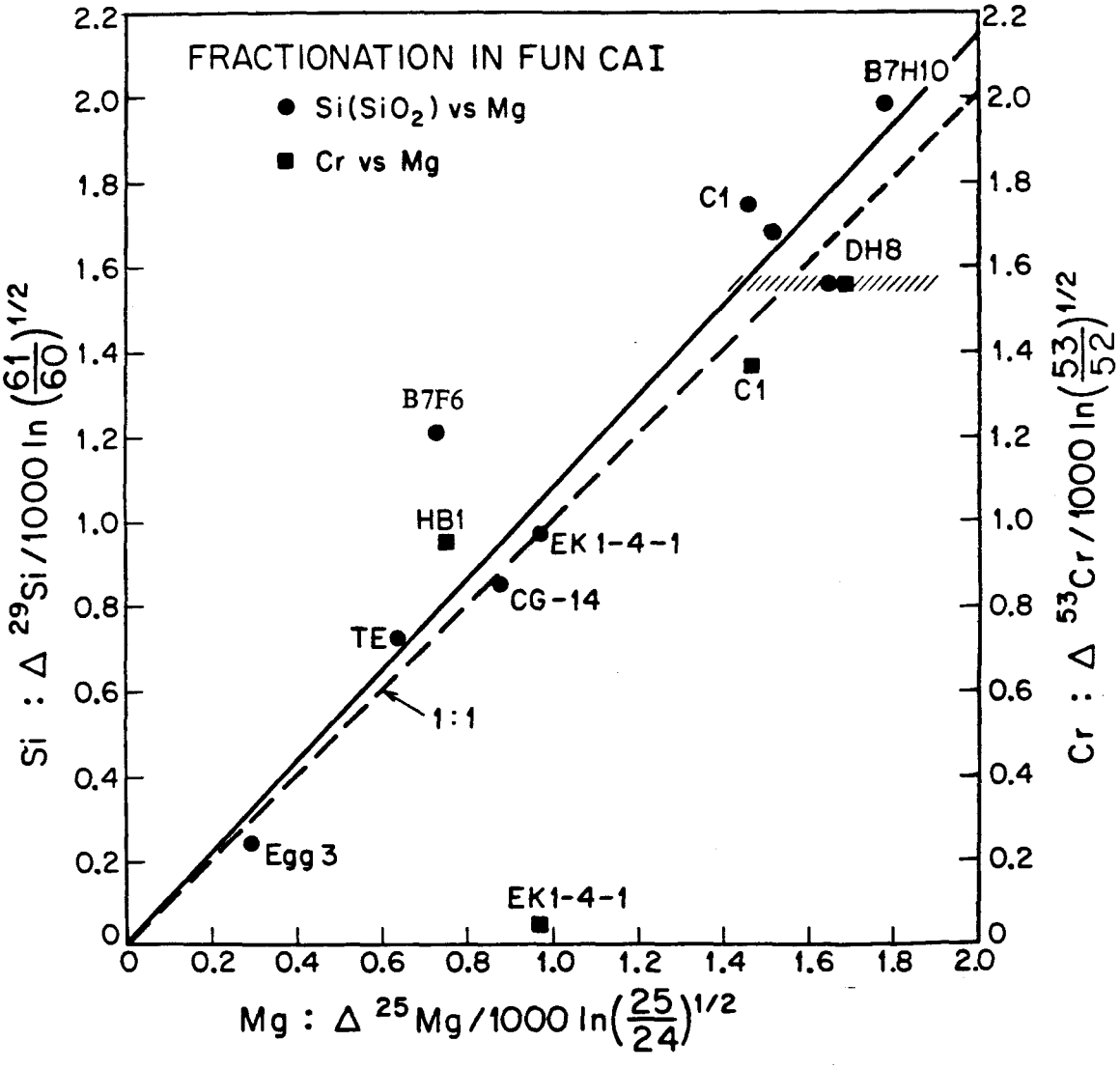

Figure 4.13. Correlations between Mg, Si and Cr isotopic fractionation in FUN inclusions. Measured fractionations have been scaled by the inverse square root of the masses. The data plot close to a 45° line, suggesting formation by mass-dependent, volatility-controlled processes.

cannot be defined. However, distillation processes may have produced a reservoir which underwent varying degrees of mixing with normal material and/or chemical fractionation, without further isotopic fractionation.

a. Complex Distillation Processes

The simple distillation model does not account for isotopic heterogeneity observed for primary phases within individual inclusions such as DH8. I will now consider physical conditions, which could influence the resulting evaporative residue, and introduce isotopic heterogeneity in primary phases; isotopic heterogeneity in secondary phases will be considered later.

The possibilities for producing isotopic heterogeneity may be summarized briefly. 1) The reservoir may be initially heterogeneous. 2) Distillation may result in a reservoir which is only partially molten, resulting in a chemically or isotopically heterogeneous residue. 3) Crystals may grow at different times throughout evaporation, and be isolated from further isotopic exchange. 4) The reservoir may change chemical composition during distillation, as exchange with a nebular gas occurs. 5) Finally, the resulting CAI may form directly as an evaporative residue, or it may form after further processing of the reservoir, i.e., after remelting or revolatilization and condensation of the reservoir. Each of these cases will now be considered in detail. It is important to note that the Rayleigh process assumes equilibrium between the reservoir and the vapor phase; this assumption is not strictly true if some crystals are isolated, as in the physical scenarios presented in this section.

First, distillation of a homogeneous, completely molten precursor would be expected to produce an isotopically homogeneous residue. However, isotopic heterogeneity may result if the precursor was initially heterogeneous.

Second, suppose that the reservoir is only partially molten, such that the unmelted solid fraction may be isolated from isotopic exchange with the vapor phase. Distillation of the molten fraction continues, producing more highly fractionated material. The resulting phases that eventually crystallize from this molten fraction, will be more highly fractionated than the previously isolated solids. For example, spinel is the most refractory phase in these inclusions, and would be the last to melt. Since spinel crystals can not react directly with the vapor phase (spinel does not sublime), spinel may be expected to be less fractionated than the other phases; this is the opposite of what is observed in DH8 (where spinel is more fractionated than fassaite).

Third, a similar scenario will result if crystals grow at different times from the melt throughout the evaporation process. The first phase to crystallize and be isolated from further isotopic exchange (spinel), would be expected to exhibit less extreme fractionation, than later-crystallizing phases (fassaite) which form after distillation has proceeded further, and the reservoir is more highly fractionated. Again, this is the opposite of observations of DH8 where spinel is the most highly fractionated phase. However, this could account for variable isotopic compositions among spinels.

The fourth alternative postulates a changing reservoir composition. During evaporation, the composition of the residue changes continuously, becoming

increasingly isotopically and chemically fractionated. Isotopic heterogeneity could be introduced, if the residue reacts with an isotopically normal gas phase as phases are crystallizing. This could also be modeled by an episode of distillation, followed by crystallization and isotopic reequilibration with the vapor phase; before subsequent episodes of distillation and isotopic reequilibration. This would result in later crystallizing phases (i.e., fassaite) being less fractionated, than early crystallizing phases (spinel). This mechanism could account for the isotopic variability observed in DH8.

Finally, the possibility must be considered that CAI are not direct evaporative residues, but formed after extensive, multistage processing of a residue resulting from distillation. The evaporative reservoir could be revolatilized and condensed, providing further opportunities for interaction and exchange with a nebular gas. The initial reservoir may have been significantly more fractionated (i.e., values of F_{Mg} up to 345‰ amu^{-1} have been observed in Murchison hibonites; Hutcheon et al., 1983). Isotopically normal material may have been added during the mixing processes. This addition of normal material is substantiated by observations of variable isotopic fractionation within inclusions.

b. Isotopic Constraints: Experimental Results

Several experiments have attempted to duplicate Rayleigh distillation and isotopic fractionation in the laboratory. Hashimoto et al. (1989) evaporated solid and liquid terrestrial forsterite samples, and measured the resulting O, Mg and Si isotopic fractionation of the residues, as a function of the fraction of residue remaining.

Large isotopic fractionation was observed only for the liquid samples, suggesting that melting of CAI may be necessary to produce isotopic fractionation during distillation.

Esat et al. (1986) performed high-temperature distillation experiments on terrestrial pyroxene, and measured Mg isotopic compositions of evaporative residues and condensates. Substantial fractionation was observed, with the residues enriched in the heavier isotopes (up to +27‰ amu^{-1}) and the condensates enriched in the lighter isotopes (up to -13.9‰). In addition, small nonlinear anomalies were observed after correction for mass fractionation.

Molini-Velsko et al. (1987) measured Si isotopes in solar furnace distillation residues as well as meteorite fusion crusts. Small isotopic fractionation effects were observed, but no nonlinear anomalies were produced.

4.6.4. ISOTOPIC HETEROGENEITY; SECONDARY PHASES

While isotopic heterogeneity in primary phases may be attributed to varying physical or chemical conditions during formation; isotopic heterogeneity in secondary phases is most likely due to later alteration involving addition and incomplete exchange with isotopically normal material. Addition of isotopically normal material may be evidenced by lower fractionation for secondary phases or gradients toward lower fractionation for inclusion rims (Fahey et al., 1985). In contrast, MacPherson et al. (1987) measured a CAI from Vigarano with isotopically

heavier Mg and Si in the rim than in the center, which they interpreted as the result of flash heating and preferential volatilization of the rim.

Isotopic variability was observed for both primary and secondary phases in the FUN inclusions. In contrast, coarse-grained inclusions typically exhibit uniform Mg fractionation in major phases within the interior of a single inclusion (Wasserburg et al., 1977; Esat et al., 1978).

B7F6 exhibited uniform F_{Mg} for interior spinel and fassaite, but lower F_{Mg} for spinel and olivine near the inclusion edge. This can be interpreted as addition of normal Mg from a nebular gas or the matrix. Variable F_{Si} but uniform F_{Mg} in B7F6 fassaite is difficult to interpret, since addition of Mg and Si should be coupled if the inclusion is reacting with a reservoir of chondritic or solar composition. The observation of isotopically normal Si in hedenbergite which rims void spaces in B7F6 (Figure 4.5a) suggests that normal Si, and presumably Fe were added in secondary, vapor phase processes.

B7H10 exhibits uniform F_{Mg} and F_{Si} for interior spinel and fassaite. However, Fe-rich spinel in a more heavily altered region of olivine and nepheline exhibits lower F_{Mg} ($\approx$34‰ amu^{-1}). This spinel is mantled and surrounded by olivine with less fractionated Mg (11‰ to 19‰ amu^{-1}) and isotopically normal Si. Isotopic and petrographic observations are consistent with formation of olivine and feldspathoid by alteration of spinel: Sp => Ol + Fp, requiring addition of Si and Na (MacPherson et al., 1981). Isotopic data are consistent with the addition or

exchange of all Si and 1/2 to 2/3 Mg in olivine from an isotopically normal reservoir.

Anorthite in DH8 exhibits highly fractionated Mg and Si; therefore, anorthite appears to be a primary phase, even though it lacks ^{26}Al. Alternatively, anorthite may have formed from a fractionated phase in the inclusion, with little new Mg or Si being added at the lower temperature of anorthite formation. Si was fractionated for anorthite grains exhibiting $^{27}Al/^{24}Mg$ = 23,000, and for grains exhibiting $^{27}Al/^{24}Mg$ = 300, suggesting that even the more Mg-rich anorthite has not undergone substantial isotopic exchange (if it is assumed that diffusion rates for Si and Mg are similar in anorthite).

DH8 exhibits variable Mg fractionation within a single phase (spinel). Spinel exhibits a range in F_{Mg} of 9‰ amu^{-1}, similar to the range in F_{Mg} observed for fine-grained CAI. This heterogeneity in spinel may be secondary due to varying degrees of isotopic exchange with normal Mg, or primary due to changing isotopic composition of the reservoir, due to the gradual addition of normal Mg during formation of spinel. F_{Mg} appears to be uniform for fassaite. DH8 also exhibited an offset in F_{Mg} between spinel and fassaite, such that F_{Mg} for fassaite lies at the lower end of the range in F_{Mg} for spinel. This difference in F_{Mg} between spinel and fassaite could be explained by intrinsic isotopic heterogeneity within the inclusion. Spinel may have crystallized from a reservoir with a continuously changing isotopic composition, due to the addition of normal Mg. Fassaite in DH8 may have formed last, consistent with the observation that F_{Mg} for fassaite lies at the lower end of F_{Mg} for spinel. Petrographic textures suggest crystallization of the inclusion from a melt;

however, it is possible that spinels with the most extreme F_{Mg} values were never molten, and did not equilibrate with fassaite. Alternatively, the inclusion may have been originally isotopically homogeneous, but fassaite may have preferentially exchanged with normal Mg during later alteration. However, data on self-diffusion of ^{18}O during gas-solid exchange, suggest similar diffusion rates for Mg-spinel and enstatite (Freer, 1981; Reddy and Cooper, 1981).

Spinels in the core of HB1 exhibit two distinct ranges in Mg fractionation. Coarse spinel grains exhibit slightly higher F_{Mg} (23.8 ± 1.4‰ amu^{-1}) than spinels occurring in veins or bands (F_{Mg} = 19.9 ± 1.2‰ amu^{-1}). Normal Mg may have preferentially diffused into the smaller spinel grains occurring in veins. Hibonite in the fine-grained mantle is as highly fractionated as the core phases, suggesting that hibonite is primary and may have been part of the core. Grossular in the mantle contains less fractionated Mg (F_{Mg} = 13.3 to 15.9‰ amu^{-1}), and isotopically normal Si. The grossular may result from the alteration of melilite: Mel => Gross + Neph. The isotopic data require that approximately half of the Mg, and most of the Si (≥ 80%) come from an isotopically normal gas.

It is clear that these purple inclusions have undergone significant alteration. FUN PSI exhibit high Na_2O, Zn and FeO contents, indicative of substantial Fe-Mg exchange and low-temperature alkali-halogen alteration. The preservation of large isotopic effects in these extensively altered CAI, attests to the resistance of the abundant spinel and fassaite to mineralogical alteration and isotopic exchange.

4.6.5. EXCESS ^{26}Mg

Observations of excesses in ^{26}Mg correlated with $^{27}Al/^{24}Mg$ in a variety of CAI (cf. review by Wasserburg and Papanastassiou, 1982; Wasserburg, 1986) have provided evidence for the in situ decay of ^{26}Al ($t_{1/2}$ = 0.72x10^6 y). See the more complete discussion in Section 2.4.3. Many Type B CAI exhibit a correlation line of slope $(^{26}Al/^{27}Al)_o$ = 5x10^{-5} on an Al-Mg evolution diagram. However, substantially lower and higher values have been reported for CAI: 5x10^{-8} ≤ $(^{26}Al/^{27}Al)_o$ ≤ 7x10^{-5}. A range in the initial value may be due to formation at different times or due to heterogeneity in ^{26}Al.

Consistently low initial values have been reported for FUN inclusions C-1 and HAL. The value $(^{26}Al/^{27}Al)_o$ = 5x10^{-8} was established by ion probe measurements of HAL hibonite (Fahey et al., 1987), while $(^{26}Al/^{27}Al)_o \approx$ 5x10^{-6} was measured for C-1 (Esat et al., 1978).

Measurements of DH8 anorthite yield no excess ^{26}Mg, and provide a limit $(^{26}Al/^{27}Al)_o \leq$ 1x10^{-7}. It should be noted that DH8 anorthite exhibited substantial isotopic fractionation for Mg and Si, consistent with values obtained for spinel and fassaite. Therefore, anorthite appears to be a primary phase; and the lack of ^{26}Al cannot be attributed to substantial alteration, unless Mg and Si exhibit drastically different diffusion rates in anorthite. B7F6 anorthite, which also exhibits highly fractionated Mg, yields $(^{26}Al/^{27}Al)_o \leq$ 5x10^{-6}. HB1 hibonite exhibits fractionated Mg but no ^{26}Al, yielding a limit $(^{26}Al/^{27}Al)_o \leq$ 7x10^{-6}. The data from C-1, HAL, DH8,

B7F6 and HB1 are consistent with evidence for a heterogeneous distribution of ^{26}Al (Hutcheon, 1982).

Alternative explanations involve the preferential loss of $^{26}Mg^{*}$, or late formation of the inclusions. The limit on $(^{26}Al/^{27}Al)_0$ for DH8 would require formation 6.5×10^6 years after formation of type B CAI with $(^{26}Al/^{27}Al)_0 = 5 \times 10^5$. The lack of ^{26}Al in FUN inclusions C-1, HAL, DH8, B7F6 and HB1 suggests that the addition of exotic nuclides to FUN inclusions is not coupled with the addition of ^{26}Al to normal CAI. It is possible that FUN inclusions are "early" condensates, i.e., before the "late" addition of ^{26}Al to solar system material.

4.6.6. UN EFFECTS

Ca, Ti and Cr isotopic data were obtained for four of the PSI inclusions (Papanastassiou and Brigham, 1989). Large nonlinear effects were observed for DH8, B7F6 and HB1, confirming their identity as FUN inclusions. These results, consisting of deficits of the most neutron-rich isotopes, will be briefly presented. Isotopic results (reported as parts in 10^4 or εu) are shown in Figure 4.14. Results are also shown for the FUN inclusion C-1.

After normalization of the Ca data, using the $^{40}Ca/^{44}Ca$ ratio, large deficits were observed in ^{48}Ca. HB1 exhibited the largest effect, with a ^{48}Ca deficit of -144εu, while DH8 and B7F6 exhibited a deficit of -31εu, identical to that observed for C-1. No effects were observed for ^{42}Ca, ^{43}Ca or ^{46}Ca.

Figure 4.14. Ca, Ti and Cr isotopic data for inclusions DH8, C-1, B7F6 and HB1, as well as an opaque assemblage (OA) from HB1. Nonlinear deviations are shown (in parts in 10^{-4}) relative to the normal composition after correction for mass fractionation (from Papanastassiou and Brigham, 1989). The reference isotopes used for the fractionation correction are shown as filled points. Large deficits are observed for ^{48}Ca, ^{50}Ti and ^{54}Cr. ^{47}Ti exhibits a small excess and ^{49}Ti a small deficit. The same general isotopic pattern is observed for all inclusions and for the opaque assemblage.

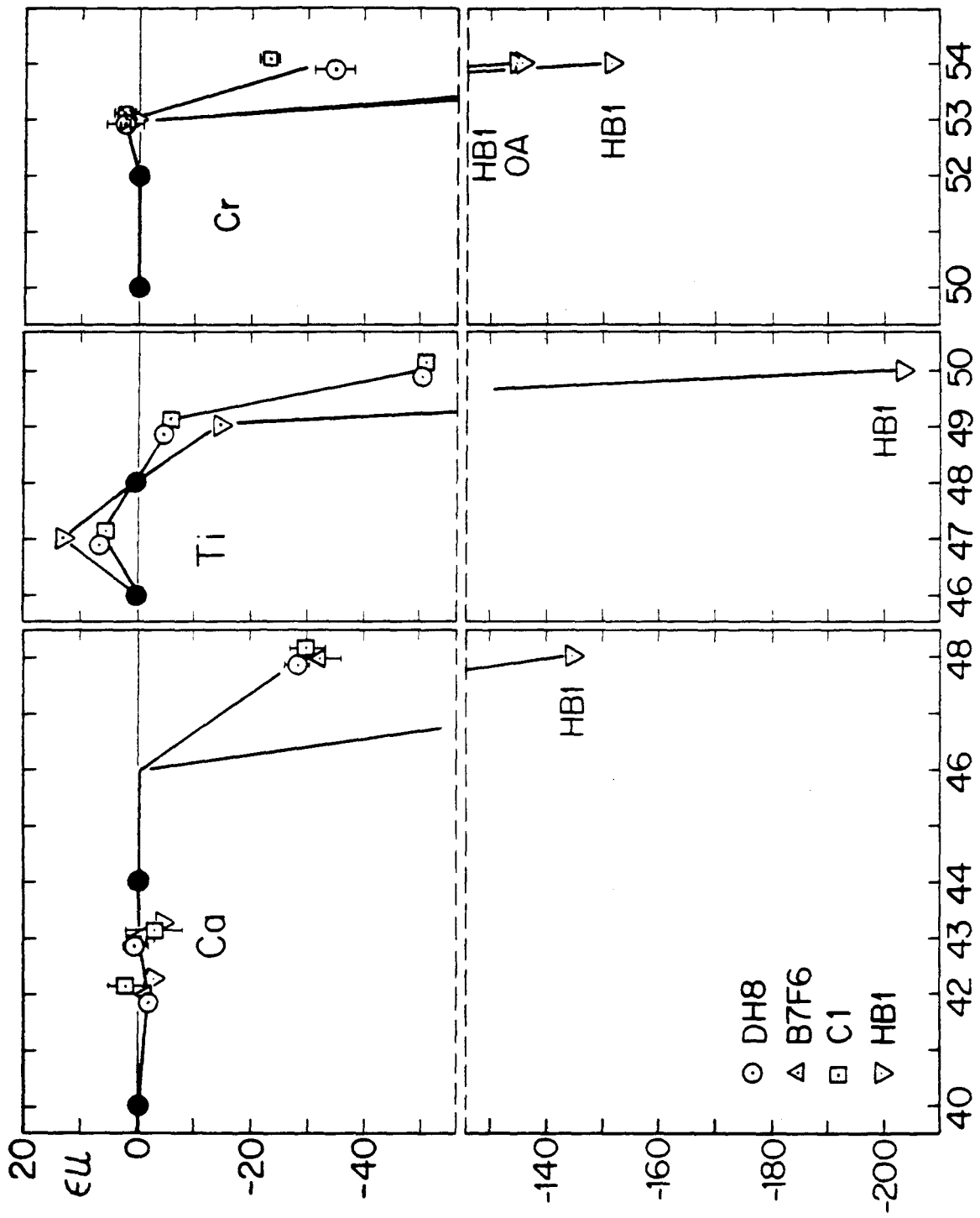
Ca
Ti
Cr
HB1
OA
HB1
HB1
HB1
HB1
DH8
B7F6
C1
HB1
εω
20
0
-20
-40
-140
-160
-180
-200
40
42
43
44
46
48
46
47
48
49
50
50
52
53
54

Ti isotopic data were normalized using the $^{46}Ti/^{48}Ti$ ratio. The inclusions showed a small, but well-resolved excess in ^{47}Ti, and a deficit in ^{49}Ti. Extremely large deficits were observed in ^{50}Ti, up to -203εu for HB1.

For Cr, large positive isotopic fractionation was observed: 18‰ amu^{-1} for DH8 and 10‰ for HB1. After normalization for fractionation, using $^{50}Cr/^{52}Cr$, large deficits were observed in ^{54}Cr, ranging up to -151εu for HB1. Cr measurements of an opaque assemblage from HB1, showed an isotopic composition identical to that for the bulk inclusion.

The isotopic patterns for Ca, Ti and Cr for the three PSI inclusions are remarkably similar to each other, and to the pattern previously observed for FUN inclusion C-1 (Lee et al., 1978; Niederer et al., 1980; Papanastassiou, 1986). In addition the magnitudes of the effects for the Type B inclusions DH8, B7F6 and C-1 are nearly identical. The similarity of the patterns for the inclusions indicates that they have sampled a distinct nucleosynthetic component. Discussions of the nucleosynthesis of Ca, Ti and Cr have been given by Niederer et al. (1985) and Papanastassiou (1986).

The exotic component sampled by these inclusions was depleted in the most neutron-rich isotopes of Ca, Ti and Cr, which are produced in explosive O and Si burning. In contrast, the component sampled by EK-1-4-1, was enriched in the most neutron-rich isotopes, as well as in other isotopes of these elements.

Ti isotopic data from FUN inclusions, and for endemic effects in CAI, have been shown to require the addition of at least three exotic nucleosynthetic components (Niederer et al., 1985).

4.6.7. PETROGENESIS

Petrographic textures exhibited by the Type B purple inclusions, consisting of poikilitic spinel in fassaite, and of anorthite laths terminating against fassaite, are strongly suggestive of crystallization of the inclusions from a melt. The angular or irregular outlines of the inclusions, as well as the absence of Wark-Lovering rims, suggest that the inclusions may be fragments. The core of the Type A inclusion HB1, consisting of poikilitic spinel in melilite, and hibonite laths surrounded by spinel, also suggests crystallization from a melt, with the early crystallization of hibonite.

The abundance of secondary phases, and the bulk chemical compositions of the PSI indicate that they have undergone substantial alteration. The high Fe, Na and Zn contents of the four FUN inclusions and C-1 indicates Fe-Mg exchange, and low temperature alteration by alkali and halogens. The high Zn contents seem to be characteristic of PSI (as well as fine-grained CAI), suggesting that PSI inclusions were formed or altered, in a nebular gas of distinct chemistry. The need for a nebular gas of distinct chemistry is substantiated by the need to sample UN effects, and by the low Ti^{3+} contents of fassaite in Type B PSI, suggesting that the inclusions formed under substantially more oxidizing conditions than normal CAI ($fO_2 \approx 10^2$ to 10^4 higher than the standard nebula; Stolper et al., 1982).

Secondary phases in the Type B inclusions occur in two types of regions. Clusters of Fe-rich spinels are embedded in intergrowths of sodalite and olivine.

The textures are suggestive of a breakdown reaction, or of late crystallization from a melt. The sodalite-olivine intergrowths exhibit a sharp boundary with adjacent fassaite (Figure 4.3a), requiring that fassaite not be affected by melting or reaction. A temperature of ≈1400°C is required to melt nepheline-forsterite; the presence of Fe and Cl in sodalite-olivine would require a lower melting temperature. However, nearby regions contain the same phases, but with different textural relationships: Fe-rich spinel surrounded by euhedral olivine and nepheline. Presumably a melting episode would have affected these nearby regions similarly. These regions may not have undergone such extensive reaction.

Comparison with FUN inclusion C-1, which exhibits regions of Fe-rich spinel, melilite, and intergrown feldspathoid and olivine, suggests that the primary phase for this breakdown reaction may have been melilite. Wark (1983) describes alkali-halogen metasomatism in C-1, which has partially altered melilite and anorthite to sodalite, nepheline and ferromagnesian silicates.

The second type of low temperature assemblage involves regions near the edge of the Type B inclusions composed of fine-grained grossular, hedenbergite, hibonite, feldspathoid, olivine and extremely Ti-rich fassaite (≈16% TiO_2). Hibonite and Ti-rich fassaite typically are minor phases found in conjunction with melilite in Type A CAI. This indirectly supports formation of secondary phases by the alteration of melilite.

Type B PSI inclusions may have originally been spinel-rich, melilite-poor objects, which underwent secondary alteration involving the addition of Na, Zn and Fe. Alternatively, these inclusions may have originated from a precursor more similar to

a typical Type B CAI, in which melilite was nearly completely altered to form secondary phases (feldspathoid, grossular, hedenbergite, olivine). This alteration may have involved partial melting in some cases to form the olivine-sodalite intergrowths observed. This alternative is supported by the bulk compositions of the inclusions. Assuming that the observed secondary phases were once melilite, a precursor bulk composition can be calculated by converting the modal abundances of secondary phases to melilite. The bulk chemical compositions obtained by this recalculation plot within the field for typical Type B CAI (Figure 4.15) on a ternary plot anorthite-gehlenite-forsterite, projected from spinel (Stolper, 1982).

This model relates purple Type B CAI to normal Type B CAI, but provides no explanation for the extreme isotopic effects common in these inclusions. Formation of PSI from an extremely spinel-rich precursor is suggestive of higher temperatures for formation than for other Type B CAI.

4.7. CONCLUSIONS

Purple spinel-rich, coarse-grained inclusions exhibit a higher frequency of FUN isotopic anomalies (≈20%) than the general population of CAI. Four new FUN inclusions were identified among twenty purple inclusions, analyzed for Mg isotopes by thermal ionization mass spectrometry.

Isotopic data for Mg and Si were obtained by ion microprobe analysis for these four FUN inclusions, which are similar in petrographic character to Type B and Type A CAI.

Figure 4.15. Ternary diagram with endmember compositions anorthite-gehlenite-forsterite, projected from spinel (Stolper, 1982). The composition range for Type B inclusions is shown. The measured bulk chemical compositions for DH8, B7F6 and B7H10 are shown. Calculated precursor compositions are plotted, by assuming that all secondary phases were originally melilite. These precursor compositions plot near or within the field for typical Type B CAI.

PURPLE SPINEL-RICH INCLUSIONS

MEASURED COMPOSITIONS ◊

RECALCULATED COMPOSITIONS ●

DH8

B7F6

B7H10

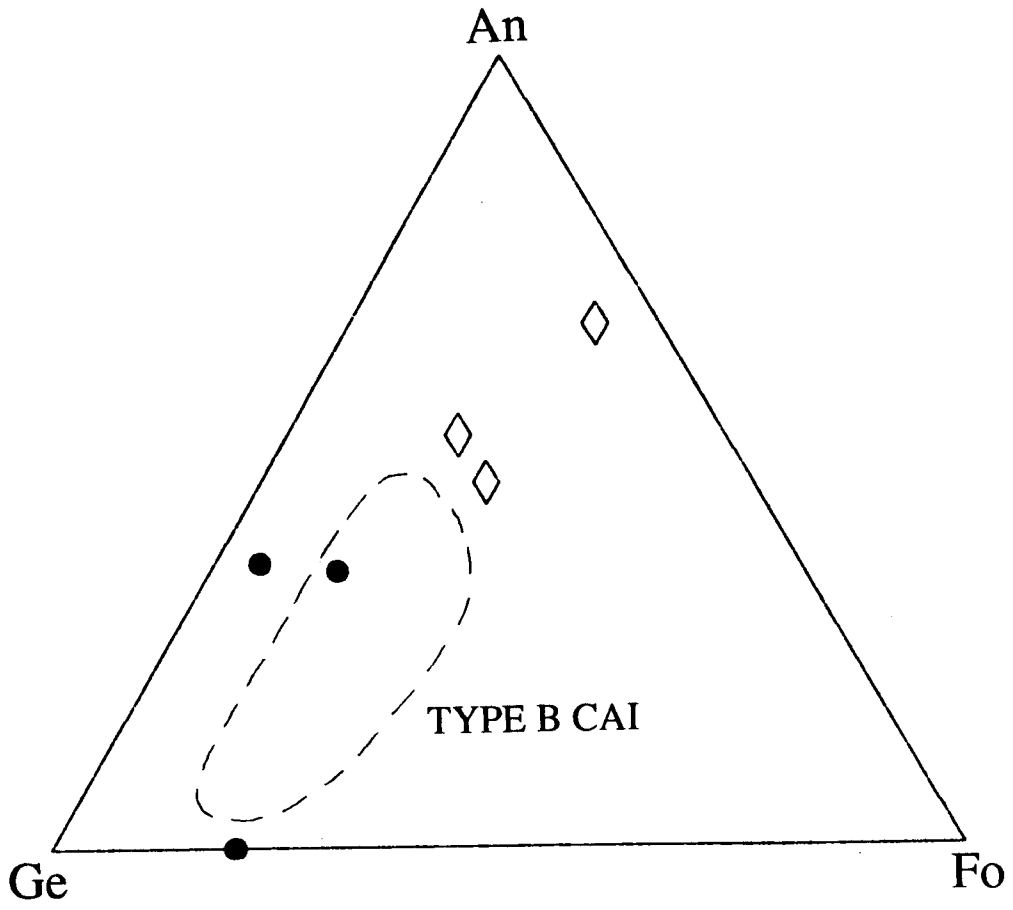

Large positive isotope fractionation was observed for Mg and Si. Mg and Si isotopic fractionation were found to be variable within individual inclusions. For example, inclusions exhibit lower F_{Mg} for phases near the edge. Secondary phases within inclusions (olivine, hedenbergite, grossular) contained fractionated Mg of a magnitude much less than for primary interior phases. These phases also exhibit isotopically normal Si, requiring secondary, vapor-phase reactions with normal Si.

DH8 is the first coarse-grained CAI to exhibit substantial variability in fractionation for primary interior phases (spinel, fassaite). The range in F_{Mg} for DH8 spinels is comparable to the range observed for fine-grained CAI. This heterogeneity may be primary, due to changes in the reservoir composition during formation, or secondary due to varying degrees of exchange with isotopically normal material.

The observation of an excellent correlation between the magnitudes of Mg, Si and Cr isotopic fractionation emphasizes the importance of mass-dependent kinetic processes involving distillation. The lack of fractionation for Fe, and for refractory Ca and Ti is also suggestive of volatility-controlled processes.

A Rayleigh model was used to estimate a precursor composition of these inclusions, assuming mass loss of Mg and Si by distillation. This calculated precursor composition is consistent with formation of FUN inclusions, by distillation of a ferromagnesian chondrule-like object. However, these inclusions are not simply distillation residues from a single reservoir, since there is no consistent correlation between the magnitudes of isotopic fractionation effects and chemical compositions. Therefore, distillation processes may have produced a reservoir with highly

fractionated isotopic abundances. The inclusions may have formed from this reservoir after chemical fractionation, but no further isotope fractionation.

The fassaite-spinel purple inclusions are distinct from Type B CAI due to their high abundance of spinel, absence or low modal abundance of melilite, and the high abundance of secondary phases. These inclusions may have formed from a precursor similar to a Type B CAI, in which the melilite has been completely altered to form secondary phases (feldspathoid, grossular, hedenbergite, olivine). Petrographic textures suggest that some of this alteration may have involved the formation of a melt.

The preservation of large isotopic anomalies in such heavily altered CAI attests to the resistance of spinel and fassaite to mineralogical alteration and isotopic reequilibration. Similar isotopic patterns observed for Mg, Si, Ca, Ti and Cr for inclusion C-1 and the PSI FUN inclusions, as well as similarities in their petrography and chemistry, suggest that the PSI may form a distinct group of FUN inclusions which have sampled a unique nucleosynthetic component and have undergone similar chemistry and alteration processes.

The identification of four new FUN inclusions which exhibit highly fractionated Mg, Si and Cr, as well as large anomalies for all heavy elements measured, again raises the suggestion that large isotopic fractionation effects may be a useful indicator of UN anomalies.

CHAPTER FIVE

ISOTOPIC CHARACTERISTICS OF OPAQUE ASSEMBLAGES IN FUN INCLUSIONS

5.1. INTRODUCTION

Ca-Al-rich inclusions exhibit large enrichments in the refractory siderophile elements Ru, Os, Re, Pt, Ir, W and Mo, in comparison with chondritic values (Wanke et al., 1974; Grossman and Ganapathy, 1976). These enrichments (≈17 x chondritic) are concentrated in micron-sized refractory metal nuggets (Wark and Lovering, 1976; Palme and Wlotzka, 1976); and in larger complex opaque assemblages (OA) consisting of metal alloys, sulfides, oxides, phosphates and silicates.

Early models attributed the refractory nature of OA to formation as aggregates of presolar material which predated CAI formation (El Goresy et al., 1978; Armstrong et al., 1985); or as representatives of the earliest condensates from the solar nebula (Wark and Lovering, 1976; Fegley and Kornacki, 1984).

OA were thus viewed as exotic objects, termed Fremdlinge (El Goresy et al., 1978), which might exhibit extreme isotopic anomalies. However, measurements of Mg, Fe, Mo, Ru and W isotopes were determined for OA, and found to be normal

(Hutcheon et al., 1987), suggesting a less exotic origin. Furthermore, diffusion and phase equilibria experiments by Blum et al. (1988a,b) demonstrated that OA formed by in situ alteration of Ca-Al-rich inclusions.

According to the model of Blum et al. (1988c), NiFe metal and refractory siderophile elements were initially incorporated into Ca-Al-rich inclusions. Heating and melting of the CAI resulted in segregation of the siderophile elements as immiscible alloys, from the molten silicates and spinels in the inclusion. Opaque assemblages formed after the metal alloys underwent oxidation and sulfidization, at low temperatures (≤870°K), and high oxygen partial pressures (pO_2 six orders of magnitude higher than in the solar nebula). It now appears that these assemblages can provide information on the low-temperature alteration history of CAI, rather than on the high-temperature nebular history.

Isotopic fractionation can provide constraints on the alteration history of these assemblages; the absence of previous observations of fractionation within OA may be due to the fact that previous isotopic analyses for OA were obtained for assemblages within isotopically normal CAI (other than Ru measurements for a refractory metal nugget in FUN inclusion C-1, Hutcheon et al., 1987).

In this chapter, I present petrographic and isotopic data for opaque assemblages, and adjacent spinel grains in a Type A FUN inclusion, which has been shown to exhibit large fractionation and nuclear anomalies. Data were obtained in situ for Mg, Si, Cr and Fe isotopes in individual phases. The data were used to correlate: 1) isotopic effects with petrographic observations, and 2) isotopic fractionation for different elements. The purpose is to investigate primary and secondary formation

processes involved in the formation of OA, specifically the roles of isotopic reequilibration and element transport during chemical alteration.

5.2. PETROGRAPHIC DESCRIPTIONS

Inclusion HB1 is a melilite-spinel rich Type A inclusion described in detail in Chapter 4. Briefly, HB1 (5x5 mm) consists of an elongated blue core (color photo in Figure 1.1b) composed predominantly of spinel (70%) arranged in veins of closely-packed crystals. Spinel-rich veins (refer to Figure 4.5) are separated by regions with euhedral spinel poikilitic in gehlenitic melilite. Toward the edge of the core, hibonite laths are enclosed by ≈100 μm regions of densely-packed spinel grains with interstitial melilite. Spinel typically contains 2 to 6% FeO and 0 to 0.5% Cr_2O_3. The core of HB1 is surrounded by a red mantle (200 to 450 μm) of loosely-packed 10 to 25 μm grains of Fe-V-rich spinel, hibonite, sodalite, nepheline, and grossular. The mantle is surrounded by a white rim (≈100 μm) of fassaite, andradite, nepheline and sodalite.

The opaque assemblages in HB1 are diverse in petrography and chemistry. Numerous 10 to 50 μm OA occur throughout the core (Figure 5.1). The smallest of these OA are spherical; the larger ones exhibit irregular or angular shapes. Mineralogically, these OA consist either of Ni_3Fe or pentlandite, without these two phases occurring together. Ca-phosphate is occasionally observed as a minor phase.

Two large opaque assemblages (OA1 and OA3) were observed in the core of HB1. OA1 (240 μm) is spherical (Figure 5.2), with a core (≈50 μm) of Ni_2Fe,

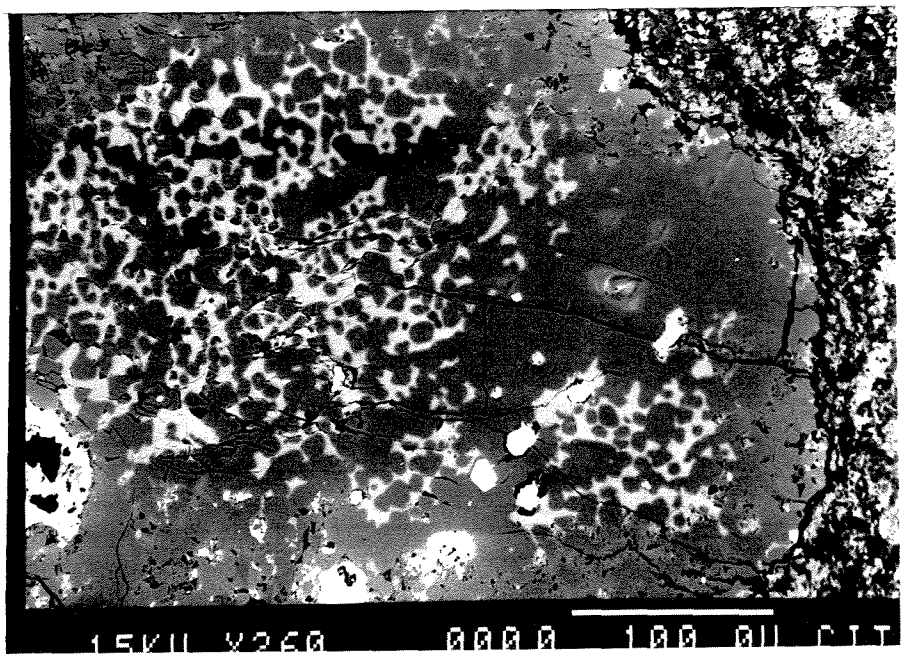

Fig. 5.1. BEI showing numerous 10 to 30 μm opaque assemblages in HB1, consisting of either Ni_3Fe or pentlandite, and surrounded by spinel.

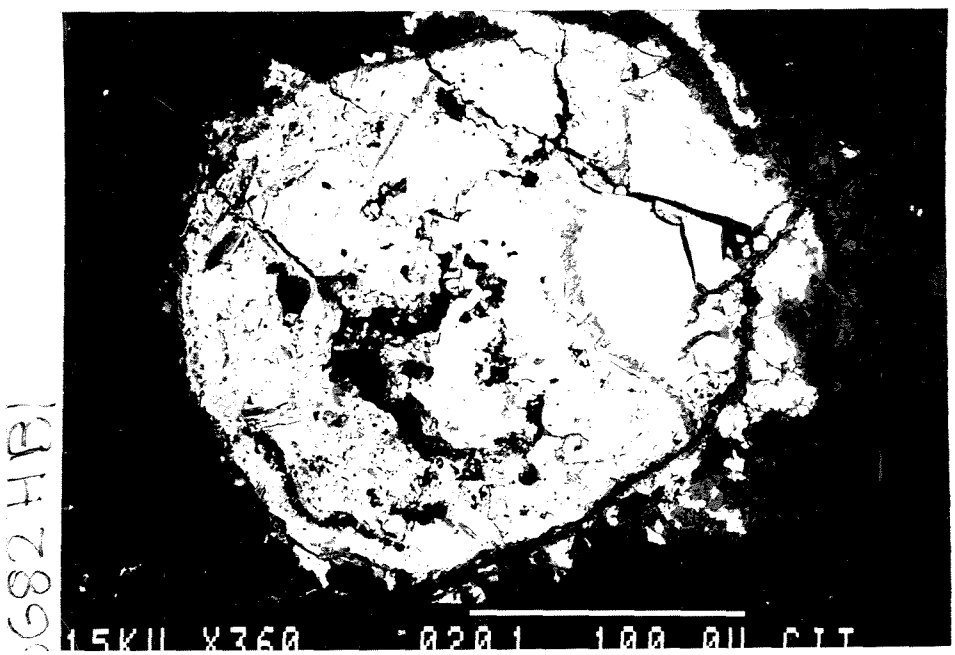

Fig. 5.2. BEI of opaque assemblage OA1. The Ni_2Fe core is surrounded by pentlandite and chains of V-rich magnetite.

surrounded by fine-grained pentlandite. The metal and pentlandite are uniform in chemical composition. Chains of V-rich magnetite (34 to 39% V_2O_3) rim the OA, and intersect the pentlandite. Trace amounts of diopside were observed.

OA3 (150 μm) is spherical, consisting of Ni_2Fe and pentlandite. Spinel adjacent to OA3 is chemically zoned in FeO content, ranging up to 18% FeO near the OA. A third large assemblage (OA4) was identified during the excavation of the inclusion. OA4 is a 200 μm aggregate of fine-grained phases (1 to 10 μm), including abundant (≈ 60 vol. %) V-Cr-rich magnetite and pentlandite (≈ 20%), with smaller amounts of olivine, spinel and Ca-phosphate. None of the other OA were observed to contain such Cr-rich magnetite (≈ 10% Cr_2O_3, ≈ 25% V_2O_3).

5.3. ISOTOPIC COMPOSITION

Isotopic fractionation data for Mg, Si, Cr and Fe in opaque assemblages and adjacent spinel grains within the FUN inclusion HB1 are tabulated (in permil per amu) in Table 5.1 and illustrated in Figure 5.3.

Spinel exhibits a range in F_{Mg}, from 19.9 ± 1.5‰ amu^{-1} for spinels in veins, to 23.8 ± 1.4 ‰ amu^{-1} for spinels near the edge of the core (see Section 4.5.1). Spinel contains isotopically heavy Cr (F_{Cr} = 9.1 ± 4.6‰ amu^{-1}), consistent with thermal ionization measurements of the bulk inclusion (Papanastassiou and Brigham, 1989). Two Fe-rich spinels (≈ 6% FeO) exhibit highly fractionated Mg, but normal Fe (F_{Fe} = -0.7 ± 1.1‰ amu-1; δ^{57}Fe -1.0 ± 1.5‰). No spinels exhibited Fe fractionation.

Analyses of Mg in Ni_2Fe and diopside in the large assemblage OA1 yield consistent F_{Mg} values (F_{Mg} = 8.1 ± 5.6‰ and 4.0 ± 2.2‰ amu^{-1} respectively), much less than F_{Mg} in neighboring spinels. Pentlandite and Ni_2Fe metal in OA1 exhibited normal, unfractionated Fe compositions (F_{Fe} = -0.8 ± 0.5‰ amu^{-1}; $\delta^{57}Fe$ = -1.8 ± 1.4‰ for pentlandite), also consistent with spinel analyses. (See Section 3.5.4 for a discussion of analytical conditions for Fe isotopic analyses, the use of standards, and problems with analyses of intergrown phases.)

The second large assemblage OA3 is distinct: both pentlandite and Ni_2Fe in OA3 exhibit fractionated Fe (F_{Fe} = 8.1 ± 0.8‰ amu^{-1} for Ni_2Fe; 6.1 ± 3.2‰ for pentlandite). Mg in Ni_2Fe is also highly fractionated (F_{Mg} = 21.8 ± 3.8‰ amu^{-1}, consistent with the value measured for adjacent spinels (Sp18, 23)).

Ni_3Fe in one of the smaller assemblages, OA2 also exhibits fractionated Fe (8.1 ± 1.7‰ amu-1). Mg isotopes were not measured.

Cr fractionation, measured for OA4 by thermal ionization (Papanastassiou and Brigham, 1989) was 8 ± 2‰ amu^{-1}, consistent with the value measured for the bulk inclusion (10 ± 2‰ amu^{-1}).

Large UN effects were observed for Ca, Ti and Cr isotopes in a bulk sample of HB1, as well as for Cr within the opaque assemblage OA4 excavated from HB1. The UN effects for Cr were consistent for the interior of HB1 and the opaque assemblage (Section 5.6.6; Papanastassiou and Brigham, 1989).

Table 5.1. Mg, Si, Cr and Fe fractionation in HB1

Phase[a]		F_{Mg}[b]	F_{Si}	F_{Cr}	F_{Fe}
Sp 1	SC	20.0±1.7	-	-	-
Sp 6	I	22.8±1.8	-	-	-
Sp 12	I	23.8±1.4	-	-	-
Sp 15	SC	19.9±1.5	-	-	-
Sp 16	I	-	20±16	-	-
Sp 18	I	17.8±1.9	-	-	-
Sp 23	I	21.3±1.4	-	9.1±4.7	-0.7±1.1
Sp 24	I	-	-	-	-2.1±1.3
Mel 2	I	-	10.7±2.3	-	-
Hib 1	M	25.5±1.8	-	-	-
Gr 1	M	15.9±2.1	1.8±2.1	-	-
And 2	R	2.5±1.6	-	-	-
Fass 3	R	0.1±1.3	-	-	-
OA1					
Diop	I	4.0±2.2	-	-	-
Ni_2Fe	I	8.1±5.6	-	-	-2.3±1.7
Pent	I	-	-	-	-0.8±1.6
OA2					
Ni_3Fe	I	-	-	-	8.1±2.3
OA3					
Ni_2Fe	I	21.8±3.8	-	-	8.1±2.6
Ni_2Fe	I	-	-	-	9.0±3.3
Pent	I	-	-	-	6.1±3.2
OA4[c]		-	-	8±2	-

[a] Sp = spinel, Mel = melilite, Hib = hibonite, Gr = grossular, And = andradite, Fass = fassaite, OA = opaque assemblage, Diop = diopside, Pent = pentlandite. Location of grain in inclusion: I = interior, SC = spinel cluster, M = mantle, R = rim.

[b] Mass-dependent isotopic fractionation factor from $^{25}Mg/^{24}Mg$, relative to 0.12663 (°/‰ amu^{-1}). Errors are 2σ.

[c] F_{Cr} analysis for OA4 is a thermal ionization result for an excavated grain (4).

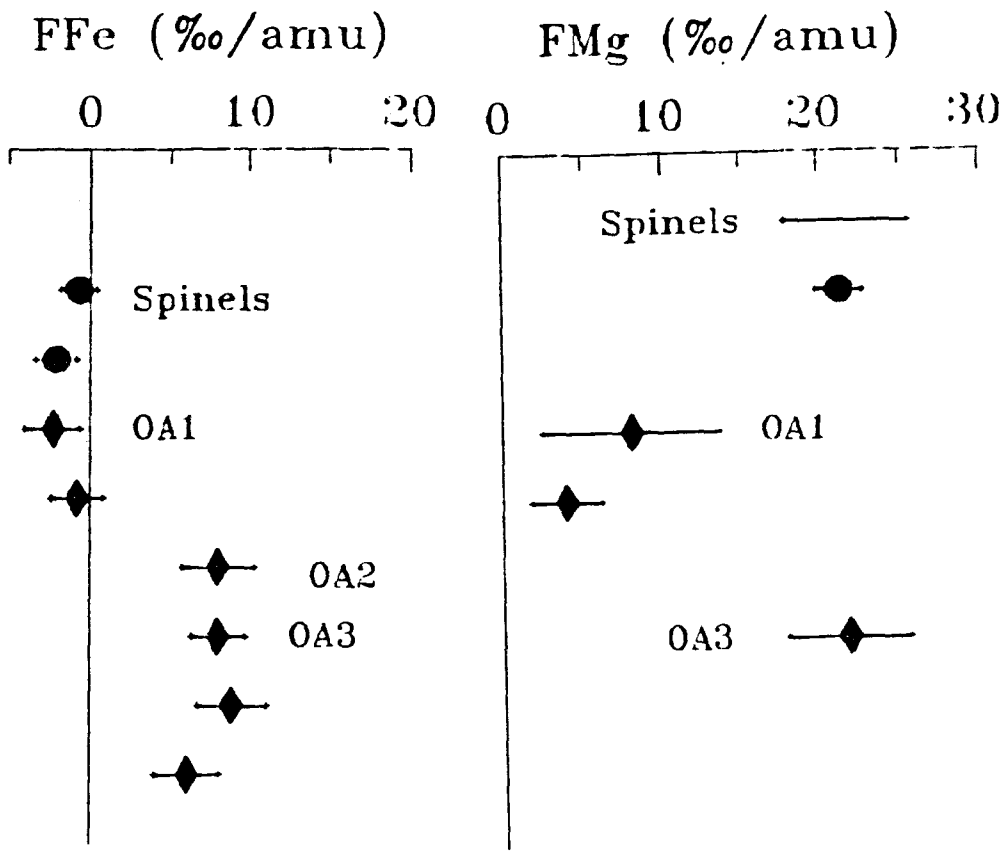

Figure 5.3. Mg and Fe isotopic fractionation (in permil per mass unit), for opaque assemblages and adjacent spinel grains in the FUN inclusion HB1. The phases analyzed within each OA are listed in Table 5.1. The total range in F_{Mg} for spinel analyses from Chapter 4 is shown for comparison.

5.4. DISCUSSION

5.4.1. ISOTOPIC FRACTIONATION

The isotopic data indicate large, positive fractionation for Mg and Cr in spinels in HB1, but no fractionation for Fe in spinel. Melilite in HB1 exhibits large Si fractionation. Opaque assemblages in HB1 exhibit large isotopic fractionation for both Mg and Fe. The measured isotopic fractionations for each element, normalized by the inverse square root of the mass of the relevant gas phase species, are remarkably similar (refer to Section 4.6.2).

The first question to be addressed is whether the isotopic compositions for opaque assemblages are consistent with formation within the CAI. Mg fractionation for OA3 is identical to that observed for spinels in the CAI, indicating formation from a single reservoir. In a like fashion, identical Cr isotopic compositions are observed for the bulk inclusion and for the opaque assemblage, consistent with formation from an isotopically uniform reservoir, followed by partitioning of Cr between the metal, silicate and spinel phases. These are the first isotopic data to confirm the formation of OA within CAI.

The Fe fractionation observed for the OA is distinct from the other phases in the CAI, which are unfractionated. This difference may be considered in terms of later chemical and isotopic exchange, since Fe is more volatile.

Therefore, the isotopic data for HB1 are consistent with a common origin for the OA and the CAI phases. However, an isolated isotopic measurements obtained by Zinner et al. (1989) is at odds with this common origin. Mg isotopes were measured for periclase in an opaque assemblage from a CAI (in the Vigarano meteorite), as well as for adjacent spinel and melilite. A 10‰ amu^{-1} difference in F_{Mg} was reported between the OA and adjacent spinel, such that the OA is isotopically light, and spinel is isotopically heavy. This case is difficult to reconcile with a common igneous origin for the CAI and OA, and is not understood.

5.4.2. ISOTOPIC HETEROGENEITY

The second question to be addressed is the source of isotopic heterogeneity within the CAI and opaque assemblages. The magnitudes of fractionation for Mg and Fe vary between phases in HB1.

As discussed above, the most extreme values of Mg fractionation observed for the OA and spinels in the CAI, are identical, and uniform within a few permil throughout the inclusion. The fact that some opaque assemblages (OA1) exhibit smaller Mg fractionation values, suggests that preferential exchange of Mg has occurred, with the incorporation of normal Mg. In particular, diopside in OA1 may be secondary, having formed with the majority of its Mg coming from an isotopically normal gas phase.

Variable Fe fractionation was observed in HB1: assemblages OA3 and OA2 exhibit fractionated Fe, while OA1 and spinels contain isotopically normal Fe.

These differences require differential exchange with normal Fe, assuming that the entire inclusion was initially fractionated. The source of fractionated Fe is unclear, since distillation models postulate the early and complete loss of Fe (see Section 4.6.3). Spinels may have been originally quite Mg-rich, then acquired their Fe content through Fe-Mg exchange with an isotopically normal gas phase. However, the fact that extremely Fe-rich spinels are observed adjacent to the assemblage OA3 (which contains fractionated Fe), requires that some spinels acquired some Fe content from the opaque assemblages; this Fe may then have exchanged with normal Fe. In addition, the lack of correlation between F_{Mg} and FeO in spinel, requires that the addition of Mg and Fe to the CAI are decoupled.

5.4.3. MODELS FOR FORMATION OF OPAQUE ASSEMBLAGES

The petrographic and isotopic data presented in this chapter can be used to constrain models for the origin of opaque assemblages in inclusion HB1. The following model, consistent with the isotopic data, postulates formation from a reservoir which was originally homogeneous, followed by later isotopic reequilibration.

The initial stage involves formation from a homogeneous reservoir, enriched in the heavier isotopes of Mg, Si, Cr and Fe, and containing UN effects for Mg, Ca, Ti and Cr (Papanastassiou and Brigham, 1989). Melting of silicates led to the segregation of proto-OA metal alloys as immiscible liquids, following the model of Blum et al. (1988b). Hibonite, spinel and melilite crystallized from the melt with a

fractionated, but homogeneous isotopic composition.

The present opaque assemblages formed by sulfidization and oxidation at lower temperatures. Spinels near OA3 became enriched in FeO, as Fe was lost from the assemblage (i.e., in converting metal to magnetite and pentlandite).

Isotopic heterogeneity within HB1 resulted from incomplete exchange of individual phases with an isotopically normal nebular gas. Since F_{Mg} in spinels is not correlated with FeO, at least two episodes are required: spinel (containing fractionated Mg, Cr and Fe) reacted with isotopically normal Mg in the gas to varying degrees, producing a range in F_{Mg}. Subsequently, Fe-Mg exchange in spinel occurred during reaction with an Fe- and volatile-rich, Mg-Cr-depleted gas. Some assemblages (e.g., OA1), and most spinel reacted extensively with the gas, producing $F_{Fe} \approx 0$; F_{Mg} in spinel was not affected.

Other opaque assemblages (e.g., OA2 and OA3) reacted minimally with this Fe-rich gas, preserving the original Fe fractionation. The small assemblage OA2 may have retained fractionated Fe due to the resistance of Ni_3Fe to chemical and isotopic exchange.

The growth of Na-rich secondary phases (feldspathoid) in HB1 also occurred by reaction with this volatile-rich gas.

In conclusion, the isotopic data support formation of opaque assemblages by alteration of CAI, although substantial isotopic exchange and reequilibration occurred subsequent to OA formation.

Figure 6.1. Optical photograph of fine-grained inclusion BG82EA-1 (10x5 mm). The inclusion has deformed around an adjacent chondrule in the matrix, and appears to have incorporated matrix material into the inclusion (darker gray regions).

CHAPTER SIX

Mg ISOTOPIC HETEROGENEITY IN FINE-GRAINED Ca-Al-RICH INCLUSIONS

6.1. INTRODUCTION

The mechanisms of formation and the relationships between coarse and fine-grained Ca-Al-rich inclusions are not well understood. Among the interesting features of fine-grained inclusions, is their enrichment in volatile elements, which can provide information on low-temperature nebular and planetary alteration processes.

Fine-grained CAI constitute approximately 9 volume percent of the Allende meteorite (Clarke et al., 1970). The inclusions are white or pink (Figure 6.1), irregularly shaped, porous collections of refractory phases (spinel, fassaite, hibonite and anorthite), coupled with phases rich in iron, alkalis and halogens (hedenbergite, nepheline and sodalite). Melilite, a major phase in coarse-grained inclusions, is rare or absent in fine-grained CAI.

One key to the relation between fine and coarse-grained CAI comes from observations of coarse-grained inclusions surrounded by sequences of thin rims

containing lower temperature phases similar to those observed in fine-grained CAI: Fe-bearing spinel, perovskite, feldspathoids and hedenbergite (Wark and Lovering, 1977; MacPherson et al., 1981).

Several mechanisms have been proposed to explain the origin of fine-grained CAI. These include formation as: 1) aggregates of condensates from the solar nebula (Grossman and Ganapathy, 1976); 2) coarse-grained inclusions that have been completely altered (MacPherson et al., 1981; Wark, 1981); 3) aggregates of the rim material (late stage condensates or reaction products) that surrounds coarse-grained inclusions (Wark and Lovering, 1977); or 4) interstellar dust aggregates that were partially melted, distilled, and separated from Ca-Si-rich melts to form fine-grained inclusions (Kornacki and Wood, 1984, 1985). In this work I address the formation of fine-grained inclusions in Allende, and their possible relation to coarse-grained inclusions, by a detailed investigation of the mineralogy, chemical composition, Mg isotopic fractionation, and ^{26}Al-^{26}Mg systematics of fine-grained CAI.

Refractory inclusions exhibit mass-dependent isotope fractionation profiles in O, Mg, Si, and Ca, which have been interpreted as kinetic isotopic effects due to condensation, vaporization and recondensation (Niederer and Papanastassiou, 1984; Clayton et al., 1985). Such processes also appear to extend to normal chondrules for oxygen and silicon (Clayton et al., 1985). Mass-dependent isotope fractionation can be used to identify formation processes that produce mass fractionation and to identify contributions from isotopically distinct reservoirs.

Mg fractionation has been found to follow distinctly different patterns in the two types of CAI. Coarse-grained inclusions exhibit an enrichment in the heavier isotopes, while fine-grained CAI are enriched in the lighter isotopes. Isotopic fractionation of Mg is generally uniform throughout the interior of most coarse-grained inclusions (Wasserburg et al., 1977; Esat et al., 1978). The PSI inclusions discussed in Chapter 4 are an exception. Fractionation effects appear to be variable within single fine-grained inclusions (Esat et al., 1984; Brigham et al., 1984, 1985).

Variations in isotope fractionation between grains within individual inclusions can be used to indicate: 1) intrinsic heterogeneity involving preservation of variable kinetic isotope effects during formation; 2) intrinsic heterogeneity involving formation of inclusions as aggregates of unrelated grains from distinct reservoirs; or 3) later alteration involving addition of variable amounts of normal Mg to inclusions which were initially homogeneous.

I have surveyed seventeen fine-grained inclusions in Allende in order to study their petrology and Mg isotopic composition. Mineralogical and chemical compositions were obtained using a scanning electron microscope with energy dispersive analysis. Isotopic data were obtained by thermal ionization mass spectrometry on acid soluble and insoluble fractions of these inclusions, while the ion microprobe was used to determine the isotopic compositions of individual grains in polished sections of inclusions.

Specifically, I have tried to establish: 1) possible correlations of Mg isotopic compositions of grains with mineralogy and chemistry; 2) the degree of

heterogeneity of fractionation within a single inclusion; 3) the amount of secondary chemical alteration and isotopic reequilibration; and 4) if there is evidence in fine-grained inclusions for the in situ decay of ^{26}Al. Preliminary reports on the mineralogy, chemistry and Mg isotopic composition of fine-grained inclusions have been presented by Brigham et al. (1985, 1986) and are here combined in a full presentation.

6.2. SUMMARY OF PREVIOUS WORK

6.2.1. PETROGRAPHY AND CLASSIFICATION

The first detailed study of a single fine-grained CAI (Grossman, 1972), characterized by loosely-packed euhedral crystals of grossular, melilite and feldspathoid projecting into cavities, attributed the texture to formation by vapor phase condensation without subsequent melting. Armstrong and Wasserburg (1981) described a porous aggregate called the Pink Angel, and proposed formation from a mixture of spinel and devitrified glass, altered by a halogen and alkali-rich gas, most likely on a planetary body. MacPherson and Grossman (1982) studied spinel-rich inclusions, porous aggregates of spinel, perovskite, nepheline, diopside, anorthite and grossular. They propose that the inclusions formed as aggregates of grains that formed independently, and were altered after aggregation, but before emplacement in a parent body.

Kornacki and Wood (1984) identify three structural components that appear to be characteristic of many fine-grained inclusions: 1) a porous interior of olivine, nepheline, sodalite and pyroxene; 2) intergrowths of grossular, Al-clinopyroxene, hedenbergite, andradite, Ti-pyroxene, anorthite and feldspathoid; and 3) spinel and perovskite-rich regions with igneous textures. Similar textures were reported by Cohen et al. (1983) and Fegley and Post (1985). Kornacki (1981) suggests that the porous texture of inclusions may result from devitrification. Kornacki and Wood (1984, 1985) argue that fine-grained inclusions formed by drag-heating of interstellar dust aggregates, leading to distillation, partial melting, and igneous separation.

Hashimoto and Grossman (1985) identified three mineralogic zones typical of fine-grained inclusions: 1) an innermost zone of loosely-packed spinel, clinopyroxene, nepheline, sodalite, grossular and anorthite; 2) a middle zone rich in hedenbergite and andradite; and 3) an outer zone of nepheline, sodalite, clinopyroxene, salite, olivine and spinel, with minerals frequently intergrown. They attribute zonation to secondary alteration, in which Ca was removed, while Na, Fe, Si and Cl were added. Spinel, hibonite, and perovskite are residual primary phases. Further petrographic and chemical analyses of zonation in fine-grained CAI were reported by McGuire and Hashimoto (1988).

Fine-grained inclusions have been subjected to various classification schemes. An early scheme by Grossman et al. (1976), proposed two types based on mineralogy and texture: fine-grained CAI, and amoeboid olivine aggregates (AOA). Wark (1979) expanded upon this scheme by proposing three basic types: fine-grained alkali-rich spinel aggregates (F); olivine aggregates (AO); and alkali-olivine

aggregates (FAO), intermediate between the two other types. Kornacki and Wood (1984) developed a five-group classification scheme based on morphology, mineralogy and texture. Types 1 and 5 are olivine-rich aggregates corresponding to the AOA; Type 2 are olivine-rich, corresponding to the FAO; Type 3 are olivine-poor, similar to Type F; and Type 4 are igneous inclusions.

6.2.2. CHEMICAL AND ISOTOPIC COMPOSITIONS

a. Chemistry

Both fine and coarse-grained inclusions are substantially enriched in the refractory lithophile elements, such as Al, Ca and Ti, relative to the chondritic values. Fine-grained CAI exhibit highly fractionated abundances of refractory lithophile elements, while most coarse-grained CAI exhibit uniform enrichments (Grossman and Ganapathy, 1976). Fine-grained CAI differ from coarse-grained CAI in their depletion in siderophile elements such as Co and Au (Grossman and Ganapathy, 1976).

Rare earth element (REE) patterns are distinct for fine and coarse-grained inclusions, as described in the classification scheme of Mason and Martin (1977). Fine-grained inclusions generally exhibit fractionated Type II REE patterns, with enrichments of 20 to 30x chondritic values for the lighter and more volatile REE, depletions in the heavier REE, negative Eu and Ce anomalies, and positive Tm and Yb anomalies. Boynton (1975) attributed this pattern to a two-stage fractional condensation process, with the removal of early perovskite condensates enriched in

the most refractory REE. The fractionated patterns result from condensation from a gas of nonsolar composition. The inclusions were then isolated before the complete condensation of all lanthanides, causing anomalies in Yb, Eu and Ce.

Grossman and Ganapathy (1976) emphasize that REE patterns vary widely between individual CAI, due to incorporation of differing amounts of REE-bearing phases. REE patterns also vary within inclusions. Analyses of the REE composition of the interior and rim of a single fine-grained inclusion (Ekambara et al., 1975) showed an enrichment of the flat REE component in the rim relative to the interior, suggesting addition of this (flat REE) component during open-stage alteration.

Fine-grained CAI are rich in feldspathoids and in volatile elements such as Na, Mn, Cl and Fe (Grossman and Ganapathy, 1975). Grossman (1972) suggested that volatile-rich phases may form by leaching of volatile elements from the surrounding meteorite matrix; however, later studies showed that matrix contamination was unlikely, due to the lack of correlation of Na and Fe in CAI. Grossman and Ganapathy (1976) proposed that some volatiles were added during planetary metamorphism, while fine-grained inclusions acquired the bulk of their volatile content during nonequilibrium condensation, of volatiles along with refractory elements remaining after the condensation of coarse-grained CAI.

b. Isotopes

Correlations of ^{129}Xe with the alkali content of inclusions (Fireman et al., 1970) indicate that the short-lived nuclide was incorporated with alkalis and halogens to

form feldspathoids soon after nucleosynthesis of ^{129}Xe. Gray et al. (1973) concluded that the introduction of alkalis must have occurred during condensation 4.5 AE ago; however, the lack of Rb-Sr isochrons for most phases indicates that the system was isotopically disturbed during planetary metamorphism 3.6 AE ago.

Fine-grained inclusions analyzed by Clayton et al. (1977) exhibit oxygen isotopic compositions which are intermediate to the range exhibited by coarse-grained inclusions. Fine-grained CAI exhibit $\delta^{18}O$ values of -15‰, which are variable within inclusions. Coarse-grained CAI exhibit $\delta^{18}O$ values of -18‰ for melilite-spinel rich (Type A) inclusions, and values ranging from -15‰ to -30‰ for fassaite-spinel rich (Type B) inclusions.

6.3. PETROGRAPHIC DESCRIPTIONS

6.3.1. SUMMARY OF OBSERVATIONS

The seventeen inclusions examined in this work are pink to white, irregularly shaped, fine-grained objects, that typically exhibit a white rim. The seven inclusions examined in thin section are similar to each other in mineralogy. Modal abundances of minerals are given in Table 6.1. The inclusions are collections of loosely-packed, micron-size grains, with the major phases being Fe-rich spinel, fassaite and anorthite, coupled with coarser-grained (5-40 μm) hedenbergite, nepheline and sodalite. The inclusions contain larger regions (10-80 μm) in which several minerals are intergrown. One inclusion (BG82D-I) is unusual in the absence

Table 6.1. Minerals in Allende Fine-grained Inclusions (modal abundances in percent)

	A47-2	A1C1-E	BG82I-F	BG82C-M	BG82EA-1	BG82D-I	B14-B
Spinel	30	57	19	56	14	15	26
Nepheline	20	14	37	5	21	35	9
Sodalite	2	1	tr	21	tr	28	10
Fassaite	36	10	32	11	47		19
Hibonite	-	-	tr	-	tr	19	-
Olivine	-	-	2	-	12	-	5
Anorthite	8	14	-	3	tr	tr	2
Hedenbergite	tr	tr	3	tr	7	1	14
Grossular	4	tr	6	3	tr	1	15
Wollastonite	tr	-	-	-	tr	-	tr
Andradite	-	tr	-	-	tr	-	tr
Ilmenite	-	tr	-	-	-	1	-
Al-diopside	-	-	-	tr	-	-	-
Perovskite	-	-	-	-	-	-	tr

Table 6.2. Bulk Chemical Compositions of Allende Fine-grained Inclusions (wt%)

Inclusion	A47-2	ALC1-E	BG82I-F	BG82C-M	BG82EA-1	BG82D-I	B14-B
Na_2O	5.7	2.0	6.7	6.5	5.8	15.0	5.4
MgO	9.3	15.6	8.8	15.1	12.5	0.5	8.9
Al_2O_3	34.4	44.4	33.0	46.0	25.1	43.5	30.4
SiO_2	33.6	22.6	33.1	20.8	35.4	30.3	31.8
Cl	0.2	0.1	0.1	1.4	0.2	2.2	0.8
K_2O	0.3	<0.1	0.6	<0.1	0.5	0.6	0.2
CaO	10.9	7.2	10.2	4.6	9.1	3.2	13.2
TiO_2	0.8	0.7	0.8	0.4	0.8	0.5	0.3
V_2O_3	<0.1	<0.1	<0.1	<0.1	<0.1	0.1	<0.1
Cr_2O_3	0.2	0.5	<0.1	0.4	0.2	0.1	0.2
FeO	4.5	6.9	6.1	4.1	10.3	3.5	8.5

of fassaite, and in the abundance of hibonite. Olivine is present in three of the seven inclusions.

Petrographic descriptions are based on backscattered electron imaging of thin sections of inclusions. For inclusions B-14B and BG82EA-1, a thin section was prepared from only a chip excavated from the inclusion.

The inclusions described here do not fit easily into the mineralogical classification scheme proposed by Kornacki and Wood (1984). This difference may be due to the fact that their classification scheme is biased toward small inclusions ($\leq$ 0.5 mm), while this study addresses large, cm-sized inclusions. These inclusions are similar to Wark's fine-grained alkali-rich spinel aggregates (Type F), in that the dominant phase is spinel; however, these inclusions are nearly devoid of perovskite.

6.3.2. INDIVIDUAL INCLUSIONS

AlC1-E (14x4 mm) is a distinctly pink, porous mass of fine-grained minerals. This inclusion could be seen on two opposing slabs. On one slab, the inclusion is completely surrounded by a 1 mm thick, white mantle of coarser-grained minerals, which composes almost 60% by area of the total inclusion (see colored photograph in Figure 1.1a). On the opposing slab, a broken surface of the inclusion is visible where part of the thick, white mantle is missing or is disconnected from the inclusion. A thin white rim layer can be found on this broken surface.

The interior consists predominantly of loosely-packed 1 to 5 μm anhedral crystals of Fe-rich spinel (7 to 11% FeO), fassaite and anorthite (Figure 6.2a). Anorthite is

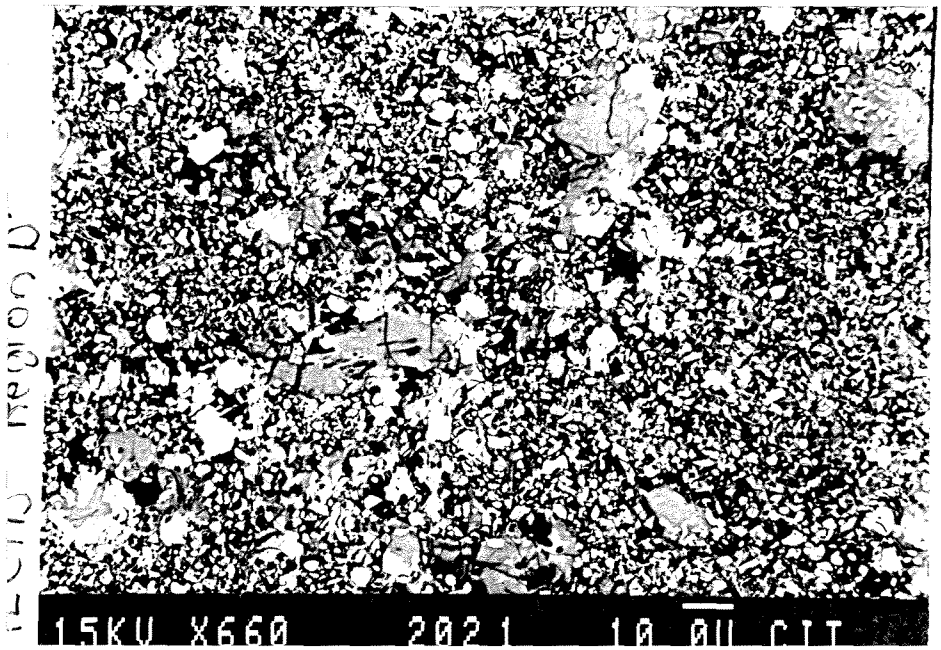

Figure. 6.2a. BEI of interior of ALC1-E, with micron-sized spinel, fassaite and anorthite. Nepheline grains (10 to 20 μm) are intergrown with spinel and fassaite.

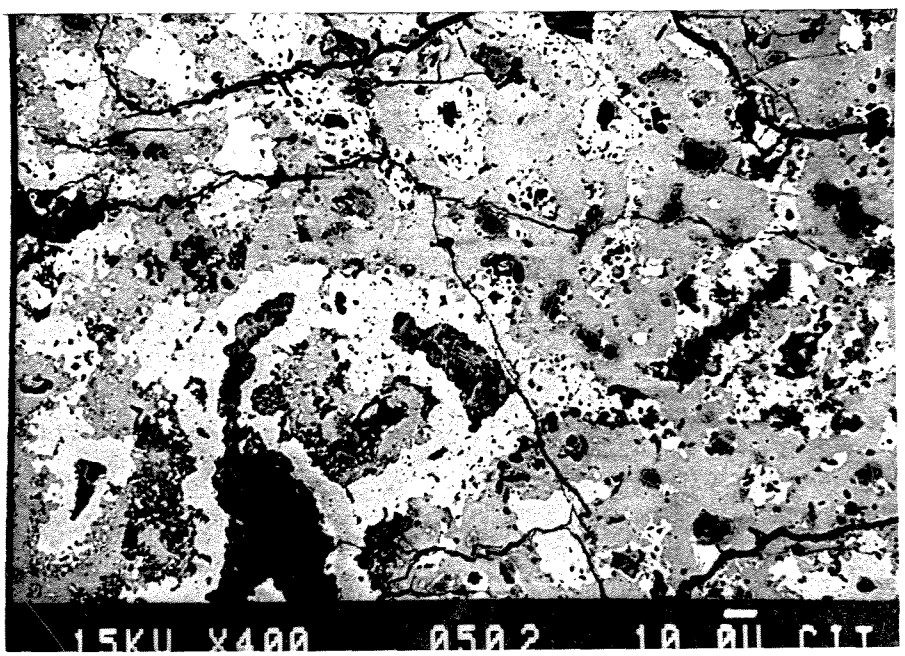

Figure 6.2b. BEI of rim of AlC1-E. Anorthite and diopside are intergrown in a eutectic-like texture. Note abundant voids.

unusually abundant in this inclusion. Nepheline and sodalite are distinctly coarser-grained (10 to 40 μm) and are often intergrown with spinel, anorthite or fassaite (Figure 6.2a). Minor amounts of andradite and ilmenite are present. Larger (10 to 30 μm) regions of intergrown hedenbergite-fassaite-spinel are observed throughout the fine-grained interior. Fassaite often surrounds hedenbergite in these assemblages.

The compact, white mantle is of varying thickness (0.2 to 1.2 mm), and consists of three layers. A thin, inner layer (≈100 μm) contains abundant hedenbergite-grossular intergrowths. The next layer, which comprises the bulk of the mantle, consists of compact intergrowths of anorthite and diopside with minor sodalite (Figure 6.2b). This layer is completely unlike the interior in mineralogy, chemical composition, degree of porosity, and color. The texture of the anorthite-diopside layer suggests crystallization from a melt. There is a thin outer layer (≈100 μm) of olivine.

BG82D-I is an elongated, teardrop-shaped inclusion (16x6 mm) consisting of a fine-grained, pink interior containing mm-sized, coarser grained, white islands. The islands comprise approximately 10% by area of the inclusion (Figure 6.3a). A thin white rim surrounds the entire inclusion.

This inclusion is unusual in the high hibonite content and lack of fassaite. The interior consists predominantly of nepheline and sodalite enclosing Fe-spinel (≈ 30% FeO) and hibonite laths (Figure 6.3b), with traces of ilmenite. Fe-spinel grains range up to 30 μm in size, and exhibit a corroded appearance. Fe-spinel is

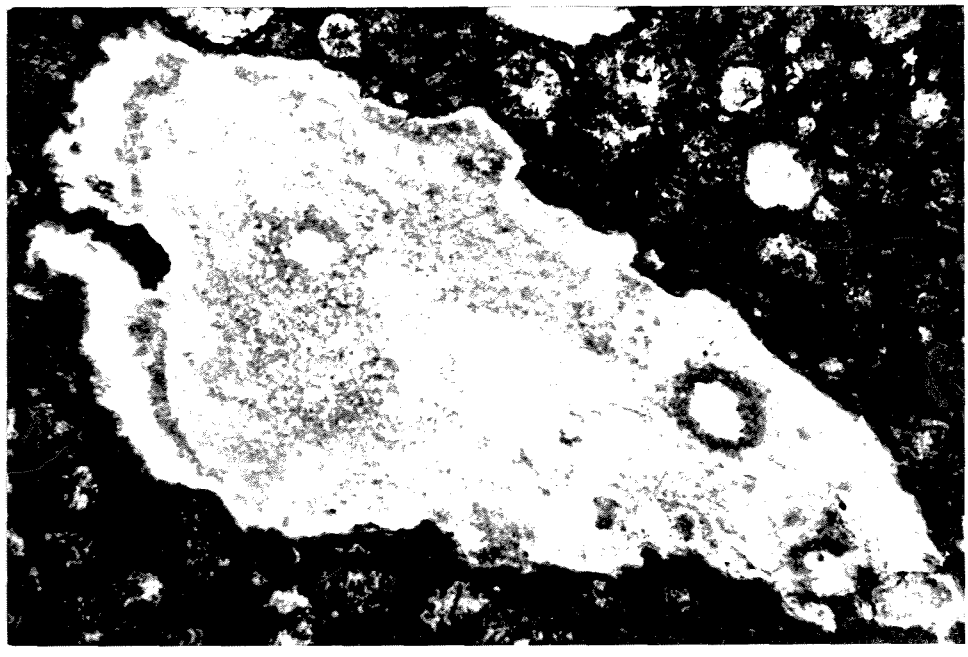

Figure. 6.3a. Fine-grained inclusion BG82D-I (16x6 mm). The spinel, hibonite and feldspathoid-rich interior is surrounded by a white rim. Millimeter-sized islands are mantled by darker rims rich in hercynite.

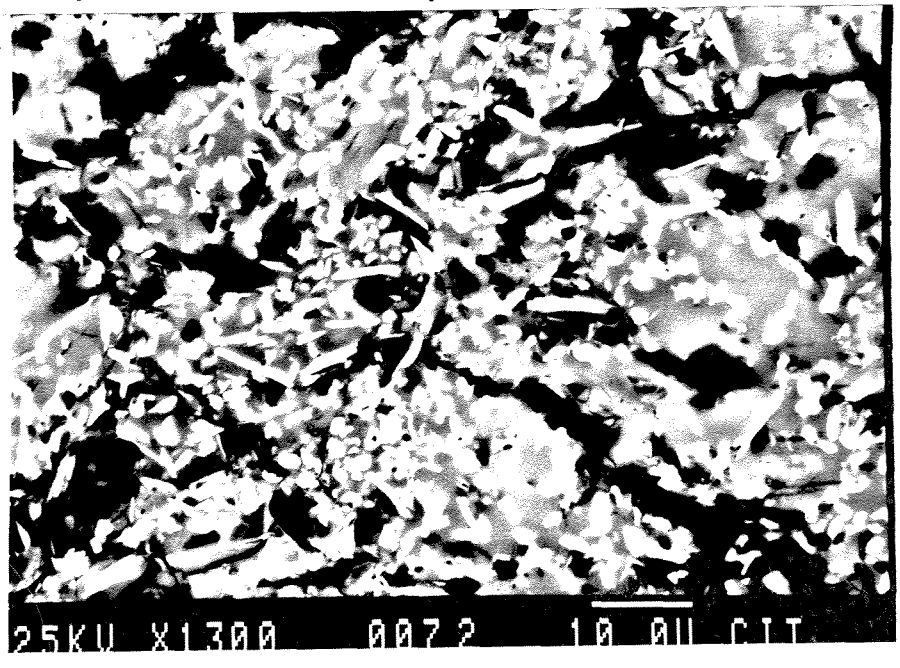

Figure. 6.3b. BEI of Inclusion BG82D-I. Abundant hibonite laths (1-10 μm) are embedded in nepheline. Note abundant void space.

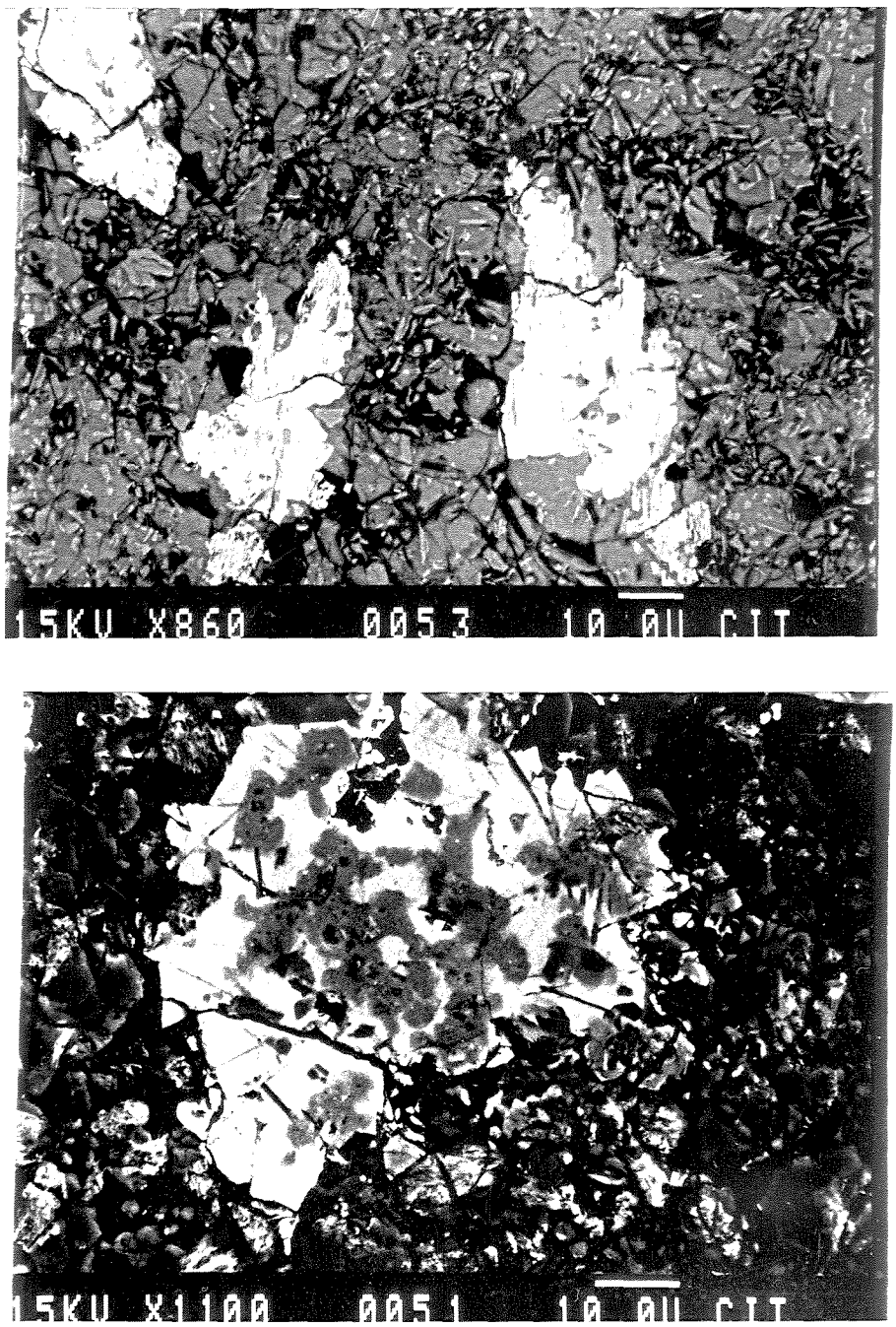

Figure 6.4. Backscattered electron images of BG82D-I. a) Corroded hercynite grains appear to be pseudomorphously replaced by nepheline. These grains are surrounded by μm-sized laths of hibonite and anhedral grains of nepheline. b) Hedenbergite and grossular are intergrown on a micron level.

intergrown with sodalite or nepheline on a micron to submicron scale (Figure 6.4a). Distributed throughout this fine-grained interior are larger (≤70 μm) intergrowths of hedenbergite and grossular (Figure 6.4b). The rim of the inclusion is rich in hedenbergite, hibonite and nepheline.

The islands consist predominantly of grossular, hedenbergite, nepheline and sodalite, with small quantities of Fe-spinel, anorthite. The islands are rimmed by regions rich in fine-grained spinel and nepheline. The islands differ from the interior of the inclusion primarily in the abundance of grossular and hedenbergite and in grain size; the islands are slightly coarser-grained.

A47-2 (11x5 mm) consists of a pink interior surrounded by a thin (≈ 0.5 mm), lighter-colored rim. The interior is a porous mass of anhedral crystals (1 to 5 μm) of Fe-rich spinel (11 to 13% FeO), nepheline, and fassaite, scattered between larger (10 to 50 μm) mineral intergrowths composed predominantly of hedenbergite, fassaite and sodalite.

Fassaite is often intergrown with, or surrounds grains of hedenbergite and/or Fe-rich spinel. Complex aggregates of intergrown fassaite, spinel and anorthite are observed (Figure 6.5a). Laths of anorthite are rimmed by grossular, suggesting that grossular formed after or by alteration of anorthite (Figure 6.5b). Sodalite is often intergrown with fassaite, spinel or nepheline. A47-2 contains a mm-sized island consisting of forsteritic olivine, Fe-Ni metal, nepheline, spinel and fassaite.

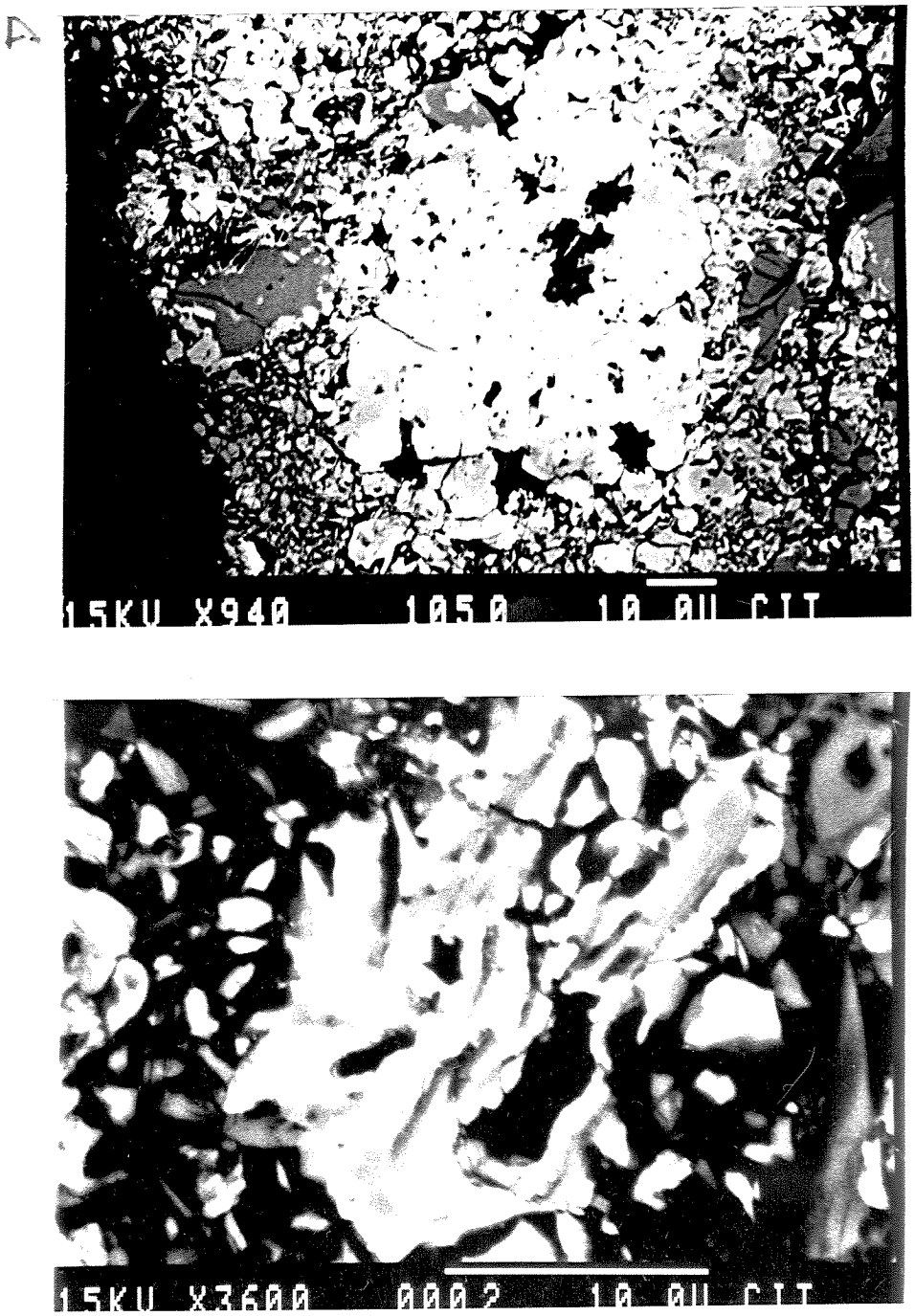

Figure 6.5. Backscattered electron images of Inclusion A47-2. a) Fassaite, spinel and anorthite are intergrown on a micron to submicron level. b) Laths of anorthite are completely rimmed by grossular.

The surrounding rim is 500 μm thick, with a two-layer sequence. The inner layer (≈250 μm) is coarse-grained and contains abundant hedenbergite grains. The outer layer (≈100 μm) consists of 10 to 20 μm anhedral nepheline grains mantling μm-size olivine grains, set in a ground mass of μm-size anhedral forsteritic olivine. Traces of Fe-Ni metal are present. This nepheline-olivine layer is similar in composition to the matrix material, but is texturally distinct.

BG82I-F is a dumbbell-shaped, pink inclusion (4x8 mm). No rim was observed. The interior is a porous mass of 1 to 10 μm anhedral crystals of Fe-rich spinel, nepheline, and fassaite with minor amounts of hedenbergite and olivine. Nepheline is typically coarser-grained (≥10 μm). Traces of sodalite, grossular and hibonite occur. Complex aggregates (≤50 μm) of intergrown spinel, fassaite, hedenbergite and nepheline are common. Fassaite frequently rims these assemblages. Hibonite occurs as laths surrounded by Fe-rich spinel.

BG82C-M (15x7 mm) consists of a pink, fine-grained interior and a thin, lighter colored rim. The interior consists of loosely-packed, micron-size, anhedral crystals of spinel (4 to 7% FeO), fassaite and anorthite. This fine-grained interior contains intergrowths (10 to 50 μm) of hedenbergite-fassaite-spinel and anorthite-fassaite-spinel-sodalite. The compact rim (≈300 μm) consists predominantly of fassaite with minor anorthite and sodalite.

BG82EA-1 is a pink, wedge-shaped inclusion (10x5 mm). One edge exhibits a hemispheric depression where the inclusion has deformed around an adjacent chondrule in the matrix, suggesting deformation of the inclusion during incorporation into the meteorite matrix (Figure 6.1). The interior contains numerous gray patches that appear to be included matrix material. No rim was observed.

The interior consists predominantly of 1 to 10 μm grains of Fe-rich spinel (18 to 20% FeO), fassaite and nepheline. Nepheline occurs as laths or irregular grains. Fe-rich spinel occurs as both anhedral crystals and grains with a corroded morphology. Hibonite occurs in trace amounts surrounded by spinel crystals. The fragment examined exhibits a zoned structure. Zones containing abundant 10 to 20 μm hedenbergite grains, surround zones containing abundant forsteritic olivine laths and hedenbergite-fassaite intergrowths. Olivine is unusually abundant in this inclusion.

B14-B is an elongated, pink inclusion (12x3 mm) containing several gray regions that may be included matrix material. The interior consists predominantly of 1 to 10 μm anhedral grains of Fe-rich spinel (≈13% FeO), fassaite, grossular and nepheline. Laths of forsteritic olivine are abundant. Hedenbergite occurs as coarser-grained regions (≤80 μm) intergrown with spinel and fassaite. Hedenbergite and grossular are unusually abundant in this inclusion. Large (10 to 20 μm) crystals of sodalite are intergrown with spinel or fassaite. There are rare occurrences of wollastonite rimmed by hedenbergite, perovskite rimmed by spinel, and traces of andradite.

6.4. MINERAL CHEMISTRY

Spinel

Spinel is one of the most abundant minerals present and it is frequently intergrown with feldspathoids, hibonite, hedenbergite or fassaite on a micron to submicron scale. Spinel in these inclusions exhibits a large range in FeO content (5 to 30% FeO). Kornacki and Wood (1985) also reported a large range in FeO content for spinel in fine-grained inclusions (3 to 20% FeO). The FeO content of spinel within a single inclusion typically varies by a only a few percent; however, spinel grains in one inclusion (BG82D-I) vary in FeO content from 23% to 34%. The Cr content of spinel ranges up to 1% in several of the inclusions and is not correlated with Fe content. Ti contents are generally less than 0.3%, but range up to ≈1% in inclusion BG82EA-1. Trace amounts (≤1.5%) of Na and Si in the spinel analyses probably result from submicron intergrowths with feldspathoids, hibonite or perovskite. Spinel in coarse-grained inclusions typically contains Cr_2O_3, FeO and TiO_2 at the 0.1 to 0.5% level (Grossman, 1975). The Fe and Cr contents of spinel in fine-grained inclusions are considerably higher than those in coarse-grained inclusions.

Pyroxene/Olivine

Fassaitic pyroxene is a major component of most inclusions. Fassaite is often intergrown with hedenbergite or spinel, and frequently surrounds these minerals. Fassaitic pyroxenes contain up to 2.6% $Ti0_2$, and 1.6 to 9.1% FeO, and are

considerably more Fe-rich than fassaite in the fine-grained inclusions analyzed by Kornacki and Wood (1985), which contained 0.2 to 1.6% FeO. In contrast, fassaite in coarse-grained CAI (Gray et al., 1973; Grossman, 1975) exhibits high TiO_2 contents (5 to 17%) and low FeO contents (≤0.3%). Hedenbergite, which is frequently intergrown with fassaite or grossular, consists primarily of the $CaFeSi_2O_6$ component but with trace amounts of MgO and Al_2O_3.

Olivine is present in trace amounts in three inclusions, and is a major constituent in two inclusions (B14-B and BG82EA-1). In inclusion A47-2, olivine is present only in the rim and in islands. The FeO content of olivine ranged up to 26% FeO.

Feldspathoid

Nepheline and sodalite are major components of all inclusions studied, and are the only feldspathoids observed. The relative abundances of nepheline and sodalite vary for different inclusions. Nepheline typically contains 1.8 to 3.3% CaO and up to 0.7% FeO, consistent with the ranges observed by Kornacki and Wood (1985) for fine-grained inclusions. Traces of FeO (0.3 to 2.0%) and CaO (0.1 to 0.4%) occur in sodalite.

Hibonite

Hibonite is present in trace amounts in half of the inclusions; it is a major constituent in one inclusion (BG82D-I), occurring as laths surrounded by feldspathoid or spinel. Hibonite analyses typically show coupled substitution of Ti and Mg, for Al. Hibonite in inclusion BG82D-I contains ≈1% each of TiO_2 and

MgO, which is on the low end of the range of TiO_2 (0.6 to 8.1%), and MgO (0.7 to 4.6%) reported by MacPherson et al. (1983) for hibonite from Murchison (CM2). Na_2O and SiO_2 levels of 0.5 to 1% may be due to contributions from surrounding feldspathoid.

6.5. BULK CHEMICAL COMPOSITIONS

Bulk chemical compositions, estimated from rastered beam EDS analyses, are presented in Table 6.2 for the fine-grained inclusions. The inclusions are enriched in volatile elements such as Na_2O, Cl and FeO. The Na_2O contents are quite high, typically 5 to 7%, however, BG82D-I contains 15% Na_2O. In comparison, Type B2 coarse-grained inclusions typically contain 0.1 to 0.9% Na_2O.

Note also the extremely low Mg0 content of BG82D-I (0.5%), which can be attributed to the high hibonite and feldspathoid abundance. The other fine-grained CAI exhibited MgO contents ranging from 9 to 15%. The bulk composition of BG82C-M is distinct from the other inclusions, with high Al_2O_3 and Cl contents, due to the abundance of sodalite (see modal abundances in Table 6.1).

Trace element data were obtained by INAA (Figure 6.6) for fine-grained inclusions BG82D-I, BG82C-M and B-14B (Palme, personal communication, 1987). The rare earth data indicate a Type II pattern for the inclusions. All inclusions were enriched in Zn (3 to 5x chondritic levels), and in other volatile elements such as Br, Cl and Rb.

Figure 6.6. Instrumental neutron activation data for rare earth elements in fine-grained inclusions: BG82D-I, BG82C-M and B14-B. BG82D-I and B14-B exhibit large isotopic fractionation, BG82C-M is isotopically normal. All inclusions exhibit Type II (fractionated) REE patterns. Errors are typically 4 to 12%; upper limits are indicated by arrows. Plotted values are measured abundances relative to the chondritic (C1) levels.

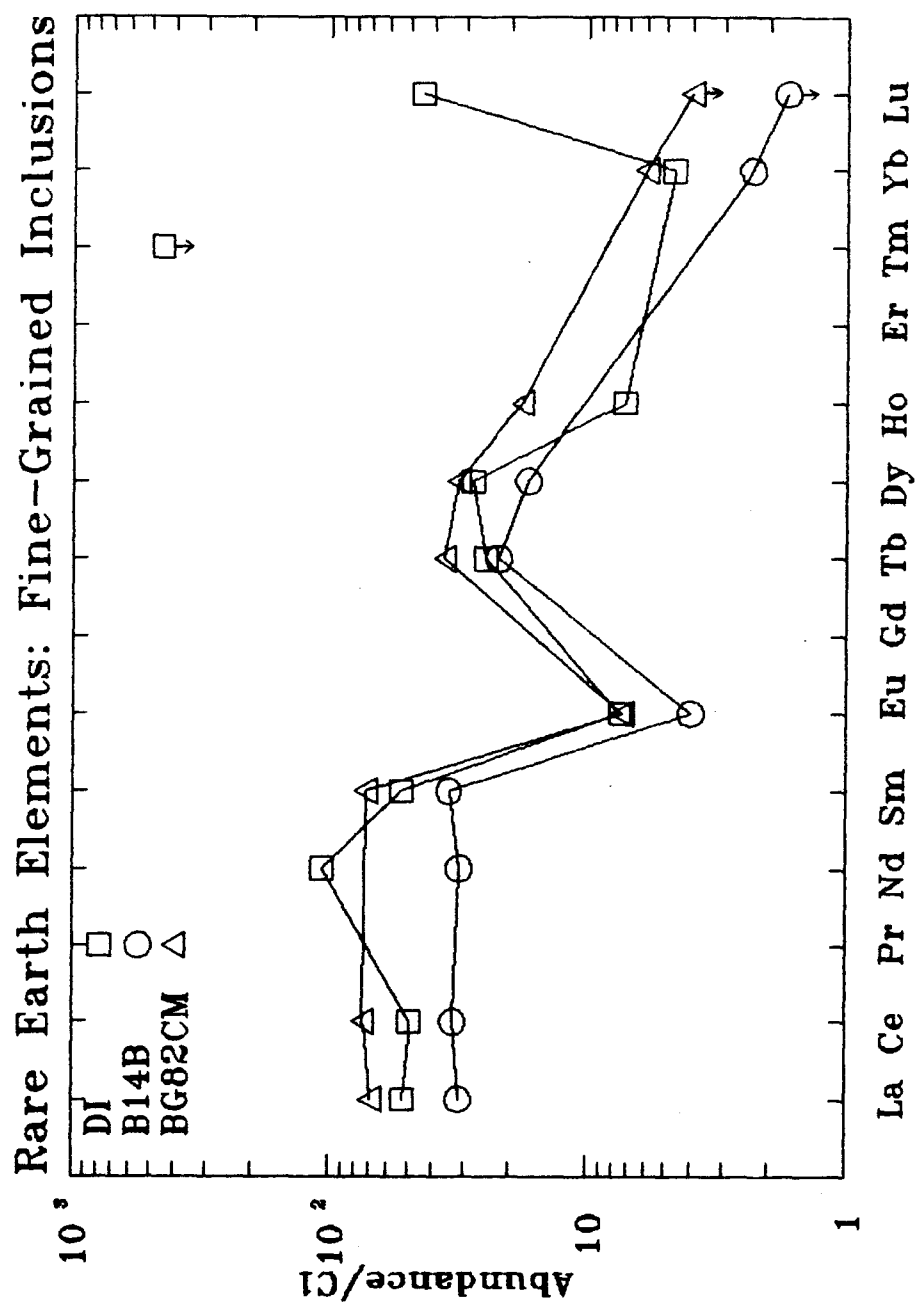
Rare Earth Elements: Fine-Grained Inclusions
DI
B14B
BG82CM
Abundance/CI
10³
10²
10
1
La Ce Pr Nd Sm Eu Gd Tb Dy Ho Er Tm Yb Lu

6.6. ISOTOPIC COMPOSITIONS

6.6.1. THERMAL IONIZATION RESULTS

Isotopic results for F_{Mg} and $\delta^{26}Mg$ of samples from fine-grained inclusions analyzed by thermal ionization mass spectrometry are shown in Table 6.3.

Most of the fine-grained inclusions exhibit small fractionation effects, with F_{Mg} ranging from 0 to -4‰ amu^{-1}. Ten of the seventeen inclusions exhibit F_{Mg} outside the range of normal Mg, that can be attributed to intrinsic shifts in $^{25}Mg/^{24}Mg$. Three inclusions (BG82D-I, BG82EA-1 and B14-B) exhibit large fractionation effects, with F_{Mg} ranging from -5.6 to -14.1‰. The spinel residue of the olivine-rich inclusion B14-B exhibited the largest fractionation (F_{Mg} = -14‰ amu^{-1}).

These fine-grained inclusions exhibit consistently negative F_{Mg}, corresponding to an enrichment in the lighter isotopes of Mg. In contrast, coarse-grained inclusions are enriched in the heavier Mg isotopes with F_{Mg} ranging up to +39‰. (See the histograms in Figure 4.8, which compare F_{Mg} for fine and coarse-grained CAI). There is little overlap observed in F_{Mg} between fine-grained and coarse-grained CAI.

A comparison of F_{Mg} for soluble and insoluble fractions of twelve inclusions (Figure 6.7) reveals resolvable differences in fractionation within six individual inclusions. The residues are commonly isotopically lighter than the soluble fractions by a few permil.

Table 6.3. Thermal ionization determination of Mg isotopic compositions of Allende fine-grained inclusions

Sample[a]		F_{Mg}[b] ‰amu^{-1} (±2σ)	δ(^{26}Mg)[c] ‰ (±2σ$_{mean}$)	DLT[d]
		ALLENDE		
BG82D-I	-s	-8.5±0.8	27.7±0.1	N
BG82D-I	-r	-9.3±1.0	47.2±0.2	Y
BG82D-I	-s	-6.6±1.2	31.6±0.2	N
BG82D-I	-r	-10.6±1.0	56.1±0.2	Y
BG82D-I(is)t		-11.1±1.4	7.3±0.2	Y
BG82D-I	-t	-6.3±3.8	35.2±0.6	Y
B14-B	-s	-12.2±1.2	3.0±0.2	Y
"	-s	-12 ±2	3.1±0.6	Y
B14-B	-r	-14.1±0.6	2.4±0.2	Y
A47-2	-s	-0.2±0.6	1.0±0.1	N
A47-2	-r	-1.5±0.6	0.7±0.1	Y
BG82C-M	-s	-1.8±0.6	1.1±0.2	N
BG82C-M	-r	-3.6±0.6	1.3±0.2	Y
BG82EA-1	-s	-5.6±0.8	1.2±0.1	Y
BG82EA-1	-r	-6.8±1.0	0.9±0.3	Y
B9Z-1	-s	0.5±1.6	1.0±0.2	Y
B9Z-1	-r	1.6±1.8	0.5±0.3	Y
B14	-s	0.0±1.6	0.1±0.3	Y
B14	-r	-4.2±0.4	0.5±0.2	Y
ALC1-E	-s	-1.3±1.0	0.5±0.2	Y
ALC1-E	-r	-2.6±1.4	0.7±0.3	Y
BG82EA-2	-s	-3.3±0.4	0.8±0.1	Y
BG82EA-2	-r	-2.6±1.2	0.8±0.2	Y
B9Z-2	-s	-1.1±1.0	0.3±0.3	Y
B9Z-2	-r	-3.0±0.6	0.0±0.2	Y
BG82I-F	-s	-0.6±2.0	1.4±0.3	Y
BG82I-F	-r	-2.0±0.8	1.4±0.2	Y
A47-1	-t	-1.6±1.2	0.6±0.1	Y
BG82I-C	-t	-2.7±1.0	1.4±0.2	Y
BG82I-I	-t	-3.0±0.4	1.0±0.1	Y
BG82JB-1	-t	-1.7±0.3	1.1±0.1	Y
BG82DI-14	-t	-1.8±0.3	0.8±0.1	Y
BG82CJ-3	-t	0.8±0.4	1.3±0.2	Y
B7F-3	-t	-2.6±0.3	1.2±0.1	

[a] s = acid soluble part of inclusion; r = acid insoluble residue; t = total sample; is = island.

[b] Mass dependent isotope fractionation factor (in permil per atomic mass unit) is determined from the raw measured ^{25}Mg/^{24}Mg ratios, relative to normal Mg. Uncertainties are 2σ of the distribution of sets of 10 ratios each.

Table 6.3 (continued).
Thermal ionization determination of Mg isotopic compositions of Allende fine-grained inclusions

[c] Deviations in the $^{26}Mg/^{24}Mg$ from normal, after correction for mass-dependent fractionation using $^{25}Mg/^{24}Mg$. Uncertainties are $2\sigma_{mean}$.

[d] Samples analyzed by the direct loading technique (DLT) are indicated by Y. Samples analyzed after chemical separation of Mg from the dissolved sample are indicated by N. For analyses by DLT, a bias of +1.5‰ has been added to the reported $\delta^{26}Mg$ due to the presence of $^{27}Al^{+}$ interference (see text).

[e] Solutions of normal Mg (nMgl) were analyzed by the conventional loading technique. Grains of terrestrial spinel and olivine were analyzed by DLT.

Figure 6.7. Mg isotopic fractionation (F_{Mg}) is plotted for acid soluble and insoluble fractions of inclusions analyzed by thermal ionization mass spectrometry. Acid insoluble fractions consisted of spinel or hibonite. F_{Mg} ranged from +2 to -14‰ amu^{-1}, indicating an enrichment in the lighter isotopes. Most inclusions exhibited small differences in fractionation factors between the two fractions; however inclusion BG82D-I exhibited a difference of 4‰ between soluble and insoluble fractions.

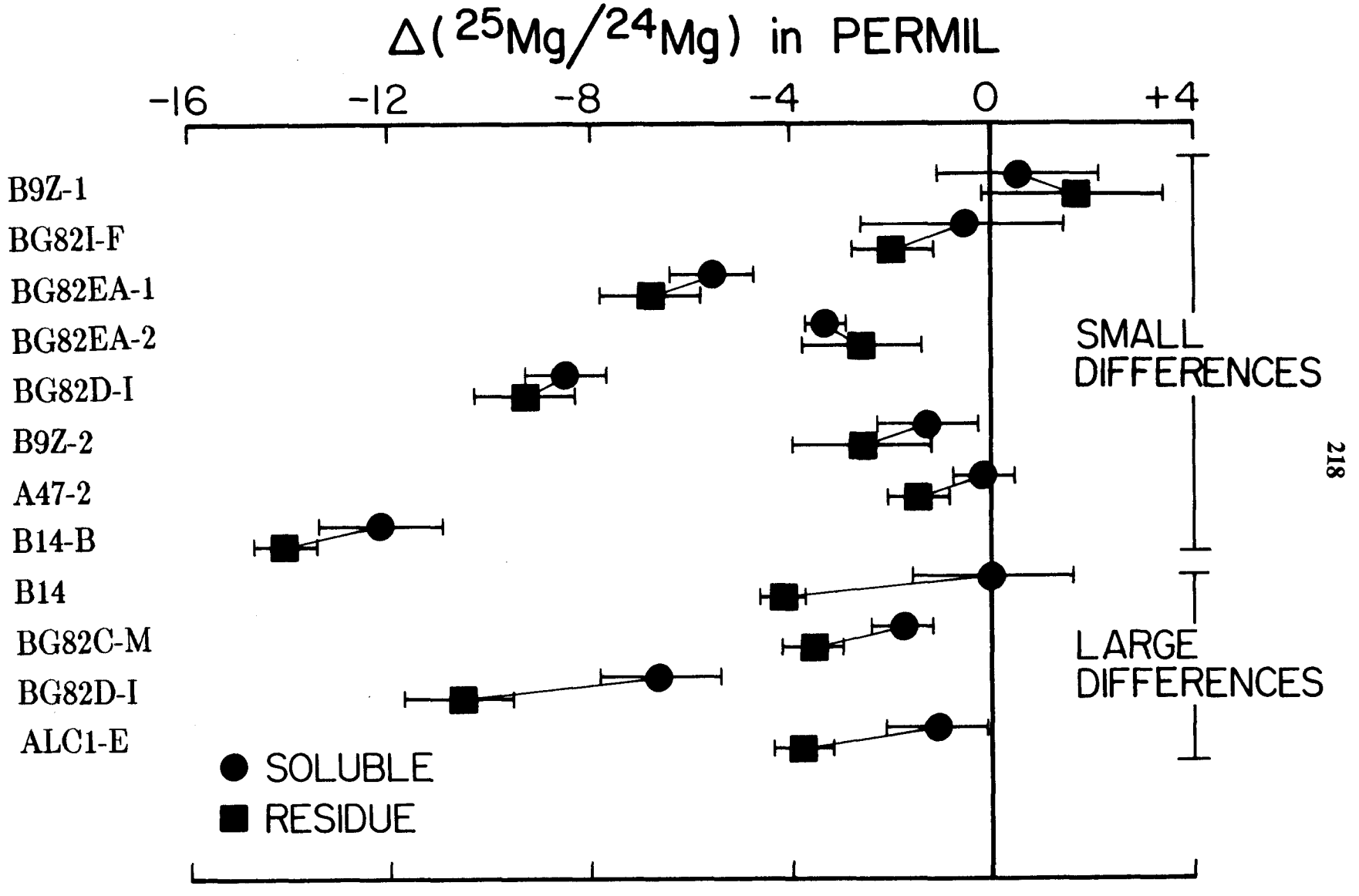
Δ(25Mg/24Mg) in PERMIL
-16
-12
-8
-4
0
+4
B9Z-1
BG82I-F
BG82EA-1
BG82EA-2
BG82D-I
B9Z-2
A47-2
B14-B
B14
BG82C-M
BG82D-I
ALC1-E
SMALL DIFFERENCES
LARGE DIFFERENCES
SOLUBLE
RESIDUE

Inclusion B14 contains a soluble fraction that is isotopically normal; however, the residue exhibits F_{Mg} = -4.2‰. Inclusion BG82D-I exhibits large differences in F_{Mg} between soluble and insoluble phases, ranging from 0.8 to 4‰ amu^{-1}. Two samples of the hibonite residue of BG82D-I, obtained by sampling different regions did not exhibit resolvable differences in fractionation (F_{Mg} = -9.3 and -10.6‰). The soluble fractions exhibited F_{Mg} ranging from -8.5 to -6.6‰. A sample from the island of the inclusion analyzed by DLT exhibited F_{Mg} = -11.1‰. Mg in the sample from the island is predominantly from spinel.

Fifteen of the seventeen fine-grained inclusions analyzed exhibit small excesses in ^{26}Mg (0.7 to 3‰), consistent with ^{26}Mg* contribution from ^{26}Al decay, assuming an initial ratio ($^{26}Al/^{27}Al$) = $5x10^{-5}$, and $^{27}Al/^{24}Mg$ ratios of 2 to 10.

The hibonite-rich inclusion BG82D-I exhibited the broadest range of isotopic effects in $^{26}Mg/^{24}Mg$. This inclusion exhibited large excesses in ^{26}Mg, ranging from 7.3‰ for the spinel-rich islands, 27.7 to 31.6‰ for the soluble, feldspathoid-rich interior, and 47.2 to 56.1‰ for the hibonite residue. There is no correlation between the magnitudes of F_{Mg} and $\delta^{26}Mg$ for these inclusions.

In summary, results obtained using thermal ionization indicate distinct isotopic compositions for fine-grained CAI, with an enrichment in the lighter isotopes of Mg. Isotopic heterogeneity was observed within several inclusions. Substantial ^{26}Mg excesses were observed for a hibonite-rich inclusion.

6.6.2. ION MICROPROBE RESULTS

Mg isotopic results for three Allende fine-grained inclusions (B14-B, BG82EA-1, BG82D-I) are presented in Table 6.4 as F_{Mg}, $\Delta^{26}Mg$, and the Al/Mg ratios in the analyzed crystal. Measured values of $\Delta^{25}Mg$ and $\delta^{26}Mg$ for different mineral standards are shown in the lower part of Table 6.4.

For inclusion B14-B, isotopic data obtained for olivine, spinel, feldspathoids, hedenbergite and fassaite are reported in Table 6.4. All phases exhibited $F_{Mg} < 0$, indicating an enrichment in the lighter isotopes. Spinel and olivine exhibited overlapping F_{Mg}, ranging from -2.2 to -5.8‰ amu^{-1}. The magnitude of F_{Mg} in spinel grains is considerably less than the value of -14‰ amu^{-1} obtained by thermal ionization for the spinel residue. Pyroxenes exhibited a large range in F_{Mg}, ranging from -6.1 to -9.3‰ amu^{-1} for fassaite, while a hedenbergite grain exhibited F_{Mg} of -12 ± 2‰ amu^{-1}.

The total range in F_{Mg} observed for inclusion Bf14-B (-2.2 to -12‰) is significantly larger than the 2‰ difference between soluble and insoluble fractions measured by thermal ionization.

Data for this inclusion plotted on a three isotope correlation diagram (Figure 6.8) lie along a mass fractionation line passing through normal Mg. There is no evidence for $^{26}Mg^*$ in any phase including a feldspathoid with $^{27}Al/^{24}Mg = 38$, corresponding to an upper limit of $(^{26}Mg^*/^{27}Al) \leq 4 \times 10^{-6}$.

Table 6.4. Ion Microprobe Determination of Mg Isotopic Compositions of Allende Fine-grained Inclusions

Sample[a]	F_{Mg}[b] ‰ amu^{-1} ($\pm 2\sigma_{mean}$)	$\delta^{26}Mg$[c] ‰ ($\pm 2\sigma_{mean}$)	$^{27}Al/^{24}Mg$[d]
	ALLENDE BG82DI		
Herc 1-1	-2.5±3.2	15.9±4.2	9.5
Herc 1-4	-1.7±2.3	10.7±3.1	8.7
Herc 1-2	-8.0±3.0	13.3±5.2	7.0
Herc 2	-12.2±5.5	30.0±9.8	14.0
Herc 3	-4.5±2.3	6.1±4.0	6.1
Herc 5	-6.6±2.7	19.2±3.2	20.0
Herc 10-is	-4.8±2.6	10.1±2.6	16.0
Herc 11	+0.4±3.4	17.0±5.2	12.5
Herc 12	-0.9±2.4	4.8±3.3	6.9
Herc 13	-10.2±2.5	22.2±3.7	14.2
Herc 15	-3.2±2.1	20.8±2.4	16
Herc 16	-5.4±1.9	7.8±3.8	4.6
Herc 17	-6.1±1.7	11.7±1.6	6.5
Herc 20	-6.6±3.1	22.7±4.7	32.9
Herc 21	+2.1±2.4	17.8±3.2	21.7
Hed 1	-6.9±3.2	1.2±5.0	2.3
Hed 2	-6.3±1.8	2.4±3.7	2.1
Feld 1	-	42.3±7.1	86
Feld 2	-	37.3±8.8	84
Feld 5-is	-	7.6±6.0	160
Feld 18	-	36.2±5.9	258
Feld 19	-	24.9±11.0	516
	ALLENDE B14B		
Ol 1	-5.5±2.2	1.0±2.1	0.07
Fass 2	-9.2±1.7	0.7±1.4	2.0
Sp 3	-3.4±1.7	-0.3±2.1	3.4
Hed 5	-12 ±2.4	0.3±3.3	0.6
Sp 6	-5.8±1.9	-1.8±1.7	2.0
Feld 8	-	-3.3±5.8	
Ol 9	-2.2±2.2	0.6±1.4	0.1
Ol 10	-3.8±2.3	1.7±2.1	0.5
Fass 11	-6.1±2.5	0.5±3.0	8.8
Feld 12	-	-1.9±2.9	37.8
	ALLENDE BG82EA-1		
Ol 1	-4.1±2.1	0.4±3.2	0.01
Ol 2	-2.7±2.2	0.7±1.8	0.03
Ol 4	-5.1±2.8	4.5±3.3	0.08
Hed 5	-1.2±2.6	-6.1±3.6	0.8
X 6	-	-2.9±2.1	4.7
Feld 7	-	9.9±10.9	315
Feld 8	-	-2.4±6.1	140

Table 6.4 (continued)

	STANDARDS[e]		
	$\Delta^{25}Mg$[f]	$\delta^{26}Mg$	$^{27}Al/^{24}Mg$
Mg-Sp	-13.9±1.2	0.2±2.1	2.1
Herc	-14.5±1.5	-0.7±1.9	4.0
Ol	-12.6±2.0	-0.1±3.0	0.0
Ol Chond	-13.4±1.0	0.8±2.2	0.5
Hed	-9.9±1.4	-3.5±2.3	0.6
Gross	-14.2±2.0	0.8±2.9	
Fass	-11.4±1.5	-2.1±3.0	2.0

[a] Herc = hercynite; Hed = hedenbergite; Feld = feldspathoid; Hib = hibonite; Ol = olivine; Fass = fassaitic pyroxene; Sp = Mg-spinel; Gross = grossular; is = data on islands; chond = ordinary chondrule. Uncertainties are $2\sigma_{mean}$.

[b] Mass-dependent isotope fractionation factor (in permil per atomic mass unit) determined from the raw measured $^{25}Mg/^{24}Mg$ ratios relative to the measured $^{25}Mg/^{24}Mg$ ratios of standards of similar mineralogy analyzed during the same period of time: ($F_{Mg} = \Delta^{25}Mg - \Delta^{25}Mg_{standard}$). The fractionation of feldspathoids is not listed because we have not measured a suitable standard. Uncertainties are $2\sigma_{mean}$.

[c] $\delta^{26}Mg$ is the deviation in $^{26}Mg/^{24}Mg$ from normal after correction for mass-dependent isotope fractionation using $^{25}Mg/^{24}Mg$.

[d] $^{27}Al/^{24}Mg$ is determined from measured ion ratios $^{27}Al^{+}/^{24}Mg^{+}$ corrected for different sensitivity factors for each mineral (see text). The uncertainties (not listed) are estimated at 5% based on the uncertainty in the sensitivity factor (Huneke et al., 1983).

[e] The reported isotopic measurements of standards are averages of repeat analyses. Errors are based on the standard deviation of the mean of the distribution.

[f] $\Delta^{25}Mg$ is the deviation of the measured $^{25}Mg/^{24}Mg$ ratio relative to 0.12663.

Figure 6.8 Three isotope correlation diagram of fractional variations in the raw measured isotopic ratios $\Delta^{25}Mg$ and $\Delta^{26}Mg$ obtained by ion microprobe analysis for inclusion B14-B. Terrestrial standards plot along a mass fractionation line of one-half. Analyses of individual grains of feldspathoid, pyroxene, olivine and spinel plot along the mass fractionation line.

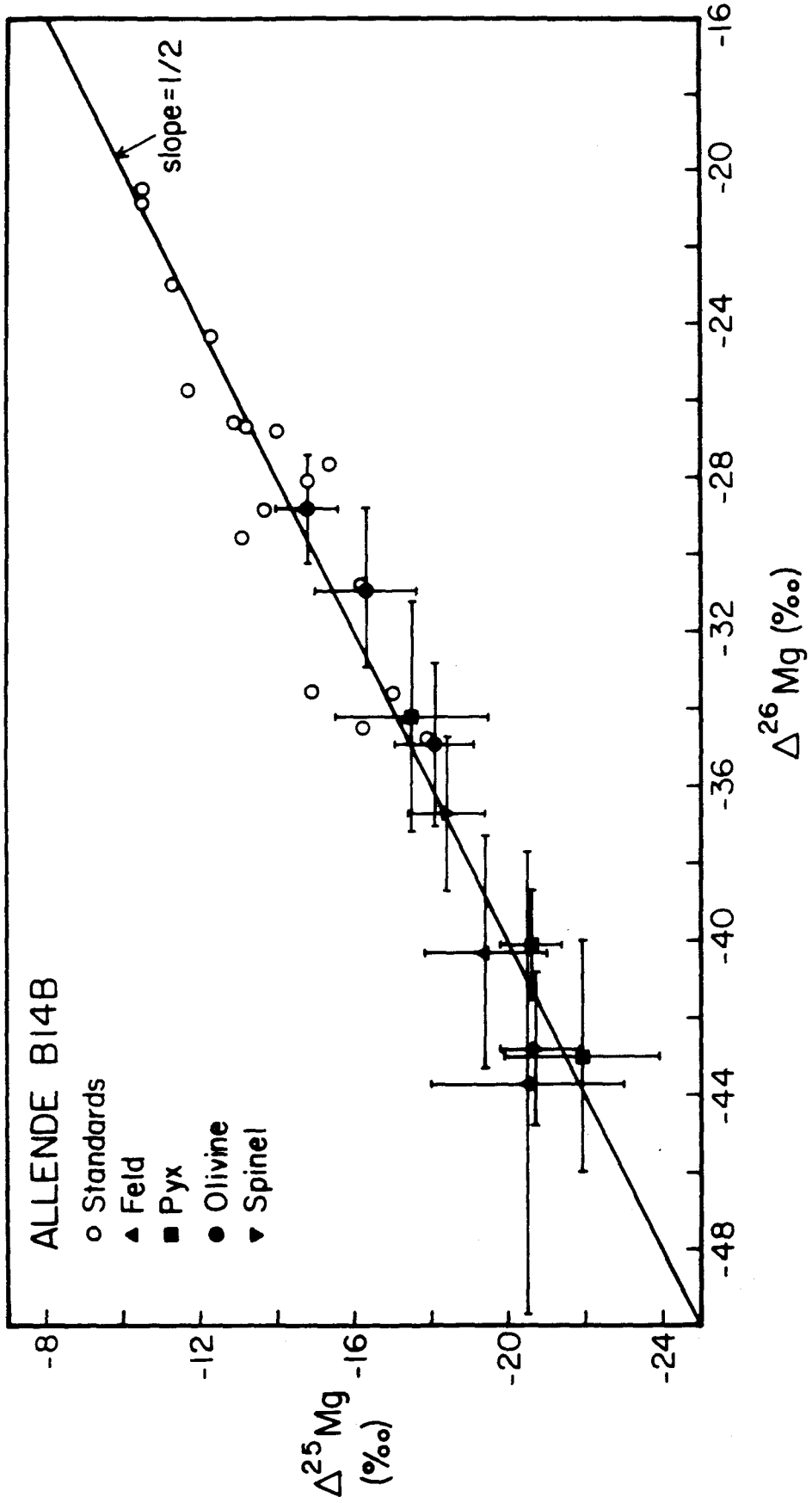
ALLENDE B14B
o Standards
▲ Feld
■ Pyx
● Olivine
▼ Spinel
slope=1/2
-8
-12
-16
-20
-24
-16
-20
-24
-28
-32
-36
-40
-44
-48
Δ^{25}Mg (‰)
Δ^{26}Mg (‰)

Analyses of inclusion BG82EA-1 are shown in Table 6.4. Isotopic data for olivine, hedenbergite and feldspathoid indicate an enrichment in the lighter Mg isotopes; however, all effects are small in this inclusion. Olivine exhibited small fractionation effects, with F_{Mg} ranging from -2.7 to -5.1‰ amu^{-1}. Hedenbergite was unfractionated. One feldspathoid grain (Feld 7) exhibits a large Al/Mg ratio, 315, and no resolvable excess in δ^{26}Mg, placing an upper limit on the initial ratio $(^{26}Al/^{27}Al)_o = 4.5x10^{-6}$ in this phase.

Data are reported for hercynite, feldspathoids and hedenbergite in the interior of inclusion BG82D-I, and for hercynite and feldspathoids in the islands of this inclusion. There is a large range in F_{Mg} within this inclusion (0 to -12‰ amu^{-1}), with an enrichment in the lighter isotopes for all phases. The magnitude of F_{Mg} appears to be correlated with mineralogy. Hedenbergite grains exhibit F_{Mg} of -6‰ amu^{-1}. Hercynite grains exhibit a range in F_{Mg} from 0 to -12‰ amu^{-1}, with no correlation between F_{Mg} and the Mg or Fe content of the hercynite grains (Figure 6.9). A hercynite grain from an island (Herc 10) exhibited F_{Mg} within the range observed for hercynite from the interior of the inclusion. Replicate analyses on a single hercynite grain (Herc 1-1 and 1-4) yield similar F_{Mg} (-2.5 and -1.7‰), showing that the isotopic composition is uniform within this 20 μm grain.

The most fractionated value observed for hercynite in BG82D-I with the ion probe, is similar to the fractionation measured for the hibonite residue of this inclusion obtained by thermal ionization.

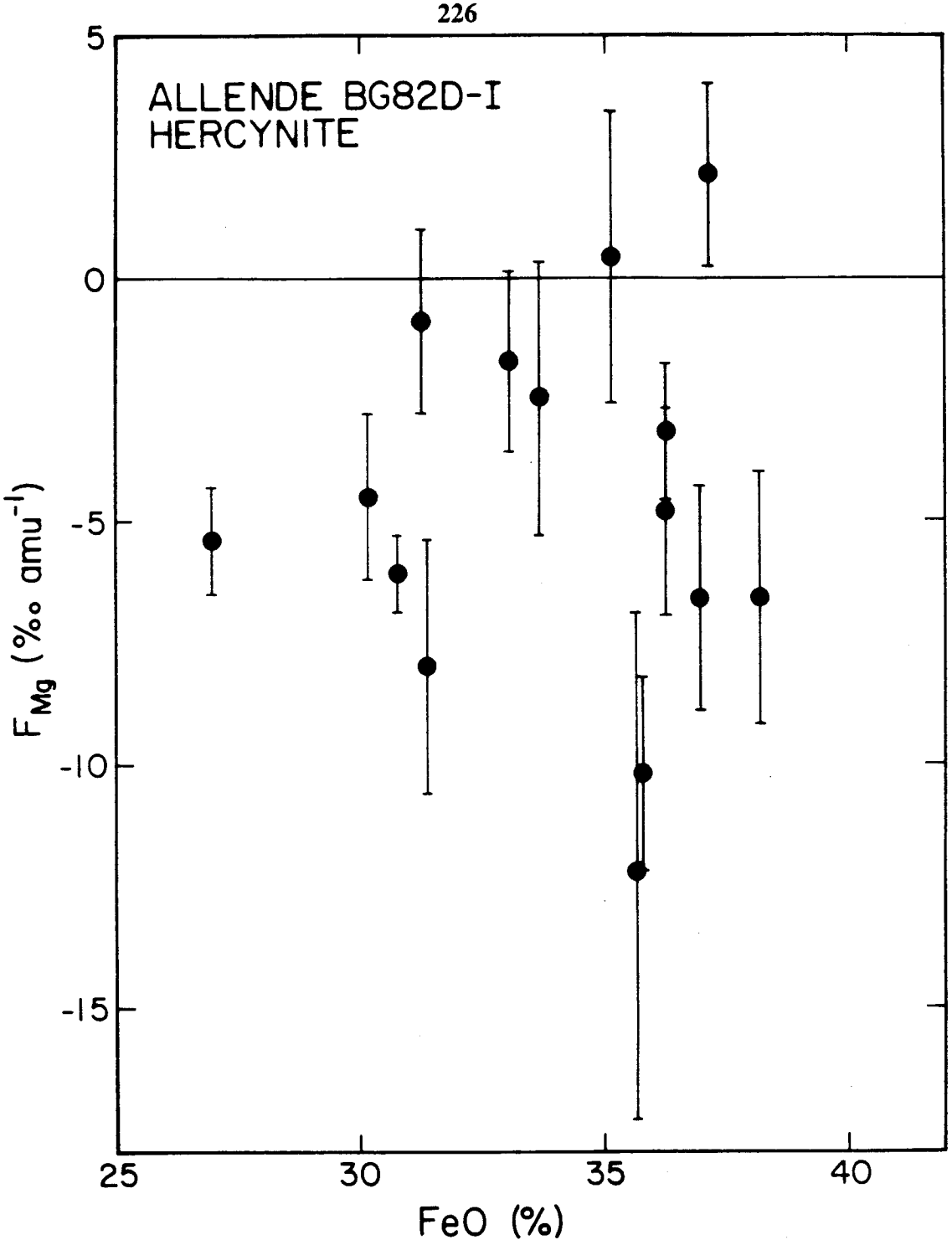

Figure 6.9. Mg fractionation for spinel in Inclusion BG82D-I. There is no correlation of F_{Mg} and FeO content for spinel.

The range in F_{Mg} from the ion probe data (+2.1 to -12.2‰) is significantly larger than the range of 4‰ observed from thermal ionization data.

Data for inclusion BG82D-I plotted on a three isotope correlation diagram (Figure 6.10) lie below and to the right of a mass fractionation line through normal Mg. Several of the hercynite and feldspathoid grains exhibit measured $^{26}Mg/^{24}Mg$ ratios well outside the range of normal isotopic composition, indicating the presence of excess ^{26}Mg in addition to mass fractionation effects.

Figure 6.11 shows the data for inclusion BG82D-I plotted on an ^{26}Al-^{26}Mg evolution diagram. Hedenbergite does not exhibit excess ^{26}Mg. Hercynite and hibonite exhibit substantial excesses in ^{26}Mg, and lie above the reference line of slope $5x10^{-5}$ characteristic of Type B CAI. The data exhibit considerable scatter such that excesses in $\delta^{26}Mg$ are not linearly correlated with Al/Mg ratios; therefore, the data cannot be explained by the single-stage in situ decay of ^{26}Al.

The feldspathoid data exhibit a large range in $^{27}Al/^{24}Mg$ ratios (84 to 516) and in $\delta^{26}Mg$ (7.6 to 42.3‰), and lie both above and well below the reference line. The absence of substantial radiogenic ^{26}Mg is emphasized by a feldspathoid grain with only small excesses in ^{26}Mg ($\delta^{26}Mg = 25 \pm 11$) for $^{27}Al/^{24}Mg = 516$, indicating an initial ratio $^{26}Mg/^{27}Al = 6x10^{-6}$ at the time of formation of this grain.

Figure 6.10 Three isotope correlation diagram of fractional variations in the raw measured isotopic ratios Δ^{25}Mg and Δ^{26}Mg obtained by ion microprobe analysis for inclusion BG82D-I. Terrestrial standards plot along a mass fractionation line of one-half. Analyses of hercynite, hedenbergite and feldspathoid plot below and to the right of the line. Several of the analyses exhibit $^{26}Mg/^{24}Mg$ ratios for standards. Deviations from the fractionation line provide evidence for excess ^{26}Mg.

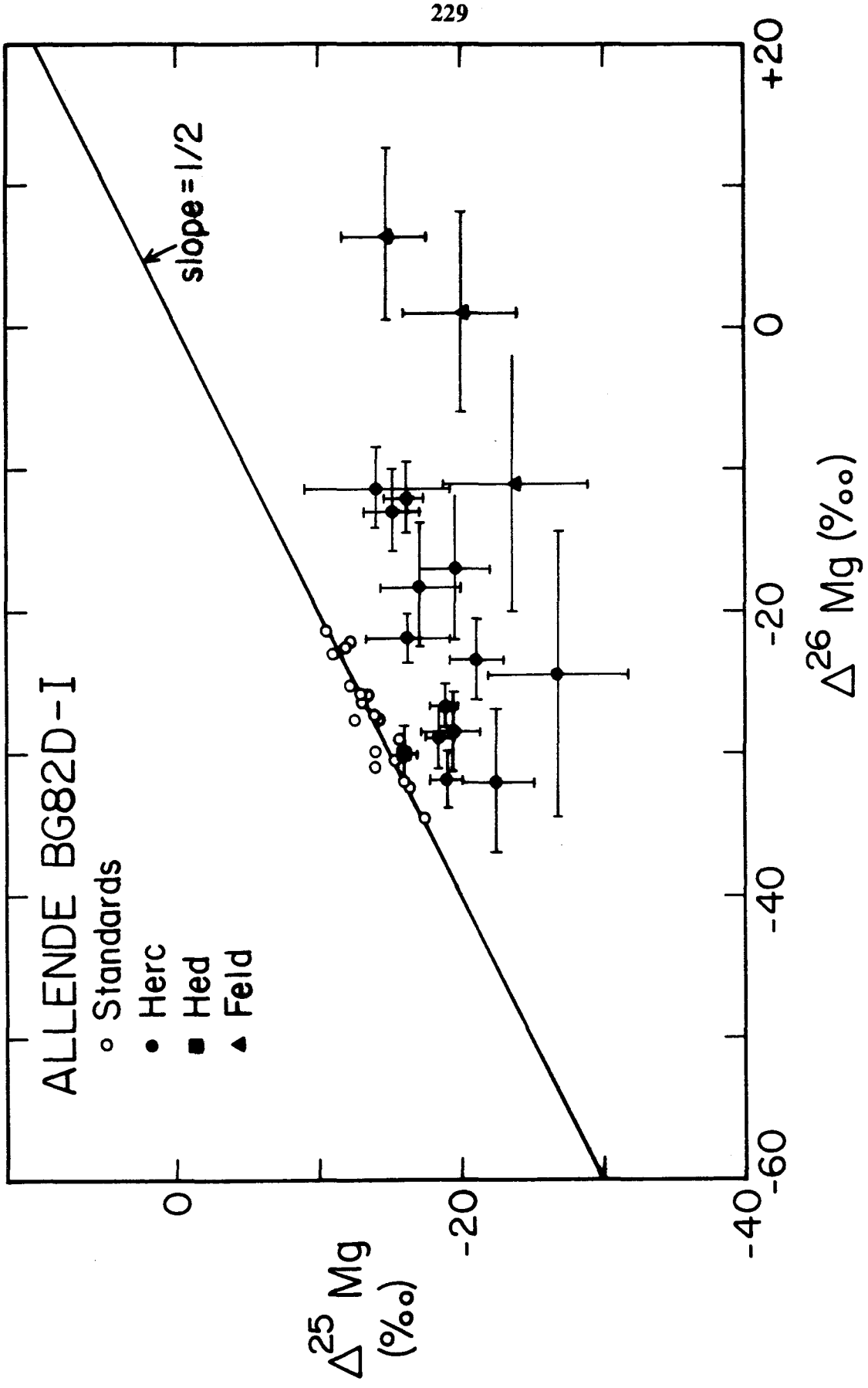
ALLENDE BG82D-I
Standards
Herc
Hed
Feld
slope = 1/2
Δ^{25} Mg (‰)
Δ^{26} Mg (‰)
0
-20
-40
-60
+20
0
-20
-40

Figure 6.11. ^{26}Al-^{26}Mg evolution diagram for inclusion BG82D-I. The residual $\delta^{26}Mg$ (corrected for mass fractionation effects) is plotted against $^{27}Al/^{24}Mg$. The reference line of slope $(^{26}Al/^{27}Al)_o = 5 \times 10^{-5}$, which is observed for most coarse-grained Type B CAI, is shown for reference. The hibonite data obtained by thermal ionization, as well as hercynite and hibonite data obtained by ion microprobe analysis, plot above this reference line, but do not display a linear correlation of $\delta^{26}Mg$ and Al/Mg. Hedenbergite data plot close to the origin. Several of the feldspathoid data exhibit small excesses in $\delta^{26}Mg$ for very large Al/Mg ratios.

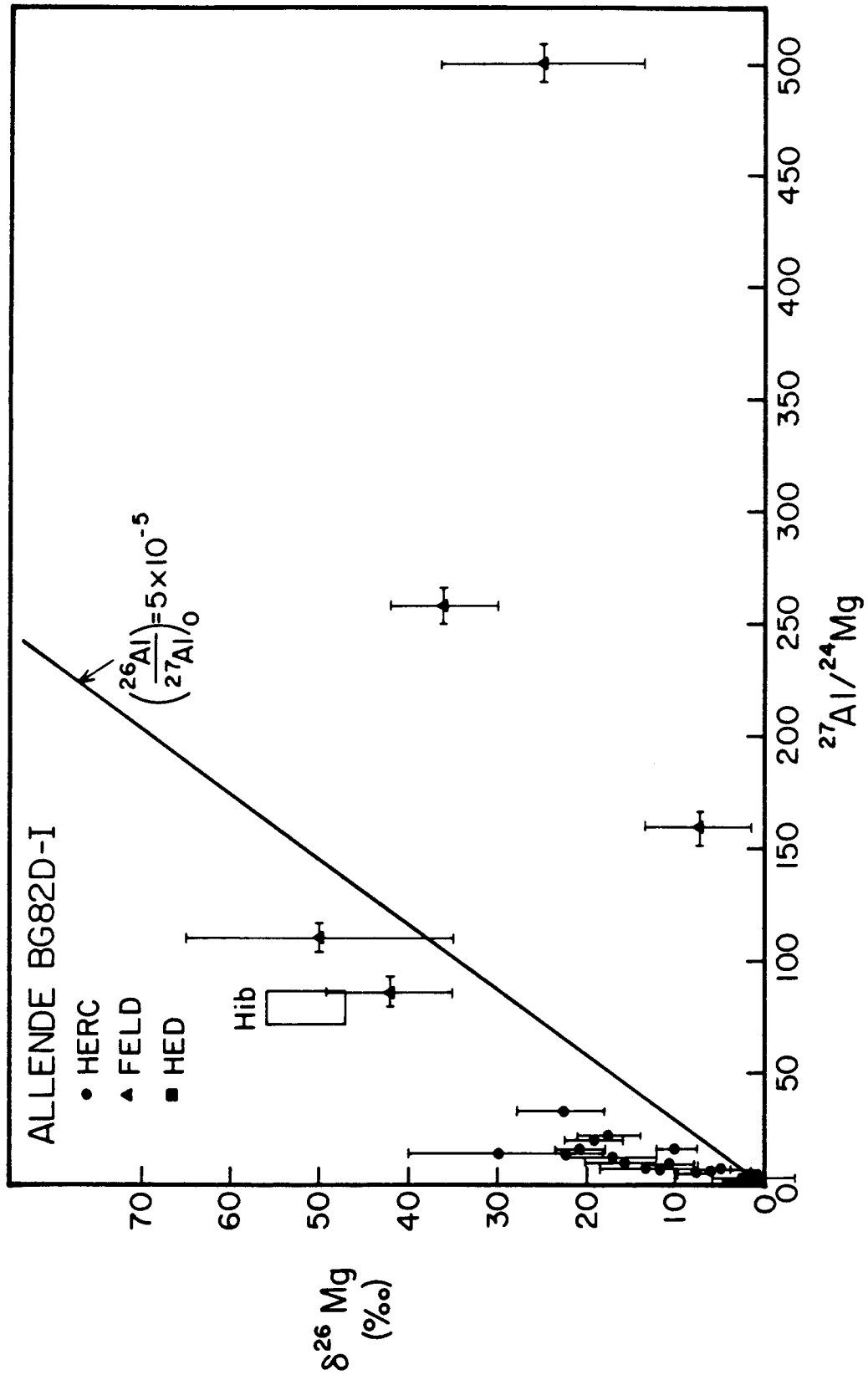
ALLENDE BG82D-I
• HERC
▲ FELD
■ HED
Hib
$\left(\frac{^{26}Al}{^{27}Al}\right)_0 = 5\times10^{-5}$
δ^{26} Mg (‰)
$^{27}Al/^{24}Mg$
0
10
20
30
40
50
60
70
0
50
100
150
200
250
300
350
400
450
500

In summary, the ion microprobe data for these inclusions show $F_{Mg} \leq 0$, indicating an enrichment in the lighter isotopes of Mg. There is no evidence for positive fractionation or for minerals exhibiting extreme F_{Mg}. There is a range in fractionation of 10 and 14‰ amu^{-1} within inclusions B14-B and BG82D-I, and a range of 4‰ for inclusion BG82EA-1. Inclusion BG82D-I exhibited excesses in $\delta^{26}Mg$ that are not correlated with $^{27}Al/^{24}Mg$ ratios.

6.7. DISCUSSION

Fine-grained inclusions are aggregates of low-temperature secondary phases, coupled with high temperature phases. Such non-equilibrium assemblages require a complex history. This study has addressed isotopic constraints on the origins of fine-grained CAI, using a combination of high-precision thermal ionization measurements of microsamples, coupled with high-spatial resolution measurements of individual phases by ion microprobe analysis.

Isotopic compositions derived by these methods can be used as tracers to investigate nebular and planetary formation processes, to investigate the mixing of isotopically distinct reservoirs, and to gain insight on the chronology of formation. In particular, it is of interest to distinguish isotopic effects due to primary formation processes, such as condensation, from those due to secondary processes and later alteration.

6.7.1. PETROGENESIS

Fine-grained inclusions are complex assemblages of refractory phases (e.g. hibonite, spinel, fassaite), coupled with phases enriched in volatile elements (nepheline, sodalite), and Fe-rich phases (hercynitic spinel, hedenbergite, Fe-rich olivine). Due to the lack of unambiguous phase relations in these loosely packed assemblages, it is difficult to distinguish primary and secondary phases solely on the basis of textural relationships. This question is addressed in the following discussion by relating Mg fractionation data with petrographic observations.

Textural relationships do allow several modes of formation to be excluded. The porous, loosely-packed textures of these inclusions, as well as their nonspherical, highly irregular shapes, indicate that they were not formed by crystallization from a melt.

In addition, the assemblages of refractory and volatile phases are inconsistent with formation under equilibrium conditions. The presence of few high-temperature condensates, as well as few intermediate temperature condensates (anorthite, diopside, olivine), and finally, the abundance of phases which are not predicted to be stable condensates from a gas of solar composition (hercynite, hedenbergite, ilmenite, sodalite) indicate that the inclusions did not form by a simple nebular condensation process. Inclusions must have undergone a multistage formation process, or later stage alteration.

Two possible formation mechanisms for fine-grained inclusions include: 1) formation as aggregates of unrelated grains, i.e., condensates (Grossman and

Ganapathy, 1976); and 2) formation by alteration of preexisting, possibly coarse-grained inclusions (MacPherson et al., 1981). Due to their similarity with phase assemblages in the most heavily altered coarse-grained CAI, one potential precursor might have consisted of hibonite, melilite and spinel. If that were the case, the absence of melilite in Allende fine-grained inclusions may be due to complete reaction of melilite to form secondary phases (Wark, 1981; MacPherson et al., 1981). Less heavily altered fine-grained inclusions in Vigarano do contain substantial amounts of melilite (Davis et al., 1987).

Either original source, i.e., a precursor coarse-grained inclusion or an aggregate of primary phases resulting from condensation, must have undergone substantial alteration involving vapor phase reactions over a large range in temperatures to produce the phase assemblages observed in fine-grained inclusions. Starting with a hibonite-spinel-melilite precursor, melilite may be altered to form anorthite, grossular, diopside and nepheline (MacPherson et al., 1981). Alternatively, melilite may have never formed if fine-grained inclusions originated from a region of the nebula depleted in Ca. In a coarse-grained Type A inclusion studied by Allen et al. (1978), fine-grained material consisting of grossular, anorthite, wollastonite, nepheline and sodalite was interpreted as an alteration product of hibonite, melilite and pyroxene. MacPherson et al. (1981) suggest that spinel can be altered to form forsterite and nepheline, with the addition of Si and Na.

The presence in fine-grained inclusions of grossular, which is not stable above 1130°K, and hedenbergite, which is not stable above 1230°K, suggests that alteration reactions occurred below ≈1100°K, and that the inclusions were not

subjected to high temperatures after alteration. Fe-rich phases (hercynitic spinel, hedenbergite, olivine, ilmenite) may result by Fe-Mg exchange during alteration of Mg-spinel, diopside, forsterite and perovskite. In particular, Mg-spinel may undergo Fe-Mg exchange in the nebula at temperatures $\leq$ 1000°K (Saxena and Eriksson, 1983) or in a planetary body. Further alteration and reaction with alkali- and halogen-rich gases is required by the abundance of nepheline and sodalite in fine-grained inclusions. In summary, fine-grained inclusions have been subjected to open-stage vapor phase reactions involving addition of Fe, Si, Na and Cl.

6.7.2. ISOTOPE FRACTIONATION

The three most significant Mg isotopic results for fine-grained inclusions from this study include evidence for: 1) Mg isotope fractionation with an enrichment in the lighter isotopes, ranging 0 to -14‰ amu^{-1}; 2) variable Mg isotopic composition within individual inclusions, but without evidence for extreme isotopic compositions, even on a microscale; 3) a range in Mg fractionation for spinel, which is not correlated with FeO content; and 4) excesses in ^{26}Mg in an inclusion with high Al/Mg, but which are not linearly correlated with $^{27}Al/^{24}Mg$. Formation models consistent with the results must involve isotopic fractionation during formation, followed by partial chemical and isotopic reequilibration.

The magnitude of fractionation observed is within the range expected for a single-stage process involving kinetic effects. Consider a distillation model: the residue becomes increasingly heavy as evaporation proceeds, and can assume any

magnitude of positive fractionation. However, the total vapor cannot exhibit a final fractionation that exceeds the fractionation factor of the process (i.e., -20.6‰ amu^{-1} for Mg). Figure 2.2 clarifies this limit for the vapor.

Similarly, consider condensation with a negative fractionation factor (Section 2.3.4b). The Rayleigh model provides a limit on the total fractionation exhibited by the condensates (-20.6‰ amu-1 for Mg). Figure 2.3 illustrates this limit for condensates.

Enrichment of fine-grained inclusions in the lighter isotopes is consistent with formation as condensates, or as recondensates of material vaporized by the distillation of previously condensed materials (Niederer and Papanastassiou, 1984).

Coarse-grained inclusions exhibit positive Mg fractionation, ranging up to 30‰ amu^{-1}, indicating an enrichment in the heavy isotopes. This difference in the sign of F_{Mg} for coarse-grained and fine-grained inclusions suggests that fine-grained inclusions could not be formed by alteration of coarse-grained inclusions, without the addition of Mg enriched in the lighter isotopes. Similarly, Molini-Velsko et al. (1983) have reported a difference in Si isotope fractionation for coarse-grained and fine-grained inclusions, such that fine-grained inclusions are enriched in the lighter isotopes of Si. The isotope fractionation of Mg and Si appear to be correlated in refractory inclusions since magnesium and silicon are of similar volatility (Clayton et al., 1985).

6.7.3. ISOTOPIC HETEROGENEITY

The Mg isotopic composition is variable within fine-grained inclusions, as indicated by differences in fractionation between acid soluble and insoluble fractions analyzed by thermal ionization, as well as by differences in fractionation between mineral phases analyzed within a single inclusion using the ion microprobe. Isotopic heterogeneity appears to be characteristic of fine-grained inclusions.

Mg isotopic variability within fine-grained inclusions suggests a lack of internal isotopic equilibrium, consistent with mineralogical and textural observations that fine-grained inclusions are aggregates of grains of unequilibrated mineralogy. The isotopic heterogeneity of fine-grained inclusions requires that these inclusions have not been completely melted or rehomogenized.

Isotopic heterogeneity in an inclusion may result from: 1) intrinsic heterogeneity involving preservation of variable kinetic isotope effects during condensation; 2) intrinsic heterogeneity involving formation of inclusions as aggregates of unrelated grains from distinct reservoirs; or 3) later alteration involving addition of variable amounts of normal Mg to inclusions which were originally homogeneous.

Kinetic effects are predicted to produce uniform Mg isotope fractionation for formation by condensation (Niederer and Papanastassiou, 1984), since Mg is cosmochemically abundant and therefore, will not be depleted in the vapor reservoir. The small fraction of Mg that condenses early into refractory inclusions will not cause depletions in the reservoir that would lead to shifts in the isotopic

composition of the condensing Mg. Generation of isotopic heterogeneities by variable kinetic effects during condensation requires a change in composition by the mixing of distinct reservoirs, or a change in pressure and temperature conditions as in a turbulent protoplanetary cloud (Morfill, 1983).

Recondensation of the vapor resulting from distillation of an isotopically normal reservoir may produce a range in fractionation, if the resulting vapor recondenses before being thoroughly mixed. The first cut of vapor resulting from distillation will be enriched in the lighter isotopes by 20‰ amu^{-1}. When ≈62% of the reservoir has been removed by distillation, the vapor will exhibit $F_{Mg} = 0$, assuming a Rayleigh model. Production of a range in F_{Mg}, from -14 to -2‰ amu^{-1}, as observed for one fine-grained inclusion analyzed, would require total recondensation and partial mixing of cuts from a vapor, which result from evaporation of 28 to 58% of the Mg in an isotopically normal reservoir. The residue resulting from this degree of mass loss would exhibit $F_{Mg} = +20‰$. However, few coarse-grained inclusions exhibit extreme F_{Mg} of this magnitude, which is associated with nonlinear isotopic anomalies in FUN inclusions (Wasserburg et al., 1980).

The possibility that the inclusions are aggregates of isotopically unrelated grains formed from distinct nebular reservoirs cannot be excluded. However, no grains of extreme isotopic composition, which might indicate the addition of exotic components, were identified in these inclusions. In addition, no grains exhibited positive F_{Mg}.

Variations in Mg isotopic composition within an inclusion can be attributed to later alteration involving addition of a component containing mass fractionated Mg,

to a reservoir containing normal Mg. This fractionated component must have $F_{Mg} \leq$ -14‰ amu^{-1}, since this is the most fractionated value observed in fine-grained inclusions. Partial isotopic exchange between these two reservoirs would produce a range in isotopic composition within an inclusion, with Mg fractionation varying between the limits $-14 \leq F_{Mg} \leq 0$‰ amu^{-1}. There is no evidence for components exhibiting positive F_{Mg} in fine-grained inclusions, which would require a third isotopic component.

This model is consistent with lower temperature minerals being less fractionated than the earliest formed or least altered phases. The measured F_{Mg} of inclusion B14-B, which ranges from -2‰ amu^{-1} for olivine grains, to -14‰ amu^{-1} for spinel, is consistent with this model. Spinel is the most refractory phase in the inclusion and may be the least altered.

6.7.4. Fe-RICH PHASES

The most abundant minerals in fine-grained inclusions are not predicted to be equilibrium condensates from a gas of solar composition: hercynite or Fe-rich spinel, hedenbergite, andradite, ilmenite, grossular, wollastonite, sodalite and nepheline. These lower temperature phases may have formed by condensation under nonequilibrium conditions, by condensation from a gas of nonsolar composition, or by the alteration of high temperature phases.

Fe-rich minerals such as hedenbergite, hercynite and Fe-bearing olivine must have formed at lower temperatures, but these phases do not contain unfractionated Mg.

Since these phases are not predicted to be stable condensates from a gas of solar composition, it is unlikely that they acquired fractionated Mg by kinetic processes during condensation. In particular, hedenbergite exhibits F_{Mg} ranging up to -12‰ amu^{-1} in one inclusion. Hedenbergite must have formed by chemical and isotopic exchange with a primary phase such as diopside. Similarly, Fe-bearing olivine is not a high temperature condensate; however, olivine is mass fractionated by a few permil in these inclusions. Olivine may have formed by the alteration and isotopic exchange of spinel (MacPherson et al., 1981).

Allen et al. (1980) suggested that the presence of Fe-rich phases in the hibonite-rich inclusion HAL, including an Al-Fe-oxide glass, Ti-Fe-oxide, andradite and Fe-rich olivine, may be due to formation in an oxidizing environment. Oxygen fugacities ranging up to 10^3 to 10^4 times the canonical value may be necessary to form Fe-rich spinel and ilmenite as primary phases in the solar nebula (Fegley and Palme, 1984).

However, isotopic data on hercynite in inclusion BG82D-I, which exhibit $\delta^{26}Mg$ values not correlated with $^{27}Al/^{24}Mg$, suggest that hercynite is a secondary phase. Hercynite may have formed by exchange with fractionated, radiogenic Mg in hibonite after ^{26}Al decay in hibonite. Hercynite and Fe-rich spinel may have condensed as Mg-spinel and undergone Fe-Mg exchange, either in the nebula at temperatures $\leq$ 1000°K (Saxena and Eriksson, 1983) or in a planetary body.

The depletion of fine-grained inclusions in refractory siderophiles (Grossman and Ganapathy, 1976), and the absence of Fe-Ni metal, suggests that Fe-rich spinel did not form by reaction of Mg-spinel with Fe-Ni metal in the inclusions (Kornacki and

Wood, 1985). The lack of correlation between F_{Mg} and FeO content of hercynitic spinel in inclusion BG82D-I (Figure 6.9) requires that Mg was not isotopically exchanged during Fe-Mg exchange. This suggests that exchange did not occur with a reservoir containing chondritic amounts of Fe and Mg.

6.7.5. EXCESS ^{26}Mg

Observations of excesses in ^{26}Mg correlated with $^{27}Al/^{24}Mg$ in a wide variety of CAI (cf. review by Wasserburg and Papanastassiou, 1982) have provided evidence for the in situ decay of ^{26}Al (see Section 2.4.3). Many Type B CAI exhibit a correlation line of slope $(^{26}Al/^{27}Al)_o = 5 \times 10^{-5}$. However, substantially lower and higher initial $(^{26}Al/^{27}Al)_o$ ratios have been observed for Allende CAI; a range in the initial value may be due to formation at different times, or due to heterogeneity in Al isotopic composition. In addition, many Al-rich phases in CAI do not exhibit excesses in ^{26}Mg.

The use of ^{26}Al as a chronometer is limited by uncertainty concerning the heterogeneity of $(^{26}Al/^{27}Al)_o$ and Mg isotopic compositions. Further complications arise from evidence of a nonlinear relation between excess ^{26}Mg and $^{26}Al/^{24}Mg$ in several inclusions (Esat et al., 1978, 1979; Armstrong et al., 1984; Hutcheon, 1982), indicating that the system has been disturbed with partial rehomogenization (Lee et al., 1977).

Most fine-grained inclusions, analyzed by thermal ionization, exhibited small or zero excesses in ^{26}Mg ($\delta^{26}Mg$ = 0.0 to 1.4‰), consistent with their low Al/Mg

ratios, assuming an initial ratio $(^{26}Al/^{27}Al)_o = 5x10^{-5}$, as typically observed for Type B coarse-grained inclusions.

Small excesses in ^{26}Mg in a feldspathoid grain with high $^{27}Al/^{24}Mg$ in inclusion BG82EA-1, analyzed by ion probe, correspond to an upper limit on the initial ratio $(^{26}Al/^{27}Al)_o = 9.4x10^{-6}$. If $^{26}Mg^*$ has not been preferentially lost during alteration, this limit is consistent with formation of feldspathoid in this inclusion at least $1.7x10^6$ years after addition of ^{26}Al to the solar nebula, assuming an initial ratio $(^{26}Al/^{27}Al)_o = 5x10^{-5}$. This timescale for feldspathoid formation may be consistent with volatile addition on small protoplanetary bodies, rather than by condensation. Grossman and Ganapathy suggested that fine-grained inclusions acquired the bulk of their volatile element content during nonequilibrium nebular condensation, along with refractory elements remaining after the condensation of coarse-grained CAI.

The presence of Mg isotopic heterogeneity in fine-grained CAI, as well as evidence for open-system behavior during alteration, limits use of ^{26}Al as a chronometer for fine-grained inclusions. Actual timescales cannot be calculated; however, it is clear that early formation is required by the presence of ^{26}Al.

One hibonite-rich inclusion (BG82D-I) exhibited large excesses in $\delta^{26}Mg$ and large F_{Mg} effects. The data for this inclusion are plotted on a three isotope correlation diagram (Figure 6.12) showing $\delta^{26}Mg$ plotted against F_{Mg}.

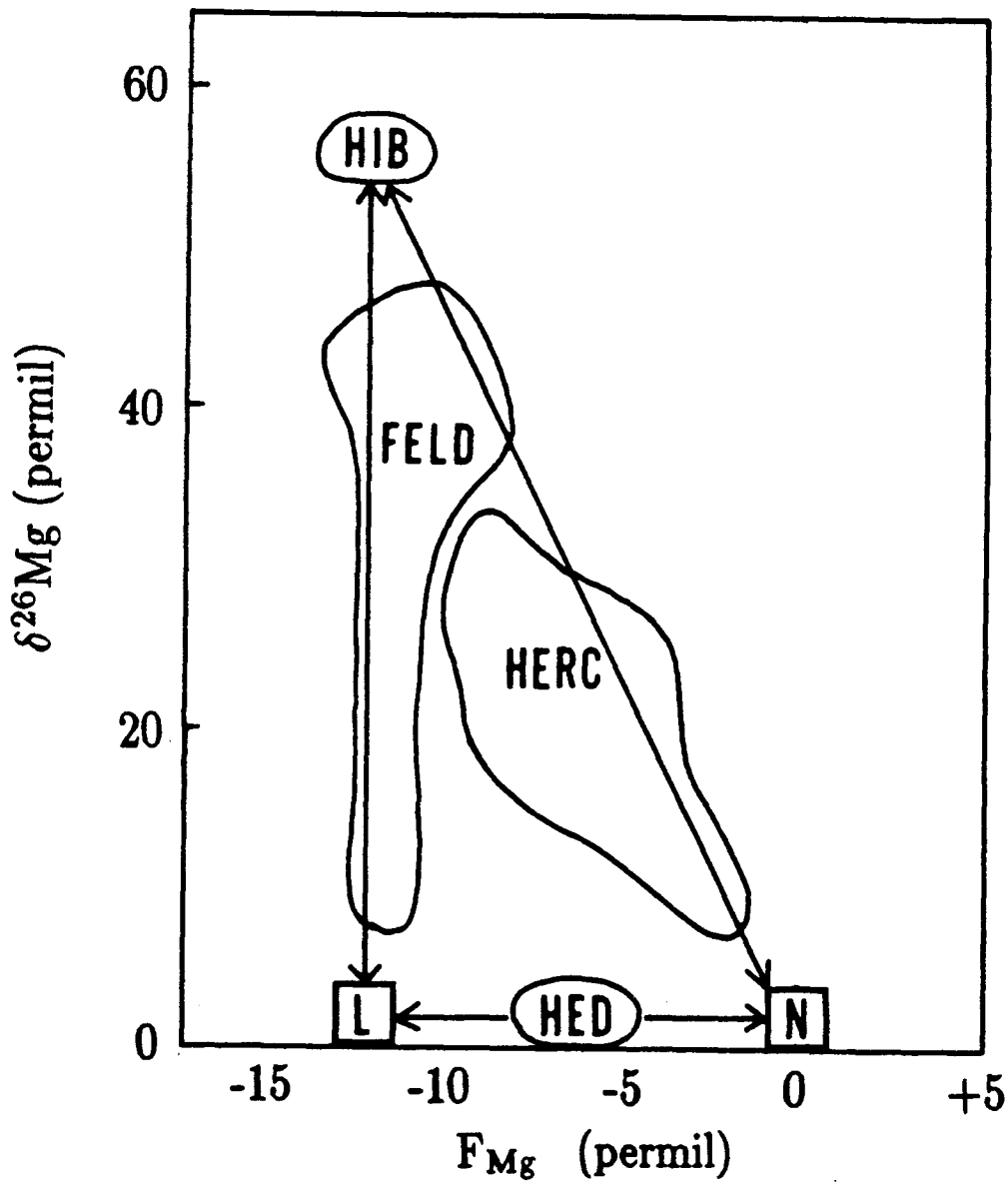

Figure 6.12. Three isotope correlation plot for inclusion BG82D-I. The residual δ^{26}Mg is plotted against F_{Mg}. The ion probe data have been normalized such that F_{Mg} equal to zero corresponds to the value for standards. Data for hibonite, feldspathoid, hercynite and hedenbergite in BG82D-I plot in a triangular region, requiring three distinct isotopic components: a normal unfractionated component (N), a component with zero excess ^{26}Mg and fractionated Mg (L), and a component with fractionated Mg and excess ^{26}Mg.

The data for hibonite, hercynite and hedenbergite in this inclusion plot within a triangular region on the diagram. On this graph, mixtures of two components define a straight line.

The data require formation by mixing of three isotopically distinct components: a normal, unfractionated component (N), a component with fractionated Mg and zero excess ^{26}Mg (L), and a component with fractionated Mg and excess ^{26}Mg (H). The isotopic composition of component H corresponds to the composition of hibonite in the inclusion.

This inclusion may have formed as an aggregate of grains with these three unrelated isotopic compositions, or it may have evolved from an initially uniform isotopic composition. A model involving formation from an initially uniform isotopic composition will be presented in the following section.

Ireland and Esat (1986) observed a linear relation between F_{Mg} and residual δ^{26}Mg for hibonite grains from Murchison, which they interpreted as either a mixing line, or as the result of nonlinear mass fractionation mechanisms similar to those produced in laboratory distillation of Mg (Esat et al., 1980). However, the data do not exhibit a single linear trend, and must be attributed to mixing of more than two components.

6.8. FORMATION OF FINE-GRAINED INCLUSIONS

6.8.1. ISOTOPIC CONSTRAINTS

Constraints on the processes that have affected fine-grained inclusions are provided by the isotopic data. I will first consider the case of inclusions which exhibit fractionated Mg, low $^{27}Al/^{24}Mg$ ratios, and no excesses in ^{26}Mg. The isotopic heterogeneity in these inclusions can be explained by the addition of normal, unfractionated Mg to a component containing fractionated (light) Mg, but no radiogenic ^{26}Mg. The fractionated component must contain isotopically light Mg with $F_{Mg} \leq -14‰$ amu^{-1}. All of this is consistent with formation from a spinel and melilite-rich precursor containing fractionated (light) Mg and Si produced by kinetic processes during condensation. This spinel-rich precursor would have continued to interact with the nebular gases as the temperature dropped. Partial Mg isotopic exchange, with a reservoir containing normal, unfractionated Mg, produced a range in F_{Mg}.

Formation of the hibonite-rich inclusion BG82D-I is more complicated due to the presence of excesses in ^{26}Mg. Data for this inclusion plotted on a three isotope correlation diagram (Figure 6.12) require three isotopically distinct components. A model involving formation from an initially uniform isotopic composition follows. This model postulates a hibonite-rich precursor, containing ^{26}Al and fractionated (light) Mg, produced by kinetic isotope fractionation during condensation. After the

decay of ^{26}Al, hibonite contained excesses in ^{26}Mg, while phases with low Al/Mg ratios contained no excess ^{26}Mg. The hibonite was partially, chemically reequilibrated, such that Mg was extracted into a secondary reservoir (component S). This secondary reservoir contained fractionated Mg, radiogenic ^{26}Mg, little or no ^{26}Al and a low Al/Mg ratio. The hercynite and feldspathoids are secondary phases formed by open-system, vapor phase reactions of the hibonite (component H) with normal Mg (component N). Reaction with a fractionated component of the inclusion with low Al/Mg and no radiogenic ^{26}Mg (component L) is also required to explain the presence of fractionated Mg in hedenbergite. Feldspathoids in BG82D-I formed later by addition of Na and Al. The range in Al/Mg and $\delta^{26}Mg$ for the feldspathoids suggest that there may have been several generations of feldspathoid formation.

With this model, the hercynite data for BG82D-I, which plot well above the standard $5x10^{-5}$ line on the ^{26}Al-^{26}Mg evolution diagram (Figure 6.11), can be explained as a secondary phase. The hercynite has acquired radiogenic ^{26}Mg by isotopic exchange with hibonite.

Alternative explanations for the large excesses in ^{26}Mg observed in the hercynite, include the possibility that the hercynite is primary and 1) formed with a higher initial value of $(^{26}Al/^{27}Al)_o = 10^{-4}$; or 2) that hercynite formed with the standard initial $(^{26}Al/^{27}Al)_o = 5x10^{-5}$, but with an initial excess in ^{26}Mg which corresponds to an offset on the y-axis on the evolution diagram. However, these alternatives are less probable due to the lack of a linear correlation between $\delta^{26}Mg$ and Al/Mg, and would require either initial isotopic heterogeneity or isotopic reequilibration after

^{26}Al decay. These alternatives would also require that hercynite formed before hibonite, or that there were heterogeneities in $(^{26}Al/^{27}Al)_o$.

The model postulates in situ decay of ^{26}Al in hibonite, since hibonite is a probable early condensate with a high Al/Mg ratio.

Although fine-grained inclusions are complex objects, both mineralogically and isotopically, the isotopic data for these inclusions can be explained by a multistage formation process, involving isotopic fractionation produced by kinetic processes during condensation, ^{26}Al decay, followed by partial chemical and isotopic reequilibration with normal Mg without requiring the addition of exotic isotopic components.

6.8.2. GENERAL MODELS

This section summarizes the petrologic, chemical and isotopic differences between coarse and fine-grained CAI, in the context of mechanisms for their formation.

Due to the similarity of phase assemblages in fine-grained inclusions to those assemblages in the most heavily altered coarse-grained inclusions (Allen et al., 1978; Wark, 1981), it has been suggested that fine-grained and coarse-grained inclusions were formed by different degrees of alteration of a melilite-rich precursor (Wark, 1981; MacPherson et al., 1981). Melilite must have been completely reacted away due to its absence in fine-grained inclusions. Formation of fine-grained and coarse-grained inclusions from a similar precursor is constrained by data on isotopic fractionation.

The observation that fine-grained inclusions are enriched in the lighter isotopes of Mg and Si while coarse-grained inclusions are enriched in the heavier isotopes, suggests that fine-grained and coarse-grained inclusions formed from distinct isotopic reservoirs. Alteration of coarse-grained inclusions with positive F_{Mg} will not result in formation of fine-grained inclusions without the addition of light Mg. In addition, Mg isotopic fractionation is heterogeneous within individual fine-grained inclusions, while coarse-grained inclusions generally exhibit uniform fractionation for major phases in the interior.

Coarse-grained inclusions are usually surrounded by a rim sequence containing Fe-bearing spinel, perovskite, feldspathoids, forsterite and hedenbergite (Wark and Lovering, 1977; MacPherson et al., 1981). Wark and Lovering (1977) proposed that fine-grained inclusions are aggregates of the rim material that surrounds coarse-grained inclusions, due to the similarity in mineralogy. Ion probe studies of Mg isotopes in rims surrounding highly fractionated coarse-grained inclusions have shown that the rims are isotopically lighter than the interior of the inclusion (Fahey et al., 1985; Davis et al., 1986). The rims are isotopically normal or slightly positive in F_{Mg}. There is no evidence that rims exhibit negative F_{Mg}, as would be the case if fine-grained inclusions were aggregates of the rim material. It is possible that material with $F_{Mg} < 0$ accreted as rim material around coarse-grained inclusions with $F_{Mg} > 0$, but was isotopically equilibrated with the interior to yield rims with $F_{Mg} \geq 0$. This model is unlikely, since the data of Fahey et al. (1985) yield a gradient from $F_{Mg} = 10‰$ amu^{-1} for interior phases, to isotopically normal Mg for rim phases. The presence of an extreme gradient in isotopic fractionation

over a distance of ≈100 μm, suggests that the rim was not completely isotopically equilibrated with the interior. Therefore, if material with $F_{Mg} < 0$ had been added to the exterior of the inclusion, one would expect to see rims with negative fractionation.

Fine-grained and coarse-grained inclusions exhibit complementary properties in isotopic (e.g., light vs. heavy isotopic enrichments) and chemical data (e.g., REE patterns). Complementary isotopic and chemical reservoirs can be produced by a process involving volatilization of an isotopically normal reservoir, to produce an evaporation residue and a corresponding vapor phase, which recondenses. The residue, which would be enriched in the heavier isotopes, may correspond to a coarse-grained inclusion. The recondensates, enriched in the lighter isotopes, may correspond to fine-grained inclusions. This model is consistent with the difference in the sign of isotopic fractionation for Mg and Si between fine-grained and coarse-grained inclusions. The lack of substantial fractionation for Ca and Ti in coarse-grained inclusions (Niederer and Papanastassiou, 1984; Niederer et al., 1985) suggests that these elements were not significantly volatilized in this process. This model is consistent with chemical data which indicate that fine-grained inclusions are enriched in volatile elements. Fine-grained inclusions exhibit a fractionated rare earth element pattern (Group II) with an enrichment in the more volatile REE and a depletion in the heavier refractory lanthanides. This fractionated REE pattern indicates that an extremely refractory component had previously condensed and been removed (Mason and Martin, 1977; Boynton, 1975).

Fine-grained inclusions may have originated as aggregates of hibonite, Mg-spinel, diopside and melilite, which condensed as primary phases, acquiring fractionated Mg by kinetic processes. These primary phases may have recondensed from a vapor phase resulting from distillation. The primary phases continued to react with gases to temperatures well below 1000°K, either in the solar nebula or on planetary bodies. Chemical exchange and isotopic exchange produced lower temperature, secondary phases such as Fe-spinel, hercynite, hedenbergite and Fe-bearing olivine. Alteration of these porous aggregates with an alkali-rich vapor at low temperatures led to the formation of feldspathoids throughout these inclusions.

The textures and isotopic data for fine-grained inclusions suggest that the inclusions were never completely molten. However, there has been significant element migration during alteration involving addition of Si, Fe and Na. The presence of coarser-grained, compact rims on several of the inclusions suggests that the inclusions may have been flash-heated to form molten rims.

6.9. CONCLUSIONS

I have surveyed a number of fine-grained Ca-Al-rich inclusions from Allende in order to study their petrology and Mg isotopic composition. Isotopic data were obtained by thermal ionization mass spectrometry on acid-soluble and insoluble fractions of these inclusions, while the ion microprobe was used to identify the isotopic compositions of individual grains in inclusions.

The Mg isotopic composition of fine-grained inclusions provides evidence for: 1) Mg isotope fractionation with an enrichment in the light isotopes; 2) variable Mg isotope fractionation within inclusions; but without evidence for extreme isotopic compositions; 3) Mg fractionation for spinel which is not correlated with FeO contents; and 4) excesses in ^{26}Mg that are not linearly correlated with Al/Mg ratios.

The isotopic data indicate that fine-grained inclusions exhibit Mg fractionation effects with an enrichment in the lighter isotopes, ranging up to -14‰. The most fractionated phases in fine-grained inclusions include hibonite and spinel. This fractionation is distinct from that of coarse-grained inclusions, which are enriched in the heavy isotopes of Mg.

Mass-dependent fractionation effects in refractory phases have been interpreted as kinetic isotopic effects due to condensation and evaporation, and can be used as tracers of Mg from distinct reservoirs. Enrichment of fine-grained inclusions in the lighter isotopes is consistent with formation as early condensates, or as recondensates resulting from the distillation of previously condensed materials (Niederer and Papanastassiou, 1984). However, the presence of fractionated Mg in lower temperature phases such as hercynite, hedenbergite, and Fe-rich olivine, which are not predicted to be stable condensates from a gas of solar composition, suggests that these phases must have acquired fractionated Mg, by chemical and isotopic exchange with primary phases.

The isotopic data also indicate a range in F_{Mg} between mineral phases within individual fine-grained inclusions of up to 14‰, suggesting a lack of internal isotopic equilibrium, consistent with textural observations that the inclusions have

not been molten. Isotopic heterogeneity may be attributed to 1) formation of inclusions as aggregates of grains of distinct isotopic composition; or 2) addition of variable amounts of normal Mg during alteration of inclusions. However, no grains of exotic isotopic composition were found in these inclusions; therefore, the isotopic heterogeneity can be attributed to partial isotopic reequilibration with normal Mg.

Distinct from the other fine-grained CAI, one hibonite-rich inclusion exhibited large excesses in ^{26}Mg and large F_{Mg}. Excesses in ^{26}Mg are not linearly correlated with $^{27}Al/^{24}Mg$ ratios, and cannot be explained by the single-stage in situ decay of ^{26}Al. The data are consistent with a multiple stage evolution model, which includes: a) kinetic isotopic fractionation during condensation; b) the presence of live ^{26}Al; c) incomplete chemical and isotopic exchange; and d) exchange with a reservoir containing normal Mg.

In conclusion, the Mg isotopic composition of fine-grained CAI is distinct from that of coarse-grained CAI; therefore, fine-grained inclusions cannot have been formed by the alteration of coarse-grained inclusions without significant transport of major elements. The isotopic heterogeneity of fine-grained CAI indicates that the inclusions have undergone partial chemical and isotopic reequilibration, involving the addition of normal Mg. Although fine-grained inclusions are aggregates of unequilibrated mineral phases, they do not appear to have incorporated grains of exotic isotopic composition.

REFERENCES

Allen J.M., Grossman L., Davis A.M. and Hutcheon I.D. (1978) Mineralogy, textures and mode of formation of a hibonite-bearing Allende inclusion. Proc. Lunar Planet. Sci. 9th, 1209-1233.

Allen J.M., Grossman L., Lee T. and Wasserburg G.J. (1980) Mineralogy and petrography of HAL, an isotopically-unusual Allende inclusion. Geochim. Cosmochim. Acta 44, 685-699.

Anderson C.A. (1973) Analytical methods and applications of the ion microprobe mass analyzer. In Microprobe Analysis (ed. C.A. Anderson), pp. 531-553. New York.

Armstrong J.T. (1982) New ZAF and a-factor correction procedures for the quantitative analysis of individual microparticles. In Microbeam Analysis/1982 (ed. K.F.J. Heinrich), pp. 175-180. San Francisco Press.

Armstrong J.T. (1984) Quantitative analysis of silicate and oxide minerals: a re-evaluation of ZAF corrections and proposal for new Bence-Albee coefficients. In Microbeam Analysis/1984 (eds. A. Romig and J.I. Goldstein), pp. 208-212. San Francisco Press.

Armstrong J.T., Huneke J.C., Shaw H.F., Finnerty T.A. and Wasserburg G.J. (1982) Standard $CaAl_2Si_2O_8$ glasses with various Mg isotopic compositions for ion microprobe characterization. In Microbeam Analysis (ed. K.F.J. Heinrich), pp 205-209. San Francisco Press.

Armstrong J.T., Hutcheon I.D. and Wasserburg G.J. (1984) Disturbed Mg isotope systematics in Allende CAI (abstr.). Lunar Planet. Sci. Conf. XV, 15-16.

Armstrong J.T. and Wasserburg G.J. (1981) The Allende Pink Angel: Its mineralogy, petrology, and the constraints of its genesis (abstr.). Lunar Planet. Sci. Conf. XII, 25-27.

Arnould M., Norgaard, H., Thielmann F.H. and Hillebrand W. (1980) Synthesis of ^{26}Al in explosive hydrogen burning. Astrophys. J. 237: 931-950.

Arrhenius G. and Alfven H. (1971) Fractionation and condensation in space. Earth Planet. Sci. Lett. 10, 253-267.

Barnes I.L., Moore L.J., Machlan L.A., Murphy T.J. and Shields W.R. (1975) Absolute isotopic abundance ratios and the atomic weight of a reference sample of silicon. J. Research NBS 79A, 727-735.

Begemann F. (1980) Isotopic anomalies in meteorites. Rep. Prog. Phys. 43, 1309-1356.

Bence A.E. and Albee A.L. (1968) Empirical correction factors for the electron microanalysis of silicates and oxides. J. Geol. 76, 383-403.

Bigeleison J. and Mayer M.G. (1947) Calculation of equilibrium constants for isotopic exchange reactions. J. Chem. Phys. 15, 261-267.

Birck J.L. and Allegre C.J. (1984) Chromium isotopic anomalies in Allende refractory inclusions. Geophys. Res. Lett. 11, 943-946.

Blander M. and Fuchs L.H. (1975) Calcium-aluminum-rich inclusions in the Allende meteorite: evidence for a liquid origin. Geochim. Cosmochim. Acta 39, 1605-1619.

Blum J.D., Wasserburg G.J., Hutcheon I.D., Beckett J.R. and Stolper E.M. (1988a) Diffusion, phase equilibria and partitioning experiments in the Ni-Fe-Ru system. Geochim. Cosmochim. Acta 53, 483-489.

Blum J.D., Wasserburg G.J., Hutcheon I.D., Beckett J.R. and Stolper E.M. (1988b) Origin of opaque assemblages in C3V meteorites: Implications for nebular and planetary processes. Geochim. Cosmochim. Acta 53: 543-556.

Blum J.D., Wasserburg G.J., Hutcheon I.D., Beckett J.R. and Stolper E.M. (1988c) Domestic Origin of opaque assemblages in refractory inclusions in meteorites. Nature 331, 405-409.

Boynton W.V. (1975) Fractionation in the solar nebula: Condensation of yttrium and the rare elements. Geochim. Cosmochim. Acta 39, 569-584.

Brigham C.A., Hutcheon I.D., Papanastassiou D.A. and Wasserburg G.J. (1986) Evidence for ^{26}Al and Mg isotopic heterogeneity in a fine-grained CAI (abstr.). Lunar Planet. Sci. XVII, 85-86.

Brigham C.A., Hutcheon I.D., Papanastassiou D.A., and Wasserburg G.J. (1988) Isotopic heterogeneity and correlated isotope fractionation in purple FUN inclusions (abstr.). Lunar Planet. Sci. Conf. XIX, 132-133.

Brigham C.A., Hutcheon I.D., Papanastassiou D.A. and Wasserburg G.J. (1988) Isotopic heterogeneity and correlated isotope fractionation in Purple FUN inclusions. Geochim. Cosmochim. Acta (in preparation, 1990).

Brigham C.A., Hutcheon I.D., Papanastassiou D.A. and Wasserburg G.J. (1989) A Petrographic and isotopic study of major phases and opaque assemblages in an Allende FUN inclusion (abstr.). Lunar Planet. Sci. Conf. XX.

Brigham C.A., Papanastassiou D.A. and Wasserburg G.J. (1984) Mg isotopic measurements in fine-grained Ca-Al-rich inclusions (abstr.). Meteoritics 19, 198.

Brigham C.A., Papanastassiou D.A. and Wasserburg G.J. (1985) Mg isotopic heterogeneity in fine-grained Ca-Al-rich inclusions (abstr.). Lunar Planet. Sci. XVI, 93-94.

Brigham C.A., Papanastassiou D.A., Hutcheon I.D., Armstrong J.T. and Wasserburg G.J. (1987) FUN anomalies in purple, spinel-rich refractory inclusions (abstr.). Lunar Planet. Sci. Conf. XVIII, 129-130.

Brigham C.A., Papanastassiou D.A., Hutcheon I.D. and Wasserburg G.J. (1989) Mg isotopic heterogeneity in fine-grained Ca-Al-rich inclusions. Geochim. Cosmochim. Acta (in preparation, 1990).

Catanzaro E.J., Murphy T.J., Garner E.L. and Shields W.R. (1966) Absolute isotopic abundance ratios and atomic weight of Magnesium. J. Res. NBS 70A, 453-458.

Champagne A.E., Howard A.J. and Parker P.D. (1983) Nucleosynthesis of ^{26}Al at low stellar temperatures. Astrophys. J. 269:686-688.

Chen J.H. and Tilton G.R. (1976) Isotopic lead investigations on the Allende carbonaceous chondrite. Geochim. Cosmochim. Acta 40, 635-643.

Chou C.L., Baedecker P.A. and Wasson J.T. (1976) Allende inclusions: Volatile element distribution and evidence for incomplete volatilization of presolar solids. Geochim. Cosmichim. Acta 40, 85-94.

Clarke R.S., Jarosewich E., Mason B., Nelen J., Gomez M. and Hyde J.R. (1970) The Allende, Mexico, Meteorite Shower. Smithon. Contrib. Earth Sci. 5, 1-53.

Clayton D.D. (1982) Cosmic chemical memory: a new astronomy. Quart. J. Roy. Astron. 23, 174-212.

Clayton R.N., Grossman L. and Mayeda T.K. (1973) A component of primitive nuclear composition in a carbonaceous meteorite. Science 182, 485-488.

Clayton R.N., MacPherson G.J., Hutcheon I.D., Davis A.M., Grossman L., Mayeda T.K., Molini-Velsko C., Allen J.M. and El Goresy A. (1984) Two forsterite-bearing FUN inclusions in the Allende meteorite. Geochim. Cosmochim. Acta 48, 535-548.

Clayton R.N. and Mayeda T.K. (1977) Correlated O and Mg isotope anomalies in Allende inclusions: I. Oxygen. Geophys. Res. Lett. 4, 295-298.

Clayton R.N., Mayeda T.K. and Epstein S. (1978) Isotopic fractionation of Si in Allende inclusions. Proc. Lunar Science Conf. 9th, 1267-1278.

Clayton R.N., Mayeda T.K. and Molini-Velsko C.A. (1985) Isotopic variations in solar system material: evaporation and condensation of silicates. In Protostars and Planets. II. (eds. D.C. Black and M.S. Matthews), pp. 755-771. Univ. of Arizona Press.

Clayton R.N., Onuma N., Grossman L. and Mayeda T.K. (1977) Distribution of the presolar component in Allende and other carbonaceous chondrites. Earth Planet. Sci. Lett. 34, 209-224.

Cohen R.E., Kornacki A.S. and Wood J.A. (1983) Mineralogy and petrology of chondrules and inclusions in the Mokoia CV3 chondrite. Geochim. Cosmochim. Acta 47, 1739-1757.

Colby J.W. (1975) Ion Microprobe mass analysis. In Practical Scanning Electron Microscopy (eds. J.I. Goldstein and H.Y. Yakowitz), pp. 529-572. Plenum, New York.

Conard R. (1976) A study of the chemical composition of Ca-Al-rich inclusions from the Allende meteorite. M.S. Thesis, Oregon State.

Davis A.M., MacPherson G.J. and Hinton R.W. (1986) Rims revealed--ion microprobe analysis of individual rim layers in a Vigarano Type A inclusion (abstr.). Meteoritics 21, 349-351.

Davis A.M., MacPherson G.J., Hinton R.W. and Laughlin J.R. (1987) An unaltered Group I fine-grained inclusion from the Vigarano carbonaceous chondrite (abstr.). Lunar Planet. Sci. Conf. XVIII, 223-224.

Eberhardt A., Delwiche R. and Geiss J. (1964) Isotopic effects in single filament thermal ion sources. Z. Naturforschg. 19a, 736-740.

Ekambarum V., Hashimoto A., Davis A.M. and Grossman L. (1985) Trace elements in petrographically distinct components of Allende inclusions. Lunar Planet. Sci. Conf. XVI, 205-206.

El Goresy A., Nagel K. and Ramdohr P. (1978) Fremdlinge and their noble relatives. Proc. Lunar Sci. Conf. 9th, 1279-1303.

Esat T.M. (1988) Physicochemical isotope anomalies. Geochim. Cosmochim. Acta 52, 1409-1429.

Esat T.M., Brownlee D.E., Papanastassiou D.A. and Wasserburg G.J. (1979) Magnesium Isotopic Composition of Interplanetary Dust Particles. Science

206, 190-197.

Esat T.M., Lee T., Papanastassiou D.A. and Wasserburg G.J. (1978) Search for ^{26}Al effects in the Allende FUN inclusion C1. Geophys. Res. Lett. 5, 807-810.

Esat T.M., Papanastassiou D.A. and Wasserburg G.J. (1979) Trials and tribulations of ^{26}Al; evidence for disturbed systems (abstr.). Lunar Planet. Sci. Conf. X, 361-363.

Esat T.M., Spear R.H. and Taylor S.R. (1986) Isotope anomalies induced in laboratory distillation. Nature 319, 576-578.

Esat T.M. and Taylor S.R. (1984) FREE FUN with Mg in Allende Group II inclusions (abstr.). Lunar Planet. Sci. XV, 254-255.

Eugster O., Tera F. and Wasserburg G.J. (1969) Isotopic analyses of barium in meteorites and in terrestrial samples. J. Geophys. Res. 74, 3897-3908.

Fahey A.J., Goswami J.N., McKeegan K.D. and Zinner E. (1985) Evidence for extreme ^{50}Ti enrichments in primitive meteorites. Astrophys. J. Lett. 296, L17-20.

Fahey A.J., Goswami J.N., McKeegan K.D. and Zinner E. (1987) ^{26}Al, ^{244}Pu, ^{50}Ti, REE, and trace element abundances in hibonite grains from CM and CV meteorites. Geochim. Cosmochim. Acta 51, 329-350.

Fahey A.J., Zinner E., Crozaz G., Kornacki A.S. and Ulyanov A.A. (1985) REE and isotopic studies of a coarse-grained CAI from Efremovka (abstr.). Meteoritics 20, 643-644.

Faure G. (1977) Principles of Isotope Geology. John Wiley & Sons, New York.

Fegley B. and Kornacki A.S. (1984) The geochemical behavior of refractory noble metals and lithophile trace elements in refractory inclusions in carbonaceous chondrites. Earth Planet. Sci. Lett. 68, 181-197.

Fegley B. and Palme H. (1985) Evidence for oxidizing conditions in the solar nebula from Mo and W depletions in refractory inclusions in carbonaceous chondrites. Earth Planet. Sci Lett. 72, 311-326.

Fegley B. and Post J.E. (1985) A refractory inclusion in the Kaba CV3 chondrite: some implications for the origin of spinel-rich objects in chondrites. Earth Planet. Sci. Lett. 75, 277-310.

Fireman E., DeFelice J. and Norton E. (1970) Ages of the Allende meteorite. Geochim. Cosmichim. Acta 34, 873-881.

Freer R. (1981) Diffusion in silicate minerals and glasses: A data digest and guide to the literature. Contrib. Mineral. Petrol. 76, 440-454.

Gnaser H. and Hutcheon I.D. (1987) Velocity-dependent isotope fractionation in secondary ion emission. Phys. Rev. B (Condensed Matter) 35, 877-879.

Gnaser H. and Hutcheon I.D. (1988) Preferential emission of lighter isotopes in the initial stage of sputtering. Surface Science 195, 499-512.

Gray C.M., Papanastassiou D.A. and Wasserburg G.J. (1973) The identification of early condensates from the solar nebula. Icarus 20, 213-239.

Grossman L. (1972) Condensation in the primitive solar nebular. Geochim. Cosmochim. Acta 36, 597-619.

Grossman L. (1975a) Petrography and mineral chamistry of Ca-rich inclusions in the Allende meteorite. Geochim. Cosmochim. Acta 39, 433-454.

Grossman L. (1975b) Scanning electron microscopy of a pink inclusion from the Allende meteorite. Geophys. Res. Lett. 2, 37-40.

Grossman L. (1980) Refractory inclusions in the Allende meteorite. Ann. Rev. Earth Planet. Sci. 8, 559-608.

Grossman L. and Ganapathy R. (1975) Volatile elements in Allende inclusions. Proc. Lunar Sci. Conf. 6th, 1729-1736.

Grossman L. and Ganapathy R. (1976) Trace elements in the Allende meteorite: II. Fine-grained Ca-rich inclusions. Geochim. Cosmochim. Acta 40, 967-977.

Grossman L. and Larimer J.W. (1974) Early chemical history of the solar system. Rev. Geophys. Space Phys. 12, 71-101.

Grossman L. and Steele I.M. (1976) Amoeboid olivine aggregates in the Allende meteorite. Geochim. Cosmochim. Acta 40, 149-155.

Hashimoto A. (1983) Evaporation metamorphism in the early solar nebula: Evaporation experiments on the melt FeO-MgO-SiO_2-CaO-Al_2O_3 and chemical fractionations of primitive materials. Geochem. J. 17, 111-145.

Hashimoto A., Davis A.M., Clayton R.N. and Mayeda T.K. (1989) Correlated isotopic mass fractionation of oxygen, magnesium and silicon in forsterite evaporation residues (abstr). Meteorites 52, 84.

Hashimoto A. and Grossman L. (1985) SEM petrography of Allende fine-grained inclusions (abstr.). Lunar Planet. Sci. XVI, 323-324.

Hashimoto A., Kumazawa M. and Onuma N. (1979) Evaporation metamorphism of primitive dust materials in the early solar nebula. Earth Planet. Sci. Lett. 43, 13-26.

Hinton R.W., Davis A.M. and Scatena-Wachel D.E. (1987) Large ^{50}Ti anomalies in refractory inclusions from the Murchison carbonaceous chondrite: Evidence for incomplete mixing of neutron-rich supernova ejecta into the solar system. Astrophys. J. 313, 420-428.

Hoefs J. (1987) Stable Isotope Geology. Springer-Verlag, New York.

Huneke J.C., Armstrong J.T. and Wasserburg G.J. (1983) FUN with PANURGE: High mass resolution ion microprobe measurements of Mg in Allende inclusions. Geochim. Cosmochim. Acta 47, 1635-1650.

Huneke J.C., Armstrong J.T. and Wasserburg G.J. (1983) FUN with PANURGE: High mass resolution ion microprobe measurements of Mg in Allende inclusions. Geochim. Cosmochim. Acta 47, 1635-1650.

Hutcheon I.D. (1982) Ion probe magnesium isotopic measurements of Allende inclusions. In Nuclear and Chemical Dating Techniques: Interpreting the Environmental Record. (ed. L.A. Curie), Amer. Chem. Soc. Symposium Series No. 176, pp. 95-128.

Hutcheon I.D., Armstrong J.T. and Wasserburg G.J. (1987) Isotopic studies of Mg, Fe, Mo, Ru and W in Fremdlinge from Allende refractory inclusions. Geochim. Cosmochim. Acta 51, 3175-3192.

Hutcheon I.D., Hutchison R. and Kennedy A. (1989) Mg isotopes and rare earth abundances in plagioclase from ordinary chondrites: a search for ^{26}Al (abstr.). Lunar Planet. Sci. XX, 434-435.

Hutcheon I.D., Hutchison R. and Wasserburg G.J. (1988) Evidence of the in situ decay of ^{26}Al in a Semarkona chondrule (abstr.) Lunar Planet. Sci. XIX, 523-524.

Hutcheon I.D., Steele I.M., Smith J.V. and Clayton R.N. (1978) Ion microprobe and cathodoluminescence data for Allende inclusions. Proc. 9th Lunar Planet. Sci. Conf. 1345-1368.

Hutcheon I.D., Steele I.M., Wachel D.E.S., MacDougall J.D. and Phinney D. (1983) Extreme Mg fractionation and evidence of Ti isotopic variations in Murchison refractory inclusions (abstr.). Lunar Planet. Sci. XIV, 339-340.

Ireland T.R., Esat T.M. and Compton W. (1986) Magnesium isotopic systematics of Murchison refractory inclusions (abstr.). Lunar Planet. Sci. XVI, 380-381.

Ireland T.R., Fahey A.J. and Zinner E.K. (1989) Isotopic and chemical constraints on the formation of HAl-type refractory inclusions. (abstr.). Lunar Planet. Sci. XX, 442-443.

Kornacki A.S. (1981) Are CAIs condensates or distillation residues? Evidence from a comprehensive survey of fine- to medium-grained inclusions in the Allende (C3V) carbonaceous chondrite. Lunar Planet. Sci. Conf. XII, 562-564.

Kornacki A.S. and Fegley B. (1984) Origin of spinel-rich chondrules and inclusions in carbonaceous and ordinary chondrites. Lunar Planet. Sci. Conf. 14th, 89, B588-596.

Kornacki A.S. and Wood J.A. (1984) Petrography and classification of Ca-Al-rich and olivine-rich inclusions in the Allende CV3 chondrite. Proc. Lunar and Planetary Sci. Conf. 14th, 89, 573-587.

Kornacki A.S. and Wood J.A. (1985) Mineral chemistry and origin of spinel-rich inclusions in the Allende C3V chondrite. Geochim. Cosmochim. Acta 49, 1219-1237.

Larimer J.W. and Anders E. (1970) Chemical fractionations in meteorites. III. Major element fractionations in chondrites. Geochim. Cosmochim. Acta 34:367-387.

Lee T. (1978) A local proton irradiation model for isotopic anomalies in the early solar system. Astrophys. J. 224:217-226.

Lee T. (1979) New isotopic clues to solar system formation. Rev. Geophys. Space Phys. 17, 1591-1611.

Lee T. and Papanastassiou D.A. (1974) Mg isotopic anomalies in the Allende meteorite and correlations with O and Sr effects. Geophys. Res. Lett. 1, 225-228.

Lee T., Papanastassiou D.A. and Wasserburg G.J. (1976) Demonstration of ^{26}Mg excess in Allende and evidence for ^{26}Al. Geophys. Res. Lett. 3, 109-112.

Lee T., Papanastassiou D.A. and Wasserburg G.J. (1977a) Mg and Ca isotopic study of individual microscopic crystals from the Allende meteorite by the direct loading technique. Geochim. Cosmochim. Acta 41, 1473-1485.

Lee T., Papanastassiou D.A. and Wasserburg G.J. (1977b) Aluminum-26 in the early solar system: Fossil or fuel? Astrophys. J. Lett. 211, L107-L110.

Lee T., Papanastassiou D.A. and Wasserburg G.J. (1978) Calcium isotopic anomalies in the Allende meteorite. Astrophys. J. Lett. 220, L21-L25.

Lee T., Russell W.A. and Wasserburg G.J. (1979) Ca isotopic anomalies and the lack of ^{26}Al in an unusual Allende inclusion. Astrophys. J. Lett. 228, L93-L98.

Liebl H. (1975a) The Ion Microprobe. Instrumentation and Techniques. In Secondary Ion Mass Spectrometry (eds. K.F.J. Heinrich and D.E. Newbury) NBS SP-427, pp. 1-31.

Liebl H. (1975b) Ion Probe microanalysis. J. Phys. 8, 797-808.

Lord H.C. III. (1965) Molecular equilibria and condensation in a solar nebula and cool stellar atmosphere. Icarus 4, 279-282.

Lorin J.C. and Christophe-Michel Levy (1978) Radiogenic ^{26}Mg fine-scale distribution in Ca-Al-rich inclusions of the Allende and Leoville meteorites. 4th Intl. Conf. Geochron. Cosmochron., USGS Report 78-701, 257-259.

Love G. and Scott V.D. (1978) Evaluation of a new correction procedure for quantitative electron probe microanalysis. J. Phys. D11, 1369-1376.

MacPherson G.J., Bar-Matthews M., Tanaka T., Olsen E. and Grossman L. (1983) Refractory inclusions in the Murchison meteorite. Geochim. Cosmochim. Acta 47, 823-839.

MacPherson G.J., Davis A.M., Laughlin J.R. and Hinton R.W. (1987) Isotopic heterogeneity in a forsterite-rich FUN inclusion (abstr.). Meteoritics 22, 451-452.

MacPherson G.J. and Grossman L. (1979) Melted and non-melted coarse-grained Ca-Al-rich inclusions in Allende (abstr.). Meteoritics 14, 479.

MacPherson G.J. and Grossman L. (1982) Fine-grained spinel-rich and hibonite-rich Allende inclusions (abstr.). Meteoritics 17, 245-246.

MacPherson G.J. and Grossman L. (1984) Fluffy Type A Ca-, Al-rich inclusions in the Allende meteorite. Geochim. Cosmochim. Acta 48, 29-46.

MacPherson G.J., Grossman L., Allen, J.M. and Beckett J.R. (1981) Origin of rims on coarse-grained inclusions in the Allende meteorite. Proc. Lunar Planet. Sci. 12th, 1079-1091.

MacPherson G.J., Hashimoto A. and Grossman L. (1985) Accretionary rims on inclusions in the Allende meteorite. Geochim. Cosmochim. Acta 49, 2267-2279.

Mahoney W.A., Ling J.C., Wheaton W.A. and Jacobsen A.S. (1984) HEAO-3 Discovery of ^{26}Al in the interstellar medium. Astrophys. J. 286, 578-585.

Manhes D., Gopel C. and Allegre C.A. (1987) Terra Cognita 7, 137.

Marvin U.B., Wood J.A. and Dickey J.S. Jr. (1970) Ca-Al-rich phases in the Allende meteorite. Earth Planet. Sci. Lett. 7, 346-350.

Mason B. and Martin P.M. (1977) Geochemical differences among components of the Allende meteorite. Smithson. Contrib. Earth Sci. 19, 84-95.

McGuire A.V. and Hashimoto A. (1988) Origin of zoned Allende fine-grained inclusions (abstr.). Lunar Planet. Sci. Conf. XIX, 754-755.

McSween H.Y. (1977a) Chemical and petrographic constraints on the origin of chondrules and inclusions in carbonaceous chondrites. Geochim. Cosmochim. Acta 41, 1843-1860.

McSween H.Y. (1977b) Petrographic variations among carbonaceous chondrites of the Vigarano type. Geochim. Cosmochim. Acta 41, 1777-1790.

Meeker G.P., Wasserburg G.J. and Armstrong J.T. (1983) Replacement textures in CAI and implications regarding planetary metamorphism. Geochim. Cosmochim. Acta 47, 707-721.

Molini-Velsko C., Mayeda T.K. and Clayton R.N. (1983) Silicon isotopes in components of the Allende meteorite (abstr.). Lunar Planet. Sci. XIV, 509-510.

Molini-Velsko C., Mayeda T.K. and Clayton R.N. (1987) Silicon isotope systematics during distillation. Lunar Planet. Sci. XVIII, 657-658.

Morfill G.E. (1983) Some cosmochemical consequences of a turbulent protoplanetary cloud. Icarus 53, 41-54.

Niederer F.R. and Papanastassiou D.A. (1984) Ca isotopes in refractory inclusions. Geochim. Cosmochim. Acta 48, 1279-1293.

Niederer F.R., Papanastassiou D.A. and Wasserburg G.J. (1980) Endemic isotopic anomalies in titanium. Astrophys. J. 240, 73-77.

Niederer F.R., Papanastassiou D.A. and Wasserburg G.J. (1981) The isotopic composition of Ti in the Allende and Leoville meteorites. Geochim. Cosmochim. Acta 45, 1017-1031.

Niederer F.R., Papanastassiou D.A. and Wasserburg G.J. (1985) Absolute isotopic abundances of Ti in meteorites. Geochim. Cosmochim. Acta 49, 835-851.

Oppenheim I. and Friedman A.S. (1961) Quantum statistical mechanics of isotope

effects. J. Chem. Phys., 35, 35-40.

Packwood R.H. and Brown J.D. (1981) A Gaussian expression to describe o(pz) curves for electron probe microanalysis. X-ray Spectrometry 10, 138-146.

Palme H. and Wlotzka F. (1976) A metal particle from a Ca-Al-rich inclusion from the meteorite Allende, and the condensation of siderophile elements. Earth Planet. Sci. Lett. 33, 45-60.

Papanastassiou D.A. (1986) Chromium isotopic anomalies in the Allende meteorite. Astrophys. J. Lett. 308, L27-L30.

Papanastassiou D.A. and Brigham C.A. (1987) FUN isotopic anomalies: Reincarnation in purple refractory inclusions (abstr.). Lunar Planet. Sci. Conf. XVIII, 756-757.

Papanastassiou D.A. and Brigham C.A. (1988) Correlated, large isotope effects in purple, spinel-rich inclusions (abstr.). Lunar Planet. Sci. Conf. XIX, 899-900.

Papanastassiou D.A. and Brigham C.A. (1988) The identification of FUN inclusions. Astrophys. J. Lett. 338, L37-L40.

Papanastassiou D.A. and Wasserburg G.J. (1983) The ongoing search for FUN inclusions (abstr.). Meteoritics 18, 370-371.

Papanastassiou D.A. and Wasserburg G.J. (1987) Rayleigh distillation constraints on Mg isotopic composition. Lunar Planet. Sci. XVIII, 758-759.

Podosek F.A. (1978) Isotopic structures in solar system materials. Ann. Rev. Astron. Astrophys. 16, 293-334.

Porter R.F., Chupka W.A. and Inghram M.G. (1954) J. Phys. 10, 216-217.

Rayleigh J.W.S. (1896) Theoretical considerations respecting the separation of gases by difffusion and similar processes. Philosoph. Magazine, 42, 493-498.

Rayleigh J.W.S. (1902) On the distillation of binary mixtures. Philosoph. Magazine, 4, 521-537.

Reddy K.P.R. and Cooper A.R. (1981) Oxygen diffusion in magnesium aluminate spinel. J. Am. Ceram. Soc. 64, 368-371.

Reynolds J.H. (1960) Determination of the age of the elements. Phys. Rev. Letters 4, 8-10.

Robert F., Halbout J. and Baudon J. (1988) A non-mass dependent isotopic fractionation effect. Earth Planet. Sci. Lett. 91, 231-238.

Russell W.A., Papanastassiou D.A. and Tombrello T.A. (1978) Ca isotope fractionation on the earth and other solar system materials. Geochim. Cosmochim. Acta 42, 1075-1090.

Russell W.A., Papanastassiou D.A. and Tombrello T.A. (1980) The fractionation of Ca isotopes by sputtering. Rad. Effects 52, 41-52.

Saxena S.K. and Eriksson G. (1983) Low-to-medium-temperature phase equilibria in a gas of solar composition. Earth Planet. Sci. Lett. 65, 7-16.

Schramm D.N., Tera F. and Wasserburg G.J.(1970) The isotopic abundance of ^{26}Mg and limits on ^{26}Al in the early solar system. Earth Planet. Sci. Lett. 10, 44-59.

Schroeer J.M. (1975) An outline of secondary ion emission models. In Secondary Ion Mass Spectrometry (eds. K.F.J. Heinrich and D.E. Newbury), NBS SP-427, pp. 121-127.

Shimamura T., Jungck M.H.A. and Lugmair G.J. (1983) Allende inclusion "TE": Is there FUN with UN? (abstr.) Meteoritics 18, 396.

Shimizu N. and Hart S.R. (1982) Applications of the ion microprobe to geochemistry and cosmochemistry. Ann. Rev. Earth Planet. Sci. 10, 483-526.

Sigmund P. (1981) In Sputtering by Particle Bombardment: Theoretical Concepts. Vol. 1, p. 9-71. Springer-Verlag.

Simonton J.R., Rightmire R.A., Long A.L. and Kohmon T.P. (1954) Phys. Rev. 96, 1711.

Slodzian G. (1975) Some problems encountered in secondary ion emission applied to elementary analysis. Surface Sci. 48, 161-186.

Slodzian G. (1980) Adv. Electron. Phys. Suppl. 13B, 1-32.

Slodzian G., Lorin J.C. and Havette A. (1980) Isotopic effects on the ionization probability in secondary ion emission. J. Physique Lett. 41, L555-558.

Stolper E. (1982) Crystallization sequences of Ca-Al-rich inclusions from Allende: An experimental study. Geochim. Cosmochim. Acta 46, 2159-2180.

Stolper E., Paque J. and Rossman G.R. (1982) The influence of oxygen fugacity and cooling rate on the crystallization of Ca-Al-rich inclusions from Allende. (abstr.) Lunar Planet. Sci. Conf. XIII, 772-773.

Tatsumoto M., Unruh D.M. and Desborough G.A. (1976) U-Th-Ph and Rb-Sr

systematics of Allende and U-Th-Pb systematics of Orgueil. Geochim. Cosmochim. Acta 40:617-634.

Thiemens M.H. and Heidenreich J.E. (1983) The mass-independent fractionation of oxygen: a novel isotope effect and its possible cosmochemical implications. Science 219, 1073-1074.

Thode H.G., Cragg C.B., Hulston J.R., Rees C.E. (1971) Sulfur isotope exchange between sulfur dioxide and hydrogen sulfide. Geochim. Cosmochim. Acta 35, 35-45.

Truran J.W. and A.G.W. Cameron (1978) ^{26}Al production in explosive carbon burning. Astrophys. J. 219: 226-229.

Urey H.C. (1947) The thermodynamic properties of isotopic substances. J. Chem. Soc. 1, 562-581.

Wanke H., Baddenhausen H., Palme H. and Spettel B. (1974) On the chemistry of the Allende inclusions and their origin as high-temperature condensates. Earth Planet. Sci. Lett. 23.1-7.

Wark D.A. (1978) Early solar system stratigraphy (abstr.). Lunar Planet. Sci. IX, 1208-1210.

Wark D.A. (1979) Birth of the presolar nebula: the sequence of condensation revealed in the Allende meteorite. Astrophys. Space Sci. 65, 275-295.

Wark D.A. (1981) Alteration and metasomatism of Allende Ca-Al-rich materials (abstr.). Lunar Planet. Sci. XII, 1145-1147.

Wark D.A. (1983) The Allende meteorite: Information from Ca-Al-rich inclusions on the formation and early evolution of the solar system. Ph.D. Thesis, Univ. of Melbourne.

Wark D.A. (1987) Plagioclase-rich inclusions in carbonaceous chondrite meteorites: Liquid condensates? Geochim. Cosmochim. Acta 51, 221-242.

Wark D.A. and Lovering J.F. (1976) Refractory/platinum metal grains and Allende Calcium-aluminum-rich clasts (CARC's): Possible exotic presolar material? Lunar Sci. VIII, 912-914.

Wark D.A. and Lovering J.F. (1977) Marker events in the early evolution of the solar system: Evidence from rims on Ca-Al-rich inclusions in carbonaceous chondrites. Proc. Lunar Sci. Conf. 8th, 95-112.

Wasserburg, G.J. (1986) Short-lived nuclei in the early solar system. In Protostars and Planets, II. (eds. D.C. Black and M.S. Matthews) pp. 703-737. Univ.

Arizona Press.

Wasserburg, G.J. and Hayden R.J. (1955) Time interval between nucleogenesis and the formation of meteorites. Nature 176, 130.

Wasserburg G.J., Lee T. and Papanastassiou D.A. (1977) Correlated O and Mg isotopic anomalies in Allende inclusions: II. Magnesium. Geophys. Res. Lett. 4, 299-302.

Wasserburg G.J. and Papanastassiou D.A. (1982) Some short-lived nuclides in the early solar system--a connection with the placental ISM. In Essays in Nuclear Astrophysics (eds. C.A. Barnes, D.D. Clayton, D. Schramm), pp. 77-140. Cambridge University Press.

Wasserburg G.J., Papanastassiou D.A. and Lee T. (1980) Isotopic heterogeneities in the solar system. In Early Solar System Processes and the Present Solar System, pp. 144-191. Soc. Italiana di Fisica, Bologna.

Wasserburg G.J., Papanastassiou D.A., Nenow E.V. and Bauman C.A. (1969) A programmable magnetic field mass spectrometer with on-line data processing. Rev. Sci. Instr. 40, 288-295.

Werner H.W. (1974) Theoretical and experimental aspects of secondary ion mass spectrometry. Vacuum 24, 493-504.

Williams P. (1979) The sputtering process and sputtered ion emission. Surface Science 90, 588-634.

Williams P. (1983) Secondary Ion Mass Spectrometry. Appl. Atomic Collision Phys. 4, 327-377.

Williams P. (1985) Secondary Ion Mass Spectrometry. Ann. Rev. Mater. Sci. 15, 517-548.

Woosley S.E. and Weaver T.A. (1982) Nucleosynthesis in two 25M stars of different population. In Essays in Nuclear Astrophysics, eds. C.A. Barnes, D.D. Clayton and D.N. Schramm (Cambridge University Press) pp. 401-426.

Zinner E.K., Caillet C., El Goresy A. (1989) Mg and O isotopic compositions of periclase, spinel and melilite from Vigarano CAI 477B. Lunar Planet. Sci. Conf. XX, 1245-1246.

Zinner E.K., Fahey A.J., Goswami J.N., Ireland T.R. and McKeegan K.D. (1986). Large ^{48}Ca anomalies are associated with ^{50}Ti anomalies: Murchison and Murray hibonites. Astrophys. J. Lett. 311, L103-107.